

# ACTIVATION AND ASSEMBLY OF MEMBRANE REMODELING ESCRT-III MACHINERY

A Dissertation

Presented to the Faculty of the Graduate School

of Cornell University

in Partial Fulfillment of the Requirements for the Degree of

Doctor of Philosophy

by

Shaogeng Tang

August 2016

© 2016 Shaogeng Tang

# ACTIVATION AND ASSEMBLY OF MEMBRANE REMODELING ESCRT-III MACHINERY

Shaogeng Tang, Ph.D.

Cornell University, 2016

The endosomal sorting complexes required for transport (ESCRTs) constitute hetero-oligomeric machines that catalyze numerous topologically equivalent membrane-remodeling processes, including multivesicular endosome biogenesis, enveloped virus budding, cytokinesis and nuclear envelope reformation. ESCRT-III subunits polymerize into spiraling filaments on lipid membrane surfaces. Understanding the protein-membrane and protein-protein associations within the ESCRT-III polymer is important for elucidating this membrane-sculpting mechanism. Snf7, the human CHMP4 ortholog in the model organism *Saccharomyces cerevisiae*, is the most abundant ESCRT-III subunit. Using a combination of genetic and biochemical approaches, two essential modules were identified required for ESCRT-III-membrane association: an electrostatic cluster and an N-terminal insertion motif. Snf7 has been tuned to maintain the topological constraints associated with ESCRT-III-mediated membrane invagination and vesicle formation.

Although ESCRT-III polymerizes into spirals, how individual subunits are activated and assembled together into a membrane-deforming filament remained unknown. I determined the first X-ray crystal structures of the Snf7 protofilament in its active conformation. Using pulsed dipolar electron spin resonance spectroscopy, I

showed that Snf7 activation requires a prominent conformational rearrangement to expose protein-membrane and protein-protein interfaces. This promotes the assembly of Snf7 arrays with ~30 Å periodicity into a membrane-sculpting filament. Using a combination of biochemical and genetic approaches, I demonstrated that mutations on these protein interfaces halt Snf7 assembly *in vitro* and block ESCRT function *in vivo*.

To dissect the coordination of ESCRT-III activation by the upstream ESCRT components at endosomes, I characterized novel mutations in ESCRT-III Snf7 that trigger activation and assembly *in vivo*. I showed that upstream ESCRTs regulate Snf7 activation at both its N-terminal core domain and the C-terminus α6 helix through two parallel ubiquitin-dependent pathways: the ESCRT-I-ESCRT-II-Vps20 pathway and the ESCRT-0-Bro1 pathway.

My dissertation provides a fundamental advance in the understanding of the molecular mechanisms underlying ESCRT-III conformational dynamics in activation, assembly and membrane binding, and thus gives crucial insights into ESCRT-dependent membrane remodeling required for diverse biological processes.

## BIOGRAPHICAL SKETCH

Shaogeng “Steven” Tang grew up in Beijing, China. In 2006, he was recruited into a B.S./M.S program in Pharmacy at Peking University. While in college, Steven developed a strong interest in biomedical and pharmaceutical research. He did his B.S. thesis in the laboratory of Dr. Zhongjun Li, developing the hydrophobically assisted switching phase (HASP) method in oligomannoside assembly for drug synthesis. In 2010, he decided to immigrate to the United States of America after his undergraduate studies. He graduated from Peking University with a B.S. in Pharmacy, without continuing the M.S. training program.

In 2011, Steven became a Ph.D. student in the field of Biochemistry, Molecular and Cell Biology (BMCB) at Cornell University. In 2012, he joined the laboratory of Dr. Scott D. Emr in the Weill Institute for Cell and Molecular Biology and began his dissertation work on understanding the activation and assembly of the endosomal sorting complex ESCRT-III membrane remodeling machinery. While at Cornell, he was a recipient of the Harry and Samuel Mann outstanding graduate student award. In 2015, he became a citizen of the United States of America in Syracuse, New York.

After graduation from Cornell in 2016, Steven will become a postdoctoral scholar with Dr. Peter S. Kim in the institute of ChEM-H at Stanford University to study the mechanism of viral membrane fusion and its inhibition by drugs and antibodies.

This work is dedicated to my dear father Guoyao Tang  
and mother Li Zhang, Ph.D.

此博士毕业论文献给我亲爱的父亲唐国尧和母亲张黎

## **ACKNOWLEDGMENTS**

I have truly enjoyed my time as a graduate student at Cornell University. I have been so fortunate to work in a highly collaborative environment and interact with many incredibly talented and helpful people. Without those who have offered their support, encouragement, advice, and expertise, none of this work would have been possible.

I would love to thank my advisor, Dr. Scott D. Emr. Scott has been a terrific mentor and role model. His father-like guidance, encouragement and insight have been instrumental in my career development, which ensured that my graduate school was intellectually rewarding and scientifically productive. He has provided me the perfect balance of direction and freedom, allowing me to run with new ideas, to attempt novel techniques outside his expertise and to interact and collaborate with other laboratories. He has offered me the valuable opportunities to take a leadership role in a subgroup in his laboratory, to guide and train undergraduate students for honors thesis, and to present my work at international conferences. Scott's constant enthusiasm and motivation for science is contagious. I have been extremely proud to be a graduate student with Scott.

I want to especially thank my co-chair, Dr. J. Christopher Fromme '99. Chris has been a tremendous mentor and friend. Chris has offered me numerous insightful suggestions to my projects throughout my graduate school. Especially, Chris taught me protein crystallization and X-ray crystallography, from bench to synchrotron, from data collection to model building and deposition, step-by-step with full support, patience and encouragement. It was under his guidance that I feel in love with crystallography and

decided to continue my scientific endeavors in structural biology. I am so grateful to be an honorary member of the Fromme laboratory.

I want to thank my committee members, Dr. Brian R. Crane and Dr. William J. Brown. It was during my first year rotation in Brian's laboratory that I learned the electron spin resonance spectroscopy, which later became an essential component of my dissertation research. Many of the questions and suggestions I received from Brian and Bill at my A-exam, student seminars and committee meetings directly translated to important experiments in my projects.

I want to especially thank Dr. Nicholas J. Buchkovich and Dr. W. Mike Henne, who have been an integral part in my training at the bench, in my writing and presentation, especially when I first started my dissertation research. Nick and Mike provided a wealth of knowledge and experience. I feel privileged to have worked with them. I wish them success in running their own laboratories.

I want to thank Dr. Peter P. Borbat and Dr. Jack H. Freed for collaboration with the electron spin resonance spectroscopy experiments. I am truly satisfied that our collaborative project, which originally was proposed as an adventurous attempt, later transformed into a breakthrough paper and an NIH grant.

Though not my official committee members, I want to thank Dr. Joshua S. Chappie, Dr. Yuxin Mao and Dr. Jeremy M. Baskin. Josh has been tremendously supportive in teaching me advanced X-ray crystallography and sharing with me his valuable X-ray beamtime at APS/NECAT and MacCHESS for data-collection; Yuxin is always willing to take the time to learn about my project, offer suggestions and importantly give me viewpoints on my work; Jeremy is always willing to share with me

refreshers in synthetic bioorganic chemistry. Importantly, all of them have offered me precious suggestions in my scientific career development.

I want to thank Yun Jung “Monica” Kim ’16, who worked with me during her junior and senior years and completed her honors thesis research under my guidance. Her intelligence, curiosity and persistence have in turn encouraged me to excel in my graduate school. I am truly proud that Monica received the highest honor, *summa cum laude* in biological sciences, from the College of Arts and Sciences for her amazing achievements in coursework and science.

I also want to thank Dr. Sudeep Banjade. Sudeep shared with me his valuable knowledge and experience in protein biochemistry and reconstitution. More importantly, he encouraged and inspired me to continue to excel in my future scientific endeavors. I wish him the best in his career development as well.

I am really grateful to be a recipient of the Harry and Samuel Mann Outstanding Graduate Student Award. I thank the Mann and Newman families for this prestigious recognition.

In addition, I want to acknowledge the current and former Emr lab members, Leonid A. Timashev ’14, Sarah T. Griffin, Anthony C. Gatts IV, Dr. Ning Liu, Yi-Chun (Athena) Yeh, Yading Ling Ph.D. ’12, Yingying Zhao Ph.D. ’13, Andrew Manford Ph.D. ’14, Mary Godec ’11, Dr. Ming Li, Dr. Yueguang Rong, Dr. Lu Zhu and Ya-Shan Chuang, the Fromme lab members, Steve L. Halaby, Laura L. Tomas, Margaret A. Gustafson and Dr. Brian C. Richardson, the Mao lab members, FoSheng Hsu Ph.D. ’15, Anil Akturk, D. Jon Wasilko and Xiaochun Wu, the Crane lab members, Nattakan (Bee) Sukomon and Dipanjan Samanta Ph.D. ’16, the Freed lab member, Dr. Elka R.

Georgieva, the Chappie lab members, Carl Schiltz and Chris J. Hosford, and the MacCHESS scientist, Dr. Qingqiu Huang. I also acknowledge Dr. Richard A. Cerione for a first year graduate student rotation opportunity. Their generosity with time, reagents and knowledge have made a difference to my graduate school.

Cornell has been a remarkable place for me to make many lifetime friends. I thank my friends and roommates, Zhewang Lin PhD '16 and Yang Gao for support in both my life and work. I thank my friends Lu Huang Ph.D. '14, Lujie Huang, Xian Qu Ph.D. '15, Xiaowen Shi Ph.D. '16, Anqi Song Ph.D. '16, Lin Wang, Wenke Wang and Zijing Zhang. I also thank my BMBB classmates Judith R. Alonzo, Najla A. Al-Sweel, Ujani Chakraborty, Ahmad A. Cluntun, Myungjoo (MJ) Shin, Jacob M. Tomb and Hansen Xu '11.

Last but not the least, I would love to thank my dear father, Guoyao Tang, and my mother Dr. Li Zhang, for their unflinching approval and unwavering support in every step of my academic and scientific endeavors. In addition, I would love to thank my cousin and my cousin-in-law, Yang Liu and Dr. Hengbing Wang and my aunt, Xianyao Tang. They always encourage and support me in my life and especially in my graduate school.

Thank you, Cornell! I love you and I will miss you!

## TABLE OF CONTENTS

|  |              |
|--|--------------|
| <b>TITLE PAGE .....</b>  | <b>i</b>     |
| <b>COPYRIGHT PAGE.....</b>   | <b>ii</b>    |
| <b>ABSTRACT.....</b>   | <b>iii</b>   |
| <b>BIOGRAPHICAL SKETCH.....</b>  | <b>v</b>     |
| <b>DEDICATION .....</b>  | <b>vi</b>    |
| <b>ACKNOWLEDGMENTS .....</b>   | <b>vii</b>   |
| <b>TABLE OF CONTENTS.....</b>  | <b>xi</b>    |
| <b>LIST OF FIGURES.....</b>  | <b>xv</b>    |
| <b>LIST OF TABLES .....</b>  | <b>xviii</b> |
| <b>CHAPTER I Introduction - The ESCRT Pathway.....</b>   | <b>1</b>     |
| <b>Summary.....</b>  | <b>1</b>     |
| <b>Introduction .....</b>  | <b>1</b>     |
| <b>The ESCRT Complexes .....</b>   | <b>8</b>     |
| ESCRT-0.....   | 8            |
| ESCRT-I.....   | 9            |
| ESCRT-II.....  | 10           |
| ESCRT-III.....   | 11           |
| Bro1/Alix.....   | 12           |
| VPS4.....  | 14           |
| <b>ESCRTs and Cellular Membrane Remodeling.....</b>  | <b>18</b>    |
| Multivesicular Body Biogenesis .....   | 18           |
| Enveloped Virus Budding.....   | 19           |
| Cytokinesis.....   | 20           |
| Nuclear Pore Complex Assembly and Nuclear Envelope Reformation .....   | 21           |
| <b>Membrane Remodeling ESCRT-III Machinery .....</b>   | <b>26</b>    |
| Membrane Topology .....  | 26           |
| ESCRT-III Auto-inhibition and Activation .....   | 26           |
| ESCRT-III Polymerization .....   | 28           |
| ESCRT-III and Membrane Deformation.....  | 31           |
| Vps4 and Membrane Scission .....   | 33           |
| <b>Closing Remarks.....</b>  | <b>35</b>    |
| <b>Reference.....</b>  | <b>38</b>    |
| <b>CHAPTER II Essential N-terminal Insertion Motif Anchors the ESCRT-III Filament<br/>During MVB Vesicle Formation .....</b> | <b>55</b>    |
| <b>Abstract .....</b>  | <b>57</b>    |
| <b>Highlights .....</b>  | <b>58</b>    |
| <b>Graphical Abstract.....</b>   | <b>58</b>    |
| <b>Introduction .....</b>  | <b>59</b>    |
| <b>Results .....</b>   | <b>60</b>    |
| Positively Charged Interfaces on ESCRT-III Interact with Membrane .....  | 60           |
| The N Termini of ESCRT-III Subunits Contribute to Membrane Binding .....   | 62           |
| The N Terminus of Snf7 Requires Hydrophobic Residues .....   | 65           |

|   |            |
|---|------------|
| The N Terminus of Snf7 Inserts into the Membrane .....  | 67         |
| The Snf7 N Terminus Can Be Replaced by Known Membrane-Inserting Motifs .....  | 68         |
| The Snf7 ANCHR Motif Balances Opposing Curvatures during ILV Formation .....  | 70         |
| The Snf7 ANCHR Motif Alters the Kinetics of Cargo Sorting .....   | 73         |
| <b>Discussion.....</b>  | <b>75</b>  |
| <b>Experimental Procedures.....</b>   | <b>108</b> |
| Yeast Strains, Plasmids, and Protein Purification.....  | 108        |
| Fluorescence Microscopy .....   | 108        |
| Mup1-pHluorin Quantitative Sorting Assay .....  | 109        |
| Western Blot and Antibodies.....  | 109        |
| Cellular Fractionation Analysis.....  | 110        |
| Liposome Sedimentation Assays.....  | 110        |
| Fluorescence Spectroscopy.....  | 111        |
| Electron Microscopy.....  | 111        |
| <b>Acknowledgments .....</b>  | <b>112</b> |
| <b>Reference.....</b>   | <b>116</b> |
| <b>CHAPTER III Structural Basis for Activation, Assembly and Membrane Binding of ESCRT-III Snf7 Filaments .....</b> | <b>120</b> |
| <b>Abstract .....</b>   | <b>122</b> |
| <b>eLife Digest.....</b>  | <b>123</b> |
| <b>Introduction .....</b>   | <b>124</b> |
| <b>Results .....</b>  | <b>127</b> |
| X-ray Crystal Structure of Snf7 <sup>core</sup> .....   | 127        |
| Snf7 “Opening” Coupled with Endosomal Recruitment .....   | 128        |
| Polymeric Snf7 Adopts the Open Conformation .....   | 129        |
| Membrane-bound Snf7 Protofilaments Exhibit A ~30Å Periodicity .....   | 131        |
| Snf7 Protomer Interactions in the Protofilament Require Two Interfaces .....  | 133        |
| The Snf7 Polymer Exposes A Cationic Membrane-binding Surface.....   | 134        |
| α4 Bridges Two Snf7 Protofilaments.....   | 135        |
| Conserved Snf7 Protein-protein and Protein-membrane Interfaces .....  | 137        |
| A Linear Snf7 Filament Transformed into A Superhelix.....   | 137        |
| <b>Discussion.....</b>  | <b>138</b> |
| Snf7 Core Domain Rearrangement Required for Protein-membrane and Protein-protein Interactions .....                 | 139        |
| Comparison of ESCRT-III Filaments with Other Membrane-Remodeling Polymers.....                                      | 141        |
| A Curved ESCRT-III Filament Mediates Membrane Remodeling .....  | 142        |
| <b>Materials and Methods .....</b>  | <b>170</b> |
| Protein Crystallization .....   | 170        |
| X-ray Crystallography .....   | 170        |
| Protein Purification .....  | 171        |
| Site-directed Spin-labeling .....   | 171        |
| Sample Preparations for DEER Spectroscopy .....   | 172        |
| DEER Data Collection and Analysis .....   | 172        |
| Subcellular Fractionation Analysis .....  | 176        |
| Dicysteine Oxidative Crosslinking .....   | 176        |
| <i>Ex vivo</i> Dicysteine Crosslinking by Crosslinker .....   | 177        |
| Flow Cytometry, Microscopy, Western Blotting, Yeast Strain and Plasmids .....                                       | 177        |
| CONSURF Analysis.....   | 177        |
| Normal Mode Analysis .....  | 178        |
| Accession Number.....   | 178        |

|  |            |
|--|------------|
| <b>Acknowledgements .....</b>  | <b>179</b> |
| <b>Reference.....</b>  | <b>184</b> |
| <b>CHAPTER IV ESCRT-III Activation by Parallel Action of ESCRT-I/II and ESCRT-0/Bro1 During MVB Biogenesis .....</b> | <b>190</b> |
| <b>Abstract .....</b>  | <b>192</b> |
| <b>Introduction .....</b>  | <b>193</b> |
| <b>Results .....</b>   | <b>194</b> |
| The $\alpha$ 1/2 Hairpin Confers Vps20 with a Unique Identity .....  | 194        |
| Screening for Vps20-independent Snf7 Activation Mutants.....   | 194        |
| Auto-activated Snf7 Bypasses Vps20.....  | 195        |
| Auto-activated Snf7 Bypasses ESCRT-I and ESCRT-II .....  | 196        |
| Auto-activated Snf7 Does Not Bypass Bro1 and ESCRT-0.....  | 198        |
| Bro1 Binds to Snf7 $\alpha$ 6 Helix and Activates Snf7 .....   | 198        |
| <b>Discussion.....</b>   | <b>199</b> |
| <b>Materials and Methods .....</b>   | <b>222</b> |
| Fluorescence Microscopy, Canavanine Plating Assay, .....   | 222        |
| Western Blotting, Protein Purification and Liposome Sedimentation.....   | 222        |
| Flow Cytometry .....   | 222        |
| Yeast Strain and Plasmids .....  | 223        |
| SNF7 Random Mutagenesis for <i>vps20<math>\Delta</math></i> Suppressor Screening .....                               | 223        |
| Circular Dichroism Spectroscopy .....  | 224        |
| Negative Stain Transmission Electron Microscopy .....  | 224        |
| <b>Acknowledgement .....</b>   | <b>225</b> |
| <b>Reference.....</b>  | <b>230</b> |
| <b>CHAPTER V Conclusion, Discussion and Future Directions .....</b>  | <b>233</b> |
| <b>Conclusion .....</b>  | <b>233</b> |
| <b>Discussion.....</b>   | <b>234</b> |
| Diversity of ESCRT Function .....  | 234        |
| Theme of ESCRT-III Recruitment .....   | 236        |
| ESCRTs and New Membrane Topology .....   | 237        |
| <b>Future Directions .....</b>   | <b>238</b> |
| Remaining Mysteries .....  | 238        |
| <b>Reference.....</b>  | <b>241</b> |
| <b>APPENDIX I Characterizing the Role of the Snf7 <math>\alpha</math>4 Helix in ESCRT-III Assembly ....</b>          | <b>243</b> |
| <b>Summary.....</b>  | <b>243</b> |
| The Snf7 $\alpha$ 4 Helix is Important for ESCRT-III Function .....  | 243        |
| Identification of a Snf7 $\alpha$ 4- $\alpha$ 4 Interface Required for Polymer Assembly .....                        | 244        |
| Snf7 $\alpha$ 4 Mutants with Increased Membrane Binding and Polymer Assembly Capabilities                            | 245        |
| Identification of the Role of the Snf7 $\alpha$ 4 Helix in Vps24 Recruitment .....                                   | 246        |
| Vps20 and Vps24 are More Tolerant to Mutations than Snf7 .....   | 248        |
| <b>Reference.....</b>  | <b>265</b> |
| <b>APPENDIX II Functional Design of ESCRT-III Tandem Fusion Proteins.....</b>  | <b>267</b> |
| <b>Summary.....</b>  | <b>267</b> |
| Design and Characterization of Snf7 Tandem Fusion Proteins .....   | 267        |
| Design and Characterization of Vps20-Vps20 and Vps20-Snf7 Tandem Fusion Proteins                                     | 268        |
| <b>Reference.....</b>  | <b>276</b> |
| <b>APPENDIX III Functional Dissection of Novel ESCRT-III Snf7 Interactor, Chm7 .....</b>                             | <b>277</b> |
| <b>Summary.....</b>  | <b>277</b> |

|   |            |
|---|------------|
| Snf7 SILAC Identified a Novel Interacting Protein, Chm7.....          | 277        |
| Chm7 Localizes to Cytoplasm and Intracellular Puncta.....             | 278        |
| Chm7 Does Not Play a Role in Endosomal Cargo Sorting .....            | 279        |
| A Functional Role of Chm7 as a Nuclear ESCRT?.....                    | 280        |
| <b>APPENDIX IV Summary of the Quantitative MVB Sorting Data .....</b> | <b>295</b> |
| <b>Summary.....</b>   | <b>295</b> |

## LIST OF FIGURES

|  |     |
|--|-----|
| Figure 1.1 Overview of the Cellular Function of the ESCRT Pathway .....  | 6   |
| Figure 1.2 Structure and Architecture of the ESCRT Complexes .....   | 16  |
| Figure 1.3 Distinct Stages of the ESCRT-mediated MVB Biogenesis.....   | 24  |
| Figure 1.4 Snf7 Spirals and Membrane Remodeling .....  | 36  |
| Figure 2.1 Identification of Electrostatic Membrane Binding Interfaces on ESCRT-III<br>Subunits .....                        | 80  |
| Figure 2.2 Expression Levels of Membrane Binding Interface Mutants with Additional<br>Functional and Localization Data ..... | 82  |
| Figure 2.3 ESCRT-III Subunits Require the N Terminus for Cargo Sorting .....   | 84  |
| Figure 2.4 Expression Levels of ESCRT-III N-terminus Mutants with Additional<br>Functional and <i>in vitro</i> data .....    | 86  |
| Figure 2.5 Snf7 Requires N-Terminal Hydrophobic Residues .....   | 88  |
| Figure 2.6 Expression Levels of Snf7 N-terminus Mutants with Functional Data from<br>Additional Supporting Mutants .....     | 90  |
| Figure 2.7 The N Terminus of Snf7 Inserts into Membrane .....  | 92  |
| Figure 2.8 Reagents and Additional Data Used for NBD-based Fluorescence<br>Spectroscopy .....                                | 94  |
| Figure 2.9 Snf7 Requires a Membrane-Inserting N-Terminal Motif.....  | 96  |
| Figure 2.10 Expression Levels of Snf7 N-Terminal Chimeras with Additional Functional<br>and Localization Data.....           | 98  |
| Figure 2.11 ILV Formation Requires Maintaining Delicate Balance of Curvatures .....  | 100 |

|   |     |
|---|-----|
| Figure 2.12 Expression Levels of Snf7 Chimeric N Terminal Mutants with Mutant Localization Data and Additional EM Images..... | 102 |
| Figure 2.13 Kinetic Sorting of Mup1-pHluorin by Snf7 N-terminal Mutants .....   | 104 |
| Figure 2.14 The N Terminus of Snf7 Is Required for Fast Cargo Sorting .....   | 106 |
| Figure 3.1 X-ray Crystal Structure of Snf7 <sup>core</sup> .....  | 144 |
| Figure 3.2 Superimposition of Snf7 <sup>core</sup> with Available ESCRT-III Structures.....                                   | 146 |
| Figure 3.3 Conformational Rearrangement of Snf7 .....   | 148 |
| Figure 3.4 DEER Analysis of Snf7 Core Domain Rearrangement .....  | 150 |
| Figure 3.5 Membrane-bound Snf7 Filament with ~30Å Periodicity .....   | 152 |
| Figure 3.6 DEER Analysis of Snf7 Filament.....  | 154 |
| Figure 3.7 Hydrophobic and Electrostatic Interactions in a Snf7 Filament.....   | 156 |
| Figure 3.8 Biochemical Analyses of Snf7 Intra-filament Interface Mutants .....  | 158 |
| Figure 3.9 Electrostatic Protein-membrane Interactions in a Snf7 Filament .....   | 160 |
| Figure 3.10 Snf7 α4 in Inter-Filament Interactions .....  | 162 |
| Figure 3.11 Comparison Between Snf7 <sup>core</sup> Open Conformation A and B.....  | 164 |
| Figure 3.12 Conservation and Normal Mode Analysis of Snf7 Filament.....   | 166 |
| Figure 3.13 Models of Snf7 Activation, Polymer Assembly and Membrane Remodeling .....   | 168 |
| Figure 4.1 Novel Snf7 Point Mutations Trigger Core Domain Activation.....   | 202 |
| Figure 4.2 Vps20-Snf7 Chimera Complements Vps20 Function.....   | 204 |
| Figure 4.3 Snf7 <sup>Q90L</sup> and Snf7 <sup>N100I</sup> Trigger Core Domain Activation .....                                | 206 |
| Figure 4.4 Auto-activated Snf7 Functionally Bypasses Vps20 .....  | 208 |
| Figure 4.5 Activation Mutants Suppress <i>snf7Δ</i> and <i>vps20Δ snf7Δ</i> <i>in vivo</i> .....                              | 210 |

|  |     |
|--|-----|
| Figure 4.6 Snf7 Core Domain Auto-activation Bypasses ESCRT-I and ESCRT-II .....  | 212 |
| Figure 4.7 Snf7 Core Domain Auto-activation Does Not Suppresses <i>vps24Δ</i> , <i>vps2Δ</i> and<br><i>vps4Δ</i> But Suppresses ESCRT-II Arm Mutants ..... | 214 |
| Figure 4.8 MVB Morphologies of <i>snf7**</i> and <i>snf7***</i> in ESCRT-I <i>vps23Δ</i> .....   | 216 |
| Figure 4.9 Snf7 Auto-activation Mutant Sort Cargo in a Ubiquitin-dependent Manner  | 218 |
| Figure 4.10 Snf7 Activation of the Core Domain and the C-terminal α6 .....   | 220 |
| Figure A1.1 Charged Residues in $\text{Snf7}^{\alpha 4}$ are Critical for Function <i>in vivo</i> .....  | 249 |
| Figure A1.2 Electrostatically Charged Residues in $\text{Snf7}^{\alpha 4}$ Form a Snf7 Binding Interface<br>.....  | 251 |
| Figure A1.3 The $\text{Snf7}^{\alpha 4}$ Interface is Sensitive to Multiple Mutations .....  | 253 |
| Figure A1.4 The $\text{Snf7}^{\alpha 4}$ Interface is Critical in Vps24 Endosomal Recruitment.....   | 255 |
| Figure A1.5 Genetic Screening for Snf7-Vps24 Interface Mutants .....   | 257 |
| Figure A1.6 Vps24 and Vps20 are Tolerant to Mutations in the Proposed Inter-Subunit<br>Interfaces.....   | 259 |
| Figure A2.1 Snf7 Tandem Fusion Dimer is Functional <i>in vivo</i> .....  | 270 |
| Figure A2.2 Vps20 Tandem Fusion Dimer and Vps20-Snf7 Fusion is Functional <i>in vivo</i><br>.....  | 272 |
| Figure A3.1 ESCRT-III like Protein Chm7 as a Novel Snf7 Interactor .....   | 282 |
| Figure A3.2 Chm7 Localizes to Cytoplasm or Intracellular Punctate Structures .....   | 284 |
| Figure A3.3 <i>chm7Δ</i> Does Not Affect Endosomal Cargo Sorting <i>in vivo</i> .....  | 286 |

## LIST OF TABLES

|   |     |
|---|-----|
| Table 1.1 Division of Labor of the ESCRT Complexes .....                                      | 5   |
| Table 2.1 Plasmids and Yeast Strains Used in Chapter 2 .....                                  | 113 |
| Table 3.1 Crystallographic Data Collection and Refinement Statistics .....                    | 180 |
| Table 3.2 Plasmids and Yeast Strains Used in Chapter 3 .....                                  | 181 |
| Table 4.1 Plasmids and Yeast Strains Used in Chapter 4 .....                                  | 226 |
| Table A1.1 Plasmids and Yeast Strains Used in Appendix 1 .....                                | 261 |
| Table A2.1 Plasmids and Yeast Strains Used in Appendix 2 .....                                | 274 |
| Table A3.1 Snf7 SILAC: WT Snf7-FLAG (Heavy) V.S. WT Untagged (Light).....                     | 288 |
| Table A3.2 Snf7 SILAC: <i>vps4Δ</i> Snf7-FLAG (Heavy) V.S. <i>vps4Δ</i> Untagged (Light)..... | 289 |
| Table A3.3 Snf7 SILAC: <i>vps4Δ</i> Snf7-FLAG (Heavy) V.S. WT Snf7-FLAG (Light).....          | 290 |
| Table A3.4 Plasmids and Yeast Strains Used in Appendix 3 .....                                | 291 |
| Table A4.1 Summary of Mup1-pHluorin MVB Sorting in <i>snf7Δ</i> Yeast.....                    | 296 |
| Table A4.2 Summary of Mup1-pHluorin MVB Sorting in <i>vps20Δ</i> Yeast.....                   | 303 |
| Table A4.3 Summary of Mup1-pHluorin MVB Sorting in <i>vps24Δ</i> Yeast.....                   | 306 |
| Table A4.4 Summary of Mup1-pHluorin MVB Sorting in <i>vps2Δ</i> Yeast.....                    | 309 |
| Table A4.5 Summary of Mup1-pHluorin MVB Sorting in <i>vps4Δ</i> Yeast.....                    | 310 |
| Table A4.6 Summary of Mup1-pHluorin MVB Sorting in <i>escrt-iiΔ</i> Yeast.....                | 311 |
| Table A4.7 Summary of Mup1-pHluorin MVB Sorting in <i>escrt-iΔ</i> Yeast.....                 | 313 |
| Table A4.8 Summary of Mup1-pHluorin MVB Sorting in <i>escrt-0Δ</i> Yeast .....                | 315 |
| Table A4.9 Summary of Mup1-pHluorin MVB Sorting in <i>bro1Δ</i> yeast.....                    | 317 |

# CHAPTER I

## Introduction - The ESCRT Pathway

### Summary

The endosomal sorting complex required for transport (ESCRT) pathway is the key mediator of multivesicular body (MVB) biogenesis for delivering cargo destined for degradation to the lysosome, but it also plays critical roles in enveloped virus budding, cytokinesis abscission, cell surface membrane repair, nuclear pore complex assembly, nuclear envelope reformation and rupture repair. Despite these diverse roles, the ESCRT pathway is a cargo-recognition and membrane-sculpting macromolecular machine. Here, I review the cellular function and molecular architecture of the ESCRT complexes, and discuss how ESCRTs drive membrane deformation and scission.

### Introduction

Cells constantly remodel the landscape of their surface to maintain cell integrity, growth, and homeostasis. Cell surface membrane cargo (signaling receptors, ion channels, nutrient transporters, and etc.) is precisely down-regulated through the endolysosomal pathway. The formation of multivesicular bodies (MVBs) is the key stage in the delivery of cargo destined for degradation in the lysosome (vacuole in yeast). In the 1950s, the laboratories of Keith R. Porter and George E. Palade first described MVBs by transmission electron microscopy (TEM) as “two large vesicles with smaller vesicles inside” (Palade, 1955; Sotelo and Porter, 1959). In the 1970s, the laboratory of

Stanley Cohen observed the sorting of epidermal growth factor (EGF) into the intraluminal vesicles (ILVs) of MVBs (Haigler et al., 1979).

In the late 1980s and early 1990s, the laboratories of Scott D. Emr and Tom H. Stevens identified a family of genes in *Saccharomyces cerevisiae*, whose loss display vacuolar protein sorting (VPS) defects (Banta et al., 1988; Robinson et al., 1988; Rothman et al., 1989; Rothman and Stevens, 1986). According to the vacuolar and endosomal morphologies in cells deficient with each VPS gene, these genes were categorized into classes A, B, C, D, E and F (Banta et al., 1988; Raymond et al., 1992). Class E VPS mutant yeast exhibits distinctive aberrant multicisternal endosomal compartments (Raymond et al., 1992). Characterization of the trafficking of the vacuolar hydrolase carboxypeptidase S (Cps1) revealed that membrane proteins can be sorted into the vacuolar lumen through the MVB pathway, and that class E vps mutants were defective for Cps1 sorting to the vacuolar lumen (Odorizzi et al., 1998; Reggiori and Pelham, 2001). Additionally, a genetic screen using a chimeric protein Cps1 fused with the histidine biosynthesis enzyme His3 (His3-Cps1) was carried out to select mutants defective in MVB sorting (Katzmann et al., 2004; Odorizzi et al., 2003).

Extensive biochemical and cell biological studies indicated that the class E VPS gene products form distinct multimeric protein complexes that intimately mediate this trafficking. In 2001, the endosomal sorting complex required for transport-I (ESCRT-I) was characterized and shown to engage ubiquitinated cargo at the endosome and mediate its sorting into MVBs (Katzmann et al., 2001). A year later, the ESCRT-II and ESCRT-III complexes were identified back-to-back as additional critical players in the delivery of ubiquitinated cargo to the yeast vacuole (Babst et al., 2002a; Babst et al.,

2002b). They were preceded by the identification of the AAA-ATPase Vps4 in 1997, which is also necessary for delivery of cargo to the vacuole (Babst et al., 1997). Together, these studies set the framework establishing the ESCRT proteins that comprise a pathway of five distinct complexes, ESCRTs -0, -I, -II, and -III, and Vps4. ESCRTs are cargo recognition, sorting and sequestration machinery that can deform the endosome-limiting membranes inward to generate ILVs through an exquisite division of labor (Table 1.1).

Subsequent work has elucidated roles for the ESCRTs in numerous topologically equivalent biological processes. Beyond MVB biogenesis (Katzmann et al., 2001), ESCRTs are well established to function in enveloped virus budding (Garrus et al., 2001b) and metazoan cytokinesis abscission (Carlton and Martin-Serrano, 2007). Recently, more cellular membrane remodeling events continue to be identified as ESCRT-dependent processes, including exosome secretion (Baietti et al., 2012; Colombo et al., 2013; Tamai et al., 2010), macroautophagy (Filimonenko et al., 2007; Lee et al., 2007; Rusten et al., 2007), plasma membrane repair (Jimenez et al., 2014; Scheffer et al., 2014), neuron pruning (Loncle et al., 2015), nuclear pore complex assembly (Webster et al., 2014), and nuclear envelope reformation and rupture repair (Denais et al., 2016; Olmos et al., 2015; Raab et al., 2016; Vietri et al., 2015) (Figures 1.1A-I).

These discoveries of the ESCRT-dependence between these seemingly unrelated processes highlight a unifying principle, which define the ESCRT pathway as a cargo-recognition and membrane-sculpting machine. I will review 1) the function and structure of each of the ESCRT complexes, 2) the functional divergence of the ESCRT

machinery, 3) the molecular mechanisms of the ESCRT-III-mediated membrane remodeling.

**Table 1.1 Division of Labor of the ESCRT Complexes**

| The ESCRT Pathway |                 |  |                |             |             |
|-------------------|-----------------|--|----------------|-------------|-------------|
| Yeast             | Human           | Function   | MVB Biogenesis | HIV Budding | Cytokinesis |
| <b>ESCRT-0</b>    |                 |  |                |             |             |
| Vps27             | Hrs             | Cargo recognition<br>PI(3)P binding                              | Yes            | No          | No          |
| Hse1              | STAM1/2         |  | Yes            | No          | No          |
| <b>ESCRT-I</b>    |                 |  |                |             |             |
| Vps23             | Tsg101          | Cargo clustering<br>Membrane binding                             | Yes            | Yes         | Yes         |
| Vps28             | Vps28           |  | Yes            | Yes         | Yes         |
| Vps37             | Vps37A-D        |  | Yes            | Yes         | Yes         |
| Mvb12             | Mvb12A,B        |  | Yes            | Yes         | Yes         |
| -                 | UBAP1           |  | Yes            | No          | No          |
| <b>ESCRT-II</b>   |                 |  |                |             |             |
| Vps36             | EAP45           | Cargo clustering<br>PI(3)P binding<br>ESCRT-III Recruitment      | Yes            | No?         | Yes         |
| Vps22             | EAP30           |  | Yes            | No?         | Yes         |
| Vps25             | EAP20           |  | Yes            | No?         | Yes         |
| <b>Bro1</b>       |                 |  |                |             |             |
| Bro1              | ALIX,<br>HD-PTP | Ub recognition<br>ESCRT-III Recruitment<br>DUB Recruitment       | Yes            | Yes         | Yes         |
| <b>ESCRT-III</b>  |                 |  |                |             |             |
| Vps20             | CHMP6           | Cargo sequestration<br>Membrane deformation<br>Vesicle formation | Yes            | No?         | Yes         |
| Snf7              | CHMP4A-C        |  | Yes            | Yes         | Yes         |
| Vps24             | CHMP3           |  | Yes            | Yes         | Yes         |
| Vps2              | CHMP2A,B        |  | Yes            | Yes         | Yes         |
| Vps60             | CHMP5           |  | Yes            | No          | Yes         |
| Did2              | CHMP1A,B        |  | Yes            | No          | Yes         |
| Ist1              | IST1            |  | No             | No          | Yes         |
| Chm7              | CHMP7           |  | No             | Yes?        | No          |
| <b>AAA+ATPase</b> |                 |  |                |             |             |
| Vps4              | VPS4A,B         | Membrane scission,<br>ESCRT-III disassembly                      | Yes            | Yes         | Yes         |
| Vta1              | LIP5            |  | Yes            | Yes         | Yes         |
| -                 | Spastin         | Microtubule severing   | No             | No          | Yes         |

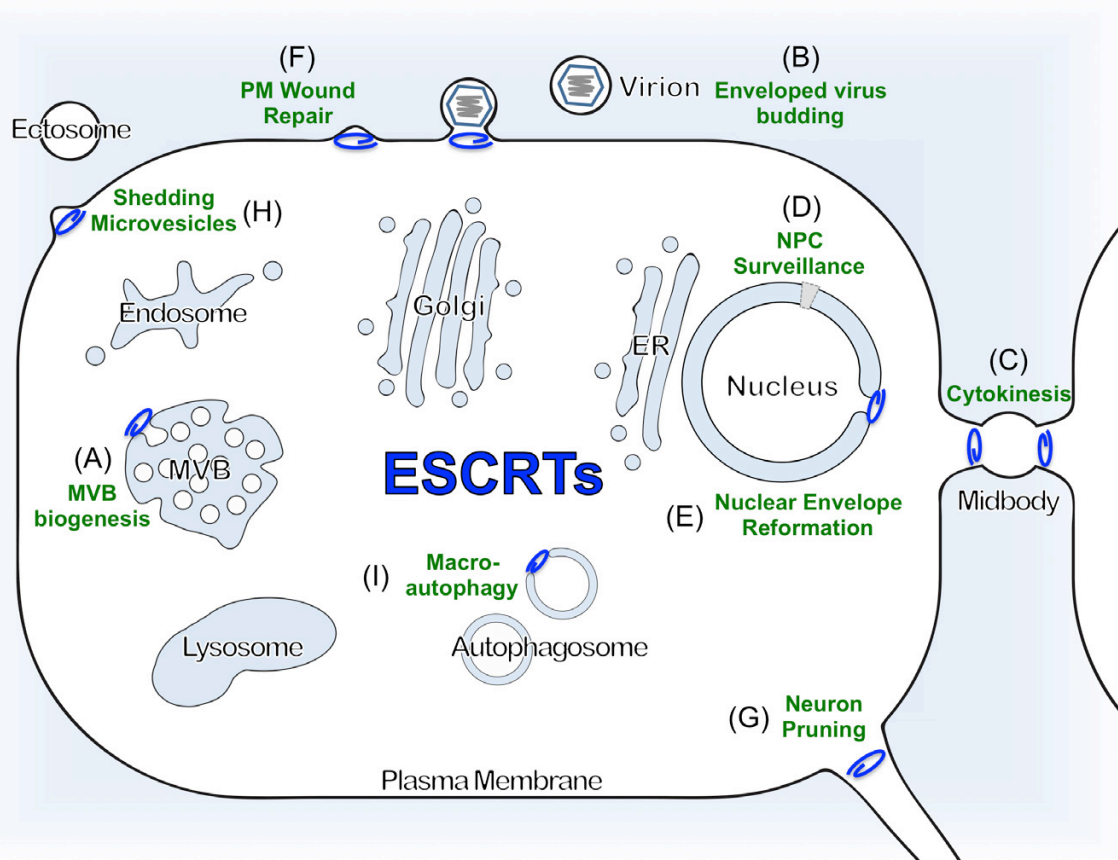


**Figure 1.1 Overview of the Cellular Function of the ESCRT Pathway**

### **Figure 1.1 Overview of the Cellular Function of the ESCRT Pathway.**

- (A) In MVB biogenesis, ESCRTs sort ubiquitinated transmembrane proteins at endosomes into ILVs.
- (B) In enveloped virus budding, ESCRTs are required at the plasma membrane (PM) for the release of infectious viral particles.
- (C) In metazoan and archeal cytokinesis, ESCRTs are required at the PM for membrane scission at the midbody that separates dividing cells.
- (D) In yeast NPC assembly, ESCRTs are recruited for the surveillance of integrity to eliminate dysfunctional NPC intermediates.
- (E) In nuclear envelope reformation, ESCRTs are recruited for the sealing of fragmented nuclear membranes.
- (F) In cell surface wound repair, ESCRTs are required at the PM damage sites for membrane regeneration.
- (G) In neuron pruning, ESCRTs are required for neurite scission for local degeneration.
- (H) In shedding microvesicles, ESCRTs are required at the PM for ectosome biogenesis (evidence is controversial).
- (I) In macroautophagy, ESCRTs are recruited for phagophore closure (evidence is controversial). ESCRTs represented by a spiral.

## The ESCRT Complexes

The class E Vps proteins comprise the ESCRT pathway of five distinct complexes, ESCRTs -0, -I, -II, and -III, and Vps4, which are recruited from the cytoplasm to the endosomal membranes in a sequential order. The upstream ESCRT complexes (ESCRTs-0, I and II) are cargo recognition and sorting machinery and the downstream ESCRT-III and Vps4 complexes are membrane-remodeling machinery (Table 1.1).

### ESCRT-0

ESCRT-0 is a heterotetramer (Mayers et al., 2011) that consists of two copies of Vps27 (Hrs, hepatocyte growth factor-regulated tyrosine kinase substrate, in human) and Hse1 (STAM, signal transducing adaptor molecule, in human). Mammalian ESCRT-0 has two isoforms of Hse1 (Asao et al., 1997; Bilodeau et al., 2002; Katzmann et al., 2003; Shih et al., 2002) (Figure 1.3A, Table 1.1). The full-length structure of the ESCRT-0 complex has not yet been determined. However, X-ray crystal structure of truncated Vps27 and Hse1 suggest that they assemble into heterodimer via the coiled-coil GAT (GGAs and Tom) domains (Asao et al., 1997; Prag et al., 2007) (Figure 1.2A). Although both subunits display structural similarities, one difference between them is a FYVE (Fab-1, YGL023, Vps27, and EEA1) zinc finger domain on Vps27/Hrs (Mao et al., 2000). The FYVE domain binds phosphatidylinositol 3-phosphate, PI(3)P, providing membrane recruitment and endosome specificity for the ESCRT-0 complex (Raiborg et al., 2001).

ESCRT-0 subunits also bind ubiquitin through the VHS domains (Vps27, Hrs, and STAM) and multiple UIMs (ubiquitin-interacting motif) (Bilodeau et al., 2002; Fisher et al., 2003; Hirano et al., 2006; Mizuno et al., 2003; Swanson et al., 2003). This provides additional targeting modules to promote their binding to cargo-enriched endosomes, and engage and cluster several cargoes simultaneously (Ren and Hurley, 2010). Additionally, ESCRT-0 contains clathrin-binding motifs, suggesting that lattices of clathrin, ESCRT-0 and ubiquitinated cargo may form microdomains on endosomes to be important for cargo sorting (Raiborg et al., 2001; Raiborg et al., 2006; Sachse et al., 2002).

## **ESCRT-I**

ESCRT-0 initiates the ESCRT pathway by recruiting the ESCRT-I complex (Bache et al., 2003; Katzmann et al., 2003; Lu et al., 2003). ESCRT-I is a heterotetramer that consists of one copy of Vps23 (Tsg101, tumor susceptibility gene 101, in human), Vps28, Vps37 (Katzmann et al., 2001) and Mvb12 (multivesicular body 12) (Chu et al., 2006; Curtiss et al., 2007). Mammalian ESCRT-I has additional isoforms of Vps37 and Mvb12 (Bache et al., 2004; Bishop and Woodman, 2001; Eastman et al., 2005; Morita et al., 2007; Stuchell et al., 2004) (Figure 1.3A, Table 1.1). X-ray crystal structure of the core yeast ESCRT-I complex reveals a ~20 nm elongated structure, with three subunits intertwined into a long coiled-coil stalk with a globular head fold (Figure 1.2B). Different from ESCRT-0, ESCRT-I binds acidic membranes weakly through electrostatic interactions at the positively charged N-terminus of Vps23 (Kostelansky et al., 2007).

ESCRT-I interacts with ESCRT-0 through the N-terminal ubiquitin-conjugating enzyme E2 variant (UEV) domain of Vps23. This UEV domain binds to the P-(S/T)-A-P motif of ESCRT-0 subunit Vps27/Hrs (Katzmann et al., 2003; Kostelansky et al., 2006), and the ubiquitin moieties from endosomal cargo (Teo et al., 2004b). Additionally, Mvb12 also contains a UBD (ubiquitin-binding domain) (Shields et al., 2009; Tsunematsu et al., 2010), highlighting the ESCRT-I complex as another cargo recognition and sorting module in the pathway.

## **ESCRT-II**

In addition to ESCRT-0, ESCRT-I also interacts with the ESCRT-II complex. ESCRT-II is a Y-shaped heterotetramer that consists of one subunit of Vps36 (EAP45, ELL-associated protein of 45kDa, in human) and Vps22 (EAP30) and two subunits of Vps25 (EAP20) (Babst et al., 2002b; Langelier et al., 2006) (Figure 1.3A, Table 1.1). X-ray crystal structures of the yeast ESCRT-II complex have been determined (Hierro et al., 2004; Teo et al., 2004a). Vps36 and Vps22 assemble into the “body” of the “Y”. Each binds one copy of Vps25, which forms the two “arms” of the “Y” (Hierro et al., 2004; Teo et al., 2004a) (Figure 1.2C). ESCRT-II engages ESCRT-I through an interaction between the GLUE (GRAM-like ubiquitin-binding in EAP45) domain of Vps36 and the C terminus of Vps28 (Gill et al., 2007; Teo et al., 2006). Two NZF (Npl4-type zinc finger) domains are inserted into the yeast GLUE domain; the first NZF binds to ESCRT-I, and the second NZF binds ubiquitin (Teo et al., 2006). The GLUE domain can also bind to endosome-specific lipid, PI(3)P, with high affinity (Slagsvold et al., 2005).

The ESCRT-II GLUE and ESCRT-0 FYVE domains provide endosomal localization specificity.

ESCRT-II also sets the architecture of the ESCRT-III complex (Henne et al., 2012; Teis et al., 2010). Co-crystal structure of ESCRT-II Vps25 subunit and the ESCRT-III nucleator Vps20 subunit suggests that the C-terminus of Vps25 binds to the N-terminal  $\alpha$ 1 helix of Vps20, revealing a critical role for ESCRT-II in initiating the activation and assembly of the ESCRT-III complex (Im et al., 2009).

### **ESCRT-III**

ESCRT-III consists of four “core” subunits, Vps20 (CHMP6, charged multivesicular body protein 6, in human), Snf7 (sucrose non-fermenting 7)/Vps32 (CHMP4), Vps24 (CHMP3), and Vps2 (CHMP2) (Babst et al., 2002a), and several accessory subunits, Vps60 (CHMP5), Did2 (Doa4-independent degradation-2)/Vps46 (CHMP1), Ist1 (Increased salt tolerance 1) and Chm7 (Horii et al., 2006; Rue et al., 2008). Mammalian ESCRT-III has additional isoforms of Snf7, Vps2 and Did2 (Figure 1.3A, Table 1.1). Unlike the upstream ESCRT complexes, ESCRT-III does not form a stable, cytoplasmic and stoichiometric complex. Rather, it assembles transiently and dynamically on membranes, which has made the characterization of the molecular architecture of ESCRT-III challenging.

ESCRT-III monomers do not localize to the endosomes but exist in an autoinhibited “closed” state in the cytoplasm. X-ray crystal structures of the monomeric ESCRT-III subunits, Vps24/CHMP3 and Ist1, reveal a common ESCRT-III structural fold with a ~7 nm long N-terminal  $\alpha$ -helical hairpin and several short  $\alpha$ -helices (Bajorek et

al., 2009b; Muziol et al., 2006). Based on the analysis of the primary sequence of ESCRT-III proteins, it was suggested that the architecture of the ESCRT-III subunits is generally conserved (Figure 1.4A) (Bajorek et al., 2009b). Upon releasing this autoinhibition, ESCRT-III subunits assemble and co-assemble into higher-order protofilaments, rings, spirals, helices or tubules with a range of different morphologies and dimensions necessary for membrane remodeling (Cashikar et al., 2014; Chiaruttini et al., 2015; Effantin et al., 2013; Hanson et al., 2008; Henne et al., 2012; Lata et al., 2008b; McCullough et al., 2015; Pires et al., 2009; Shen et al., 2014; Tang et al., 2015) (Figure 1.2E).

Although all ESCRT-III subunits share a common domain organization, each subunit appears to contribute a specific function (Figure 1.4A). ESCRT-II directly engages Vps20 to trigger a sequential activation and ordered assembly of ESCRT-III subunits at endosomes (Im et al., 2009; Teis et al., 2010). Vps20 nucleates the homopolymerization of the most abundant ESCRT-III subunit, Snf7, which then recruits Vps24 and Vps2, completing ESCRT-III complex assembly (Teis et al., 2008). ESCRT-III finally engages the Vps4 complex for ESCRT-III disassembly (Lata et al., 2008b; Obita et al., 2007), through an interaction between the MIM (MIT-interacting motif) of Vps2 and the MIT (microtubule interacting and trafficking) domain of Vps4. This allows individual ESCRT-III subunits available for subsequent rounds of vesicle formation.

## Bro1/ALIX

The ESCRT-III Snf7 subunit also binds the Bro1 family protein Bro1 (BCK1-like resistance to osmotic shock protein-1)/Vps31 (Alix, apoptosis-linked gene-2 interacting

protein X, and HD-PTP, histidine domain phosphotyrosine phosphatase, in human) (Figure 1.3A, Table 1.1). Bro1 has an N-terminal globular Bro1 domain, a coiled-coil V domain and a C-terminal unstructured PRR (proline-rich region) (Figure 1.2D). The Bro1 domain binds and activates Snf7, and stabilizes the Snf7 polymer, through an interaction with the C-terminal  $\alpha$ 6 helix of Snf7 (McCullough et al., 2008; Pires et al., 2009; Tang et al., 2016; Wemmer et al., 2011).

Genetic, biochemical and structural analyses suggest that the Bro1 domain directly engages the ESCRT-0 complex (Lee et al., 2016; Pashkova et al., 2013). Remarkably, the V domain has been recently shown to directly bind ubiquitin with low affinity (Pashkova et al., 2013). Together, these studies indicate a novel role of Bro1 as part of both the upstream and downstream ESCRT machinery in cargo recognition and sorting (Tang et al., 2016).

The PRR is responsible for the recruitment of the yeast deubiquitinase Doa4 (degradation of alpha-4) (Nikko and Andre, 2007; Richter et al., 2007), necessary for cargo deubiquitination prior to their packaging into ILVs (Luhtala and Odorizzi, 2004; Odorizzi et al., 2003). Similar to the Bro1-Doa4 complex, which binds both ESCRT-0 and ESCRT-III in yeast, human deubiquitinases AMSH (associated molecule with the SH3 domain of STAM) and UBPY (ubiquitin isopeptidases Y) directly interact with both ESCRT-0 and ESCRT-III (McCullough et al., 2006; Row et al., 2007; Sierra et al., 2010; Solomons et al., 2011), responsible for cargo deubiquitination (Kyuma et al., 2006; Row et al., 2006). Thus, ESCRTs have an important role in recruiting the deubiquitinating machinery required for removing ubiquitin from cargo and maintain cellular ubiquitin pools (Amerik et al., 2000; Swaminathan et al., 1999).

## VPS4

Once assembled, the ESCRT-III complex requires energy to disassociate from the membranes. This energy is provided by the class I AAA (ATPase associated with various cellular activities) ATPase Vps4 (Babst et al., 1998). Mammalian Vps4 has two isoforms (Figure 1.3A, Table 1.1). Vps4 is a multimeric mechanoenzyme that binds ESCRT-III subunits via an N-terminal MIT domain that recognizes C-terminal MIMs present in the ESCRT-III subunits (Figure 1.2F). Notably, the Vps20, Snf7 and Vps60 MIMs (MIM2), which fold into a coil, bind a different area of the Vps4 MIT than the Vps24, Vps2, Did2 and Ist1 MIMs (MIM1), which fold into an  $\alpha$ -helix (Babst et al., 1997; Guo and Xu, 2015; Kieffer et al., 2008; Kojima et al., 2016; Obita et al., 2007; Scott et al., 2005b; Stuchell-Brereton et al., 2007). Vps2 and Did2 bind MIT with higher affinity than other ESCRT-III subunits, suggesting that multiple ESCRT-III subunits must interact with Vps4 for stable recruitment (Shestakova et al., 2010).

Vps4 exists *in vitro* as a monomer or dimer in the nucleotide-free or ADP-bound state but multimerizes into a stable hexamer or dodecamer of two stacked hexameric rings and a supercomplex with Vta1 (Babst et al., 1997; Caillat et al., 2015; Scott et al., 2005a; Yu et al., 2008). Vta1 (Vps twenty-associated-1) promotes the ATPase activity of Vps4 with a 1:2 stoichiometry (Azmi et al., 2006; Yang and Hurley, 2010; Yu et al., 2008). The presence of MIT domains on Vta1 and on each Vps4 subunits indicates that the Vps4-Vta1 complex contains up to 24 MIT domains, allowing it to interact with multiple ESCRT-III subunits simultaneously. Thus, Vta1 may function as an adaptor bridging Vps4 and ESCRT-III (Azmi et al., 2008; Shiflett et al., 2004).

Recently, a novel Vps4 binding protein, Vfa1 (Vps four-associated 1), was identified in a yeast genetic screen, whose overexpression causes altered vacuole size, indicative of MVB dysfunction (Arlt et al., 2011). Vfa1 has a C-terminal MIM2, which binds the MIT domain of Vps4 and stimulates Vps4 ATPase activity (Kojima et al., 2016; Vild and Xu, 2014).

ATP hydrolysis is promoted by multimerization and association with ESCRT-III subunits and is necessary for the removal of ESCRT-III subunits from the membrane, because expression of a hydrolysis mutant Vps4<sup>E233Q</sup> leads to the accumulation of hyperoligomeric ESCRT-III on the endosome and a class E VPS phenotype in a dominant negative manner (Adell et al., 2014; Babst et al., 1998). It has been suggested that the Vps4 complex mediates ESCRT-III disassembly through global protein unfolding by threading ESCRT-III proteins through a narrow pore in the AAA hexamer in an ATP-dependent process (Gonciarz et al., 2008; Yang et al., 2015), like other AAA ATPases in the cell (Reid et al., 2001; Siddiqui et al., 2004; Weber-Ban et al., 1999). However, how ESCRT-III subunits are refolded after dissociation remains to be elucidated.

Notably, ESCRT-III and Vps4 do not bind ubiquitin directly, which is consistent with their roles in membrane deformation and vesicle formation, but not in cargo recognition and sorting. This highlights the division of labor between the ESCRT complexes.

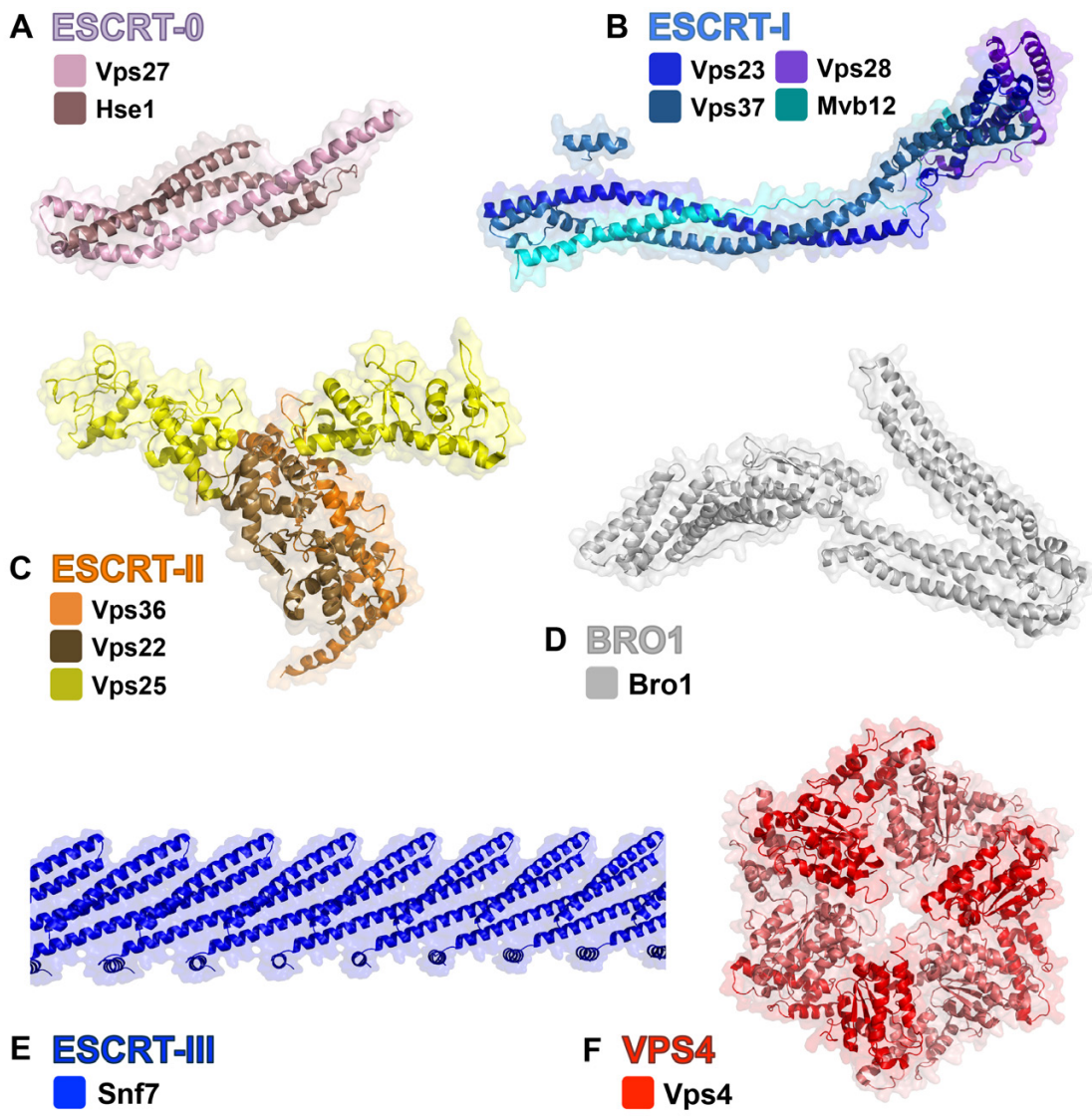


**Figure 1.2 Structure and Architecture of the ESCRT Complexes**

**Figure 1.2 Structure and Architecture of the ESCRT Complexes.**

- (A) Crystal structure of the *Homo sapiens* ESCRT-0 “core” complex (PDB: 3F1I).
- (B) Crystal structure of the *Saccharomyces cerevisiae* ESCRT-I complex (PDB: 2P22).
- (C) Crystal structure of the *Saccharomyces cerevisiae* ESCRT-II complex (PDB: 1U5T).
- (D) Crystal structure of the *Homo sapiens* ALIX Bro1 and V domains (PDB: 2XS1).
- (E) Crystal structure of the *Saccharomyces cerevisiae* ESCRT-III Snf7<sup>core</sup> filament (PDB: 5FD9)
- (F) Crystal structure of the *Metallosphaera sedula* Vps4 hexamer (PDB: 4D80)

## **ESCRTs and Cellular Membrane Remodeling**

The unifying principle of all ESCRT-dependent processes is a membrane budding and scission reaction with a topology that drives membrane budding away from the cytoplasm. Here, I review the ESCRT-dependent cellular processes: MVB biogenesis, enveloped virus budding, cytokinesis and nuclear envelope reformation (Table 1.1).

### **Multivesicular Body Biogenesis**

Historically, the ESCRT pathway was first described as a network of complexes at the endosomes that function cooperatively to sort ubiquitinated transmembrane proteins (cargo) for lysosomal degradation (Katzmann et al., 2001; Odorizzi et al., 1998). Ubiquitinated cargo is clustered into regions of the endosomal membrane that bud into to the lumen (ILVs) and are then degraded when the MVB fuses with the lysosome. MVB cargo is initially organized into a flat clathrin lattice on the endosomal membrane by ESCRT-0 (Katzmann et al., 2003). ESCRT-0 recruits ESCRT-I. The ESCRT-I and ESCRT-II complexes further recognize and cluster ubiquitinated cargo (Babst et al., 2002a; Babst et al., 2002b). Both ESCRT-II and Bro1 (ALIX and HD-PTP in human) function as ubiquitin receptors (Pashkova et al., 2013) and set up the assembly and architecture of ESCRT-III (Tang et al., 2016; Teis et al., 2010), which polymerizes into a spiraling helical polymer for cargo sequestration and membrane deformation (Henne et al., 2012; Wollert and Hurley, 2010; Wollert et al., 2009). ESCRT-III further recruits Vps4 (Obita et al., 2007) for membrane scission and vesicle formation and generates cargo-laden ILVs (Figures 1.3B-C).

The E3 ubiquitin ligase Rsp5 (Reverses Spt-phenotype 5) (NEDD4, neural precursor cell expressed developmentally down-regulated protein 4, in human) is the most important class of the ESCRT-associated ubiquitin ligase for the MVB pathway (Katzmann et al., 2004; Lin et al., 2008; Morvan et al., 2004; Reggiori and Pelham, 2001). Ubiquitination is ultimately removed from cargoes prior to ILV incorporation by the deubiquitinases, Doa4 in yeast (Amerik et al., 2000; Luhtala and Odorizzi, 2004; Swaminathan et al., 1999), or AMSH and UBPY in human (McCullough et al., 2006; Row et al., 2007; Sierra et al., 2010; Solomons et al., 2011).

### **Enveloped Virus Budding**

In 2001, very shortly after the ESCRTs were reported to function in the MVB pathway, ESCRTs were discovered to be essential factors in the budding of human immunodeficiency virus type 1 (HIV-1) from the plasma membrane of infected cells (Garrus et al., 2001a). Unlike MVB formation, it has been suggested that HIV-1 budding does not require ESCRT-0, ESCRT-II, or the ESCRT-III subunit CHMP6 (Vps20) (Langelier et al., 2006), although a recent study reported that ESCRT-II is needed for efficient HIV-1 release (Meng et al., 2015) (Table 1.1). Exploitation of the ESCRT machinery is driven by virally encoded Gag proteins, which recruit ESCRT-I and ALIX (Bro1) to the membrane microdomain where new viruses are being packaged. This recruitment is through an interaction mimicking the binding between the P-(S/T)-A-P motif of ESCRT-0 and the UEV domain of ESCRT-I (Pornillos et al., 2003). ALIX nucleates the ESCRT-III complex (Carlson and Hurley, 2012; Jouvenet et al., 2011), which together with Vps4, catalyzes membrane scission necessary for the virion release

from the host cell membrane. Interestingly, the ubiquitination of Gag can also enhance its interaction with the ESCRTs by providing additional binding sites for Tsg101 (Garrus et al., 2001a). Accordingly, a role for Nedd4 (Rsp5) and the ubiquitin ligase machinery has been identified in the release of enveloped viruses (Strack et al., 2000).

## Cytokinesis

In 2007, the discovery that the ESCRTs are necessary for cell abscission, the final stage of cytokinesis in which the cell midbody is constricted, finally establishes the central role of the ESCRTs in executing topologically equivalent membrane-deforming processes (Carlton and Martin-Serrano, 2007). Cytokinesis requires membrane scission, and the creation of membrane curvature that is topologically consistent with the curvatures needed in MVB biogenesis and viral budding.

ESCRT-I Tsg101 (Vps23) and ALIX (Bro1) were the first ESCRT proteins found to localize to late-stage midbodies (Carlton and Martin-Serrano, 2007; Spitzer et al., 2006). They are recruited to the midbody by CEP55, a microtubule bundling protein essential for a late stage in cell division (Carlton et al., 2008; Carlton and Martin-Serrano, 2007). ALIX directly recruits ESCRT-III CHMP4B (Snf7) to the midbody. Three-dimensional electron tomography of the midbody revealed 17-nm-thick spiraling ESCRT-III filaments adjacent to membrane (Guizetti et al., 2011) (Figure 1.4C).

The ESCRT-III IST1 and CHMP1 also localize to the midbody and are essential for abscission (Agromayor et al., 2009; Bajorek et al., 2009a). Recent insight into how microtubule disassembly at the midbody occurs demonstrated that IST1 and CHMP1 recruit the AAA ATPase Spastin to the midbody to sever microtubules as abscission

progresses (Yang et al., 2008). This suggests that ESCRT-III can recruit at least two AAA-ATPases to sites of scission (Table 1.1).

It has been suggested that the recruitment of ESCRT-I and ALIX by CEP55 directly triggers the activation and assembly of ESCRT-III, independent of ESCRT-II. However, a very recent study suggested that ALIX and ESCRT-II function as parallel ESCRT-III recruiters in cytokinetic abscission (Christ et al., 2016), similar to those found in the MVB biogenesis pathway (Tang et al., 2016) (Table 1.1). This raises the possibility that ESCRT-III activation during cytokinesis could be mechanistically related to that of MVB biogenesis.

Remarkably, ESCRTs first emerged in Archaea. *Crenarchaeota* of the genus *Sulfolobus* utilizes its ESCRT-III and Vps4 orthologs directly in cytokinesis (Lindas et al., 2008), suggesting an ancient role for these proteins in cell division. Furthermore, a Vps25-like protein CdvA can interact with and recruit ESCRT-III-like subunits to membranes in *Sulfolobus* (Samson et al., 2011). Thus, the primal biochemical function of the ESCRTs is to constrict and sever membrane necks.

## **Nuclear Pore Complex Assembly and Nuclear Envelope Reformation**

In 2001, CHMP1 (Did2/Vps46) was identified as both a cytoplasmic vesicle trafficking protein (Howard et al., 2001) and a nuclear matrix protein (Stauffer et al., 2001). Given its ambiguous nature, CHMP1 was named charged multivesicular body protein / chromatin modifying protein-1. Well explored was the cytosolic membrane-remodeling activity of CHMP1 and other CHMPs. However, the possible role of the CHMP proteins in chromatin remodeling has not been pursued further.

It took until 2014 for the physiological functions to emerge for the nuclear ESCRTs. The budding yeast *Saccharomyces cerevisiae* undergo “closed” mitosis, in which the nuclear envelope does not break down during the cell cycle. Strikingly, ESCRT-III and Vps4 were identified important for nuclear pore complex (NPC) integrity (Webster et al., 2014). Interestingly, ESCRT-III is directly recruited by the nuclear inner membrane protein and the NPC quality control factor Heh2, but not by the canonical upstream ESCRTs.

In contrast, metazoan cell division undergoes “open” mitosis, in which the nuclear envelope is broken down at mitotic onset to allow the chromosomes to access the mitotic spindle. This process involves the disassembly and dispersal of all the main elements of the nuclear envelope, including the nuclear membranes, NPCs and the lamina. The resealing of fragmented nuclear membranes is an ESCRT-dependent processes. In 2015, two back-to-back studies characterized mechanistic insights into the ESCRTs in the nuclear envelope reformation during telophase of cell division (Olmos et al., 2015; Vietri et al., 2015). Notably, cancer cell metastasis incurs substantial physical stress on the nuclear envelope, whose repair also requires a resealing action by the ESCRTs (Denais et al., 2016).

Mechanistically, ESCRT-III and Vps4 are recruited transiently to sites of annular fusion in reforming the nuclear envelope. As with NPC quality control, upstream ESCRTs do not appear to be required. Rather, UFD1, a subunit of the p97 complex, directly recruits ESCRT-III (Olmos et al., 2015). Similar to its role in cytokinetic abscission, the AAA-ATPase Spastin is recruited by the ESCRT-III IST1 subunit for the severing of spindle microtubules (Vietri et al., 2015), highlighting a conservation of the

machinery that regulate mitotic membrane remodeling events (Table 1.1). Remarkably, the previously uncharacterized CHMP7 protein, which has been suggested as an ESCRT-III-ESCRT-III hybrid (Horii et al., 2006) or an ESCRT-II-ESCRT-III hybrid (Bauer et al., 2015), was identified as an essential CHMP4B (Snf7) recruiter. This initiates the ESCRT-III machinery with sequential recruitment of CHMP4 (Snf7), CHMP3 (Vps24) and CHMP2 (Vps2) (Vietri et al., 2015). The yeast CHMP7 ortholog, the open reading frame YJL049W, has recently been implicated in NPC assembly, which may further link NPC surveillance and membrane sealing functions at this membrane (Bauer et al., 2015).

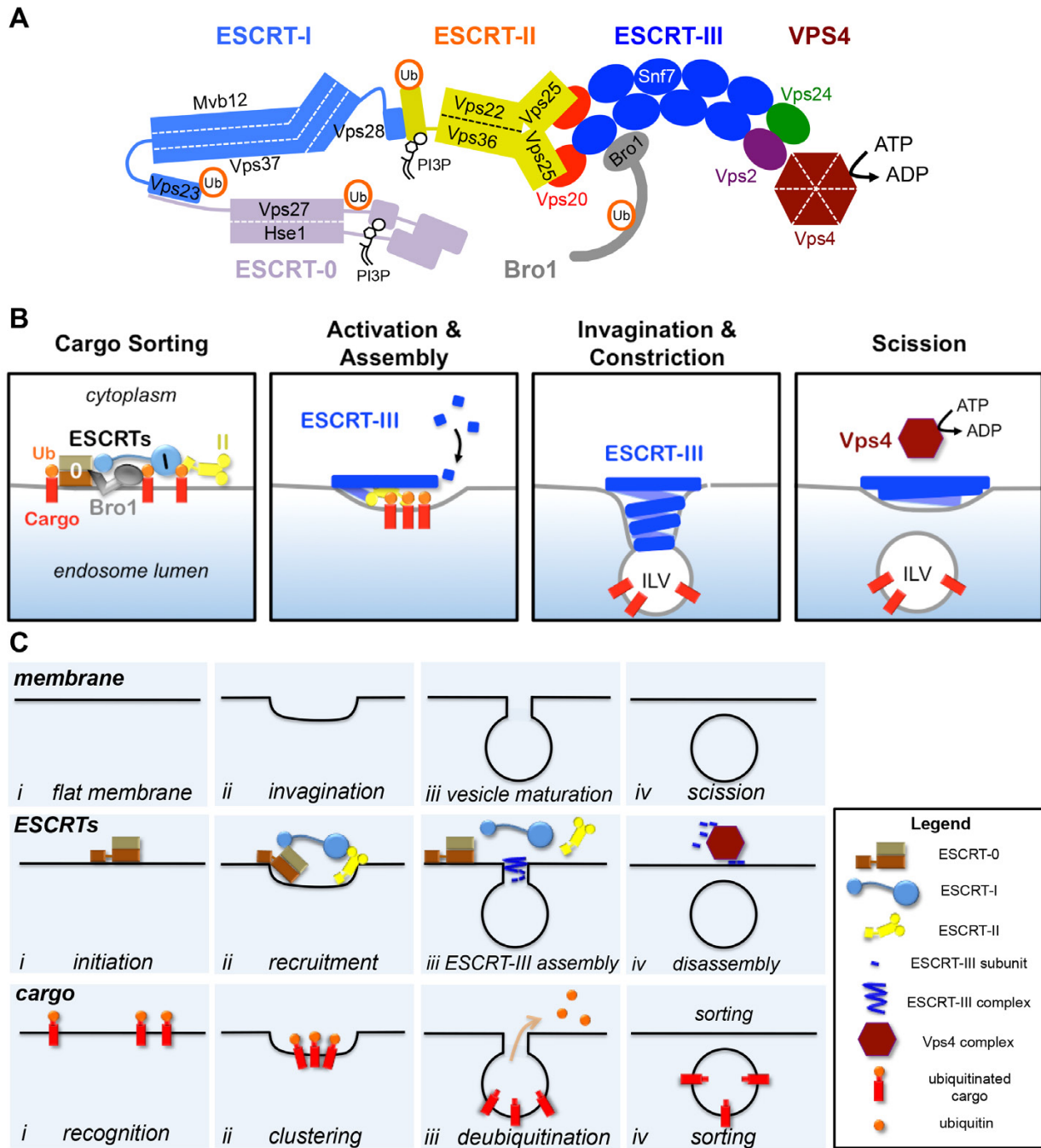


**Figure 1.3 Distinct Stages of the ESCRT-mediated MVB Biogenesis**

### **Figure 1.3 Distinct Stages of the ESCRT-mediated MVB Biogenesis**

(A) Cartoon of the ESCRT pathway in MVB Biogenesis. Adopted from Tang et al. 2016.

(B) Speculative cartoons illustrating four stages in ESCRT-mediated vesicle budding: cargo sorting by the upstreams ESCRTs, ESCRT-0, I, II and Bro1, ESCRT-III activation and assembly, ESCRT-III-mediated membrane invagination and constriction, and Vps4-mediated ESCRT-III disassembly and membrane scission. Adopted from Tang et al. 2015.

(C) Perspectives of ESCRT-mediated vesicle budding. (top) From the membrane perspective, there are four distinct stages of ILV budding. A flat membrane (i) is invaginated (ii) and matures into a vesicle that is still attached to the limiting membrane by a “neck” region (iii). The neck may undergo constriction and a scission event (iv) to complete vesicle budding. (middle) From the ESCRT protein perspective, ESCRT-0 initiates the pathway by engaging ubiquitinated cargo (i). Downstream ESCRT-I and ESCRT-II complexes bind cargo and each other to create an ESCRT-cargo enriched zone (ii). ESCRT-II nucleates ESCRT-III assembly (iii) which drives vesicle budding and is disassembled by the Vps4 complex (iv). (bottom) From the cargo perspective, ubiquitinated cargo is first recognized by the ESCRT-0 ubiquitin binding regions (i) and clustered by the ESCRT-0, -I, and -II complexes (ii). ESCRT-III assembly recruits deubiquitination machinery (iii) and packages cargo into the maturing vesicle, which is finally sorted upon vesicle budding (iv). Adopted from Henne et al. 2011.

## **Membrane Remodeling ESCRT-III Machinery**

### **Membrane Topology**

ESCRT-mediated cellular processes involve membrane deformation and scission, with a membrane topology pushing away from the cell cytoplasm. This is in contrast to the “classical” budding events like COP-I, COP-II, and clathrin vesicle formation, which invoke vesicle budding into the cytoplasm (Doherty and McMahon, 2009; Lee et al., 2005b; Rothman and Wieland, 1996; Shiloni and Schekman, 2002). “Classical” vesicle formation involves a cytoplasmic protein coat that encapsulates the vesicle, adaptor proteins that sequester cargo and promote vesicle maturation, and a scission module that releases the nascent vesicle.

ESCRTs may sculpt the membranes in a similar way but with a distinct topology, which made the characterization of the molecular mechanisms challenging and exciting. In ESCRT-mediated vesicle formation, ESCRTs cannot coat the vesicle exterior because they are segregated in the cytoplasm by the limiting membrane of the endosome. Because the vesicle neck and scission mechanism is topologically inverted, ESCRTs are unable to encircle the neck of a nascent vesicle. Despite this, the observation that ILVs retain a consistent diameter strongly indicates that the ESCRT-mediated vesicle budding is highly regulated (Nickerson et al., 2010; Teis et al., 2010).

### **ESCRT-III Auto-inhibition and Activation**

From the “classical” coated vesicles view, vesicle formation is promoted by three distinct mechanisms: (1) protein oligomeric assembly, (2) individual protein scaffolding via electrostatic protein-membrane interactions, and (3) membrane insertion of

hydrophobic residues . Despite their different topologies, “classical” vesicle budding mechanisms may provide critical insight into the ESCRT-mediated vesicle budding (Henne et al., 2011).

In 2002, the laboratory of Scott D. Emr reported the identification of the ESCRT-III hetero-oligomer (Vps20, Snf7, Vps24 and Vps2) as a key regulator for MVB biogenesis (Table 1.1). In 2006, the laboratory of Winfried Weissenhorn determined the first X-ray crystal structure of ESCRT-III subunit, CHMP3 (Vps24) (Muziol et al., 2006). Since then, numerous studies have defined key roles for ESCRT-III in particular as a membrane deformation and scission machine that share the characteristics from the “classical” vesicle coats (Buchkovich et al., 2013; Kashikar et al., 2014; Hanson et al., 2008; Henne et al., 2012; McCullough et al., 2015; Saksena et al., 2009; Tang et al., 2015; Wollert and Hurley, 2010; Wollert et al., 2009).

ESCRT-III subunits are small, soluble, and electrostatically charged proteins that all share a common domain organization and architectural fold (Bajorek et al., 2009b; Muziol et al., 2006; Rue et al., 2008; Shim et al., 2007). The N-terminal core domain is highly structured and is composed of four  $\alpha$ -helices that fold into a bundle approximately 7 nm in length. The core domain is positively charged in the  $\alpha$ 1- $\alpha$ 3 region, which binds the acidic lipids within the lipid bilayers, although it appears that Snf7 is primarily relies on the  $\alpha$ 2/3 helix, while Vps24, Vps2 and Did2 utilize the  $\alpha$ 1 helix (Buchkovich et al., 2013; McCullough et al., 2015; Muziol et al., 2006; Tang et al., 2015). The carboxyl-terminus, in contrast, is negatively charged and largely unstructured (Figure 1.3C).

Elegant biochemical studies and X-ray crystal structure of CHMP3 (Vps24) and IST1 indicated that the acidic C-terminus of ESCRT-III proteins formed intramolecular

contacts with the basic core domain, rendering ESCRT-III in a monomeric autoinhibited “closed” conformational state (Bajorek et al., 2009b; Lata et al., 2008a; Muziol et al., 2006; Zamborlini et al., 2006). In this state, the core domain folds into a four-helical bundle coiled-coil. The C-terminal short  $\alpha$ -helix,  $\alpha$ 5, forms intramolecular contacts along the tips the  $\alpha$ 1/2 helix in the N-terminal core domain. Displacement of the C-terminal auto-inhibitory region drives both membrane binding and polymerization (Ghazi-Tabatabai et al., 2008; Henne et al., 2012; Shim et al., 2007; Tang et al., 2016; Tang et al., 2015). Thus, it has been suggested that ESCRT-III subunits exist as “closed” monomers in the cell cytoplasm until their activation and recruitment to membrane surfaces during ESCRT-III assembly.

Indeed, structural and biophysical studies suggest that individual ESCRT-III subunits can adopt distinct conformations in the cytoplasm or in the assembled membrane bound polymer. Small angle X-ray scattering (SAXS) experiment suggested that Vps20 appears to preferentially exhibit an extended conformation in solution (Schuh et al., 2015). Together with its N-terminal myristoylation (Babst et al., 2002a), this extended conformation appears to favor membrane binding and initiate Snf7 polymerization (Teis et al., 2010). This is in contrast to Vps24, in which both the “closed” globular and the “open” extended conformations were observed by SAXS under different ionic strength (Lata et al., 2008a).

## **ESCRT-III Polymerization**

Much effort has been focused on Snf7 to understand ESCRT-III activation and assembly, as Snf7 is the predominant ESCRT-III component and is ubiquitously found

in all ESCRT-dependent processes. In 2008, the laboratory of Phyllis I. Hanson reported the first observation that overexpressed Snf7 (CHMP4 in *Homo sapiens*) assembles into spiraling filament on membranes in COS-7 cells (Hanson et al., 2008) (Figure 1.4B). In 2012, the laboratory of Scott D. Emr characterized a single charge inversion substitution on Arg52 of Snf7 (*Saccharomyces cerevisiae*) that promotes the release of the C-terminal autoinhibition for Snf7 activation and polymer assembly. Conformationally active Snf7 assembles into ~9 nm double-stranded spiraling protofilaments on lipid membranes *in vitro*, directly visible to negative stain transmission electron microscopy (TEM) (Henne et al., 2012) (Figure 1.4E). In 2014, the laboratory of Anjon Audhya visualized Snf7 (VPS-32 in *Caenorhabditis elegans*) spirals by cryo-electron microscopy (cryoEM) (Figure 1.4F). Despite the relative low resolution, together with molecular dynamics (MD) simulations, this study revealed that Snf7 protomers in the protofilament are flexible and able to accommodate a range of bending angles (Shen et al., 2014). In 2015, the laboratory of Aurélien Roux measured the polymerization energy and the rigidity of Snf7 (*Saccharomyces cerevisiae*) filaments through optical tweezers and atomic force microscopy (AFM). It was demonstrated that Snf7 spirals could function as spiral springs that undergo elastic expansion for membrane deformation and fission (Chiaruttini et al., 2015) (Figure 1.4G).

Despite the direct visualization of Snf7 polymer assembly by TEM and AFM, it took until late 2015 for the first structural determination of Snf7 protofilament. In my dissertation work, I determined the first X-ray crystal structures of Snf7 in its conformationally active and polymeric state, revealing for the first time at atomic resolution, the molecular mechanisms governing Snf7 activation, assembly and

membrane binding (Tang et al., 2015). Strikingly, the Snf7 core domain, which was long believed as a rigid fold that remains unchanged during activation (Henne et al., 2012; Saksena et al., 2009; Shen et al., 2014), undergoes a global conformational rearrangement from the proposed autoinhibitory four-helical bundle state. Although the N-terminal  $\alpha$ 1/2 hairpin fold is largely unchanged, two short  $\alpha$ -helices  $\alpha$ 3 and  $\alpha$ 4 undergo large scale conformational rearrangements that lead to the extension of  $\alpha$ 2 and  $\alpha$ 3 into an ~10nm extended  $\alpha$ -helix ( $\alpha$ 2/3) and a repositioning of  $\alpha$ 4 (Figure 1.4H). This results in the exposure of new hydrophobic and electrostatic surfaces in the core domain to promote Snf7 polymerization into a 30 Å periodicity between protomers. Remarkably, conserved positively charged residues in  $\alpha$ 2 and  $\alpha$ 3 helices (Buchkovich et al., 2013) are now arrayed in an elongated  $\alpha$ 2/3 helix, ideal for interacting with the acidic membranes (Figure 1.4I). Thus, the crystal structure of Snf7 protofilament revealed mechanisms for coupling Snf7 activation and polymerization with stable membrane association (Tang et al., 2015) (See Chapter III).

Very recent genetic studies suggested that the upstream ESCRTs regulate Snf7 activation at both its N-terminal core domain and the C-terminal  $\alpha$ 6 helix. This regulation is achieved through parallel activation pathways: the canonical ESCRT-I-ESCRT-II-Vps20 pathway activates the N-terminal core domain of Snf7 to trigger its structural rearrangement; the ESCRT-0-Bro1 pathway directly acts on the  $\alpha$ 6 helix to release the autoinhibitory C-terminus (Tang et al., 2016) (Figure 1.4H). This is consistent with the recent finding of Snf7 (CHMP4B) recruitment by ESCRT-II and ALIX in cytokinesis (Christ et al., 2016), reconciling the pathway-specific upstream ESCRTs in mediating Snf7 recruitment, activation and assembly (See Chapter IV).

## **ESCRT-III and Membrane Deformation**

So far, Snf7 protofilaments are the best characterized. However, higher order assemblies of ESCRT-II-Vps20-Snf7 (ESCRT-II-CHMP6-CHMP4), Snf7-Vps24-Vps2 (CHMP4-CHMP3-CHMP2), Vps24 (CHMP3), Vps2 (CHMP2), Vps24-Vps2 (CHMP3-CHMP2), Ist1 (IST1), Did2 (CHMP1A, CHMP1B) and Ist1-Did2 (IST1-CHMP1B) have also been observed (Bajorek et al., 2009b; Cashikar et al., 2014; Dobro et al., 2013; Ghazi-Tabatabai et al., 2008; Henne et al., 2012; Lata et al., 2008b; McCullough et al., 2015).

Although ESCRT-III-dependent membrane remodeling events require Snf7 homo-polymerization, the presence of ESCRT-II and Vps20 appears to constrain Snf7 into ESCRT-III rings with a diameter of ~65 nm. These ESCRT-III rings appear to confine a membrane area in size sufficient for ILV budding. The formation of a membrane-bound Snf7 ring acts as a physical barrier preventing transmembrane cargo clustered by the upstream ESCRTs from escaping the Snf7 ring. The addition of the downstream ESCRT-III subunits Vps24 and Vps2 convert the two-dimensional Snf7 spirals into three-dimensional superhelices (Cashikar et al., 2014; Hanson et al., 2008; Henne et al., 2012). Co-polymers of Vps24-Vps2 (CHMP3-CHMP2) or Ist1-Did2 (IST1-CHMP1) form tubes of different dimensions that taper into dome-shaped ends (Bajorek et al., 2009b; Lata et al., 2008b; McCullough et al., 2015; Morita et al., 2011) with the capacity to deform lipid membranes.

In cells, overexpressed Snf7 (CHMP4) assembles into flat circular filaments at the inner leaflet of the plasma membrane (Figure 1.4B). Upon depletion of Vps4 or

expression of a dominant negative Vps4 hydrolysis mutant (Babst et al., 1997), the flat Snf7 spirals tighten and form tubular structures that bud the plasma membrane outwards (Cashikar et al., 2014; Hanson et al., 2008) (Figure 1.4C), suggesting either that the integration of the downstream ESCRT-III subunits Vps24 and Vps2, which are responsible for the recruitment of Vps4, transform the internal organization of the Snf7 polymer.

Generation of a nascent vesicle requires an intricate balance of competing membrane curvatures (Figure 1.4J). Snf7 localizes to both the curved necks of invaginations and along highly curved edges of membranes (Buchkovich et al., 2013; Fyfe et al., 2011; Lee et al., 2015; Wollert and Hurley, 2010). The amphipathic N-terminus containing hydrophobic residues (ANCHR) motif of Snf7 acts to sense and stabilize the positively curved rim of the invagination (Buchkovich et al., 2013). Coinciding with this positive curvature stabilization, the helical Snf7 polymer acts as a circular protein spring that triggers and stabilizes the negatively curved circumference of the neck of the invagination. As a two-dimensional Snf7 spiral elongates into a three-dimensional superhelix by the recruitment of the downstream ESCRT-III subunits, the tight membrane binding of the “corkscrew” may concentrate transmembrane cargoes ahead of the leading edge of the forming and narrowing filament, packaging them into the nascent ILV (Figure 1.4J) (See Chapter II).

In late 2015, the laboratories of Adam S. Frost and Wesley I. Sundquist determined a remarkable 4 Å cryoEM structure of helical IST1-CHMP1B (Ist1-Did2) co-polymer. CHMP1B (Did2) adopts an extended conformation in its N-terminal core domain, reminiscent of Snf7, while IST1 retains the closed conformation (McCullough et

al., 2015). Thus, ESCRT-III subunits could adopt specific conformations to expose distinct surfaces for protein interactions. Remarkably, overexpressed CHMP1B (Did2) polymers form external coats to drive positive membrane curvature and tubulate membranes into the cell cytoplasm (McCullough et al., 2015), similar to what has been observed from its binding partner, IST1 (Allison et al., 2013). It remains unclear whether CHMP1B promotes fission of recycling tubules from the endosome. These distinct properties could help to build ESCRT-III polymers with different sizes and shapes that are ideally suited to remodel different target membranes.

Currently, the cross-talk between four ESCRT-III core (Vps20, Snf7, Vps24 and Vps2) and accessory (Did2/Vps46, Ist1, Vps60 and Chm7) subunits remains a mystery in the field. The wide spectrum of morphology of the observed ESCRT-III protein assemblies and co-assemblies is difficult to reconcile. It is likely that the smaller and curved ESCRT-III spirals and rings differ in subunit composition, stoichiometry and dynamics from the long ESCRT-III protofilaments or tubules, which may represent the diverse functional states of dynamic ESCRT-III complexes during membrane remodeling.

### **Vps4 and Membrane Scission**

Although the AAA-ATPase Vps4 is necessary for ESCRT-III disassembly, contradictory studies have made it unclear whether Vps4 plays a direct role in vesicle scission (Chiaruttini et al., 2015; Lata et al., 2008b; Obita et al., 2007; Wollert et al., 2009). However, as with the requirement of ESCRT-III, Vps4 is also ubiquitously found

in all ESCRT-dependent processes, indicating that the activities between ESCRT-III and Vps4 are tightly coupled.

Several recent studies have suggested that ESCRT-III alone is not sufficient to complete vesicle formation. Rather, binding of Vps4 to ESCRT-III is directly coupled to membrane deformation and constriction *in vitro* and *in vivo* (Adell et al., 2014; Hanson et al., 2008; Henne et al., 2012). One hypothesis is that Vps4 engages ESCRT-III following its assembly and, like a mechanical motor, helps generate the constrictive force necessary for scission at the vesicle neck and mediates the stepwise disassembly of the ESCRT-III complex. This stepwise disassembly could generate force along the ESCRT-III polymer and mediate neck constriction as the ESCRT-III circular polymer shrinks into smaller rings to bring membranes into close proximity. Disassembly could also potentially generate translocation where Snf7 filaments move past one another, creating constrictive force (Henne et al., 2011). Alternatively, Vps4 could engage multiple ESCRT-III subunits simultaneously and mediate concerted ESCRT-III disassembly. The drastic removal of ESCRT-III from the neck of the budding ILV may destabilize the highly curved membrane, leading to buckling and scission (Chiaruttini et al., 2015). In all models, the late recruitment of Vps4 ensures that ESCRT-III is not prematurely disassembled (Adell et al., 2014; Merrill and Hanson, 2010; Nickerson et al., 2010; Shestakova et al., 2010; Teis et al., 2008).

An alternative hypothesis suggests that Vps4 does not mediate ILV budding directly but rather serves only to recycle ESCRT-III subunits after scission has occurred (Wollert et al., 2009). This is in contrast to other vesicle budding events like dynamin-dependent endocytosis, where the hydrolysis of GTP causes the dynamin oligomer to

change conformations and mediate scission (Bashkirov et al., 2008). The proposed “spiral spring” model for ESCRT-III-dependent membrane remodeling suggested that the expansion of Snf7 springs into the membrane releases resulting in membrane distortions that would be sufficient to drive budding reactions independent of Vps4 (Chiaruttini et al., 2015). Here, Vps4 would function primarily to remove ESCRT-III subunits from the membrane and potentially reset them into the autoinhibited conformation. Moreover, a recent hydrogen/deuterium exchange mass spectrometry (HDX-MS) study suggested a mechanism in which Vps4 disassembles ESCRT-III through global unfolding and threading through its central pore (Yang et al., 2015). This is similar to that of the AAA-ATPase ClpX unfoldase (Burton et al., 2001; Reid et al., 2001; Siddiqui et al., 2004), although the mechanism of ESCRT-III refolding into the their autoinhibited conformation remains unclear.

## Closing Remarks

Recent studies have highlighted the remarkable ability of the ESCRT machinery to remodel membranes in diverse cellular pathways. Using high-resolution methodologies, the mechanisms that govern this membrane remodeling are beginning to be understood at extreme spatial and temporal detail. No doubt future studies will continue to reveal new and exciting properties of this remarkable membrane sculpting machinery.

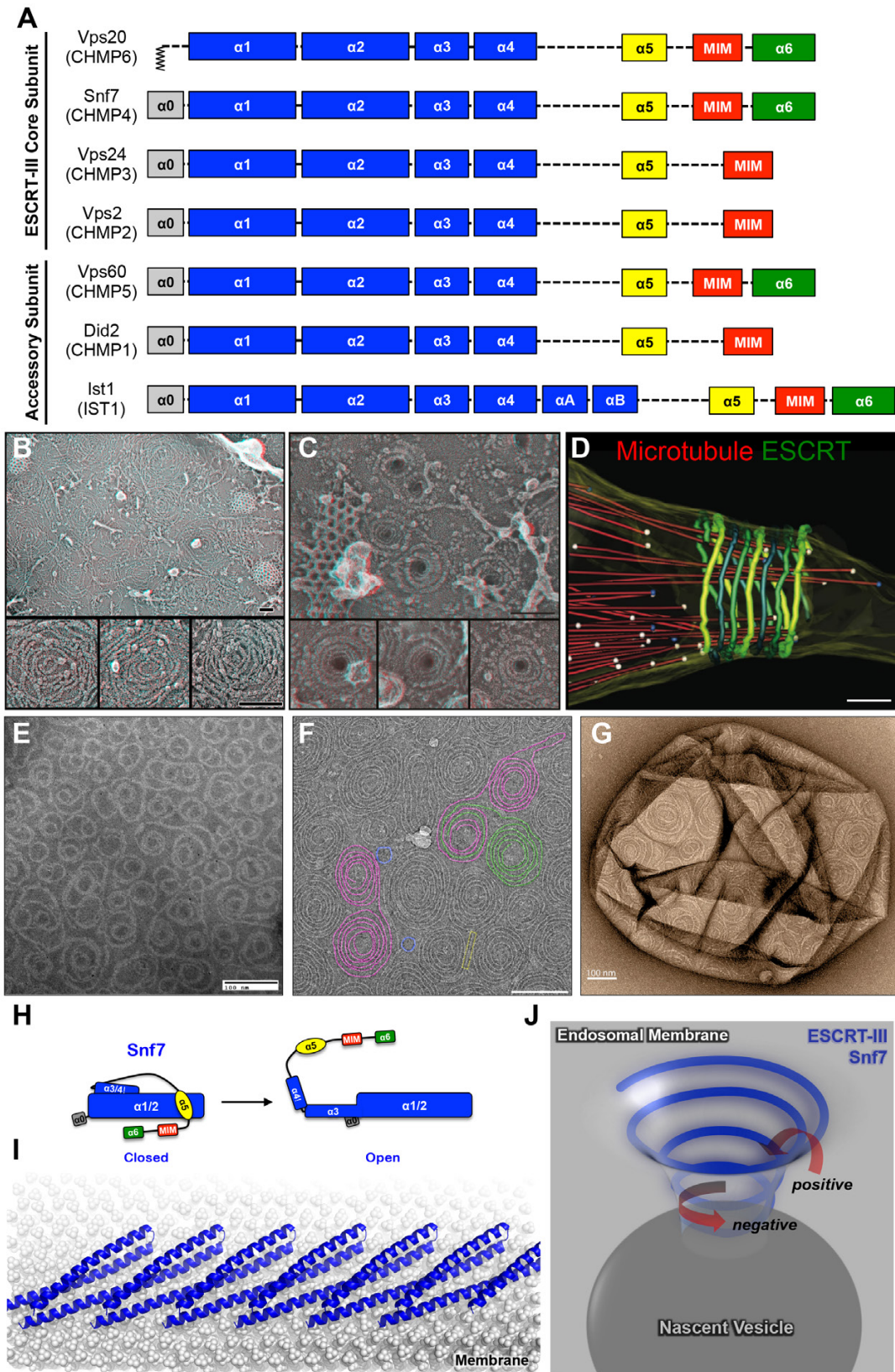


Figure 1.4 Snf7 Spirals and Membrane Remodeling

## Figure 1.4 Snf7 Spirals and Membrane Remodeling

- (A) Domain organization of the ESCRT-III core and accessory subunits. The N-terminal core domain is colored in blue. The myristoylation of Vps20 is shown in zigzag.
- (B) Deep-etch transmission electron micrograph of overexpressed FLAG-CHMP4A (Snf7) form curved filaments on the plasma membrane of COS-7 cells. Adopted from Hanson et al. 2008.
- (C) Deep-etch transmission electron micrograph of ESCRT-III spiraling filaments in HeLa cells depleted both VPS4A and VPSB. Adopted from Kashikar et al. 2014.
- (D) Reconstructed electron tomography of high-pressure frozen cells, showing 17-nm filaments spiraling along the constriction zone of the midbody during cytokinesis. Adopted from Guizetti et al. 2011.
- (E) Negative stain transmission electron micrograph of *Saccharomyces cerevisiae* Snf7<sup>R52E</sup> spiraling filaments on lipid monolayer. Adopted from Henne et al. 2012.
- (F) Cryo-electron micrograph of *Caenorhabditis elegans* VPS-32 (Snf7) spiraling filaments. Adopted from Shen et al. 2014. Scale bars, 100nm.
- (G) Negative stain transmission electron micrograph of *Saccharomyces cerevisiae* Snf7 spiraling filaments coated large unilamellar vesicle. Adopted from Chiaruttini et al. 2015.
- (H) Schematic cartoons of Snf7 conformational rearrangement during activation.
- (I) Ribbon structure of Snf7 protofilament (PDB: 5FD9) on a lipid membrane.
- (J) Schematic of a Snf7 homo-polymer in the neck of a nascent ILV with positive and negative membrane curvatures.

## Reference

Adell, M.A., Vogel, G.F., Pakdel, M., Muller, M., Lindner, H., Hess, M.W., and Teis, D. (2014). Coordinated binding of Vps4 to ESCRT-III drives membrane neck constriction during MVB vesicle formation. *J Cell Biol* 205, 33-49.

Agromayor, M., Carlton, J.G., Phelan, J.P., Matthews, D.R., Carlin, L.M., Ameer-Beg, S., Bowers, K., and Martin-Serrano, J. (2009). Essential Role of hIST1 in Cytokinesis. *Mol Biol Cell* 20, 1374-1387.

Allison, R., Lumb, J.H., Fassier, C., Connell, J.W., Ten Martin, D., Seaman, M.N.J., Hazan, J., and Reid, E. (2013). An ESCRT-spastin interaction promotes fission of recycling tubules from the endosome. *Journal of Cell Biology* 202, 527-543.

Amerik, A.Y., Nowak, J., Swaminathan, S., and Hochstrasser, M. (2000). The Doa4 deubiquitinating enzyme is functionally linked to the vacuolar protein-sorting and endocytic pathways. *Mol Biol Cell* 11, 3365-3380.

Arlt, H., Perz, A., and Ungermann, C. (2011). An Overexpression Screen in *Saccharomyces cerevisiae* Identifies Novel Genes that Affect Endocytic Protein Trafficking. *Traffic* 12, 1592-1603.

Asao, H., Sasaki, Y., Arita, T., Tanaka, N., Endo, K., Kasai, H., Takeshita, T., Endo, Y., Fujita, T., and Sugamura, K. (1997). Hrs is associated with STAM, a signal-transducing adaptor molecule - Its suppressive effect on cytokine-induced cell growth. *Journal of Biological Chemistry* 272, 32785-32791.

Azmi, I., Davies, B., Dimaano, C., Payne, J., Eckert, D., Babst, M., and Katzmann, D.J. (2006). Recycling of ESCRTs by the AAA-ATPase Vps4 is regulated by a conserved VSL region in Vta 1. *Journal of Cell Biology* 172, 705-717.

Azmi, I.F., Davies, B.A., Xiao, J.Y., Babst, M., Xu, Z.H., and Katzmann, D.J. (2008). ESCRT-III family members stimulate Vps4 ATPase activity directly or via Vta1. *Developmental Cell* 14, 50-61.

Babst, M., Katzmann, D.J., Estepa-Sabal, E.J., Meerloo, T., and Emr, S.D. (2002a). ESCRT-III: an endosome-associated heterooligomeric protein complex required for mvb sorting. *Dev Cell* 3, 271-282.

Babst, M., Katzmann, D.J., Snyder, W.B., Wendland, B., and Emr, S.D. (2002b). Endosome-associated complex, ESCRT-II, recruits transport machinery for protein sorting at the multivesicular body. *Dev Cell* 3, 283-289.

Babst, M., Sato, T.K., Banta, L.M., and Emr, S.D. (1997). Endosomal transport function in yeast requires a novel AAA-type ATPase, Vps4p. *EMBO J* 16, 1820-1831.

Babst, M., Wendland, B., Estepa, E.J., and Emr, S.D. (1998). The Vps4p AAA ATPase regulates membrane association of a Vps protein complex required for normal endosome function. *EMBO J* 17, 2982-2993.

Bache, K.G., Raiborg, C., Mehlum, A., and Stenmark, H. (2003). STAM and Hrs are subunits of a multivalent ubiquitin-binding complex on early endosomes. *Journal of Biological Chemistry* 278, 12513-12521.

Bache, K.G., Slagsvold, T., Cabezas, A., Rosendal, K.R., Raiborg, C., and Stenmark, H. (2004). The growth-regulatory protein HCRP1/hVps37A is a subunit of mammalian ESCRT-I and mediates receptor down-regulation. *Mol Biol Cell* 15, 4337-4346.

Baietti, M.F., Zhang, Z., Mortier, E., Melchior, A., Degeest, G., Geeraerts, A., Ivarsson, Y., Depoortere, F., Coomans, C., Vermeiren, E., et al. (2012). Syndecan-syntenin-ALIX regulates the biogenesis of exosomes. *Nat Cell Biol* 14, 677-685.

Bajorek, M., Morita, E., Skalicky, J.J., Morham, S.G., Babst, M., and Sundquist, W.I. (2009a). Biochemical Analyses of Human IST1 and Its Function in Cytokinesis. *Mol Biol Cell* 20, 1360-1373.

Bajorek, M., Schubert, H.L., McCullough, J., Langelier, C., Eckert, D.M., Stubblefield, W.M., Uter, N.T., Myszka, D.G., Hill, C.P., and Sundquist, W.I. (2009b). Structural basis for ESCRT-III protein autoinhibition. *Nat Struct Mol Biol* 16, 754-762.

Banta, L.M., Robinson, J.S., Klionsky, D.J., and Emr, S.D. (1988). Organelle assembly in yeast: characterization of yeast mutants defective in vacuolar biogenesis and protein sorting. *J Cell Biol* 107, 1369-1383.

Bashkirov, P.V., Akimov, S.A., Evseev, A.I., Schmid, S.L., Zimmerberg, J., and Frolov, V.A. (2008). GTPase Cycle of Dynamin Is Coupled to Membrane Squeeze and Release, Leading to Spontaneous Fission. *Cell* 135, 1276-1286.

Bauer, I., Brune, T., Preiss, R., and Kolling, R. (2015). Evidence for a Nonendosomal Function of the *Saccharomyces cerevisiae* ESCRT-III-Like Protein Chm7. *Genetics* 201, 1439-1452.

Bilodeau, P.S., Urbanowski, J.L., Winistorfer, S.C., and Piper, R.C. (2002). The Vps27p Hse1p complex binds ubiquitin and mediates endosomal protein sorting. *Nat Cell Biol* 4, 534-539.

Bishop, N., and Woodman, P. (2001). TSG101/mammalian VPS23 and mammalian VPS28 interact directly and are recruited to VPS4-induced endosomes. *Journal of Biological Chemistry* 276, 11735-11742.

Buchkovich, N.J., Henne, W.M., Tang, S., and Emr, S.D. (2013). Essential N-terminal insertion motif anchors the ESCRT-III filament during MVB vesicle formation. *Dev Cell* 27, 201-214.

Burton, B.M., Williams, T.L., and Baker, T.A. (2001). ClpX-mediated remodeling of Mu transpososomes: Selective unfolding of subunits destabilizes the entire complex. *Molecular Cell* 8, 449-454.

Caillat, C., Macheboeuf, P., Wu, Y., McCarthy, A.A., Boeri-Erba, E., Effantin, G., Gottlinger, H.G., Weissenhorn, W., and Renesto, P. (2015). Asymmetric ring structure of Vps4 required for ESCRT-III disassembly. *Nat Commun* 6, 8781.

Carlson, L.A., and Hurley, J.H. (2012). In vitro reconstitution of the ordered assembly of the endosomal sorting complex required for transport at membrane-bound HIV-1 Gag clusters. *Proc Natl Acad Sci U S A* 109, 16928-16933.

Carlton, J.G., Agromayor, M., and Martin-Serrano, J. (2008). Differential requirements for Alix and ESCRT-III in cytokinesis and HIV-1 release. *Proc Natl Acad Sci U S A* 105, 10541-10546.

Carlton, J.G., and Martin-Serrano, J. (2007). Parallels between cytokinesis and retroviral budding: a role for the ESCRT machinery. *Science* 316, 1908-1912.

Cashikar, A.G., Shim, S., Roth, R., Maldazys, M.R., Heuser, J.E., and Hanson, P.I. (2014). Structure of cellular ESCRT-III spirals and their relationship to HIV budding. *Elife* 3.

Chiaruttini, N., Redondo-Morata, L., Colom, A., Humbert, F., Lenz, M., Scheuring, S., and Roux, A. (2015). Relaxation of Loaded ESCRT-III Spiral Springs Drives Membrane Deformation. *Cell* 163, 866-879.

Christ, L., Wenzel, E.M., Liestol, K., Raiborg, C., Campsteijn, C., and Stenmark, H. (2016). ALIX and ESCRT-I/II function as parallel ESCRT-III recruiters in cytokinetic abscission. *J Cell Biol* 212, 499-513.

Chu, T., Sun, J., Saksena, S., and Emr, S.D. (2006). New component of ESCRT-I regulates endosomal sorting complex assembly. *Journal of Cell Biology* 175, 815-823.

Colombo, M., Moita, C., van Niel, G., Kowal, J., Vigneron, J., Benaroch, P., Manel, N., Moita, L.F., Thery, C., and Raposo, G. (2013). Analysis of ESCRT functions in exosome biogenesis, composition and secretion highlights the heterogeneity of extracellular vesicles. *Journal of Cell Science* 126, 5553-5565.

Curtiss, M., Jones, C., and Babst, M. (2007). Efficient cargo sorting by ESCRT-I and the subsequent release of ESCRT-I from multivesicular bodies requires the subunit Mvb12. *Mol Biol Cell* 18, 636-645.

Denais, C.M., Gilbert, R.M., Isermann, P., McGregor, A.L., te Lindert, M., Weigelin, B., Davidson, P.M., Friedl, P., Wolf, K., and Lammerding, J. (2016). Nuclear envelope rupture and repair during cancer cell migration. *Science* 352, 353-358.

Dobro, M.J., Samson, R.Y., Yu, Z.H., McCullough, J., Ding, H.J., Chong, P.L.G., Bell, S.D., and Jensen, G.J. (2013). Electron cryotomography of ESCRT assemblies and dividing Sulfolobus cells suggests that spiraling filaments are involved in membrane scission. *Mol Biol Cell* 24, 2319-2327.

Doherty, G.J., and McMahon, H.T. (2009). Mechanisms of Endocytosis. *Annual Review of Biochemistry* 78, 857-902.

Eastman, S.W., Martin-Serrano, J., Chung, W., Zang, T., and Bieniasz, P.D. (2005). Identification of human VPS37C, a component of endosomal sorting complex required for transport-I important for viral budding. *Journal of Biological Chemistry* 280, 628-636.

Effantin, G., Dordor, A., Sandrin, V., Martinelli, N., Sundquist, W.I., Schoehn, G., and Weissenhorn, W. (2013). ESCRT-III CHMP2A and CHMP3 form variable helical polymers in vitro and act synergistically during HIV-1 budding. *Cell Microbiol* 15, 213-226.

Filimonenko, M., Stuffers, S., Raiborg, C., Yamamoto, A., Malerod, L., Fisher, E.M., Isaacs, A., Brech, A., Stenmark, H., and Simonsen, A. (2007). Functional multivesicular bodies are required for autophagic clearance of protein aggregates associated with neurodegenerative disease. *J Cell Biol* 179, 485-500.

Fisher, R.D., Wang, B., Alam, S.L., Higginson, D.S., Robinson, H., Sundquist, W.I., and Hill, C.P. (2003). Structure and ubiquitin binding of the ubiquitin-interacting motif. *Journal of Biological Chemistry* 278, 28976-28984.

Fyfe, I., Schuh, A.L., Edwardson, J.M., and Audhya, A. (2011). Association of the endosomal sorting complex ESCRT-II with the Vps20 subunit of ESCRT-III generates a curvature-sensitive complex capable of nucleating ESCRT-III filaments. *J Biol Chem* 286, 34262-34270.

Garrus, J.E., von Schwedler, U.K., Pornillos, O.W., Morham, S.G., Zavitz, K.H., Wang, H.E., Wettstein, D.A., Stray, K.M., Cote, M., Rich, R.L., et al. (2001a). Tsg101 and the vacuolar protein sorting pathway are essential for HIV-1 budding. *Cell* 107, 55-65.

Garrus, J.E., von Schwedler, U.K., Pornillos, O.W., Morham, S.G., Zavitz, K.H., Wang, H.E., Wettstein, D.A., Stray, K.M., Côté, M., Rich, R.L., et al. (2001b). Tsg101 and the vacuolar protein sorting pathway are essential for HIV-1 budding. *Cell* 107, 55-65.

Ghazi-Tabatabai, S., Saksena, S., Short, J.M., Pobbat, A.V., Veprintsev, D.B., Crowther, R.A., Emr, S.D., Egelman, E.H., and Williams, R.L. (2008). Structure and disassembly of filaments formed by the ESCRT-III subunit Vps24. *Structure* 16, 1345-1356.

Gill, D.J., Teo, H., Sun, J., Perisic, O., Veprintsev, D.B., Emr, S.D., and Williams, R.L. (2007). Structural insight into the ESCRT-I-II link and its role in MVB trafficking. *EMBO J* 26, 600-612.

Gonciarz, M.D., Whitby, F.G., Eckert, D.M., Kieffer, C., Heroux, A., Sundquist, W.I., and Hill, C.P. (2008). Biochemical and Structural Studies of Yeast Vps4 Oligomerization. *Journal of Molecular Biology* 384, 878-895.

Guizetti, J., Schermelleh, L., Mantler, J., Maar, S., Poser, I., Leonhardt, H., Muller-Reichert, T., and Gerlich, D.W. (2011). Cortical constriction during abscission involves helices of ESCRT-III-dependent filaments. *Science* 331, 1616-1620.

Guo, E.Z., and Xu, Z.H. (2015). Distinct Mechanisms of Recognizing Endosomal Sorting Complex Required for Transport III (ESCRT-III) Protein IST1 by Different Microtubule Interacting and Trafficking (MIT) Domains. *Journal of Biological Chemistry* *290*, 8396-8408.

Haigler, H.T., McKenna, J.A., and Cohen, S. (1979). Direct visualization of the binding and internalization of a ferritin conjugate of epidermal growth factor in human carcinoma cells A-431. *J Cell Biol* *81*, 382-395.

Hanson, P.I., Roth, R., Lin, Y., and Heuser, J.E. (2008). Plasma membrane deformation by circular arrays of ESCRT-III protein filaments. *J Cell Biol* *180*, 389-402.

Henne, W.M., Buchkovich, N.J., and Emr, S.D. (2011). The ESCRT pathway. *Dev Cell* *21*, 77-91.

Henne, W.M., Buchkovich, N.J., Zhao, Y., and Emr, S.D. (2012). The endosomal sorting complex ESCRT-II mediates the assembly and architecture of ESCRT-III helices. *Cell* *151*, 356-371.

Hierro, A., Sun, J., Rusnak, A.S., Kim, J., Prag, G., Emr, S.D., and Hurley, J.H. (2004). Structure of the ESCRT-II endosomal trafficking complex. *Nature* *431*, 221-225.

Hirano, S., Kawasaki, M., Ura, H., Kato, R., Raiborg, C., Stenmark, H., and Wakatsuki, S. (2006). Double-sided ubiquitin binding of Hrs-UIM in endosomal protein sorting. *Nature Structural & Molecular Biology* *13*, 272-277.

Horii, M., Shibata, H., Kobayashi, R., Katoh, K., Yorikawa, C., Yasuda, J., and Maki, M. (2006). CHMP7, a novel ESCRT-III-related protein, associates with CHMP4b and functions in the endosomal sorting pathway. *Biochem J* *400*, 23-32.

Howard, T.L., Stauffer, D.R., Degn, C.R., and Hollenberg, S.M. (2001). CHMP1 functions as a member of a newly defined family of vesicle trafficking proteins. *Journal of Cell Science* *114*, 2395-2404.

Im, Y.J., Wollert, T., Boura, E., and Hurley, J.H. (2009). Structure and function of the ESCRT-II-III interface in multivesicular body biogenesis. *Dev Cell* *17*, 234-243.

Jimenez, A.J., Maiuri, P., Lafaurie-Janvore, J., Divoux, S., Piel, M., and Perez, F. (2014). ESCRT machinery is required for plasma membrane repair. *Science* 343, 1247136.

Jouvenet, N., Zhadina, M., Bieniasz, P.D., and Simon, S.M. (2011). Dynamics of ESCRT protein recruitment during retroviral assembly. *Nature Cell Biology* 13, 394-U124.

Katzmann, D.J., Babst, M., and Emr, S.D. (2001). Ubiquitin-dependent sorting into the multivesicular body pathway requires the function of a conserved endosomal protein sorting complex, ESCRT-I. *Cell* 106, 145-155.

Katzmann, D.J., Sarkar, S., Chu, T., Audhya, A., and Emr, S.D. (2004). Multivesicular body sorting: Ubiquitin ligase Rsp5 is required for the modification and sorting of carboxypeptidase S. *Mol Biol Cell* 15, 468-480.

Katzmann, D.J., Stefan, C.J., Babst, M., and Emr, S.D. (2003). Vps27 recruits ESCRT machinery to endosomes during MVB sorting. *J Cell Biol* 162, 413-423.

Kieffer, C., Skalicky, J.J., Morita, E., De Domenico, I., Ward, D.M., Kaplan, J., and Sundquist, W.I. (2008). Two distinct modes of ESCRT-III recognition are required for VPS4 functions in lysosomal protein targeting and HIV-1 budding. *Dev Cell* 15, 62-73.

Kojima, R., Obita, T., Onoue, K., and Mizuguchi, M. (2016). Structural Fine-Tuning of MIT-Interacting Motif 2 (MIM2) and Allosteric Regulation of ESCRT-III by Vps4 in Yeast. *J Mol Biol* 428, 2392-2404.

Kostelansky, M.S., Schluter, C., Tam, Y.Y., Lee, S., Ghirlando, R., Beach, B., Conibear, E., and Hurley, J.H. (2007). Molecular architecture and functional model of the complete yeast ESCRT-I heterotetramer. *Cell* 129, 485-498.

Kostelansky, M.S., Sun, J., Lee, S.H., Kim, J., Ghirlando, R., Hierro, A., Emr, S.D., and Hurley, J.H. (2006). Structural and functional organization of the ESCRT-I trafficking complex. *Cell* 125, 113-126.

Kyuma, M., Kikuchi, K., Kojima, K., Sugawara, Y., Sato, M., Mano, N., Goto, J., Takeshita, T., Yamamoto, A., Sugamura, K., et al. (2006). AMSH, an ESCRT-III associated enzyme, deubiquitinates cargo on MVB/late endosomes. *Cell Structure and Function* 31, 159-172.

Langelier, C., von Schwedler, U.K., Fisher, R.D., De Domenico, I., White, P.L., Hill, C.P., Kaplan, J., Ward, D., and Sundquist, W.I. (2006). Human ESCRT-II complex and its role in human immunodeficiency virus type 1 release. *Journal of Virology* 80, 9465-9480.

Lata, S., Roessle, M., Solomons, J., Jamin, M., Gottlinger, H.G., Svergun, D.I., and Weissenhorn, W. (2008a). Structural basis for autoinhibition of ESCRT-III CHMP3. *J Mol Biol* 378, 818-827.

Lata, S., Schoehn, G., Jain, A., Pires, R., Piehler, J., Gottlinger, H.G., and Weissenhorn, W. (2008b). Helical structures of ESCRT-III are disassembled by VPS4. *Science* 321, 1354-1357.

Lee, I.H., Kai, H., Carlson, L.A., Groves, J.T., and Hurley, J.H. (2015). Negative membrane curvature catalyzes nucleation of endosomal sorting complex required for transport (ESCRT)-III assembly. *Proc Natl Acad Sci U S A* 112, 15892-15897.

Lee, J., Oh, K.J., Lee, D., Kim, B.Y., Choi, J.S., Ku, B., and Kim, S.J. (2016). Structural Study of the HD-PTP Bro1 Domain in a Complex with the Core Region of STAM2, a Subunit of ESCRT-0. *PLoS One* 11, e0149113.

Lee, J.A., Beigneux, A., Ahmad, S.T., Young, S.G., and Gao, F.B. (2007). ESCRT-III dysfunction causes autophagosome accumulation and neurodegeneration. *Current Biology* 17, 1561-1567.

Lee, M.C.S., Orci, L., Hamamoto, S., Futai, E., Ravazzola, M., and Schekman, R. (2005). Sar1p N-terminal helix initiates membrane curvature and completes the fission of a COPII vesicle. *Cell* 122, 605-617.

Lin, C.H., MacGurn, J.A., Chu, T., Stefan, C.J., and Emr, S.D. (2008). Arrestin-related ubiquitin-ligase adaptors regulate endocytosis and protein turnover at the cell surface. *Cell* 135, 714-725.

Lindas, A.C., Karlsson, E.A., Lindgren, M.T., Ettema, T.J.G., and Bernander, R. (2008). A unique cell division machinery in the Archaea. *Proc Natl Acad Sci U S A* 105, 18942-18946.

Loncle, N., Agromayor, M., Martin-Serrano, J., and Williams, D.W. (2015). An ESCRT module is required for neuron pruning. *Scientific Reports* 5.

- Lu, Q., Hope, L.W.Q., Brasch, M., Reinhard, C., and Cohen, S.N. (2003). TSG101 interaction with HRS mediates endosomal trafficking and receptor down-regulation. *Proc Natl Acad Sci U S A* **100**, 7626-7631.
- Luhtala, N., and Odorizzi, G. (2004). Bro1 coordinates deubiquitination in the multivesicular body pathway by recruiting Doa4 to endosomes. *J Cell Biol* **166**, 717-729.
- Mao, Y.X., Nickitenko, A., Duan, X.Q., Lloyd, T.E., Wu, M.N., Bellen, H., and Quiocho, F.A. (2000). Crystal structure of the VHS and FYVE tandem domains of Hrs, a protein involved in membrane trafficking and signal transduction. *Cell* **100**, 447-456.
- Mayers, J.R., Fyfe, I., Schuh, A.L., Chapman, E.R., Edwardson, J.M., and Audhya, A. (2011). ESCRT-0 assembles as a heterotetrameric complex on membranes and binds multiple ubiquitinylated cargoes simultaneously. *J Biol Chem* **286**, 9636-9645.
- McCullough, J., Clippinger, A.K., Talledge, N., Skowyra, M.L., Saunders, M.G., Naismith, T.V., Colf, L.A., Afonine, P., Arthur, C., Sundquist, W.I., *et al.* (2015). Structure and membrane remodeling activity of ESCRT-III helical polymers. *Science*.
- McCullough, J., Fisher, R.D., Whitby, F.G., Sundquist, W.I., and Hill, C.P. (2008). ALIX-CHMP4 interactions in the human ESCRT pathway. *Proc Natl Acad Sci U S A* **105**, 7687-7691.
- McCullough, J., Row, P.E., Lorenzo, O., Doherty, M., Beynon, R., Clague, M.J., and Urbe, S. (2006). Activation of the endosome-associated ubiquitin isopeptidase AMSH by STAM, a component of the multivesicular body-sorting machinery. *Current Biology* **16**, 160-165.
- Meng, B., Ip, N.C., Prestwood, L.J., Abbink, T.E., and Lever, A.M. (2015). Evidence that the endosomal sorting complex required for transport-II (ESCRT-II) is required for efficient human immunodeficiency virus-1 (HIV-1) production. *Retrovirology* **12**, 72.
- Merrill, S.A., and Hanson, P.I. (2010). Activation of human VPS4A by ESCRT-III proteins reveals ability of substrates to relieve enzyme autoinhibition. *J Biol Chem* **285**, 35428-35438.
- Mizuno, E., Kawahata, K., Kato, M., Kitamura, N., and Komada, M. (2003). STAM proteins bind ubiquitinated proteins on the early endosome via the VHS domain and ubiquitin-interacting motif. *Mol Biol Cell* **14**, 3675-3689.

Morita, E., Sandrin, V., Alam, S.L., Eckert, D.M., Gygi, S.P., and Sundquist, W.I. (2007). Identification of human MVB12 proteins as ESCRT-I Subunits that function in HIV budding. *Cell Host Microbe* 2, 41-53.

Morita, E., Sandrin, V., McCullough, J., Katsuyama, A., Baci Hamilton, I., and Sundquist, W.I. (2011). ESCRT-III protein requirements for HIV-1 budding. *Cell Host Microbe* 9, 235-242.

Morvan, J., Froissard, M., Haguenuuer-Tsapis, R., and Urban-Grimal, D. (2004). The ubiquitin ligase Rsp5p is required for modification and sorting of membrane proteins into multivesicular bodies. *Traffic* 5, 383-392.

Muziol, T., Pineda-Molina, E., Ravelli, R.B., Zamborlini, A., Usami, Y., Gottlinger, H., and Weissenhorn, W. (2006). Structural basis for budding by the ESCRT-III factor CHMP3. *Dev Cell* 10, 821-830.

Nickerson, D.P., West, M., Henry, R., and Odorizzi, G. (2010). Regulators of Vps4 ATPase activity at endosomes differentially influence the size and rate of formation of intraluminal vesicles. *Mol Biol Cell* 21, 1023-1032.

Nikko, E., and Andre, B. (2007). Split-ubiquitin two-hybrid assay to analyze protein-protein interactions at the endosome: application to *Saccharomyces cerevisiae* Bro1 interacting with ESCRT complexes, the Doa4 ubiquitin hydrolase, and the Rsp5 ubiquitin ligase. *Eukaryot Cell* 6, 1266-1277.

Obita, T., Saksena, S., Ghazi-Tabatabai, S., Gill, D.J., Perisic, O., Emr, S.D., and Williams, R.L. (2007). Structural basis for selective recognition of ESCRT-III by the AAA ATPase Vps4. *Nature* 449, 735-739.

Odorizzi, G., Babst, M., and Emr, S.D. (1998). Fab1p PtdIns(3)P 5-Kinase Function Essential for Protein Sorting in the Multivesicular Body. *Cell* 95, 847-858.

Odorizzi, G., Katzmann, D.J., Babst, M., Audhya, A., and Emr, S.D. (2003). Bro1 is an endosome-associated protein that functions in the MVB pathway in *Saccharomyces cerevisiae*. *J Cell Sci* 116, 1893-1903.

Olmos, Y., Hodgson, L., Mantell, J., Verkade, P., and Carlton, J.G. (2015). ESCRT-III controls nuclear envelope reformation. *Nature* 522, 236-239.

Palade, G.E. (1955). Studies on the endoplasmic reticulum. II. Simple dispositions in cells *in situ*. *J Biophys Biochem Cytol* *1*, 567-582.

Pashkova, N., Gakhar, L., Winistorfer, S.C., Sunshine, A.B., Rich, M., Dunham, M.J., Yu, L., and Piper, R.C. (2013). The yeast alix homolog bro1 functions as a ubiquitin receptor for protein sorting into multivesicular endosomes. *Dev Cell* *25*, 520-533.

Pires, R., Hartlieb, B., Signor, L., Schoehn, G., Lata, S., Roessle, M., Moriscot, C., Popov, S., Hinz, A., Jamin, M., *et al.* (2009). A crescent-shaped ALIX dimer targets ESCRT-III CHMP4 filaments. *Structure* *17*, 843-856.

Pornillos, O., Higginson, D.S., Stray, K.M., Fisher, R.D., Garrus, J.E., Payne, M., He, G.P., Wang, H.E., Morham, S.G., and Sundquist, W.I. (2003). HIV Gag mimics the Tsg101-recruiting activity of the human Hrs protein. *Journal of Cell Biology* *162*, 425-434.

Prag, G., Watson, H., Kim, Y.C., Beach, B.M., Ghirlando, R., Hummer, G., Bonifacino, J.S., and Hurley, J.H. (2007). The Vps27/Hse1 complex is a GAT domain-based scaffold for ubiquitin-dependent sorting. *Developmental Cell* *12*, 973-986.

Raab, M., Gentili, M., de Belly, H., Thiam, H.R., Vargas, P., Jimenez, A.J., Lautenschlaeger, F., Voituriez, R., Lennon-Dumenil, A.M., Manel, N., *et al.* (2016). ESCRT III repairs nuclear envelope ruptures during cell migration to limit DNA damage and cell death. *Science* *352*, 359-362.

Raiborg, C., Bremnes, B., Mehlum, A., Gillooly, D.J., D'Arrigo, A., Stang, E., and Stenmark, H. (2001). FYVE and coiled-coil domains determine the specific localisation of Hrs to early endosomes. *Journal of Cell Science* *114*, 2255-2263.

Raiborg, C., Wesche, J., Malerod, L., and Stenmark, H. (2006). Flat clathrin coats on endosomes mediate degradative protein sorting by scaffolding Hrs in dynamic microdomains. *Journal of Cell Science* *119*, 2414-2424.

Raymond, C.K., Howald-Stevenson, I., Vater, C.A., and Stevens, T.H. (1992). Morphological classification of the yeast vacuolar protein sorting mutants: evidence for a prevacuolar compartment in class E vps mutants. *Mol Biol Cell* *3*, 1389-1402.

Reggiori, F., and Pelham, H.R.B. (2001). Sorting of proteins into multivesicular bodies: ubiquitin-dependent and -independent targeting. *EMBO Journal* *20*, 5176-5186.

Reid, B.G., Fenton, W.A., Homwich, A.L., and Weber-Ban, E.U. (2001). ClpA mediates directional translocation of substrate proteins into the ClpP protease. *Proc Natl Acad Sci U S A* **98**, 3768-3772.

Ren, X.F., and Hurley, J.H. (2010). VHS domains of ESCRT-0 cooperate in high-avidity binding to polyubiquitinated cargo. *EMBO Journal* **29**, 1045-1054.

Richter, C., West, M., and Odorizzi, G. (2007). Dual mechanisms specify Doa4-mediated deubiquitination at multivesicular bodies. *EMBO J* **26**, 2454-2464.

Robinson, J., Klionsky, D., Banta, L., and Emr, S. (1988). Protein sorting in *Saccharomyces cerevisiae*: isolation of mutants defective in the delivery and processing of multiple vacuolar hydrolases. *Mol Cell Biol* **8**(11), 4936-4948.

Rothman, J.E., and Wieland, F.T. (1996). Protein sorting by transport vesicles. *Science* **272**, 227-234.

Rothman, J.H., Howald, I., and Stevens, T.H. (1989). Characterization of genes required for protein sorting and vacuolar function in the yeast *Saccharomyces cerevisiae*. *EMBO J* **8**, 2057-2065.

Rothman, J.H., and Stevens, T.H. (1986). Protein sorting in yeast: mutants defective in vacuole biogenesis mislocalize vacuolar proteins into the late secretory pathway. *Cell* **47**, 1041-1051.

Row, P.E., Liu, H., Hayes, S., Welchman, R., Charalabous, P., Hofmann, K., Clague, M.J., Sanderson, C.M., and Urbe, S. (2007). The MIT domain of UBPY constitutes a CHMP binding and endosomal localization signal required for efficient epidermal growth factor receptor degradation. *J Biol Chem* **282**, 30929-30937.

Row, P.E., Prior, I.A., McCullough, J., Clague, M.J., and Urbe, S. (2006). The ubiquitin isopeptidase UBPY regulates endosomal ubiquitin dynamics and is essential for receptor down-regulation. *J Biol Chem* **281**, 12618-12624.

Rue, S.M., Mattei, S., Sakseña, S., and Emr, S.D. (2008). Novel Ist1-Did2 complex functions at a late step in multivesicular body sorting. *Mol Biol Cell* **19**, 475-484.

Rusten, T.E., Vaccari, T., Lindmo, K., Rodahl, L.M., Nezis, I.P., Sem-Jacobsen, C., Wendler, F., Vincent, J.P., Brech, A., Bilder, D., *et al.* (2007). ESCRTs and Fab1 regulate distinct steps of autophagy. *Current Biology* 17, 1817-1825.

Sachse, M., Urbe, S., Oorschot, V., Strous, G.J., and Klumperman, J. (2002). Bilayered clathrin coats on endosomal vacuoles are involved in protein sorting toward lysosomes. *Mol Biol Cell* 13, 1313-1328.

Saksena, S., Wahlman, J., Teis, D., Johnson, A.E., and Emr, S.D. (2009). Functional reconstitution of ESCRT-III assembly and disassembly. *Cell* 136, 97-109.

Samson, R.Y., Obita, T., Hodgson, B., Shaw, M.K., Chong, P.L.G., Williams, R.L., and Bell, S.D. (2011). Molecular and Structural Basis of ESCRT-III Recruitment to Membranes during Archaeal Cell Division. *Molecular Cell* 41, 186-196.

Scheffer, L.L., Sreetama, S.C., Sharma, N., Medikayala, S., Brown, K.J., Defour, A., and Jaiswal, J.K. (2014). Mechanism of Ca<sup>2+</sup>-triggered ESCRT assembly and regulation of cell membrane repair. *Nature Communications* 5.

Schuh, A.L., Hanna, M., Quinney, K., Wang, L., Sarkeshik, A., Yates, J.R., 3rd, and Audhya, A. (2015). The VPS-20 subunit of the endosomal sorting complex ESCRT-III exhibits an open conformation in the absence of upstream activation. *Biochem J* 466, 625-637.

Scott, A., Chung, H.Y., Gonciarz-Swiatek, M., Hill, G.C., Whitby, F.G., Gaspar, J., Holton, J.M., Viswanathan, R., Ghaffarian, S., Hill, C.P., *et al.* (2005a). Structural and mechanistic studies of VPS4 proteins. *EMBO Journal* 24, 3658-3669.

Scott, A., Gaspar, J., Stuchell-Brereton, M.D., Alam, S.L., Skalicky, J.J., and Sundquist, W.I. (2005b). Structure and ESCRT-III protein interactions of the MIT domain of human VPS4A. *Proc Natl Acad Sci U S A* 102, 13813-13818.

Shen, Q.T., Schuh, A.L., Zheng, Y., Quinney, K., Wang, L., Hanna, M., Mitchell, J.C., Otegui, M.S., Ahlquist, P., Cui, Q., *et al.* (2014). Structural analysis and modeling reveals new mechanisms governing ESCRT-III spiral filament assembly. *J Cell Biol* 206, 763-777.

Shestakova, A., Hanono, A., Drosner, S., Curtiss, M., Davies, B.A., Katzmann, D.J., and Babst, M. (2010). Assembly of the AAA ATPase Vps4 on ESCRT-III. *Mol Biol Cell* 21, 1059-1071.

Shields, S.B., Oestreich, A.J., Winistorfer, S., Nguyen, D., Payne, J.A., Katzmann, D.J., and Piper, R. (2009). ESCRT ubiquitin-binding domains function cooperatively during MVB cargo sorting. *Journal of Cell Biology* 185, 213-224.

Shiflett, S.L., Ward, D.M., Huynh, D., Vaughn, M.B., Simmons, J.C., and Kaplan, J. (2004). Characterization of Vta1p, a class E Vps protein in *Saccharomyces cerevisiae*. *Journal of Biological Chemistry* 279, 10982-10990.

Shih, S.C., Katzmann, D.J., Schnell, J.D., Sutanto, M., Emr, S.D., and Hicke, L. (2002). Epsins and Vps27p/Hrs contain ubiquitin-binding domains that function in receptor endocytosis. *Nature Cell Biology* 4, 389-393.

Shim, S., Kimpler, L.A., and Hanson, P.I. (2007). Structure/function analysis of four core ESCRT-III proteins reveals common regulatory role for extreme C-terminal domain. *Traffic* 8, 1068-1079.

Shimoni, Y., and Schekman, R. (2002). Vesicle budding from endoplasmic reticulum. *Guide to Yeast Genetics and Molecular and Cell Biology*, Pt C 351, 258-278.

Siddiqui, S.M., Sauer, R.T., and Baker, T.A. (2004). Role of the processing pore of the ClpX AAA+ ATPase in the recognition and engagement of specific protein substrates. *Genes & Development* 18, 369-374.

Sierra, M.I., Wright, M.H., and Nash, P.D. (2010). AMSH Interacts with ESCRT-0 to Regulate the Stability and Trafficking of CXCR4. *Journal of Biological Chemistry* 285, 13990-14004.

Slagsvold, T., Aasland, R., Hirano, S., Bache, K.G., Raiborg, C., Trambaiolo, D., Wakatsuki, S., and Stenmark, H. (2005). Eap45 in mammalian ESCRT-II binds ubiquitin via a phosphoinositide-interacting GLUE domain. *Journal of Biological Chemistry* 280, 19600-19606.

Solomons, J., Sabin, C., Poudevigne, E., Usami, Y., Hulsik, D.L., Macheboeuf, P., Hartlieb, B., Gottlinger, H., and Weissenhorn, W. (2011). Structural basis for ESCRT-III CHMP3 recruitment of AMSH. *Structure* 19, 1149-1159.

Sotelo, J.R., and Porter, K.R. (1959). An electron microscope study of the rat ovum. *J Biophys Biochem Cytol* 5, 327-342.

Spitzer, C., Schellmann, S., Sabovljevic, A., Shahriari, M., Keshavaiah, C., Bechtold, N., Herzog, M., Muller, S., Hanisch, F.G., and Hulskamp, M. (2006). The *Arabidopsis* elch mutant reveals functions of an ESCRT component in cytokinesis. *Development* 133, 4679-4689.

Stauffer, D.R., Howard, T.L., Nyun, T., and Hollenberg, S.M. (2001). CHMP1 is a novel nuclear matrix protein affecting chromatin structure and cell-cycle progression. *Journal of Cell Science* 114, 2383-2393.

Strack, B., Calistri, A., Accola, M.A., Palu, G., and Gottlinger, H.G. (2000). A role for ubiquitin ligase recruitment in retrovirus release. *Proc Natl Acad Sci U S A* 97, 13063-13068.

Stuchell, M.D., Garrus, J.E., Muller, B., Stray, K.M., Ghaffarian, S., McKinnon, R., Krausslich, H.G., Morham, S.G., and Sundquist, W.I. (2004). The human endosomal sorting complex required for transport (ESCRT-I) and its role in HIV-1 budding. *Journal of Biological Chemistry* 279, 36059-36071.

Stuchell-Brereton, M.D., Skalicky, J.J., Kieffer, C., Karren, M.A., Ghaffarian, S., and Sundquist, W.I. (2007). ESCRT-III recognition by VPS4 ATPases. *Nature* 449, 740-744.

Swaminathan, S., Amerik, A.Y., and Hochstrasser, M. (1999). The Doa4 deubiquitinating enzyme is required for ubiquitin homeostasis in yeast. *Mol Biol Cell* 10, 2583-2594.

Swanson, K.A., Kang, R.S., Stamenova, S.D., Hicke, L., and Radhakrishnan, I. (2003). Solution structure of Vps27 UIM-ubiquitin complex important for endosomal sorting and receptor downregulation. *EMBO J* 22, 4597-4606.

Tamai, K., Tanaka, N., Nakano, T., Kakazu, E., Kondo, Y., Inoue, J., Shiina, M., Fukushima, K., Hoshino, T., Sano, K., et al. (2010). Exosome secretion of dendritic cells is regulated by Hrs, an ESCRT-0 protein. *Biochemical and Biophysical Research Communications* 399, 384-390.

Tang, S., Buchkovich, N.J., Henne, W.M., Banjade, S., Kim, Y.J., and Emr, S.D. (2016). ESCRT-III activation by parallel action of ESCRT-I/II and ESCRT-0/Bro1 during MVB biogenesis. *Elife* 5.

Tang, S., Henne, W.M., Borbat, P.P., Buchkovich, N.J., Freed, J.H., Mao, Y., Fromme, J.C., and Emr, S.D. (2015). Structural basis for activation, assembly and membrane binding of ESCRT-III Snf7 filaments. *Elife* 4.

Teis, D., Saksena, S., and Emr, S.D. (2008). Ordered assembly of the ESCRT-III complex on endosomes is required to sequester cargo during MVB formation. *Dev Cell* 15, 578-589.

Teis, D., Saksena, S., Judson, B.L., and Emr, S.D. (2010). ESCRT-II coordinates the assembly of ESCRT-III filaments for cargo sorting and multivesicular body vesicle formation. *EMBO J* 29, 871-883.

Teo, H., Perisic, O., Gonzalez, B., and Williams, R.L. (2004a). ESCRT-II, an endosome-associated complex required for protein sorting: Crystal structure and interactions with ESCRT-III and membranes. *Developmental Cell* 7, 559-569.

Teo, H., Veprintsev, D.B., and Williams, R.L. (2004b). Structural insights into endosomal sorting complex required for transport (ESCRT-I) recognition of ubiquitinated proteins. *Journal of Biological Chemistry* 279, 28689-28696.

Teo, H.L., Gill, D.J., Sun, J., Perisic, O., Veprintsev, D.B., Vallis, Y., Emr, S.D., and Williams, R.L. (2006). ESCRT-I core and ESCRT-II GLUE domain structures reveal role for GLUE in linking to ESCRT-I and membranes. *Cell* 125, 99-111.

Tsunematsu, T., Yamauchi, E., Shibata, H., Maki, M., Ohta, T., and Konishi, H. (2010). Distinct functions of human MVB12A and MVB12B in the ESCRT-I dependent on their posttranslational modifications. *Biochemical and Biophysical Research Communications* 399, 232-237.

Vetri, M., Schink, K.O., Campsteijn, C., Wegner, C.S., Schultz, S.W., Christ, L., Thoresen, S.B., Brech, A., Raiborg, C., and Stenmark, H. (2015). Spastin and ESCRT-III coordinate mitotic spindle disassembly and nuclear envelope sealing. *Nature* 522, 231-235.

Vild, C.J., and Xu, Z.H. (2014). Vfa1 Binds to the N-terminal Microtubule-interacting and Trafficking ( MIT) Domain of Vps4 and Stimulates Its ATPase Activity. *Journal of Biological Chemistry* 289, 10378-10386.

Weber-Ban, E.U., Reid, B.G., Miranker, A.D., and Horwich, A.L. (1999). Global unfolding of a substrate protein by the Hsp100 chaperone ClpA. *Nature* 401, 90-93.

Webster, B.M., Colombi, P., Jager, J., and Lusk, C.P. (2014). Surveillance of nuclear pore complex assembly by ESCRT-III/Vps4. *Cell* 159, 388-401.

Wemmer, M., Azmi, I., West, M., Davies, B., Katzmann, D., and Odorizzi, G. (2011). Bro1 binding to Snf7 regulates ESCRT-III membrane scission activity in yeast. *J Cell Biol* 192, 295-306.

Wollert, T., and Hurley, J.H. (2010). Molecular mechanism of multivesicular body biogenesis by ESCRT complexes. *Nature* 464, 864-869.

Wollert, T., Wunder, C., Lippincott-Schwartz, J., and Hurley, J.H. (2009). Membrane scission by the ESCRT-III complex. *Nature* 458, 172-U172.

Yang, B., Stjepanovic, G., Shen, Q.T., Martin, A., and Hurley, J.H. (2015). Vps4 disassembles an ESCRT-III filament by global unfolding and processive translocation. *Nature Structural & Molecular Biology* 22, 492-U488.

Yang, D., and Hurley, J.H. (2010). Structural Role of the Vps4-Vta1 Interface in ESCRT-III Recycling. *Structure* 18, 976-984.

Yang, D., Rismanchi, N., Renvoise, B., Lippincott-Schwartz, J., Blackstone, C., and Hurley, J.H. (2008). Structural basis for midbody targeting of spastin by the ESCRT-III protein CHMP1B. *Nature Structural & Molecular Biology* 15, 1278-1286.

Yu, Z.H., Gonciarz, M.D., Sundquist, W.I., Hill, C.P., and Jensen, G.J. (2008). Cryo-EM structure of dodecameric Vps4p and its 2 : 1 complex with Vta1p. *Journal of Molecular Biology* 377, 364-377.

Zamborlini, A., Usami, Y., Radoshitzky, S.R., Popova, E., Palu, G., and Gottlinger, H. (2006). Release of autoinhibition converts ESCRT-III components into potent inhibitors of HIV-1 budding. *Proc Natl Acad Sci U S A* 103, 19140-19145.

## **CHAPTER II**

### **Essential N-terminal Insertion Motif Anchors the ESCRT-III Filament During MVB Vesicle Formation**

Nicholas J. Buchkovich<sup>1,2,3</sup>, W. Mike Henne<sup>1,2,4</sup>, Shaogeng Tang<sup>1,2</sup>,  
and Scott D. Emr<sup>1,2</sup>

<sup>1</sup> Weill Institute for Cell and Molecular Biology, Cornell University, Ithaca, NY 14853,  
USA

<sup>2</sup> Department of Molecular Biology and Genetics, Cornell University, Ithaca, NY 14853,  
USA

<sup>3</sup> Present Address: Department of Microbiology and Immunology, The Pennsylvania  
State University College of Medicine, Hershey, PA 17033, USA

<sup>4</sup> Present Address: Department of Cell Biology, The University of Texas Southwestern  
Medical Center, Dallas, TX 75390, USA

Shaogeng Tang contributed data to Figures 2.1I, 2.3I, 2.4D H, 2.5G, 2.9B, 2.11C, 2.14D-E, and assisted in designing experiments and preparation of the manuscript for publication.

Chapter II was originally published in *Developmental Cell* 27:201-214 (**2013**)

Buchkovich, N.J., Henne, W.M., Tang, S., and Emr, S.D. (**2013**). Essential N-terminal insertion motif anchors the ESCRT-III filament during MVB vesicle formation. *Developmental Cell* 27, 201-214.

DOI: 10.1016/j.devcel.2013.09.009.

## **Abstract**

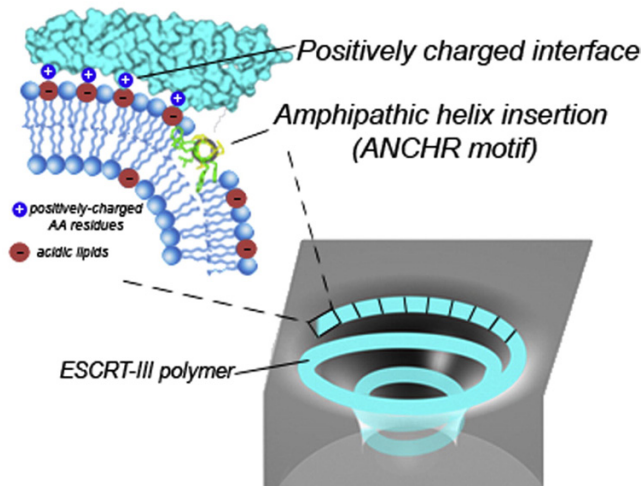
The endosomal sorting complexes required for transport (ESCRTs) have emerged as key cellular machinery that drive topologically unique membrane deformation and scission. Understanding how the ESCRT-III polymer interacts with membrane, promoting and/or stabilizing membrane deformation, is an important step in elucidating this sculpting mechanism. Using a combination of genetic and biochemical approaches, both *in vivo* and *in vitro*, we identify two essential modules required for ESCRT-III-membrane association: an electrostatic cluster and an N-terminal insertion motif. Mutating either module in yeast causes cargo sorting defects in the MVB pathway. We show that the essential N-terminal insertion motif provides a stable anchor for the ESCRT-III polymer. By replacing this N-terminal motif with well-characterized membrane insertion modules, we demonstrate that the N terminus of Snf7 has been tuned to maintain the topological constraints associated with ESCRT-III-filament-mediated membrane invagination and vesicle formation. Our results provide insights into the spatially unique, ESCRT-III-mediated membrane remodeling.

## Highlights

1. ESCRT-III subunits mediate a topologically unique scission event
2. ESCRT-III binds membrane via a basic interface and an N-terminal amphipathic helix
3. The N-terminal ANCHR motif senses curvature and anchors ESCRT-III to membrane
4. Vesicle formation involves maintaining an intricate balance of opposing curvatures

## Graphical Abstract

### ESCRT-III Membrane Interaction



## Introduction

The endosomal sorting complexes required for transport (ESCRTs) are critical for sorting certain transmembrane proteins into vesicles that bud into the lumen of the endosome. In addition to sorting cargo into intraluminal vesicles (ILVs) of multivesicular bodies (MVBs) (Babst et al., 2002a; Babst et al., 2002b; Babst et al., 1997; Katzmann et al., 2001), ESCRTs drive ILV formation and scission. Additionally, the ESCRT machinery is involved in viral budding from the plasma membrane and in cytokinesis, where they function as part of the scission machinery (Carlton and Martin-Serrano, 2007; Garrus et al., 2001a; Spitzer et al., 2006). ESCRT-dependent membrane deformation is unique when compared to other vesicle formation events in the cell as it is topologically inverted relative to those formed by coats, such as clathrin, COPI, or COPII. Furthermore, the ESCRT machinery localizes only to the neck of the invaginated vesicle and is not incorporated into the nascent vesicle. How the ESCRT machinery achieves this unique form of membrane deformation and scission is the focus of extensive research.

The ESCRT-III polymer, consisting of four core subunits, Vps20, Snf7, Vps24, and Vps2, is believed to play a key role in membrane invagination and vesicle scission. The transient nature of this hetero-oligomeric filament has made characterizing the filament difficult. However, recent efforts to visualize the ESCRT-III polymer on lipid monolayers using high-resolution electron microscopy techniques have identified a key role for electrostatically charged lipids in modulating ESCRT-III filament architecture (Henne et al., 2012). This raises key questions about the ESCRT-III-lipid interaction. For example, how does ESCRT-III bind membrane, and what is the role of this interaction in

invaginating membrane, sculpting the vesicle, and promoting scission? Understanding how the ESCRT-III subunits interact with lipid is critical to elucidating the mechanism for ESCRT-mediated membrane deformation. Here, we identify two key components for its membrane binding: a charged interaction surface and a membrane-inserting N terminus. Interestingly, we find that although membrane insertion modules often drive curvature, the membrane-inserting motif of Snf7 has been tuned to maximize its role as a membrane anchor for the ESCRT-III polymer without disrupting the topologically inverted curvature associated with ILV formation.

## Results

### **Positively Charged Interfaces on ESCRT-III Interact with Membrane**

ESCRT-III subunits are structurally similar, consisting of a core domain, a flexible linker, an autoinhibitory alpha-helix, and a MIT-interacting motif (MIM) (Figure 2.1A). The core domain consists of four tightly bundled alpha-helices. The first elongated helix of Vps24, termed *helix-1*, forms a highly basic surface consisting of arginine and lysine residues (Figure 2.1B; Figure 2.2A) (Muñoz et al., 2006). Alignment analysis showed not only a high degree of conservation of the positive charges on *helix-1* between the human and yeast orthologs of Vps24 (12 and 10, respectively) but also with the ESCRT-III subunit Vps2 (11) (Figure 2.1B). These conserved, positively charged residues may constitute the membrane interaction interface during binding of ESCRT-III to endosomes.

To investigate the role of *helix-1* in membrane binding, we generated mutants of Snf7, Vps2, and Vps24 that had an increasing number of charge inversions on *helix-1*.

In the absence of Vps4, which recycles ESCRT-III subunits from membrane, greater than 90% of Vps24 localized to the P13 membrane fraction in cellular fractionation experiments (Figures 2.1C and 2.1F). There was very little effect on this membrane association with a single charge inversion. However, inverting the charges of two, three, or four residues on helix-1 sequentially reduced the Vps24 association with the membrane fraction (Figures 2.1C and 2.1F). Although membrane-associated Vps24 was reduced after three or four charge inversions, we also noticed that these mutations affected protein stability (Figure 2.2B). To ensure this reduction was not due to the instability of the mutant Vps24, we changed two positive charges to glutamate and two to neutral alanine residues ( $\text{Vps24}^{\text{EEAA}}$ ). This approach led to a stable construct that, similar to the four charge inversion mutant, had reduced localization to the membrane fraction (Figure 2.2C). These results show that the positive charges on helix-1 of Vps24 are important for membrane association. Accumulating charge inversions on helix-1 of Vps2 produced similar results to Vps24 (Figures 2.1D and 2.1F). Importantly, mutations on helix-1 of Vps2 did not abolish its ability to bind to and modify Snf7 filaments, suggesting that they did not affect its ability to interact with other ESCRT-III subunits (data not shown). This suggests that both Vps2 and Vps24 utilize helix-1 for their interaction with membrane.

Strikingly, similar mutations on Snf7 resulted in greater than 90% of protein remaining membrane associated (Figures 2.1E and 2.1F), indicating that helix-1 may not contribute to the membrane binding of Snf7. Sequence alignments revealed that many of the helix-1-positive charges are not conserved on Snf7 (Figure 2.1B). Because Snf7 is the most abundant ESCRT-III subunit (Teis et al., 2008), understanding its

membrane interaction is essential. An alternative membrane-binding interface on Snf7, consisting of a series of highly conserved lysines on helices-2 and -3, was identified from a structure generated using the comparative structural program Modeler (Figure 2.1G) (Eswar et al., 2008). Single or multiple charge inversions on this interface impaired the sorting of Mup1-pHluorin to the vacuole lumen (Figure 2.2F). These inversions also decreased the membrane association of Snf7 by cellular fractionation (Figure 2.1H). These results were confirmed by light microscopy, as the charge inversion mutants increasingly relocalized Snf7-GFP to the cytoplasm (Figure 2.2H). To further investigate these residues, we performed liposome sedimentation assays using the Snf7core domain, which is sufficient to bind membrane *in vitro* (Henne et al., 2012). As expected, introducing two charge inversions from helix-3 onto the Snf7<sup>core</sup> background reduced membrane association (Figure 2.1I). This provides direct *in vitro* confirmation of our *in vivo* results, placing residues from helices-2 and -3 at the membrane interface. Importantly, mutations on this interface did not disrupt the ability to form filaments, suggesting that the altered membrane localization was not due to disrupting Snf7's ability to oligomerize (data not shown). Thus, Snf7 surprisingly utilizes a different cationic interface for membrane binding, suggesting that ESCRT-III subunits uniquely orient in the polymer to contact membrane.

### **The N Termini of ESCRT-III Subunits Contribute to Membrane Binding**

One ESCRT-III subunit, Vps20, is N-terminally myristoylated. This lipid modification often works in cooperation with other lipid binding modules, such as an electrostatic interface, to provide a high-affinity protein-membrane interaction. We

wondered if the other ESCRT-III subunits were similarly utilizing a second membrane-interacting module. Many membrane-associated proteins utilize hydrophobic residues that insert into lipid bilayers to stabilize membrane binding. We noted the presence of bulky hydrophobic residues at the N termini of Snf7, Vps2, and Vps24 (Figure 2.3A) and hypothesized that, similar to the myristylation of Vps20, these residues stabilize membrane interactions. Consistent with this idea, liposome binding of human Vps2 was dependent on two conserved N-terminal hydrophobic residues (Bodon et al., 2011). We tested the functional significance of the N termini of the ESCRT-III subunits by assaying the delivery of GFP-Cps1 to the vacuole. Similar to what was previously reported for the Vps20 myristylation mutant (Babst et al., 2002a), deletion of the N-terminal region upstream of helix-1 on Vps20 resulted in a partial block in GFP-Cps1 sorting. The cargo accumulated both in the vacuole lumen and on the vacuole membrane, but not at the aberrant endosomal E dot, where cargo accumulates when Vps20 is absent (Figure 2.3B). Similar to Vps20, deletion of this N-terminal region on Vps2 also resulted in a partial sorting defect (Figure 2.3E). This was in contrast to deletion of the homologous N-terminal regions of Snf7 or Vps24, in which GFP-Cps1 was present at the E dot, suggesting a severe sorting defect (Figures 2.3C and 2.3D). These data suggest that the extreme N termini of the ESCRT-III subunits are functionally important for efficient cargo sorting.

To better understand the partial sorting defects observed with the N-terminal deletion mutants, we used a quantitative sorting assay that takes advantage of the pH-sensitive nature of the GFP-derivative pHluorin and the acidic environment of the vacuole. By tagging the plasma membrane cargo Mup1 with pHluorin and monitoring its

fluorescence after internalization, one can determine whether the cargo is efficiently delivered to the vacuole, partially missorted, or trapped at the E dot. By calculating the percent of fluorescence that is quenched, the efficiency of sorting can be quantified and used to assess the severity of the sorting defect (Figure 2.3F). Using this approach, we found that Vps20 and Vps2 had sorting efficiency ratings of 71% and 74%, respectively, indicative of the partial sorting defect observed with GFP-Cps1. In contrast, Snf7 and Vps24 had sorting efficiencies of 13% and 25% (Figure 2.3G), consistent with severe sorting defects. These results confirm that although the N termini of all four ESCRT-III subunits are required for efficient cargo sorting, they do not all contribute equally.

Because the N terminus of Snf7 had the greatest effect on cargo sorting, we replaced the N termini of the other ESCRT-III subunits with the N terminus of Snf7. This resulted in completely normal MVB sorting (Figure 2.4E). In contrast, replacing the N terminus of Snf7 with that of Vps24 or Vps2 only weakly rescued cargo sorting (Figure 2.4F). This was surprising due to the homology between the N termini of Snf7 and Vps2 (Figure 2.3A). Accordingly, changing a negatively charged glutamate in Vps2 to glycine (E5G), as it is in Snf7, greatly enhanced this rescue (Figure 2.4F). These data confirm the differential importance of the N termini of ESCRT-III subunits in MVB sorting. Because Snf7 is the most abundant ESCRT-III subunit and is the predominant subunit in the ESCRT-III polymer and has the greatest N-terminal deletion phenotype, we focused our analysis on the N terminus of Snf7.

We next used GFP-fusion constructs to assess the effect of the N-terminal deletion on Snf7 endosomal localization. When expressed in WT yeast, Snf7-GFP was located in puncta. Deletion of the N terminus of Snf7 redistributed Snf7-GFP from its

punctal localization to the cytoplasm (Figure 2.3H), consistent with a role for the N terminus in associating with membrane. To further demonstrate that the N-terminal sorting defect was due to reduced membrane binding, we performed liposome sedimentation assays using Snf7core and  $\Delta$ N-Snf7core. As expected, deletion of the N terminus nearly completely abolished the ability of Snf7core to associate with membrane (Figure 2.3I). Similar to what was observed for the human Vps2 (Bodon et al., 2011), deletion of the N terminus of Vps2 also resulted in reduced membrane association, although not nearly as drastic as Snf7 (Figure 2.4H). This provides further correlation between the sorting results and membrane association.

To ensure the altered localization was not due to oligomerization defects, we introduced a mutation on  $\Delta$ N-Snf7 that promotes Snf7 filament formation (Henne et al., 2012).  $\Delta$ N-Snf7<sup>R52E</sup> was able to form filaments on EM grids, confirming that the N terminus did not affect oligomerization (Figure 2.4I). Furthermore, filaments formed by Snf7<sup>R52E</sup> can be clearly visualized associating with liposomes by electron microscopy. However, deletion of the N terminus abolished this association (Figure 2.4J). These data clearly demonstrate that the N terminus of Snf7 is important for membrane association.

### **The N Terminus of Snf7 Requires Hydrophobic Residues**

By sequence alignment, we noticed the conserved position of key hydrophobic residues at the N terminus (Figure 2.5A). We next wanted to investigate the contribution of these large hydrophobic residues to membrane binding. Mapping the N-terminal sequence of Snf7 on a helical wheel revealed an amphipathic helix, with a hydrophobic

surface made up of these large N-terminal residues aligned opposite of a polar interface made up of several serine residues (Figure 2.5B). Substitution of the N-terminal tryptophans ( $\text{Snf7}^{\text{W2E}}$  and  $\text{Snf7}^{\text{W8E}}$ ) or the highly conserved phenylalanine ( $\text{Snf7}^{\text{F6E}}$ ) with negatively charged glutamate resulted in the aberrant sorting of both GFP-Cps1 (Figures 2.5C and 2.6B) and Mup1-pHluorin (Figures 2.5D and 2.6C). Importantly, replacing the phenylalanine with other hydrophobic residues did not affect the sorting of either cargo. Point mutations of key residues on the other ESCRT-III subunits similarly resulted in reduced sorting of Mup1-pHluorin (Figure 2.6D), thus demonstrating the importance of the hydrophobicity of the N terminus.

We next sought to correlate the functional defect associated with the hydrophobicity of the N terminus with membrane association. Importantly, addition of the F6E mutation to the cationic interface mutant (4KE) further reduced membrane binding, reducing the amount of protein associated with the P13 fraction from 52% to 24% (Figure 2.6E). By light microscopy, addition of F6E to Snf7-GFP redistributed the protein from puncta to the cytoplasm, similar to what was observed for  $\Delta\text{N-Snf7-GFP}$  (Figure 2.6F). Although some puncta were still present, the F6E mutation in combination with the cationic interface mutant ( $\text{Snf7}^{\text{F6E/4KE}}\text{-GFP}$ ) resulted in nearly complete cytoplasmic localization. These results confirm a role for both the hydrophobic N terminus and the cationic interface of Snf7 in membrane binding.

Liposome sedimentation assays were used as an additional confirmation for the role of the N-terminal hydrophobics in membrane binding. Both purified  $\text{Snf7}^{\text{core/W2E}}$  and  $\text{Snf7}^{\text{core/F6E}}$  had impaired binding to liposomes in vitro. In contrast,  $\text{Snf7}^{\text{core/F6W}}$  associated with liposomes at similar levels as the wild-type (WT)  $\text{Snf7}^{\text{core}}$  (Figure 2.5G).

Thus, two regions in Snf7 mediate membrane interactions: a positively charged cationic interface and an N-terminal hydrophobic motif.

### The N Terminus of Snf7 Inserts into the Membrane

N-terminal amphipathic helices on proteins, such as Arf1 or the N-BAR family, insert into membrane bilayers to induce membrane curvature (Farsad and De Camilli, 2003). Because the N terminus of Snf7 is involved in membrane binding and is dependent on hydrophobic residues, we reasoned that these residues might insert into the membrane bilayer to generate or stabilize membrane deformations. To test this, we first utilized the fluorescent dye 7-nitrobenz-2-oxa-1,3-diazole (NBD), which undergoes an increase in emission intensity and a change in its maximum emission upon shifting to a hydrophobic environment (Johnson, 2005 and Saksena et al., 2009). We labeled Snf7<sup>core</sup> with NBD on cysteine residues introduced into the N terminus (Snf7<sup>core/F6C</sup>), helix-1 (Snf7<sup>core/K35C</sup>), helix-2 (Snf7<sup>core/Q75C</sup>), or helix-3 (Snf7<sup>core/H118C</sup>) (Figures 2.7A and 2.8A). A large increase in emission intensity and a shift in maximum emission was observed upon addition of excess liposomes to the Snf7<sup>core</sup> domain labeled at the N terminus (Figures 2.7B, 2.7C, and 2.8B). In contrast, addition of liposomes to Snf7<sup>core</sup> labeled with NBD on helices-1, -2, or -3 resulted in only a very slight increase in intensity (Figures 2.7B, 2.7C, and 2.8C). Thus, the N terminus shifts to a hydrophobic environment in the presence of liposomes.

Membrane-inserting motifs prefer to bind liposomes with smaller radii because of their high-membrane curvature (Bigay et al., 2005). To investigate if the Snf7 N-terminal motif could sense membrane curvature, we tested the ability of Snf7<sup>core</sup> to bind

liposomes of different sizes. To mitigate the contribution of the cationic interface, we used uncharged liposomes composed of 1,2-dioleoyl-*sn*-glycero-3-phosphocholine (DOPC) alone, generated by extrusion through progressively smaller filter pores (800, 100 and 30 nm). In liposome sedimentation assays, Snf7<sup>core</sup> bound best to liposomes prepared with the smallest filter. Liposome binding was completely dependent on the N terminus, as the Snf7<sup>core/F6E</sup> did not bind liposomes, even those with high-membrane curvature (Figure 2.7D). This observation, in combination with the previous results, provides strong evidence that Snf7 contains a membrane-inserting N-terminal motif.

### The Snf7 N Terminus Can Be Replaced by Known Membrane-Inserting Motifs

We next investigated if the N terminus of Snf7 is a general insertion module or a sequence-specific recognition module by testing if unrelated membrane-inserting motifs could rescue the ΔN-Snf7-sorting defect. We replaced the N terminus of Snf7 with the well-characterized membrane-inserting modules of the curvature-sensing ALPS motif of Osh4 (ALPS-Snf7), curvature-inducing helix-0 of Rvs161 (h0-NBAR-Snf7), or the scission-promoting N terminus of Arf1 (Arf1-Snf7) (Beck et al., 2011; Bigay et al., 2005; Drin et al., 2007). Both the well-characterized helix-0 of Rvs161 and the ALPS motif were able to rescue the sorting of Mup1-pHluorin (Figure 2.9A). This rescue was dependent on key N-terminal hydrophobic residues, similar to what was observed for Snf7, as substituting these residues for glutamate failed to rescue cargo sorting (Figure 2.10C). As expected, the ability to rescue cargo sorting correlated with a rescue in membrane association, as h0-NBAR-Snf7core was able to bind liposomes *in vitro* (Figure 2.9B).

Unexpectedly, addition of the Arf1 N-terminal amphipathic helix to  $\Delta N$ -Snf7 did not rescue Mup1-pHluroin sorting (Figure 2.9A), despite maintaining the ability to localize to membrane puncta (Figure 2.10D). Because this helix is posttranslationally modified with a myristoyl group, we reasoned that this modification would adversely affect Snf7 function by providing too high of an affinity reaction with membrane. To test this, we replaced the N terminus of Snf7 with the myristylation sequence of Vps20 (Myr-Snf7) and found, surprisingly, that it was sufficient to rescue Mup1-pHluroin sorting. This rescue was dependent on the myristoyl group, as mutating the glycine residue at position two to alanine ( $\text{Myr-Snf7}^{\text{G2A}}$ ) did not rescue Mup1-pHlourin sorting (Figure 2.9C). Perhaps even more surprising, we found that mutation of the myristoylated glycine residue of Arf1-Snf7 to an alanine ( $\text{Arf1-Snf7}^{\text{G2A}}$ ) also restored sorting to wild-type levels (Figure 2.9C). Therefore, addition of the unmyristoylated, but not myristoylated, Arf1 N-terminal helix to Snf7 is sufficient to rescue cargo sorting. These data show that a myristoyl group or a known membrane-inserting amphipathic helix, but not both, are able to function at the N terminus of Snf7.

We were intrigued by the rescue of cargo sorting by both the membrane curvature-sensing and curvature-inducing helices and the myristoyl group. We reasoned that one role of the N terminus of Snf7 could be to insert into the bilayer and drive membrane curvature during ILV morphogenesis. Alternatively, membrane deformation could be driven by the previously visualized ESCRT-III helices (Hanson et al., 2008; Henne et al., 2012). In this model, the predominant role of the N terminus is to act as a membrane-inserting anchor to allow the polymer assembly to exert the mechanical forces necessary for driving membrane deformation. Because the well-characterized

modules that rescue cargo sorting are predicted to deform membrane to differing degrees, the first model would predict that they would produce intraluminal vesicles of varying morphology; the amphipathic helices that promote deformation would result in smaller vesicles. In contrast, the latter model predicts that the N terminus allows the mechanical force of ESCRT-III polymer assembly to drive deformation and that the intraluminal vesicle morphology would be independent of the N-terminal insertion module. Expression of either h0-NBAR-Snf7 or Myr-Snf7 resulted in ILVs with wild-type size and morphology (Figures 2.9D and 2.9E), providing support for the latter model. We thus propose that the ESCRT-III oligomer is the predominant driver and stabilizer of membrane deformation during intraluminal vesicle morphogenesis. The N terminus, by inserting into membrane, provides a high-affinity anchor that allows for the oligomer-membrane interaction to drive this deformation. We will hereafter refer to the N terminus of Snf7 as the amphipathic N terminus containing hydrophobic residues motif (ANCHR).

### **The Snf7 ANCHR Motif Balances Opposing Curvatures during ILV Formation**

Generation of an intraluminal vesicle requires maintaining an intricate balance of competing curvatures. Although the rim of the invagination contains a high degree of positive curvature, the curvature of the membrane at the inside and bottom of the invagination is negative (Figure 2.11A). Whereas the helical nature of the ESCRT-III oligomer (Henne et al., 2012) could stabilize the negative curvature of the invagination, the insertion of its N-terminal amphipathic anchor would have a competing effect and promote the opposing positive curvature.

The ability of an amphipathic helix to insert into and deform membrane is dependent upon both the residency time in membrane and the shape (length and bulkiness) of the helix. Helices, such as the ALPS motif, that are believed to sense, but not actively promote, deformation contain polar residues on the hydrophilic interface (Drin et al., 2007). In contrast, amphipathic helices that contain positively charged residues on the hydrophilic interface have increased residency time in the membrane because of the interaction of these positive charges with the negatively charged lipid head groups (Drin and Antonny, 2010). Insertion of an amphipathic helix with high deforming properties that would generate positive curvature would compete with the negative curvature stabilized by the oligomer and would be detrimental to intraluminal vesicle formation. In support of this hypothesis, the properties of the ANCHR motif of Snf7 are consistent with anchoring and not deformation-promoting helices, namely, it is small in size and contains only polar residues on the hydrophilic interface (Figure 2.5B). Experimentally, this would explain why the myristoyl group and ALPS motif were better able to rescue cargo sorting than were the chimeras with known membrane-deforming helices, such as the helix-0 of N-BAR proteins, ENTH domain, and the N terminus of Arf1 (Figures 2.9A and 2.10F).

To further test the effect of altering the insertion properties of the ANCHR motif of Snf7 on intraluminal vesicle formation, we generated several N-terminal amino acid extensions. We first added a string of positive charges (6K-Snf7) and then converted it to an amphipathic helix by substituting three lysines for three tryptophans (6WK-Snf7; MWKKWWK). We then varied the length of the N terminus by adding lysine and tryptophan residues to generate progressively longer helices with more membrane

deforming potential (10WK-Snf7 and 14WK-Snf7). As expected, the 6K-Snf7 construct did not rescue sorting (Figure 2.11B), demonstrating that positive charges were insufficient to anchor Snf7 and reaffirming the requirement for a membrane-inserting element. In contrast, the 6WK-Snf7 construct sorted Mup1-pHluorin at wild-type levels. Intriguingly, increasing the length of the N-terminal motif through addition of tryptophan and lysine residues progressively decreased the ability of the chimeras to efficiently sort Mup1-pHluorin (Figure 2.11B). Further analysis of the 10WK-Snf7 mutant showed that its decreased ability to sort cargo was not due to its mislocalization in cells (Figure 2.12B) or the inability to bind membrane. In fact, 10WK-Snf7<sup>core</sup> bound liposomes in vitro better than did both Snf7<sup>core</sup> and 6WK-Snf7<sup>core</sup> (Figure 2.11C), two N termini that efficiently rescue the ΔN-Snf7-sorting defect *in vivo*.

To further demonstrate the negative correlation between efficient cargo sorting and promoting membrane deformation, we assayed the ability of the chimeras to deform membrane. The insertion of hydrophobic amino acids into membrane can generate bilayer asymmetry and drive membrane curvature (Gallop et al., 2006). In order to assay the membrane curvature-generating ability of the N-terminal chimeras separate from the curvature generated by the filaments, we took advantage of the Snf7<sup>core</sup> domain, which is unable to form Snf7 filaments (Henne et al., 2012). Addition of purified Snf7<sup>core</sup> to liposomes did not result in tubulation or deformation of liposomes. In contrast, addition of purified h0-NBAR-Snf7<sup>core</sup> to liposomes resulted in membrane tubule formation, which appeared to be stabilized by a protein coat (Figures 2.11D and 2.12C). Although some tubules were present after addition of 10WK-Snf7<sup>core</sup> to liposomes, most of the liposomes were converted to small vesicles (Figures 2.11D and

2.12C). Tubulation has been described as a highly unstable vesicle budding intermediate formed by scaffolding proteins, such as a BAR domain or coat protein, which can subsequently promote vesiculation (Boucrot et al., 2012; Mim et al., 2012). Addition of the highly deforming 10WK-Snf7<sup>core</sup> promoted this transition to vesiculation. Although whether the vesicles were independent vesicles or connected like beads on a string was unclear, 10WK-Snf7<sup>core</sup> clearly promoted the highest degree of membrane remodeling. Notably, a similar trend in the ability to deform membrane was observed when full-length constructs of the chimeras were used (Figure 2.12D). These results are consistent with the decreasing ability of the respective chimeras to sort cargo, providing evidence that the ability to strongly induce positive curvature during ILV invagination decreases the ability to efficiently sort cargo.

### The Snf7 ANCHR Motif Alters the Kinetics of Cargo Sorting

The factors involved in generating and stabilizing the membrane curvature associated with ILV morphogenesis, both positive and negative, have been tuned to maintain the delicate balance of opposing curvatures. Disrupting this balance decreases the efficiency of vesicle formation and slows the kinetics of cargo sorting. Although steady-state sorting assays were sufficient to detect mutants that adversely affect this intricate balance, we sought to further test these mutants using a kinetic assay to monitor cargo sorting. We monitored the fluorescence quenching of Mup1-pHluorin after methionine stimulation using a mutant with impaired membrane localization (Snf7<sup>F6E</sup>), with a nondeforming N-terminal motif (Myr-Snf7) and a deformation-promoting N-terminal helix (h0-NBAR-Snf7). As expected, Myr-Snf7 sorted with wild-type kinetics,

whereas Snf7F6E exhibited a very slow quenching rate (Figures 2.14A and 2.14B). Interestingly, cargo sorting by h0-NBAR-Snf7 was significantly delayed compared to the wild-type sample, even though under steady-state conditions h0-NBAR-Snf7 had the ability to significantly rescue cargo sorting (Figures 2.14A and 2.14B). Thus, although h0-NBAR-Snf7 functions, it does so less efficiently than wild-type Snf7, consistent with the hypothesis that the presence of the NBAR helix-0 disrupts the delicate membrane curvature equilibrium in ILV formation. By light microscopy, Mup1-pHluorin was found in highly dynamic green puncta in the wild-type and Myr-Snf7 samples, but in larger, less mobile structures in the h0-NBAR-Snf7 and Snf7<sup>F6E</sup> samples, consistent with the accumulation of endosomal intermediates (Figure 2.13). Thus, the N-terminal interaction with membrane is important for fast cargo sorting.

Our mutational analysis has provided key insights into the role of the endogenous Snf7 ANCHR motif by identifying three functional categories of N-terminal mutants (Figure 2.14C). Mutants that are unable to insert into membrane, for example, Snf7<sup>F6E</sup> or ΔN-Snf7, cannot provide the anchoring function necessary to allow the ESCRT-III polymer to exert the required forces to stabilize the invagination and are therefore functionally defective (Figure 2.14D). Mutants that are able to provide a membrane anchor without promoting a high degree of positive curvature, such as Myr-Snf7 or ALPS-Snf7, are able to efficiently rescue cargo sorting to near wild-type levels. In contrast, the ability to rescue cargo sorting decreases as the ability to deform membrane increases. This is likely due to disrupting the intricate balance of positive and negative curvatures associated with forming a nascent vesicle.

## Discussion

Although ESCRT-III drives MVB morphogenesis, the mechanistic basis for membrane remodeling is unclear. The inability to visualize the ESCRT-III polymer at atomic resolution has hindered efforts to elucidate ESCRT-III's role in membrane deformation and scission. Our approach to address these issues has been to focus on the distinct functions of ESCRT-III: (1) membrane binding, (2) oligomer assembly, (3) cargo sequestration, (4) membrane invagination, (5) ILV neck narrowing, and (6) scission. We have recently provided visual evidence of the ESCRT-II/ESCRT-III ring architecture capable of cargo sequestration (Henne et al., 2012). Although constructs that promote filament formation have provided insights into the nature of the ESCRT-III filament (Ghazi-Tabatabai et al., 2008; Hanson et al., 2008; Lata et al., 2008b), other assays are required to define ESCRT-III's role in membrane remodeling.

Recent studies have highlighted that ESCRT-III accumulates at the highly curved neck of an invagination. This, and the fact that ESCRT-III is not consumed during ILV morphogenesis, underscores the importance of studying ESCRT-III membrane interactions. Through a series of complimentary *in vivo* and *in vitro* approaches, we provide a detailed analysis of ESCRT-III membrane binding and remodeling. We identified two features shared among the four core ESCRT-III subunits important for membrane binding: a cationic interface consisting of a cluster of positively charged residues on one face of the ESCRT-III proteins and a membrane-inserting N-terminal ANCHR motif consisting of an amphipathic helix on Snf7, Vps24, and Vps2, and a myristoyl group in Vps20. The first feature, the cationic interface, was unexpectedly different on Snf7, suggesting that the subunits may uniquely orient in the ESCRT-III

polymer. This heterogeneity underscores the functional difference among a group of structurally similar subunits. The presence of the N-terminal ANCHR motif is not surprising as the generation of other cellular vesicles is associated with membrane-inserting motifs, including the topologically equivalent budding of influenza virus, which requires the amphipathic helix of the M2 viral protein (Antony et al., 1997; Ford et al., 2002; Gallop et al., 2006; Lee et al., 2005a; Rossman et al., 2010).

Any model to describe ESCRT-III-mediated scission needs to account for both the structural features of the ESCRT-III polymer and the properties of the various scission events it mediates. In other words, the ESCRT-III filament must have the ability to mediate diverse scission events, from the generation of small intraluminal vesicles at the endosome and HIV viral particles at the plasma membrane, to the much larger-scale abscission during cytokinesis. One key feature that allows ESCRT-III to mediate such diverse events is the regulated assembly of the ESCRT-III polymer by key upstream factors, such as ESCRT-I and -II, in ILV formation or the HIV Gag protein in viral budding. This regulated assembly likely accounts for one remarkable feature of ILV's, their consistently regular size; however, future experiments must investigate this further.

Another key feature shared among these scission events requires that ESCRT-III binds tightly to and constricts membrane, acting as a membrane scaffold. This requires maintaining membrane binding under conditions of increased force due to membrane tension. The tightening spiral must therefore be anchored to membrane and thus requires a high-affinity membrane anchor. As the polymer elongates and the number of protein-membrane contacts increase, the affinity of the polymer to membrane is amplified, allowing the polymer to provide the mechanical force necessary to act as a

scaffold and stabilize the invagination. Under conditions in which Snf7's ANCHR motif is compromised ( $\text{Snf7}^{\text{F6E}}$  or  $\Delta\text{N-Snf7}$ ), the ESCRT-III polymer is unable to drive membrane invagination and efficiently progress to vesicle formation (Figure 2.14E).

Our study of Snf7's ANCHR motif addresses the balance of curvatures associated with ILV formation. The rim of the invagination is positively curved (Figure 2.11A) and may initially be generated by upstream ESCRT machinery and clustered cargo (Boura et al., 2012; Wollert and Hurley, 2010). Snf7's ANCHR motif may act as both a sensor of this positive curvature and a curvature stabilizer. Studies have shown that Snf7 localizes to both invaginations and along highly curved membranes (Fyfe et al., 2011; Henne et al., 2012; Wollert and Hurley, 2010). An invagination also contains negative curvature around its circumference. The ESCRT-III polymer acts as a circular scaffold that binds the membrane and stabilizes this invagination (inward deformation and cargo-laden nascent vesicle). We observed that other well-characterized membrane-inserting wedge domains known to promote or sense positive curvature ( $\text{h0-NBAR-Snf7}$  and  $\text{ALPS-Snf7}$ ) rescue the  $\Delta\text{N-Snf7}$ -sorting defect to varying degrees. Interestingly,  $\text{Arf1-Snf7}$  did not rescue cargo sorting, likely due to its strong membrane deformation and scission-promoting properties (Beck et al., 2011), which cause it to disrupt the intricate balance of curvatures associated with ILV formation. This is consistent with the reduced functionality of the synthetic 10WK-Snf7 chimera, which also has the ability to promote a high degree of membrane deformation (Figure 2.11D). Furthermore, the  $\text{Arf1-Snf7}$  chimera was able to rescue cargo sorting when its membrane affinity was reduced by preventing its myristoylation (Figure 2.9C). These results demonstrate that the properties of different amphipathic helices have been tuned

to their specific roles in curvature sensing and anchoring (ALPS motif, Snf7's ANCHR motif), membrane bending ( $\text{h}_0$  on N-BAR proteins), or vesicle scission (Arf1). We have exploited these helices to provide insights into the delicate balance of competing curvatures that exist during ILV morphogenesis between the ESCRT-III polymer and the insertion events.

How does the growing ESCRT-III polymer deform membrane as it assembles?

We propose that the ESCRT-III polymer initially forms a ring on the surface of the endosome, (restricting the ANCHR motifs to the circular rim of the membrane invagination), surrounding the cargo clustered by the upstream ESCRT machinery. The elongating ESCRT-III filament assembles into a three-dimensional (3D) helical spiral (corkscrew), which is anchored to membrane by the ANCHR motif, further invaginating the membrane domain contained within the ESCRT-III ring. In this model, the tight membrane binding of the growing filament may keep the transmembrane protein cargo concentrated in this membrane domain, ahead of the growing, narrowing filament, ultimately forming the vesicle at the front, leading edge, of the ESCRT-III spiral. Upon scission at the leading edge, and narrowest point of the filament, the concentrated cargo would be packaged into the nascent ILV, excluding the ESCRT-III filament from the nascent vesicle (Figure 2.14D). What promotes the ESCRT-mediated scission event? As the polymer elongates, the counterforce due to the increasing resistance from the deforming membrane and the tension from the insertion of the ANCHR motif into the bud neck may restrict the elongating helix into a tightening 3D spiral that promotes scission at its narrow end. Alternatively, the constriction of the ESCRT-III polymer may be coupled to the binding and disassembly reaction driven by the AAA-

ATPase Vps4. The ANCHR motif of Snf7 forms a tight association between the ESCRT-III polymer and the membrane prior to vesicle scission and removal of the membrane-anchored ESCRT-III scaffold may destabilize or buckle the membrane, triggering fission. Altering the properties of the ANCHR motif may also affect the ability of Vps4 to disassemble the ESCRT-III scaffold, delaying the kinetics of ILV formation.

The ESCRTs have emerged as cargo recognition, cargo sequestering, and membrane remodeling machinery, with a particular emphasis on a role for the ESCRT-III polymer in membrane deformation. Of the six distinct stages of ESCRT-III activity, this study provides important insights into ESCRT-dependent membrane bending and vesicle formation. Additional studies and new assays will be required to further analyze the neck narrowing and scission steps, including a precise role for the Vps4 ATPase in these reactions.

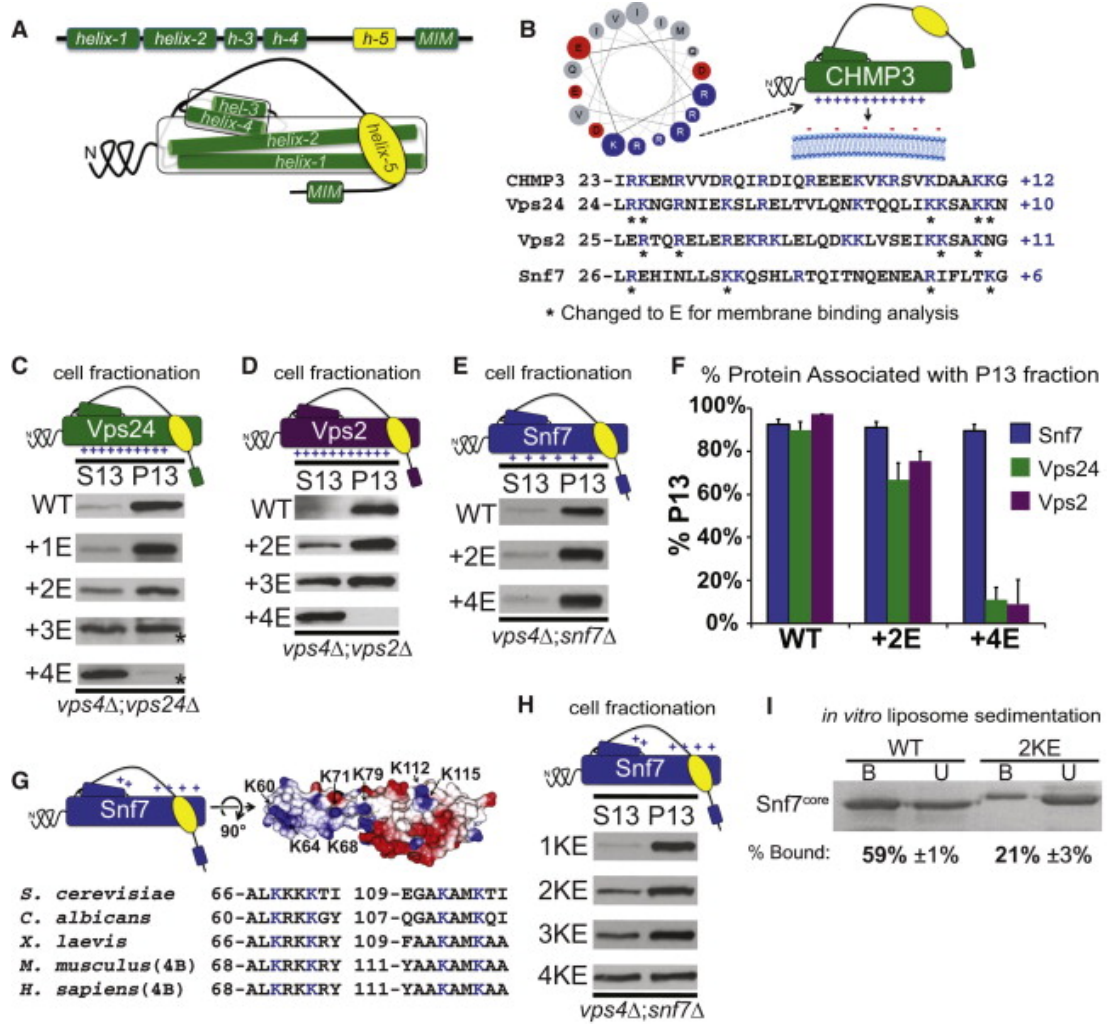


**Figure 2.1 Identification of Electrostatic Membrane Binding Interfaces on ESCRT-**

### III Subunits

## **Figure 2.1 Identification of Electrostatic Membrane Binding Interfaces on ESCRT-III Subunits**

- (A) Schematic showing helical arrangement of ESCRT-III subunits both linearly (top) and in the four-helical core bundle (bottom). Core helices and MIM (green); autoinhibitory helix-5 (yellow).
- (B) Helical wheel depicting positively charged interface on helix-1 of hVps24. Positively charged residues (blue); negatively charged residues (red). Cartoon depicts potential interaction with membrane. Sequence alignments of helix-1 of ESCRT-III subunits (positive charges, blue). Asterisk indicates residues mutated in this study.
- (C–E) Cellular fractionation analyses of *vps4Δ* and (C) *vps24Δ*, (D) *vps2Δ*, or (E) *snf7Δ* yeast exogenously expressing the respective wild-type gene (WT), or a gene with one (+1E), two (+2E), three (+3E), or four (+4E) charge inversions on helix-1. Asterisk indicates darker exposures.
- (F) Graphs representing percentage of protein associated with membrane fraction (P13) from data in (C)–(E).
- (G) Cartoon schematic and electrostatic surface model (positive residues, blue; negative residues, red) portraying the location of positively charged residues from helices-2 and -3. Sequence alignments of positive charges (blue) on this interface among eukaryotic species.
- (H) Cellular fraction analysis of *vps4Δ snf7Δ* yeast exogenously expressing WT Snf7 or a gene with one (1KE), two (2KE), three (3KE), or four (4KE) charge inversions on interface described in (G).
- (I) Liposome sedimentation assay of Snf7core (WT) and Snf7core/2KE (2KE). Protein-free (unbound, U); liposome-associated protein (bound, B).

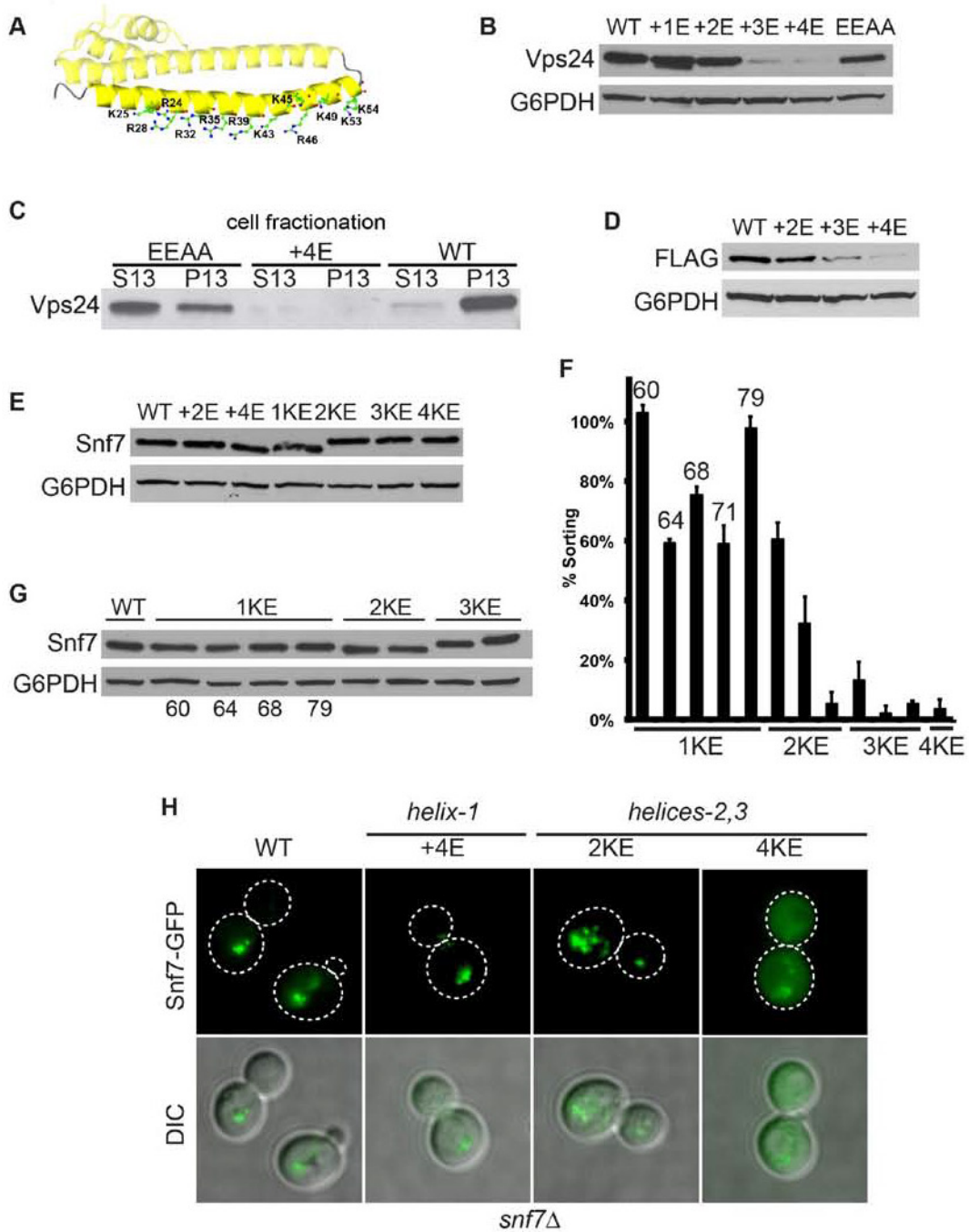


## Figure 2.2 Expression Levels of Membrane Binding Interface Mutants with Additional Functional and Localization Data

**Figure 2.2 Expression Levels of Membrane Binding Interface Mutants with Additional Functional and Localization Data**

- (A) Ribbon diagram of hVps24 showing location of positively charged residues on helix-1.
- (B) Western blots showing expression levels of Vps24 mutants.
- (C) Cellular fractionation analysis of *vps24Δ* yeast exogenously expressing Vps24<sup>WT</sup>, Vps24<sup>+4E</sup> or Vps24<sup>EEAA</sup>.
- (D-E) Western blots showing expression levels of (D) Vps2 mutants or (E) Snf7 mutants. All Snf7 constructs in this study are expressed within levels that do not functionally affect the MVB sorting of cargo.
- (F) Quantitative sorting data identifying key functional residues on potential Snf7 membrane binding interface. Error bars represent standard deviation.
- (G) Western blot showing expression levels of mutants in (F).
- (H) Representative images of *snf7Δ* yeast exogenously expressing WT Snf7-GFP, Snf7<sup>+4E</sup>-GFP (+4E), Snf7<sup>2KE</sup>-GFP (2KE) and Snf7<sup>4KE</sup>-GFP (4KE). GFP images (upper row); composite images of GFP & DIC (bottom row).

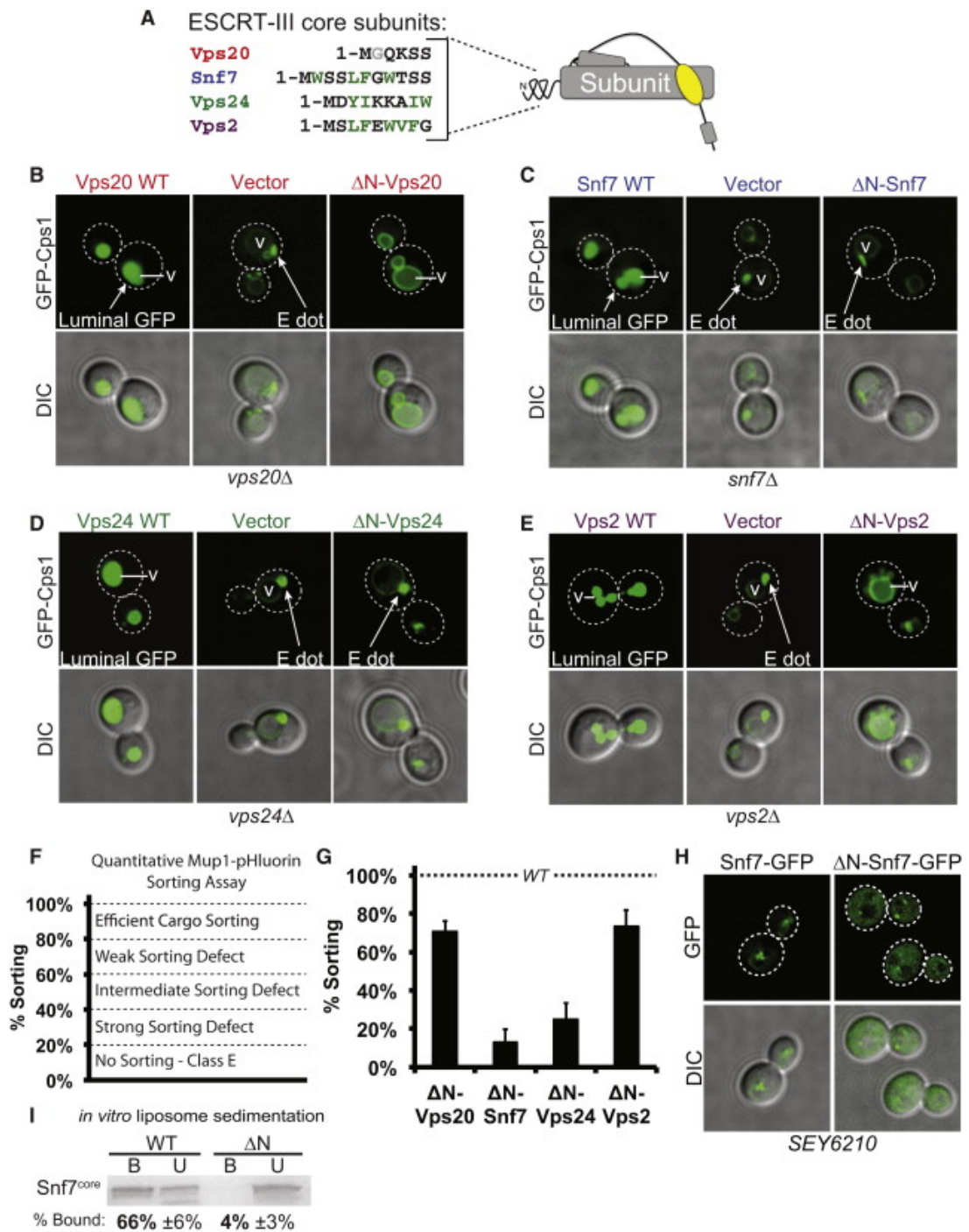


**Figure 2.3 ESCRT-III Subunits Require the N Terminus for Cargo Sorting**

### Figure 2.3 ESCRT-III Subunits Require the N Terminus for Cargo Sorting

- (A) Sequence alignment of ESCRT-III N termini. Hydrophobic residues (green); N-terminal myristoylated glycine (gray).
- (B–E) Representative images of mid-log (B) *vps20Δ*, (C) *snf7Δ*, (D) *vps24Δ*, and (E) *vps2Δ* yeast exogenously expressing GFP-Cps1 and the WT, ΔN, or vector control (Vec) for the corresponding ESCRT-III subunit. GFP images (upper row); composite images of GFP and DIC (bottom row). White arrows denote the GFP signal localized within the vacuole lumen and at the aberrant endosome (class E compartment). Vacuole (v).
- (F) Schematic of quantitative sorting scale for Mup1-pHluroin sorting assay.
- (G) Quantitative sorting data for ΔN-ESCRT-III subunits. Error bars represent standard deviation.
- (H) Representative images of mid-log yeast exogenously expressing Snf7-GFP or ΔN-Snf7-GFP. GFP images (upper row); composite images of GFP and DIC (bottom row).
- (I) Liposome sedimentations of Snf7<sup>core</sup> or ΔN-Snf7<sup>core</sup>. Protein-free (unbound, U); liposome-associated protein (bound, B).

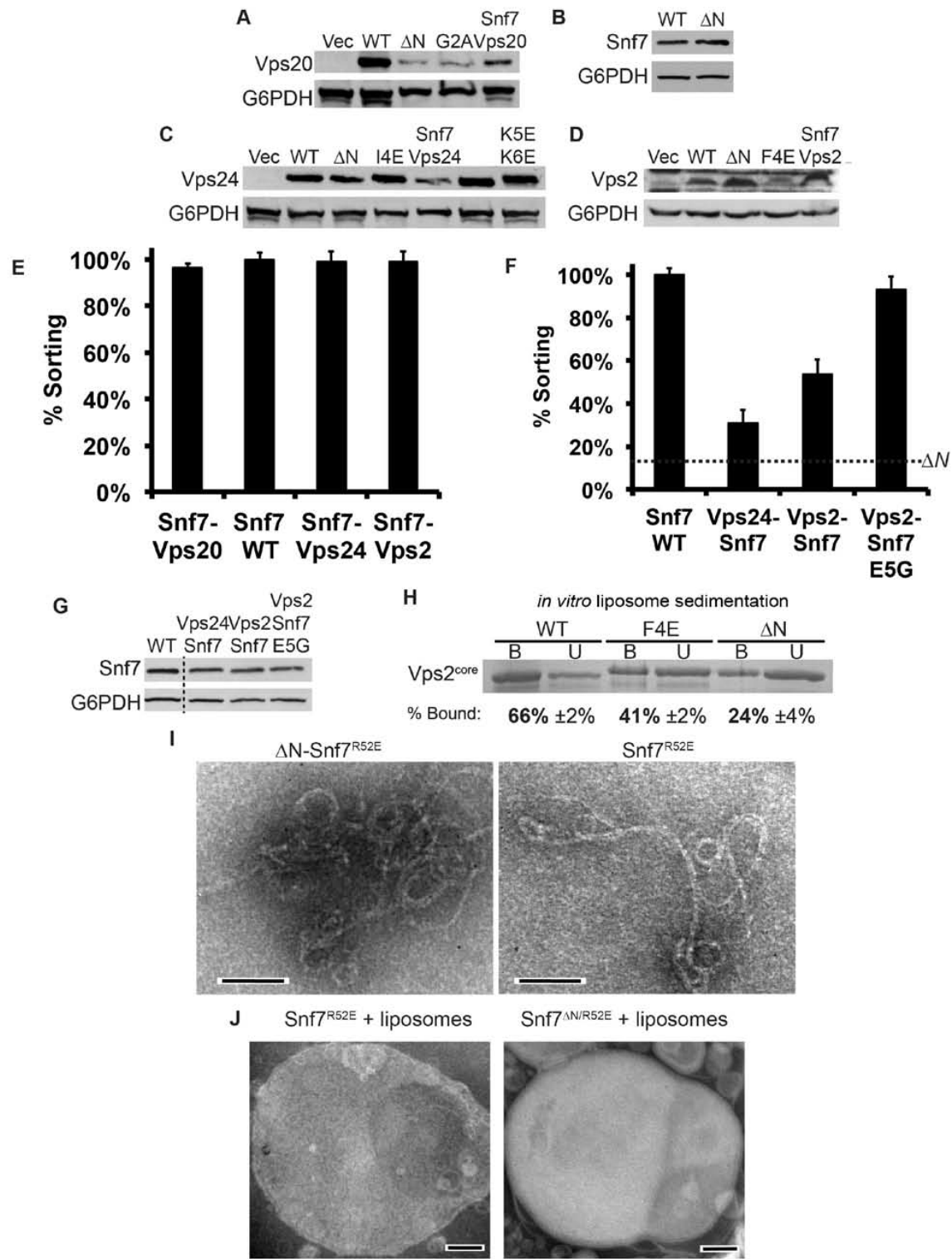


**Figure 2.4 Expression Levels of ESCRT-III N-terminus Mutants with Additional Functional and *in vitro* data**

**Figure 2.4 Expression Levels of ESCRT-III N-terminus Mutants with Additional Functional and *in vitro* data**

- (A-D) Western blots showing expression levels of (A) Vps20 mutants, (B) Snf7 mutants, (C) Vps24 mutants or (D) Vps2 mutants.
- (E) Quantitative sorting data of ESCRT-III N-terminal deletion chimeras containing the N- terminus of Snf7.
- (F) Quantitative sorting data of  $\Delta N$ -Snf7 chimeras containing N- terminus of other ESCRT-III subunits. Error bars in (E) and (F) represent standard deviation.
- (G) Western blot showing expression levels of Snf7 chimeras used in (F).
- (H) Liposome sedimentation assay of GST-Vps2<sup>core</sup>, GST-Vps2<sup>core/F4E</sup> and GST- $\Delta N$ -Vps2<sup>core</sup>. Protein-free (unbound, U); liposome-associated protein (bound, B).
- (I) Representative EM images of Snf7<sup>R52E</sup> or  $\Delta N$ -Snf7<sup>R52E</sup> added to EM grids and visualized after ammonium molybdate negative staining. Scale bar, 100 nm.
- (J) Representative EM images of Snf7<sup>R52E</sup> or  $\Delta N$ -Snf7<sup>R52E</sup> incubated with liposomes, added to EM grids and visualized after ammonium molybdate negative staining. Scale bar, 100 nm.

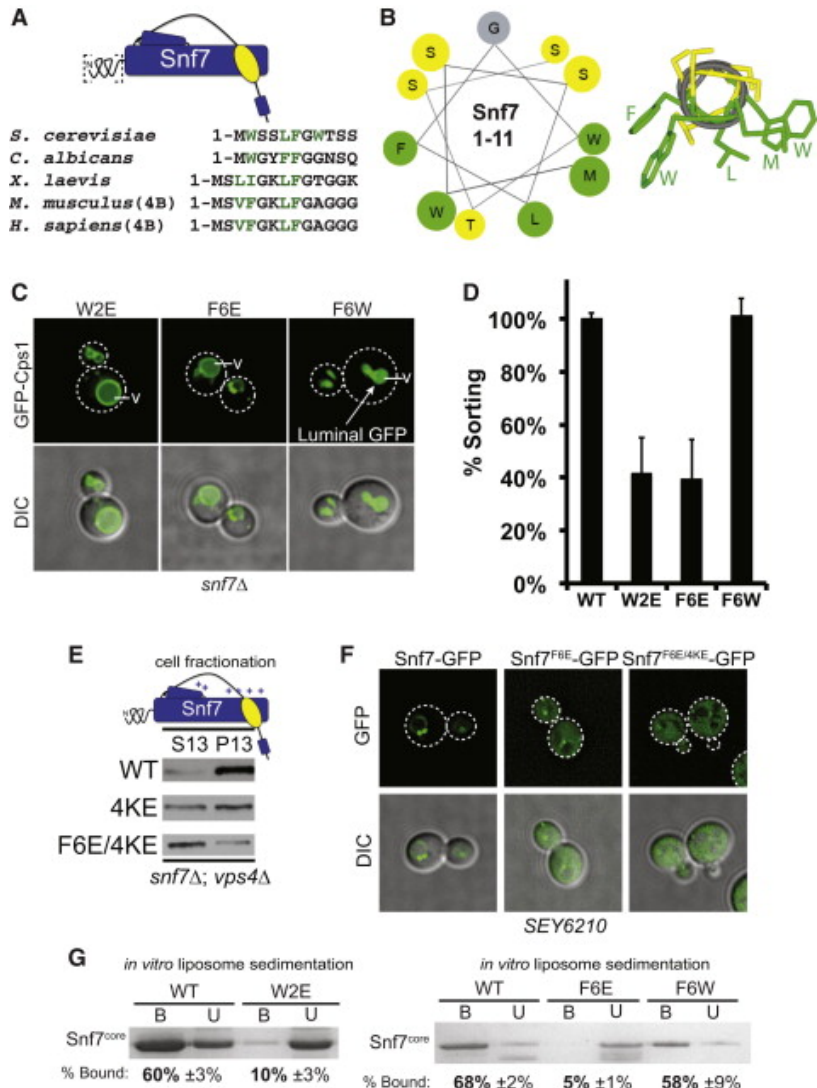


**Figure 2.5 Snf7 Requires N-Terminal Hydrophobic Residues**

## Figure 2.5 Snf7 Requires N-Terminal Hydrophobic Residues

- (A) Sequence alignment of N termini of Snf7 in eukaryotic species. Hydrophobic residues (green).
- (B) Helical wheel depictions of Snf7 N terminus.
- (C) Representative images of mid-log *snf7Δ* yeast exogenously expressing GFP-Cps1 and Snf7<sup>W2E</sup>, Snf7<sup>F6E</sup>, or Snf7<sup>F6W</sup>. GFP images (upper row); composite images of GFP and DIC (bottom row). White arrows denote luminal GFP. Vacuole (v).
- (D) Quantitative sorting data for Snf7, Snf7<sup>W2E</sup>, Snf7<sup>F6E</sup>, and Snf7<sup>F6W</sup>. Error bars represent standard deviation.
- (E) Cellular fractionation analyses of *snf7Δ vps4Δ* yeast exogenously expressing WT Snf7, Snf7<sup>4KE</sup> (4KE), and Snf7<sup>F6E/4KE</sup>. 4KE sample from same set in Figure 2.1H.
- (F) Representative images of mid-log yeast exogenously expressing Snf7-GFP, Snf7<sup>F6E</sup>-GFP, and Snf7<sup>F6E/4KE</sup>-GFP. GFP images (upper row); composite images of GFP and DIC (bottom row).
- (G) Liposome sedimentation assays of Snf7<sup>core</sup>, Snf7<sup>core/W2E</sup>, Snf7<sup>core/F6E</sup>, and Snf7<sup>core/F6W</sup>. Protein-free (unbound, U); liposome-associated protein (bound, B).

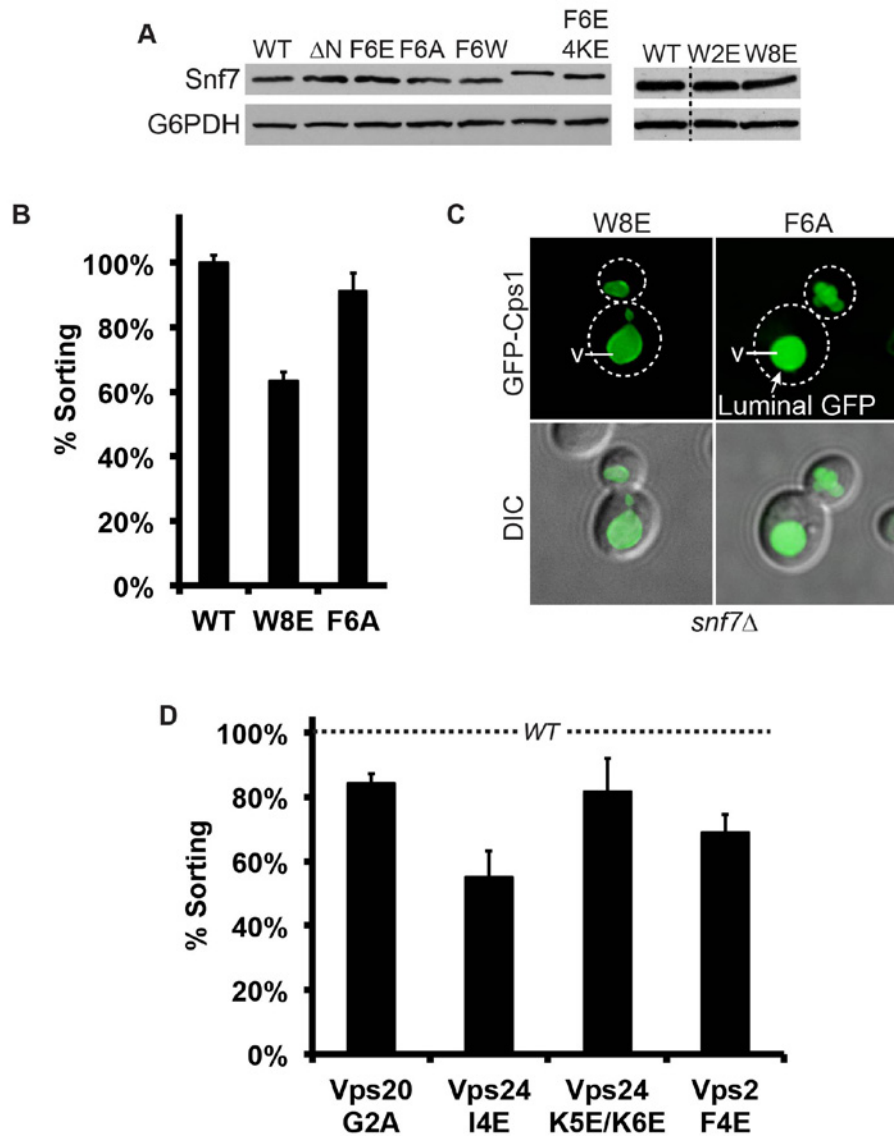


**Figure 2.6 Expression Levels of Snf7 N-terminus Mutants with Functional Data from Additional Supporting Mutants**

**Figure 2.6. Expression Levels of Snf7 N-terminus Mutants with Functional Data from Additional Supporting Mutants**

- (A) Western blots showing expression levels of Snf7 N-terminal hydrophobic mutants.
- (B) Quantitative sorting data of  $\text{Snf7}^{\text{W8E}}$  and  $\text{Snf7}^{\text{F6A}}$ . Error bars represent standard deviation.
- (C) Representative images of mid-log  $\text{snf7}\Delta$  yeast exogenously expressing GFP-Cps1 and  $\text{Snf7}^{\text{W8E}}$  or  $\text{Snf7}^{\text{F6A}}$ . GFP images (upper row); composite images of GFP & DIC (bottom row). White arrows denote the GFP signal localized within the vacuole (v) lumen.
- (D) Quantitative sorting data of ESCRT-III subunit N-terminal point mutations. Error bars represent standard deviation.

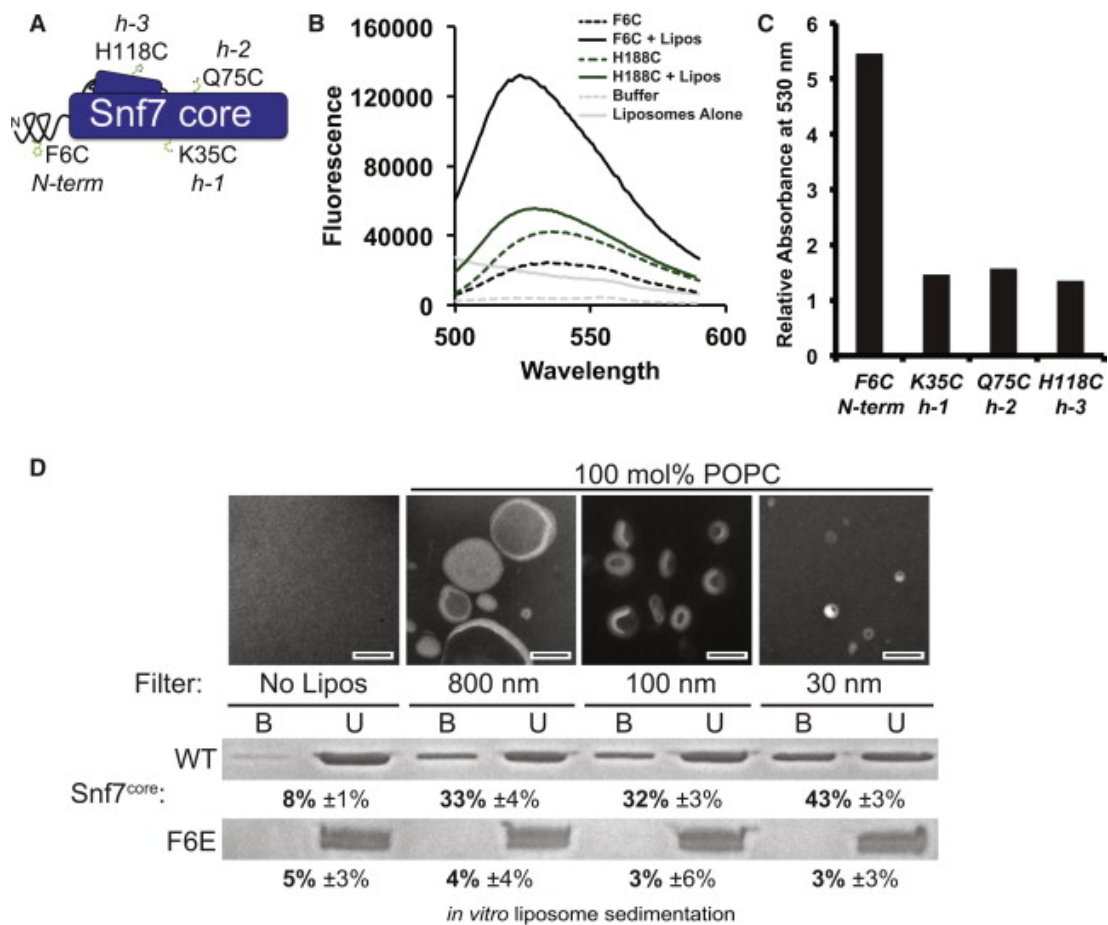


**Figure 2. 7 The N Terminus of Snf7 Inserts into Membrane**

## Figure 2.7 The N Terminus of Snf7 Inserts into Membrane

- (A) Cartoon schematic of NBD-labeled residues.
- (B) Emission spectra for buffer, liposomes, and  $\text{Snf7}^{\text{core/F6C}}$  or  $\text{Snf7}^{\text{core/H118C}}$  with and without liposomes.
- (C) Graph of relative absorbance at 530 nm ((protein + liposome sample) / protein alone sample) for  $\text{Snf7}^{\text{core/F6C}}$  (*N-term*),  $\text{Snf7}^{\text{core/K35C}}$  (*h-1*),  $\text{Snf7}^{\text{core/Q75C}}$  (*h-2*), and  $\text{Snf7}^{\text{core/H118C}}$  (*h-3*).
- (D) Liposome sedimentation assay of  $\text{Snf7}^{\text{core}}$  and  $\text{Snf7}^{\text{core/F6E}}$  with liposomes of varying sizes. Protein-free (unbound, U); liposome-associated protein (bound, B). Liposomes were visualized by negative-stain transmission electron microscopy. Scale bars, 100 nm.

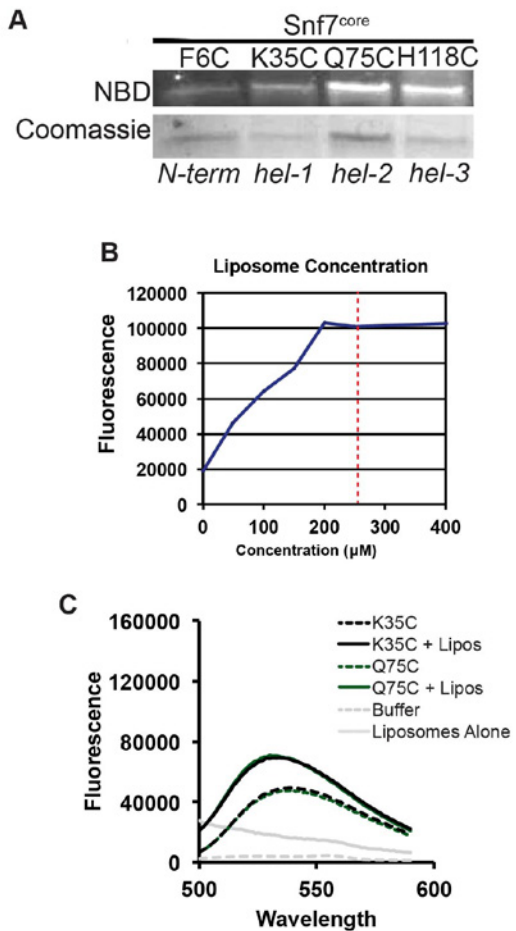


**Figure 2.8 Reagents and Additional Data Used for NBD-based Fluorescence Spectroscopy**

**Figure 2.8 Reagents and Additional Data Used for NBD-based Fluorescence Spectroscopy**

- (A) Snf7<sup>core</sup> labeled with NBD on cysteine residues introduced at positions 6 (F6C), 35 (K35C), 75 (Q75C) and 118 (H118C) were visualized by Coomassie staining (upper panel) and exposure to UV light (bottom panel).
- (B) Emission spectra of 3  $\mu$ M NBD-labeled Snf7<sup>core/F6C</sup> added to increasing amounts of liposomes (0-400  $\mu$ M). Dashed red line at 250  $\mu$ M indicates concentration used for experiments.
- (C) Emission spectra for buffer, liposomes, and Snf7<sup>core/K35C</sup> or Snf7<sup>core/Q75C</sup> with and without liposomes.

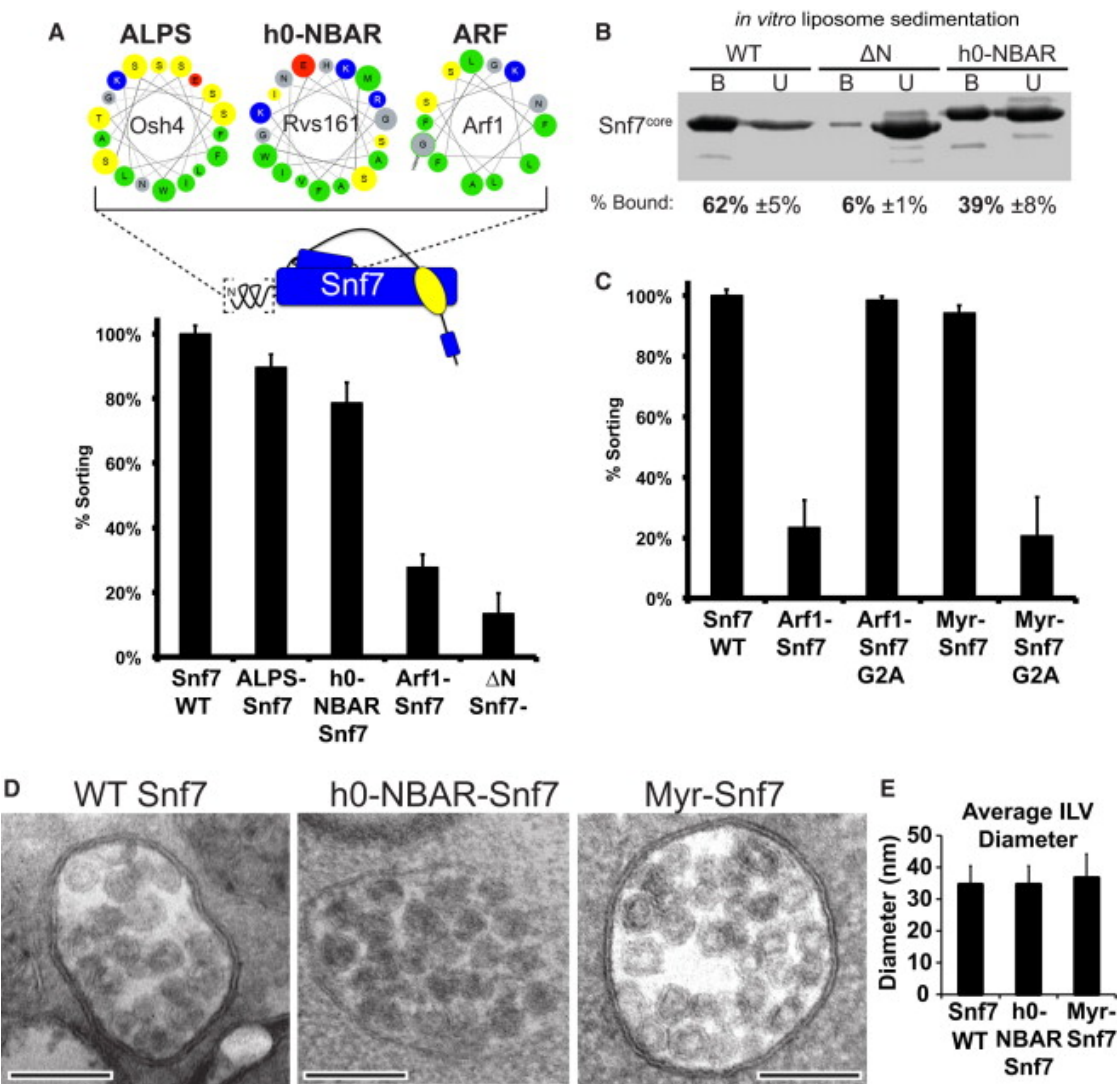


**Figure 2.9 Snf7 Requires a Membrane-Inserting N-Terminal Motif**

### Figure 2.9 Snf7 Requires a Membrane-Inserting N-Terminal Motif

- (A) Cartoon schematic with N-terminal helical wheels of chimeras used in quantitative sorting assay. Graph represents quantitative sorting data for *snf7Δ* yeast exogenously expressing WT Snf7, ALPS-Snf7, h0-NBAR-Snf7, Arf1-Snf7, and ΔN-Snf7.
- (B) Liposome sedimentation assays of  $\text{Snf7}^{\text{core}}$ ,  $\Delta\text{N-Snf7}^{\text{core}}$ , and h0-NBAR-Snf7 $^{\text{core}}$ . Protein-free (unbound, U); liposome-associated protein (bound, B).
- (C) Quantitative sorting data for Snf7, Arf1-Snf7, Arf1-Snf7 $^{G2A}$ , Myr-Snf7, and Myr-Snf7 $^{G2A}$ .
- (D) Representative EM images of ILV-containing MVBs from *snf7Δ;vam7Δ* yeast exogenously expressing Vam7ts and Snf7 (left panel), h0-NBAR-Snf7 (middle panel), or Myr-Snf7 (right panel). Scale bar, 100 nm.
- (E) Graph of mean ILV size of samples in (D). N = 100. Error bars in (A), (C), and (E) represent standard deviation.

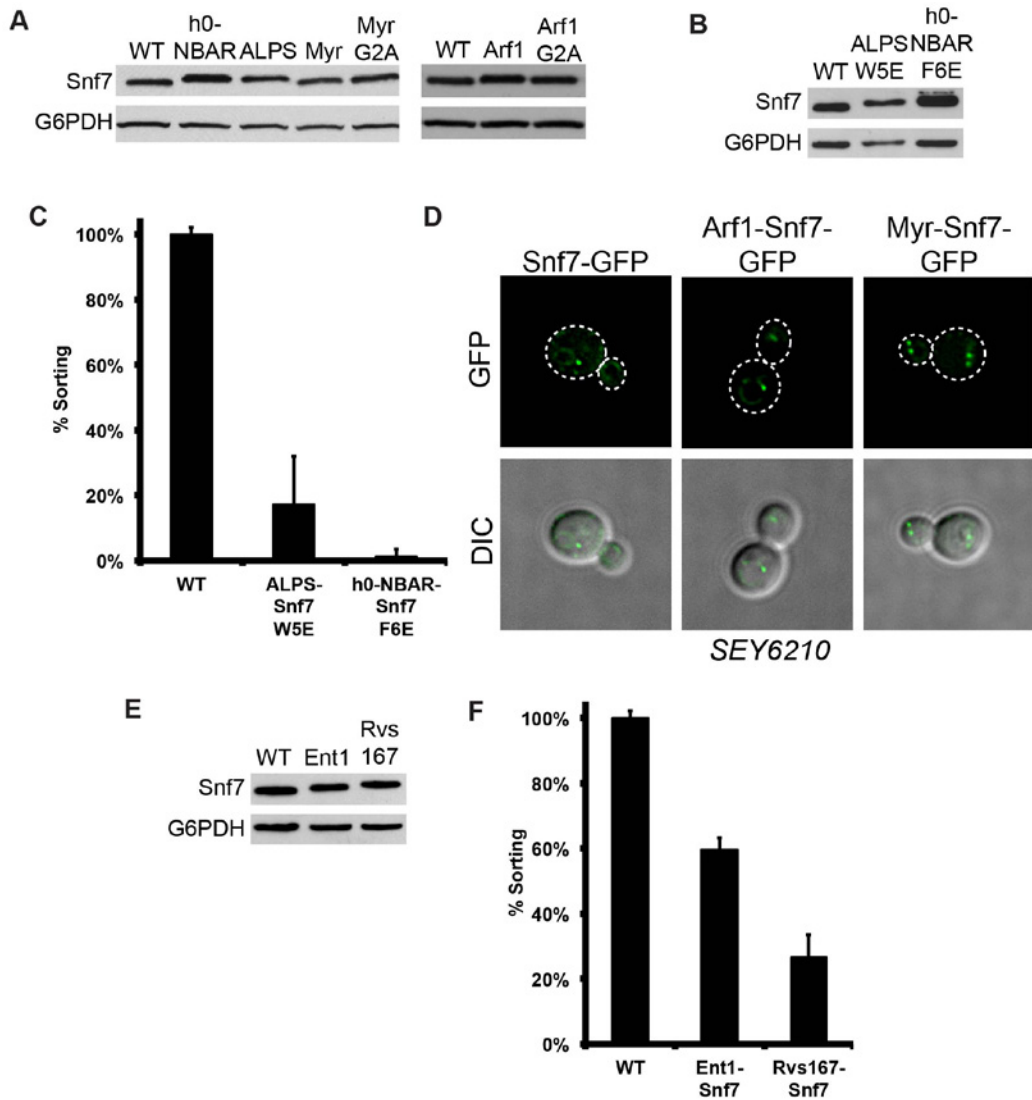


**Figure 2.10 Expression Levels of Snf7 N-Terminal Chimeras with Additional Functional and Localization Data**

**Figure 2.10 Expression Levels of Snf7 N-Terminal Chimeras with Additional Functional and Localization Data**

- (A-B) Western blots showing expression levels of Snf7 (A) N-terminal chimeras and (B) N-terminal chimera point mutations.
- (C) Quantitative sorting data of N-terminal chimeras with point mutations.
- (D) Representative images of mid-log yeast exogenously expressing Arf1-Snf7-GFP or Myr-Snf7-GFP. GFP images (upper row); composite images of GFP & DIC (bottom row).
- (E) Western blot showing expression levels of additional N-terminal chimeras.
- (F) Quantitative sorting data of additional N-terminal chimeras. Error bars in (C) and (F) represent standard deviation.

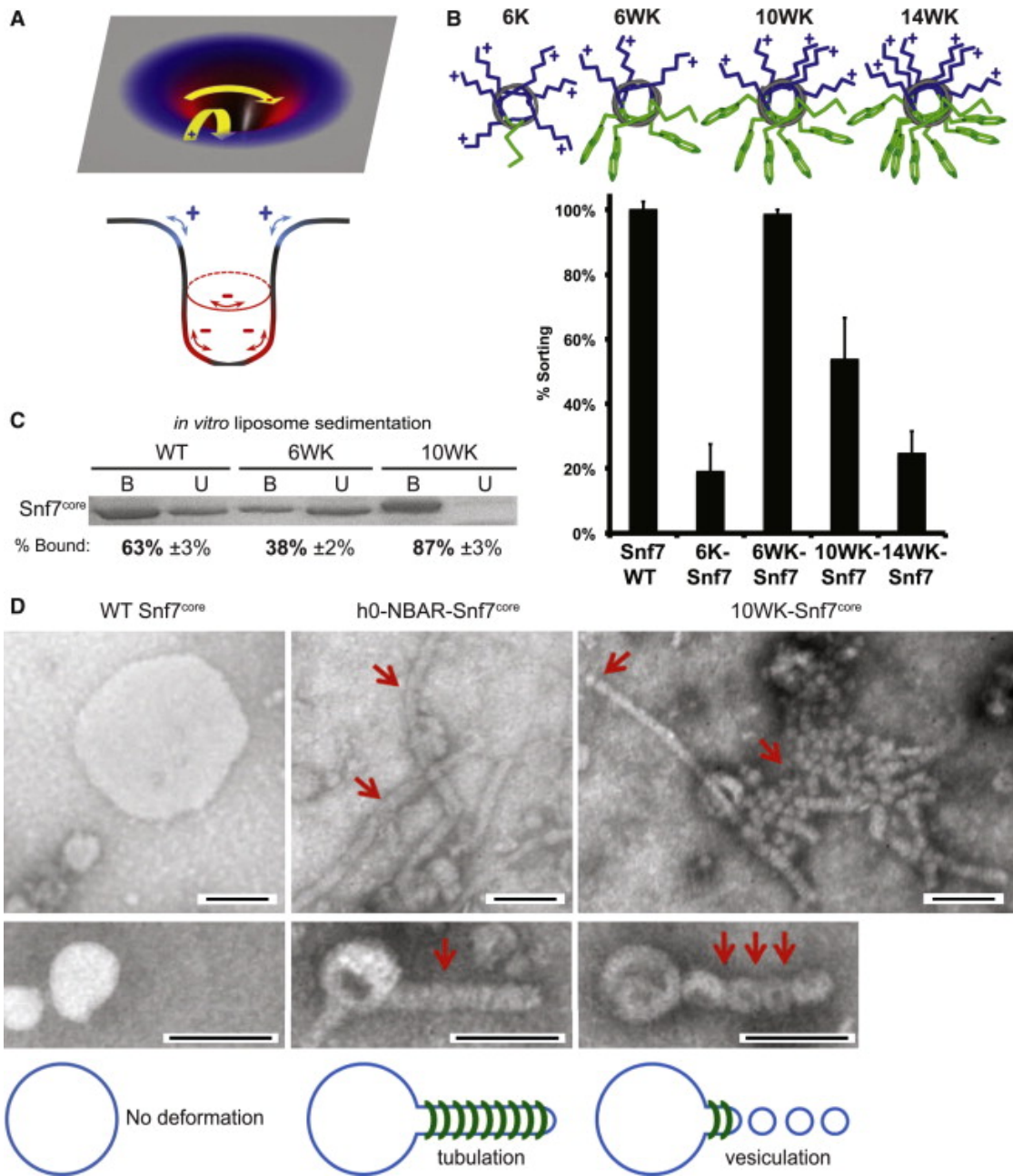


**Figure 2.11 ILV Formation Requires Maintaining Delicate Balance of Curvatures**

## Figure 2.11 ILV Formation Requires Maintaining Delicate Balance of Curvatures

- (A) Cartoon schematic demonstrating distribution of positive (blue) and negative (red) curvatures in a membrane invagination.
- (B) 3D-helical wheel depictions of Snf7 chimeric N termini. Quantitative sorting data for WT Snf7, 6K-Snf7, 6WK-Snf7, 10WK-Snf7, and 14WK-Snf7.
- (C) Liposome sedimentation assays of  $\text{Snf7}^{\text{core}}$ , 6WK-Snf7 $^{\text{core}}$ , and 10WK-Snf7 $^{\text{core}}$ . Protein-free (unbound, U); liposome-associated protein (bound, B).
- (D) Representative EM images of samples containing liposomes and 10  $\mu\text{M}$  Snf7 $^{\text{core}}$  (left panel), h0-NBAR-Snf7 $^{\text{core}}$  (middle panel) or 10WK-Snf7 $^{\text{core}}$  (right panel). Scale bars, 100 nm. Red arrows highlight areas of deformation. Cartoon schematic illustrates different degrees of membrane deformation.

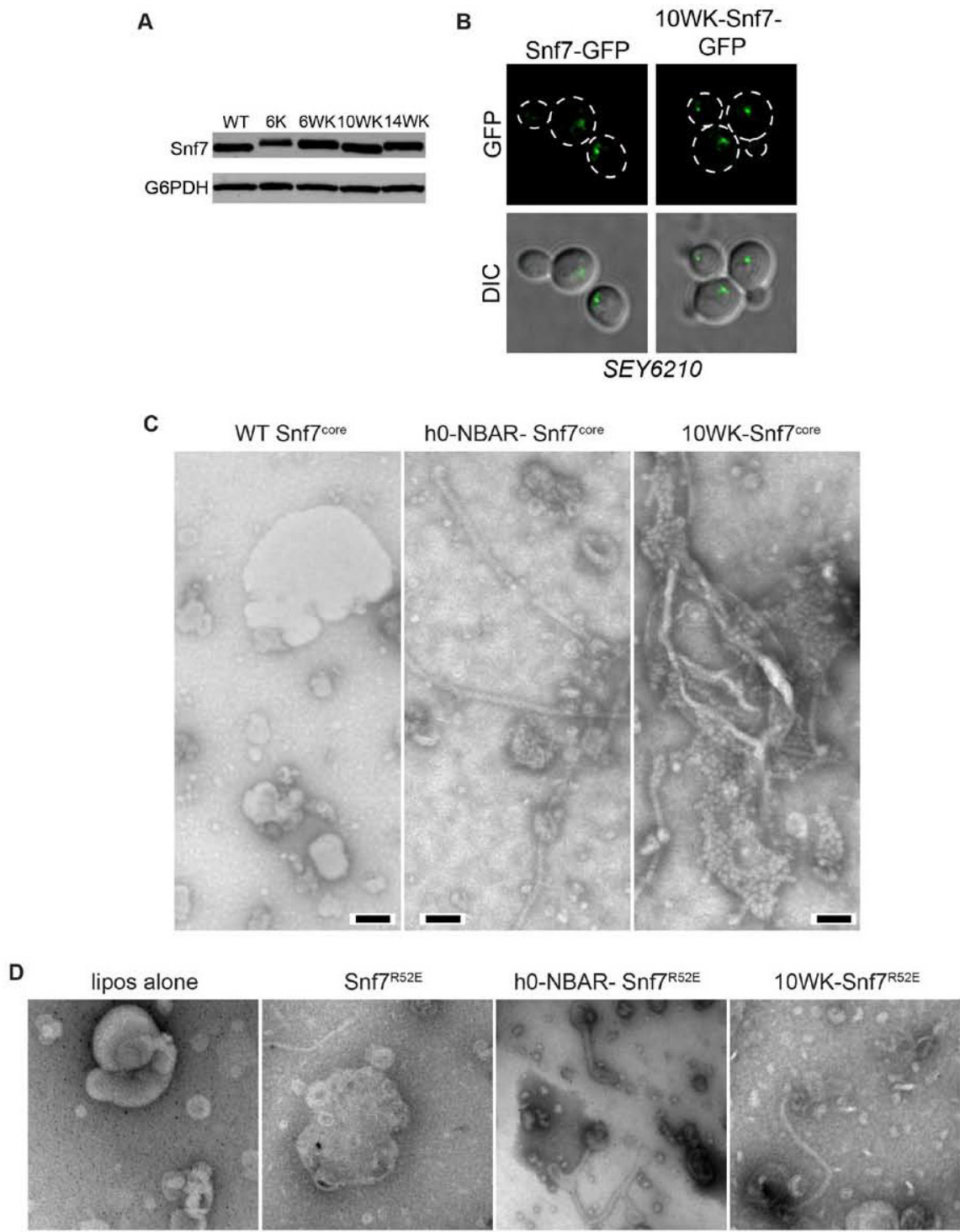


**Figure 2.12 Expression Levels of Snf7 Chimeric N Terminal Mutants with Mutant Localization Data and Additional EM Images**

**Figure 2.12 Expression Levels of Snf7 Chimeric N Terminal Mutants with Mutant Localization Data and Additional EM Images**

- (A) Western blots showing expression levels of Snf7 artificial N-terminal chimeras.
- (B) Representative images of mid-log yeast exogenously expressing 10WK-Snf7-GFP and 6K-Snf7-GFP. GFP images (upper row); composite images of GFP & DIC (bottom row).
- (C) Additional representative EM images of negative stained samples containing liposomes with 10  $\mu$ M Snf7<sup>core</sup> (left panel), h0-NBAR-Snf7<sup>core</sup> (middle panel) and 10WK-Snf7<sup>core</sup> (right panel).
- (D) Representative EM images of liposomes alone (lipos alone, far left panel), Snf7<sup>R52E</sup> (left center panel), h0-NBAR-Snf7<sup>R52E</sup> (right center panel) and 10WK-Snf7<sup>R52E</sup> (right panel) prepared as described in (C). Scale bars in (C) and (D), 100 nm.

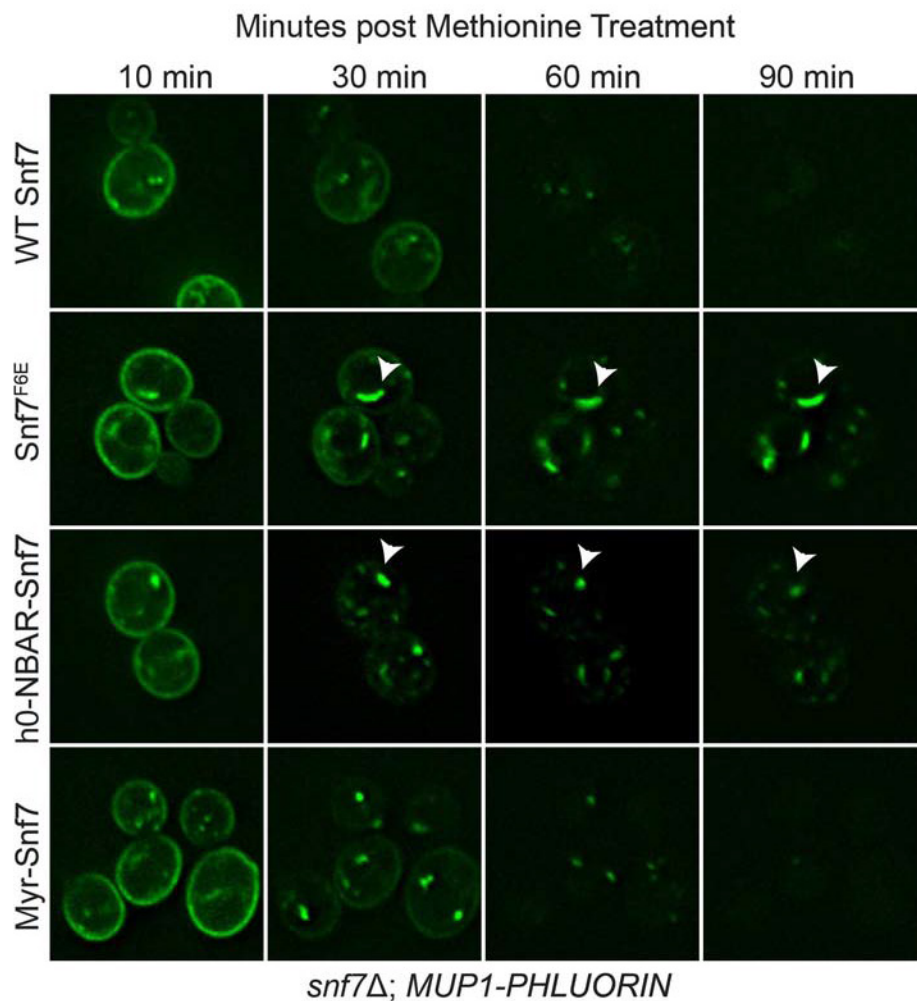


**Figure 2.13 Kinetic Sorting of Mup1-pHluorin by Snf7 N-terminal Mutants**

**Figure 2.13 Kinetic Sorting of Mup1-pHluorin by Snf7 N-terminal Mutants**

Light microscopy of Mup1-pHluorin for *snf7Δ* yeast expressing Snf7<sup>WT</sup>, Snf7<sup>F6E</sup>, h0-NBAR-Snf7 and Myr-Snf7 treated with methionine and imaged every two minutes for 94 minutes. White arrowheads indicate stable Mup1-pHluorin puncta.

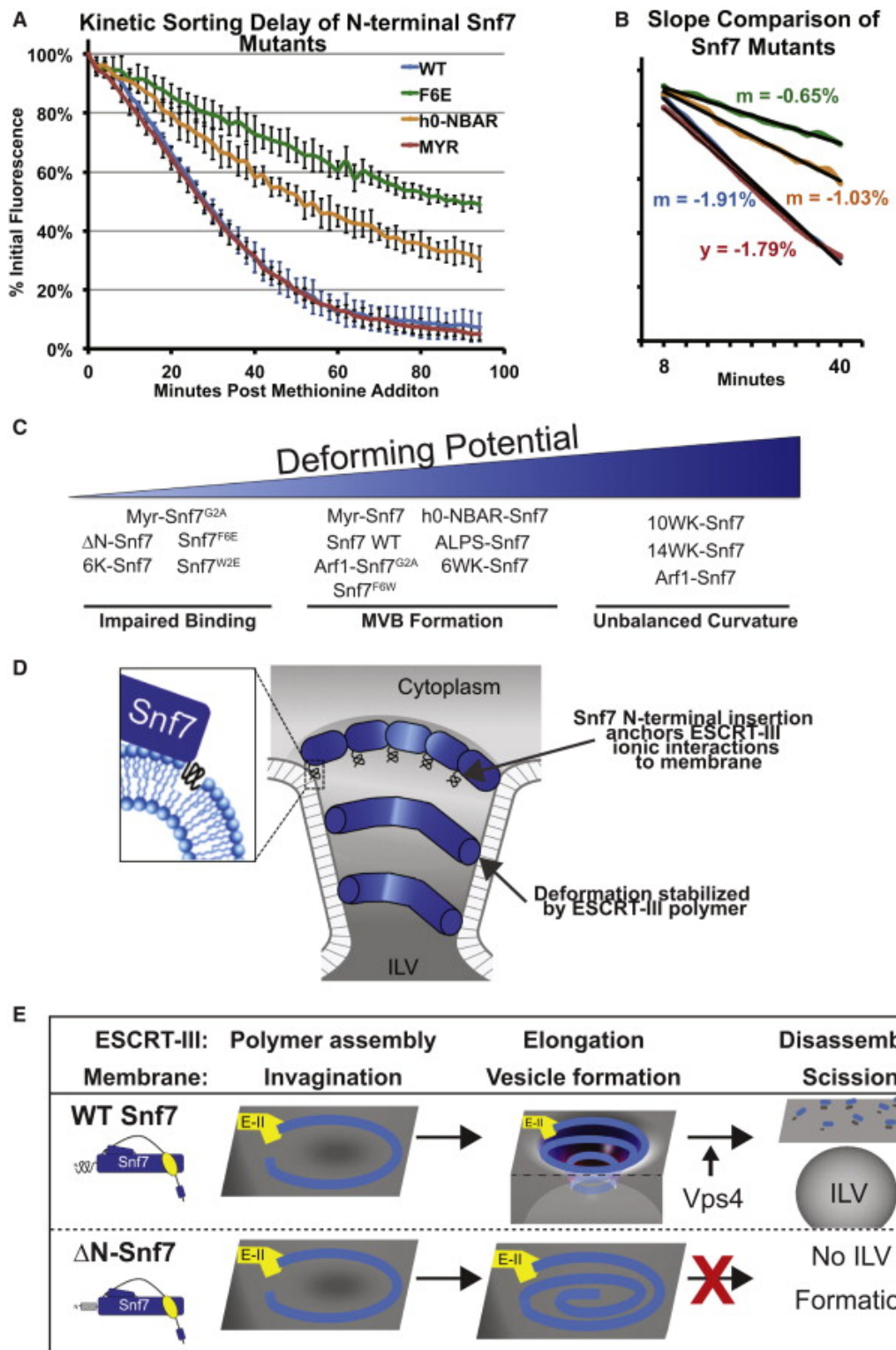


Figure 2.14 The N Terminus of Snf7 Is Required for Fast Cargo Sorting

**Figure 2.14 The N Terminus of Snf7 Is Required for Fast Cargo Sorting**

- (A) Kinetic sorting of mid-log cultures of *snf7Δ* yeast exogenously expressing WT Snf7, Snf7<sup>F6E</sup>, h0-NBAR-Snf7, and Myr-Snf7.
- (B) Plot depicting slope calculated from linear trendlines for samples in (A), 8-40 min poststimulation. Slope of trend line is shown.
- (C) Schematic depicting relationship between quantitative sorting efficiency of Snf7 N-terminal mutants and the predicted ability to deform membrane.
- (D) Cartoon schematic showing stabilization of invagination by ESCRT-III polymer anchored to membrane by ANCHR motif.
- (E) Model showing ILV formation is dependent upon N-terminal anchoring of ESCRT-III polymer to membrane.

## **Experimental Procedures**

### **Yeast Strains, Plasmids, and Protein Purification**

Strains and plasmids from this study are listed in the Supplemental Experimental Procedures. Snf7core and full-length constructs were cloned using the pET23d bacterial expression vector (Novagen) with an added N-terminal His6-tag. Vps2 core domain constructs were cloned into pGEX6P1. Constructs were expressed in BL21 or C41(DE3) *Escherichia coli* cells and purified by either TALON beads (Clontech) or GSH-Sepharose beads (GE Healthcare). All expression preps were grown at 37°C until a cell OD<sub>600</sub> of 0.6–0.8 and were then induced with 1 mM IPTG and grown for 4 hr at 37°C. During purification, proteins were reconstituted in 500 mM NaCl and 20 mM HEPES (pH 7.4). TALON beads were eluted in 150 mM NaCl, 20 mM HEPES (pH 7.4), and 400 mM imidazole; GSH-Sepharose beads were eluted in 20 mM glutathione (Sigma-Aldrich). Samples were dialyzed overnight to remove excess imidazole or glutathione.

### **Fluorescence Microscopy**

All fluorescent microscopy was performed on mid-log yeast. Images were acquired using a DeltaVision RT system (Applied Precision) with Photometrics CoolSNAP HQ Camera. Postacquisition deconvolution and image analysis were performed in Softworx and Photoshop (Adobe).

### **Mup1-pHluorin Quantitative Sorting Assay**

For steady-state analysis, mid-log cultures grown in 20 µg/ml methionine for 2 hr were transferred to PBS. Mean fluorescence of 100,000 events was recorded on a BD Accuri C6 flow cytometer. After background subtraction, the WT sample was set to 100%, the vector control to 0%, and the mutant sorting efficiency was calculated based on the mean fluorescence. Each sample is represented by the mean of at least three independent readings of 100,000 cells. Error bars represent standard deviation.

For kinetic analysis, events were recorded for 30 s intervals every 2 min immediately after methionine addition. The mean fluorescence of each time point was plotted after background subtraction. Each time point is the average of three independent kinetic experiments plotted with SD. Slopes were calculated from the linear trendline from time points 8 to 40.

### **Western Blot and Antibodies**

Total cell lysates were prepared from 5 OD600 mid-log cultures by incubating on ice 1 hr in 10% TCA. Following two acetone wash-sonication cycles, samples were bead-beated 5 min in boiling buffer (50 mM Tris [pH 7.5], 1 mM EDTA, and 1% SDS) and incubated 5 min at 95°C. After addition of 2× urea buffer (150 mM Tris [pH 6.8], 6 M urea, 6% SDS, and bromophenol blue), samples were bead-beated for 5 min and heated 10 min at 65°C. Samples were run on 10% polyacrylamide gels and transferred to nitrocellulose membranes. Antibodies used for blotting were G6PDH and FLAG (Sigma-Aldrich), Snf7 and Vps24 (Babst et al., 1998), Vps20 (generated in-house as previously described (Babst et al., 1998)), and Vps2 (a gift from David Teis).

## **Cellular Fractionation Analysis**

About 15–20 OD600 of mid-log cultures were spheroplasted using 10 µg zymolyase/OD cells. Yeast were lysed using Dounce homogenizer on ice in 1 ml lysis buffer (50 mM Tris [pH 7.5], 1 mM EDTA, 200 mM sorbitol with protease inhibitors). Lysates were cleared by spinning at 500 × g for 5 min at 4°C before centrifugation at 13,000 × g for 10 min at 4°C. The pellet was resuspended in lysis buffer, and proteins were TCA precipitated from both the supernatant and pellet fractions as described under western blot section.

## **Liposome Sedimentation Assays**

To conduct the experiment, 14 µM protein and 600 µM liposomes were incubated for 10 min and directly centrifuged in a TLA-100 (Beckman Coulter) for 10 min at 55,000 rpm at 20°C. Liposomes were made in 20 mM HEPES (pH 7.4) and 150 mM NaCl by classical dehydration and sonication for 1 min. The liposome composition was 60% DOPC:30% phosphatidylserine:10% phosphatidylinositol 3-phosphate. Variations of the composition were 100% DOPC or 25% DOPC:75% PS. All lipids were purchased from Avanti or CellSignals. Where indicated, liposomes were extruded through 800, 100, or 30 nm filters. The supernatant (unbound) and pellet (bound) were directly prepared for SDS-PAGE and visualized with Coomassie stain. Value is average of three independent sedimentation assays.

## **Fluorescence Spectroscopy**

Cysteine residues on purified Snf7core constructs were labeled with excess IANBD (*N,N'*-dimethyl-*N'*-(iodoacetyl)-*N'*-(7-nitrobenz-2-oxa-1,3-diazole-4-yl)ethylenediamine) (Molecular Probes) for 2 hr at 4°C protected from light. Samples were double dialyzed into buffer containing 20 mM HEPES (pH 7.4), 150 mM NaCl, and 0.1% β-mercaptoethanol to quench and remove excess IANBD. All reactions were performed in 150 μL final volume in quartz cuvettes. Liposomes were incubated in excess (250 μM) with protein for 10 min. The excitation wavelength was 468 nm and the emission was scanned at 500–590 nm.

## **Electron Microscopy**

Visualization of Snf7 polymers on EM grids with or without liposomes was performed as previously described (Henne et al., 2012). For Snf7 liposome assays, 15 μM Snf7R52E was mixed with 600 μM liposomes for 10 min and was added to EM grid. For tubulation experiments, 10 μM protein was added to 600 μM liposomes and incubated for 15 min. Samples were negative stained with ammonium molybdate.

Yeast cells were fixed with 2.5% (v/v) glutaraldehyde for 1 hr and spheroplasted with 250 μg zymolyase and 50 μL gluculase before embedding in 2% ultra-low temperature agarose. Cells were incubated in 1% osmium tetroxide/1% potassium ferrocyanide (30 min), 1% thiocarbohydrazide (5 min), and 1% osmium tetroxide/1% postassium ferrocyanide (5 min). Cells were extensively washed in water after each treatment. After dehydration through an ethanol series, samples were transitioned into 100% propylene oxide and embedded in Spurr's resin. All electron microscopy was

performed on a Morgnani 268 transmission electron microscope (FEI) with an AMT digital camera.

## Acknowledgments

N.J.B. is supported by an American Cancer Society Postdoctoral Fellowship (PF-12-062-01-DMC). W.M.H. is supported by a Sam and Nancy Fleming Research Fellowship. The authors would like to particularly thank Sunil Adige, Jeanne Quirit, William Valley, and Ning Liu for their scientific support. The authors also thank Chris Stefan, Yuxin Mao, Chris Fromme, and Leonid Timashev for helpful discussions and their critical editing of the manuscript.

**Table 2.1 Plasmids and Yeast Strains Used in Chapter 2**

| <b>Plasmids for <i>Saccharomyces cerevisiae</i> Expression</b> |  |                             |
|--|--|-----------------------------|
| <b>Plasmid</b>   | <b>Mutations</b>   | <b>Reference</b>            |
| pRS415-Vps24   | Wild-type  | this study                  |
| pRS415-Vps24 <sup>+1E</sup>                                    | K50E   | this study                  |
| pRS415-Vps24 <sup>+2E</sup>                                    | R25E/K26E  | this study                  |
| pRS415-Vps24 <sup>+3E</sup>                                    | R25E/K26E/K50E   | this study                  |
| pRS415-Vps24 <sup>+4E</sup>                                    | R25E/K26E/K54E/K55E                                      | this study                  |
| pRS415-Vps2-FLAG   | Wild-type; FLAG  | this study                  |
| pRS415-Vps2 <sup>+2E</sup> -FLAG                               | R27E/R30E; FLAG  | this study                  |
| pRS415-Vps2 <sup>+3E</sup> -FLAG                               | R27E/R30E/K51E/K52E; FLAG                                | this study                  |
| pRS415-Vps2 <sup>+4E</sup> -FLAG                               | R27E/R30E/K51E; FLAG                                     | this study                  |
| pRS416-Snf7  | Wild-type  | (Henne et al., 2012)        |
| pRS416-Snf7 <sup>+2E</sup>                                     | R27E/R52E  | this study                  |
| pRS416-Snf7 <sup>+4E</sup>                                     | R27E/K35E/R52E/K57E                                      | this study                  |
| pRS416-Snf7 <sup>1KE</sup>                                     | K71E   | this study                  |
| pRS416-Snf7 <sup>2KE</sup>                                     | K112E/K115E  | this study                  |
| pRS416-Snf7 <sup>3KE</sup>                                     | K71E/K112E/K115E   | (Henne et al., 2012)        |
| pRS416-Snf7 <sup>4KE</sup>                                     | K68E/K71E/K112E/K115E                                    | this study                  |
| pRS424-GFP-Cps1  | GFP; Cps1  | (Odorizzi et al., 1998)     |
| pRS415-Vps20   | Wild-type  | this study                  |
| pRS415   |  | (Sikorski and Hieter, 1989) |
| pRS415-ΔN-Vps20  | 5-221 (MSSKVHITKTDR...)                                  | this study                  |
| pRS416   |  | (Sikorski and Hieter, 1989) |
| pRS416-ΔN-Snf7   | 10-240 (MSSNAKNKESPT...)                                 | this study                  |
| pRS426-GFP-Cps1  | GFP; Cps1  | (Odorizzi et al., 1998)     |
| pRS414-Vps24   | Wild-type  | this study                  |
| pRS414   |  | (Sikorski and Hieter, 1989) |
| pRS414-ΔN-Vps24  | 8-224 (MIWGPDPKEQ...)                                    | this study                  |
| pRS415-Vps2  | Wild-type  | this study                  |
| pRS415-ΔN-Vps2   | 8-232 (MFGKNVTPQE...)                                    | this study                  |
| pRS416-Snf7-GFP  | 10-240; GFP  | (Henne et al., 2012)        |
| pRS416-ΔN-Snf7-GFP   | 10-240; GFP  | this study                  |
| pRS416-Snf7 <sup>W2E</sup>                                     | W2E  | this study                  |
| pRS416-Snf7 <sup>F6E</sup>                                     | F6E  | this study                  |
| pRS416-Snf7 <sup>F6W</sup>                                     | F6W  | this study                  |
| pRS416-Snf7 <sup>F6E/4KE</sup>                                 | Snf7 F6E/K68E/K71E/K112E/K115E                           | this study                  |
| pRS416-Snf7 <sup>F6E-4KE</sup> -GFP                            | Snf7 F6E; GFP  | this study                  |
| pRS416-Snf7 <sup>F6E/4KE</sup> -GFP                            | Snf7 F6E/K68E/K71E/K112E/K115E; GFP                      | this study                  |
| pRS416-ALPS-Snf7   | Osh4 7-29; Snf7 10-240<br>(MSSSWTSFLKSIASFNGDLSSLSASS..) | this study                  |

|                                    |   |                     |
|------------------------------------|---|---------------------|
| pRS416-NBAR-Snf7                   | Rvs161 1-22; Snf7 10-240<br>(MSWEGFKKAINRAGHSVIIKNVSS...) | this study          |
| pRS416-Arf1-Snf7                   | Arf1 1-14; Snf7 10-240<br>(MALFASKLFSNLFGSS...)           | this study          |
| pRS416-Arf1-Snf7 <sup>G2A</sup>    | Arf1 1-14; G2A; Snf7 10-240<br>(MALFASKLFSNLFGSS...)      | this study          |
| pRS416-Myr-Snf7                    | Vps20 1-4; Snf7 10-240 (MGQKSS...)                        | this study          |
| pRS416-Myr-Snf7 <sup>G2A</sup>     | Vps20 1-4; G2A; Snf7 10-240 (MAQKSS...)                   | this study          |
| pRS414-Vam7 <sup>ts</sup>          | Vam7 <sup>ts</sup> -167                                   | (Sato et al., 1998) |
| pRS416-6K-Snf7                     | 6K; Snf7 10-240 (MKKKKKKKSS...)                           | this study          |
| pRS416-6WK-Snf7                    | 6WK; Snf7 10-240 (MWKKWWKWWKSS...)                        | this study          |
| pRS416-10WK-Snf7                   | 10WK; Snf7 10-240 (MWKKWWKKWWKWWKSS...)                   | this study          |
| pRS416-14WK-Snf7                   | 14WK; Snf7 10-240<br>(MWKKWWKKWWKWWKSS...)                | this study          |
| pRS415-Vps24 <sup>EEAA</sup>       | R27E/K35E/R52A/K57A                                       | this study          |
| pRS416-Snf7 <sup>K60E</sup>        | K60E  | this study          |
| pRS416-Snf7 <sup>K64E</sup>        | K64E  | this study          |
| pRS416-Snf7 <sup>K68E</sup>        | K68E  | this study          |
| pRS416-Snf7 <sup>K79E</sup>        | pRS416-Snf7 <sup>K79E</sup>                               | this study          |
| pRS416-Snf7 <sup>2KE-S1</sup>      | K79E  | this study          |
| pRS416-Snf7 <sup>3KE-S1</sup>      | K68E/K71E   | this study          |
| pRS416-Snf7 <sup>3KE-S2</sup>      | K68E/K112E/K115E  | this study          |
| pRS416-Snf7 <sup>+4E</sup> -GFP    | K79E/K112E/K115E  | this study          |
| pRS416-Snf7-Vps20                  | Snf7 R27E/K35E/R52E/K57E; GFP                             | this study          |
| pRS414-Snf7-Vps24                  | Snf7 1-9; Vps20 5-221 (MWSSLFGWTSSKV...)                  | this study          |
| pRS415-Snf7-Vps2                   | Snf7 1-9; Vps24 8-224 (MWSSLFGWTI...)                     | this study          |
| pRS416-Vps24-Snf7                  | Snf7 1-9; Vps2 8-232 (MWSSLFGWTFG...)                     | this study          |
| pRS416-Vps2-Snf7 <sup>E5G</sup>    | Vps24 1-7; Snf7 10-240 (MDYIKKASSNAKNK...)                | this study          |
| pRS416-Vps2-Snf7                   | Vps2 1-7; Snf7 10-240 (MSLFEWVSSNAKNK...)                 | this study          |
| pRS416-Snf7 <sup>W8E</sup>         | Vps2 1-7; E5G; Snf7 10-240 (MSLFGWVSS...)                 | this study          |
| pRS416-Snf7 <sup>F6A</sup>         | W8E   | this study          |
| pRS415-Vps20 <sup>G2A</sup>        | F6A   | this study          |
| pRS414-Vps24 <sup>I4E</sup>        | G2A   | this study          |
| pRS414-Vps24 <sup>K5E/K6E</sup>    | I4E   | this study          |
| pRS415-Vps2 <sup>F4E</sup>         | K5E/K6E   | this study          |
| pRS416-ALPS-Snf7 <sup>W5E</sup>    | F4E   | this study          |
| pRS416-h0-NBAR-Snf7 <sup>F6E</sup> | Osh4 7-29; Snf7 10-240<br>(MSSSETSFLKSIASFNGDLSSLSASS...) | this study          |
| pRS416-Arf1-Snf7-GFP               | Rvs161 1-22; Snf7 10-240<br>(MSWEGEKKAINRAGHSVIIKNVSS...) | this study          |
| pRS416-Myr-Snf7-GFP                | Arf1 1-14; Snf7 10-240; GFP<br>(MGLFASKLFSNLFGSS...)      | this study          |
| pRS416-Ent1-Snf7                   | Vps20 1-4; Snf7 10-240; GFP (MGQKSS...)                   | this study          |
| pRS416-Rvs167-Snf7                 | Ent1 3-15; Snf7 10-240<br>(MKQFVRSAKNLVKGSS...)           | this study          |
| pRS416-10WK-Snf7-GFP               | Rvs167 1-24; Snf7 10-240                                  | this study          |

(MSFKGFTKAVSRAPQSFRQKFKMGSS...)

### Plasmids for *Escherichia coli* Expression for Protein Purification

| Plasmid                              | Mutations   | Reference            |
|--------------------------------------|---|----------------------|
| pET23d-Snf7 <sup>core</sup>          | 1-150   | (Henne et al., 2012) |
| pET23d-Snf7 <sup>core/+2E</sup>      | 1-150; K112E/K115E  | this study           |
| pET23d-ΔN-Snf7 <sup>core</sup>       | Snf7 10-150   | this study           |
| pET23d-Snf7 <sup>core/W2E</sup>      | 1-150; W2E  | this study           |
| pET23d-Snf7 <sup>core/F6E</sup>      | 1-150; F6E  | this study           |
| pET23d-Snf7 <sup>core/F6W</sup>      | 1-150; F6W  | this study           |
| pET23d-Snf7 <sup>core/F6C</sup>      | 1-150; F6C (N-term)   | this study           |
| pET23d-Snf7 <sup>core/K35C</sup>     | 1-150; K35C (h-1)   | this study           |
| pET23d-Snf7 <sup>core/Q75C</sup>     | 1-150; Q75C (h-2)   | this study           |
| pET23d-Snf7 <sup>core/H118C</sup>    | 1-150; H118C (h-3)  | this study           |
| pET23d-h0-NBAR-Snf7 <sup>core</sup>  | Rvs161 1-22; Snf7 10-150<br>(MSWEGFKKAINRAGHSVIIKNVSS...)       | this study           |
| pET23d-10WK-Snf7 <sup>core</sup>     | 10WK; Snf7 10-150;<br>(MWKKWWKKWWKSS...)                        | this study           |
| pGEX6P1-GST-Vps2 <sup>core</sup>     | GST-Vps2 1-143  | this study           |
| pGEX6P1-GST-ΔN-Vps2 <sup>core</sup>  | GST-Vps2 8-143  | this study           |
| pGEX6P1-GST-Vps2 <sup>core/F4E</sup> | GST-Vps2 1-143 F4E  | this study           |
| pET23d-Snf7 <sup>R52E</sup>          | R52E  | (Henne et al., 2012) |
| pET23d-ΔN-Snf7 <sup>R52E</sup>       | Snf7 10-240; R52E   | this study           |
| pET23d-h0-NBAR-Snf7 <sup>R52E</sup>  | Rvs161 1-22; Snf7 10-240; R52E<br>(MSWEGFKKAINRAGHSVIIKNVSS...) | this study           |
| pET23d-10WK-Snf7 <sup>R52E</sup>     | 10WK; Snf7 10-150; R52E<br>(MWKKWWKKWWKSS...)                   | this study           |

### Yeast Strains Used in This Study

| Strain    | Genotype  | Reference               |
|-----------|---|-------------------------|
| SEY6210   | <i>Mat a, leu2-3, 2-112, ura3-52, his3-Δ200, trp1-Δ901, lys2-801, suc2-Δ9</i> | (Robinson et al., 1988) |
| SEY6210.1 | <i>Mat a, leu2-3, 2-112, ura3-52, his3-Δ200, trp1-Δ901, lys2-801, suc2-Δ9</i> | (Robinson et al., 1988) |
| MBY12     | SEY6210; <i>vps4Δ::TRP1; vps24Δ::HIS3</i>                                     | (Babst et al., 2002a)   |
| MBY41     | SEY6210; <i>vps4Δ::TRP1; vps2Δ::HIS3</i>                                      | (Babst et al., 2002a)   |
| EEY12     | SEY6210; <i>vps4Δ::TRP1; snf7Δ::HIS3</i>                                      | (Babst et al., 2002a)   |
| EEY2-1    | SEY6210; <i>vps20Δ::HIS3</i>  | (Babst et al., 2002a)   |
| EEY9      | SEY6210; <i>snf7Δ::HIS3</i>   | (Babst et al., 2002a)   |
| BWY102    | SEY6210; <i>vps24Δ::HIS3</i>  | (Babst et al., 1998)    |
| MBY28     | SEY6210; <i>vps2Δ::HIS3</i>   | (Babst et al., 2002a)   |
| NBY42     | SEY6210.1; <i>vps20Δ::HIS3; MUP1-PHLOURIN::KAN</i>                            | this study              |
| NBY44     | SEY6210.1; <i>snf7Δ::HIS3; MUP1-PHLOURIN::KAN</i>                             | (Henne et al., 2012)    |
| NBY47     | SEY6210.1; <i>vps24Δ::HIS3; MUP1-PHLOURIN::KAN</i>                            | this study              |
| NBY69     | SEY6210.1; <i>vps2Δ::HIS3; MUP1-PHLOURIN::KAN</i>                             | this study              |

## Reference

- Antony, B., Beraud-Dufour, S., Chardin, P., and Chabre, M. (1997). N-terminal hydrophobic residues of the G-protein ADP-ribosylation factor-1 insert into membrane phospholipids upon GDP to GTP exchange. *Biochemistry* 36, 4675-4684.
- Babst, M., Katzmann, D.J., Estepa-Sabal, E.J., Meerloo, T., and Emr, S.D. (2002a). ESCRT-III: an endosome-associated heterooligomeric protein complex required for mvb sorting. *Dev Cell* 3, 271-282.
- Babst, M., Katzmann, D.J., Snyder, W.B., Wendland, B., and Emr, S.D. (2002b). Endosome-associated complex, ESCRT-II, recruits transport machinery for protein sorting at the multivesicular body. *Dev Cell* 3, 283-289.
- Babst, M., Sato, T.K., Banta, L.M., and Emr, S.D. (1997). Endosomal transport function in yeast requires a novel AAA-type ATPase, Vps4p. *EMBO J* 16, 1820-1831.
- Babst, M., Wendland, B., Estepa, E.J., and Emr, S.D. (1998). The Vps4p AAA ATPase regulates membrane association of a Vps protein complex required for normal endosome function. *EMBO J* 17, 2982-2993.
- Beck, R., Prinz, S., Diestelkotter-Bachert, P., Rohling, S., Adolf, F., Hoehner, K., Welsch, S., Ronchi, P., Brugger, B., Briggs, J.A., *et al.* (2011). Coatomer and dimeric ADP ribosylation factor 1 promote distinct steps in membrane scission. *J Cell Biol* 194, 765-777.
- Bigay, J., Casella, J.F., Drin, G., Mesmin, B., and Antony, B. (2005). ArfGAP1 responds to membrane curvature through the folding of a lipid packing sensor motif. *EMBO J* 24, 2244-2253.
- Bodon, G., Chassefeyre, R., Pernet-Gallay, K., Martinelli, N., Effantin, G., Hulsik, D.L., Belly, A., Goldberg, Y., Chatellard-Causse, C., Blot, B., *et al.* (2011). Charged multivesicular body protein 2B (CHMP2B) of the endosomal sorting complex required for transport-III (ESCRT-III) polymerizes into helical structures deforming the plasma membrane. *J Biol Chem* 286, 40276-40286.
- Boucrot, E., Pick, A., Camdere, G., Liska, N., Evergren, E., McMahon, H.T., and Kozlov, M.M. (2012). Membrane fission is promoted by insertion of amphipathic helices and is restricted by crescent BAR domains. *Cell* 149, 124-136.
- Boura, E., Rozycki, B., Chung, H.S., Herrick, D.Z., Canagarajah, B., Cafiso, D.S., Eaton, W.A., Hummer, G., and Hurley, J.H. (2012). Solution structure of the ESCRT-I

and -II supercomplex: implications for membrane budding and scission. *Structure* 20, 874-886.

Carlton, J.G., and Martin-Serrano, J. (2007). Parallels between cytokinesis and retroviral budding: a role for the ESCRT machinery. *Science* 316, 1908-1912.

Drin, G., and Antonny, B. (2010). Amphipathic helices and membrane curvature. *FEBS Letters* 584, 1840-1847.

Drin, G., Casella, J.F., Gautier, R., Boehmer, T., Schwartz, T.U., and Antonny, B. (2007). A general amphipathic alpha-helical motif for sensing membrane curvature. *Nat Struct Mol Biol* 14, 138-146.

Eswar, N., Eramian, D., Webb, B., Shen, M.Y., and Sali, A. (2008). Protein Structure Modeling with MODELLER. *Methods Mol Biol* 426, 145-159.

Farsad, K., and De Camilli, P. (2003). Mechanisms of membrane deformation. *Curr Opin Cell Biol* 15, 372-381.

Ford, M.G., Mills, I.G., Peter, B.J., Vallis, Y., Praefcke, G.J., Evans, P.R., and McMahon, H.T. (2002). Curvature of clathrin-coated pits driven by epsin. *Nature* 419, 361-366.

Fyfe, I., Schuh, A.L., Edwardson, J.M., and Audhya, A. (2011). Association of the endosomal sorting complex ESCRT-II with the Vps20 subunit of ESCRT-III generates a curvature-sensitive complex capable of nucleating ESCRT-III filaments. *J Biol Chem* 286, 34262-34270.

Gallop, J.L., Jao, C.C., Kent, H.M., Butler, P.J., Evans, P.R., Langen, R., and McMahon, H.T. (2006). Mechanism of endophilin N-BAR domain-mediated membrane curvature. *EMBO J* 25, 2898-2910.

Garrus, J.E., von Schwedler, U.K., Pornillos, O.W., Morham, S.G., Zavitz, K.H., Wang, H.E., Wettstein, D.A., Stray, K.M., Cote, M., Rich, R.L., et al. (2001). Tsg101 and the vacuolar protein sorting pathway are essential for HIV-1 budding. *Cell* 107, 55-65.

Ghazi-Tabatabai, S., Saksena, S., Short, J.M., Pobbat, A.V., Veprintsev, D.B., Crowther, R.A., Emr, S.D., Egelman, E.H., and Williams, R.L. (2008). Structure and disassembly of filaments formed by the ESCRT-III subunit Vps24. *Structure* 16, 1345-1356.

Hanson, P.I., Roth, R., Lin, Y., and Heuser, J.E. (2008). Plasma membrane deformation by circular arrays of ESCRT-III protein filaments. *J Cell Biol* 180, 389-402.

Henne, W.M., Buchkovich, N.J., Zhao, Y., and Emr, S.D. (2012). The endosomal sorting complex ESCRT-II mediates the assembly and architecture of ESCRT-III helices. *Cell* 151, 356-371.

Katzmann, D.J., Babst, M., and Emr, S.D. (2001). Ubiquitin-dependent sorting into the multivesicular body pathway requires the function of a conserved endosomal protein sorting complex, ESCRT-I. *Cell* 106, 145-155.

Lata, S., Schoehn, G., Jain, A., Pires, R., Piehler, J., Gottlinger, H.G., and Weissenhorn, W. (2008). Helical structures of ESCRT-III are disassembled by VPS4. *Science* 321, 1354-1357.

Lee, M.C., Orci, L., Hamamoto, S., Futai, E., Ravazzola, M., and Schekman, R. (2005). Sar1p N-terminal helix initiates membrane curvature and completes the fission of a COPII vesicle. *Cell* 122, 605-617.

Mim, C., Cui, H., Gawronski-Salerno, J.A., Frost, A., Lyman, E., Voth, G.A., and Unger, V.M. (2012). Structural basis of membrane bending by the N-BAR protein endophilin. *Cell* 149, 137-145.

Muziol, T., Pineda-Molina, E., Ravelli, R.B., Zamborlini, A., Usami, Y., Gottlinger, H., and Weissenhorn, W. (2006). Structural basis for budding by the ESCRT-III factor CHMP3. *Dev Cell* 10, 821-830.

Odorizzi, G., Babst, M., and Emr, S.D. (1998). Fab1p PtdIns(3)P 5-Kinase Function Essential for Protein Sorting in the Multivesicular Body. *Cell* 95, 847-858.

Robinson, J., Klionsky, D., Banta, L., and Emr, S. (1988). Protein sorting in *Saccharomyces cerevisiae*: isolation of mutants defective in the delivery and processing of multiple vacuolar hydrolases. *Mol Cell Biol* 8(11), 4936-4948.

Rossman, J.S., Jing, X., Leser, G.P., and Lamb, R.A. (2010). Influenza virus M2 protein mediates ESCRT-independent membrane scission. *Cell* 142, 902-913.

Sato, T.K., Darsow, T., and Emr, S.D. (1998). Vam7p, a SNAP-25-like molecule, and Vam3p, a syntaxin homolog, function together in yeast vacuolar protein trafficking. *Mol Cell Biol* 18, 5308-5319.

Sikorski, R.S., and Hieter, P. (1989). A system of shuttle vectors and yeast host strains designed for efficient manipulation of DNA in *Saccharomyces cerevisiae*. *Genetics* 22, 19-27.

Spitzer, C., Schellmann, S., Sabovljevic, A., Shahriari, M., Keshavaiah, C., Bechtold, N., Herzog, M., Muller, S., Hanisch, F.G., and Hulskamp, M. (2006). The *Arabidopsis* elch mutant reveals functions of an ESCRT component in cytokinesis. *Development* 133, 4679-4689.

Teis, D., Saksena, S., and Emr, S.D. (2008). Ordered assembly of the ESCRT-III complex on endosomes is required to sequester cargo during MVB formation. *Dev Cell* 15, 578-589.

Wollert, T., and Hurley, J.H. (2010). Molecular mechanism of multivesicular body biogenesis by ESCRT complexes. *Nature* 464, 864-869.

## CHAPTER III

### Structural Basis for Activation, Assembly and Membrane Binding of ESCRT-III Snf7 Filaments

Shaogeng Tang<sup>1,2</sup>, W. Mike Henne<sup>1,2,5</sup>, Peter P. Borbat<sup>3,4</sup>,  
Nicholas J. Buchkovich<sup>1,2,6</sup>, Jack H. Freed<sup>3,4</sup>, Yuxin Mao<sup>1,2</sup>,  
J. Christopher Fromme<sup>1,2</sup>, and Scott D. Emr<sup>1,2</sup>

<sup>1</sup> Weill Institute for Cell and Molecular Biology, Cornell University, Ithaca, NY 14853,  
USA

<sup>2</sup> Department of Molecular Biology and Genetics, Cornell University, Ithaca, NY 14853,  
USA

<sup>3</sup> National Biomedical Center for Advanced Electron Spin Resonance Technology  
(ACERT), Cornell University, Ithaca, NY 14853, USA

<sup>4</sup> Department of Chemistry and Chemical Biology, Cornell University, Ithaca, NY 14853,  
USA

<sup>5</sup> Present Address: Department of Cell Biology, The University of Texas Southwestern  
Medical Center, Dallas, TX 75390, USA

<sup>6</sup> Present Address: Department of Microbiology and Immunology, The Pennsylvania  
State University College of Medicine, Hershey, PA 17033, USA

Shaogeng Tang contributed significantly to all figures in this chapter (Figures 3.1-3.13), and wrote and prepared the manuscript.

Chapter III was originally published in *eLife* 4, (2015)

Tang, S., Henne, W.M., Borbat, P.P., Buchkovich, N.J., Freed, J.H., Mao, Y., Fromme, J.C., and Emr, S.D. (2015). Structural basis for activation, assembly and membrane binding of ESCRT-III Snf7 filaments. *eLife* 4.

DOI: 10.7554/eLife.12548.

## Abstract

The endosomal sorting complexes required for transport (ESCRTs) constitute hetero-oligomeric machines that catalyze multiple topologically similar membrane-remodeling processes. Although ESCRT-III subunits polymerize into spirals, how individual ESCRT-III subunits are activated and assembled together into a membrane-deforming filament remains unknown. Here, I determine X-ray crystal structures of the most abundant ESCRT-III subunit Snf7 in its active conformation. Using pulsed dipolar electron spin resonance spectroscopy (PDS), I show that Snf7 activation requires a prominent conformational rearrangement to expose protein-membrane and protein-protein interfaces. This promotes the assembly of Snf7 arrays with ~30Å periodicity into a membrane-sculpting filament. Using a combination of biochemical and genetic approaches, both *in vitro* and *in vivo*, I demonstrate that mutations on these protein interfaces halt Snf7 assembly and block ESCRT function. The architecture of the activated and membrane-bound Snf7 polymer provides crucial insights into the spatially unique ESCRT-III-mediated membrane remodeling.

## eLife Digest

A cell constantly remodels its surface to adapt to its environment, as well as to replace old or damaged proteins. To achieve this, cell-surface receptors are taken inside the cell and delivered to organelles called endosomes, where a molecular machine called ESCRT governs the receptors' fate. Distinct ESCRT complexes remodel the endosomal membrane to form vesicle packages that encapsulate the receptor proteins. These vesicles bud off into the endosome, which is then targeted to another organelle called the lysosome where the receptor proteins are degraded.

If the vesicles are unable to make their deliveries, the resulting sustained receptor activity can lead to numerous developmental and neurodegenerative diseases, as well as cancer. Remarkably, the ESCRT machinery also plays critical roles during cell division and the release of the human immunodeficiency virus (HIV) from host cells.

Previous studies demonstrated that a particular ESCRT complex, called ESCRT-III, forms spiraling filaments on membranes to generate vesicles. However, how the individual components of ESCRT-III assemble into such filaments was a mystery. Now, Tang et al. have determined the first X-ray crystal structures of the main component of ESCRT-III, a polymer of the protein called Snf7, and thus uncovered how these membrane-bound Snf7 spirals assemble.

Using a combination of cell biology, genetics and biochemistry techniques, Tang et al. also demonstrated that the Snf7 structures are necessary for ESCRT-III to work correctly inside living cells. Despite this achievement, key questions remain. The main one is how the other subunits of ESCRT-III interact and work together to remodel the membrane to form the vesicle packages at the endosomes.

## Introduction

The endosomal sorting complexes required for transport (ESCRTs) are membrane remodeling machinery that mediate diverse fundamental cellular processes, including the biogenesis of multivesicular body (MVB) during receptor down-regulation (Katzmann et al., 2001), enveloped virus budding (Garrus et al., 2001b), cytokinesis (Carlton and Martin-Serrano, 2007), plasma membrane repair (Jimenez et al., 2014), nuclear pore complex assembly (Webster et al., 2014), and nuclear envelope reformation (Olmos et al., 2015; Vietri et al., 2015). Originally identified using yeast genetics, ESCRTs package ubiquitinated transmembrane proteins into intraluminal vesicles (ILVs) that bud into the interior of the late endosome, creating a MVB that ultimately delivers cargos into the yeast lysosome (vacuole). The ESCRT pathway achieves receptor sorting through an elaborate division of labor. Upstream ESCRT components, ESCRTs-0, I, and II, assemble into stable hetero-multimers to sort ubiquitinated cargo on the endosomal surface by binding ubiquitin and endosomal lipid, phosphatidylinositol 3-phosphate (PI(3)P). In addition, ESCRT-II sets the architecture and initiates the assembly of the ESCRT-III complex, which together with Vps4 is responsible for remodeling endosomal membranes (Henne et al., 2011; Hurley and Hanson, 2010).

ESCRT-III is a unique protein complex in that it is metastable and conformationally dynamic, forming hetero-oligomeric filaments of multiple subunits on membranes (Saksena et al., 2009; Teis et al., 2008). Its subunits are inactive monomers in the cytoplasm, which activate and assemble into spiraling polymers on endosomes to drive cargo sequestration, membrane invagination and constriction

(Buchkovich et al., 2013; Hanson et al., 2008; Henne et al., 2012; Wollert and Hurley, 2010).

ESCRT-III is a hetero-polymer of four “core” subunits of Vps20, Snf7/Vps32, Vps24 and Vps2 (Babst et al., 2002a), and “accessory” subunits of Ist1, Did2/Vps46, Vps60 (Rue et al., 2008) and Chm7 (Horii et al., 2006). Although all ESCRT-III subunits share a common domain organization, each subunit appears to contribute a specific function. ESCRT-II directly engages Vps20 to trigger a sequential activation and ordered assembly of ESCRT-III subunits at endosomes (Teis et al., 2010). Vps20 nucleates the homo-oligomerization of the most abundant ESCRT-III subunit, Snf7, which then recruits Vps24 and Vps2 (Teis et al., 2008). Vps2 finally engages the Vps4 complex for ESCRT-III disassembly (Lata et al., 2008b; Obita et al., 2007), making individual subunits available for subsequent rounds of vesicle formation.

ESCRT-mediated membrane remodeling produces membrane curvature that pushes away from the cytoplasm, which is topologically opposite to that of the “classical” clathrin and COP-I/II vesicle budding reactions. This unique membrane bending topology highlights an ancient and central role of the ESCRT machinery in cellular remodeling events. However, due to the relative instability and heterogeneity of ESCRT-III polymers, high-resolution structural studies have generally been problematic. Structural work on Snf7 in particular has been difficult, due to its ability to assemble readily into polymers that interfere with crystallization. Ultimately, atomic-resolution structural information is necessary to understand how ESCRT-III achieves ordered assembly and membrane remodeling in diverse cellular pathways.

Even with limited structural information, previous studies have revealed distinct regions of Snf7 critical to ESCRT function. Snf7 contains a highly structured “core” domain of four  $\alpha$ -helices (Muziol et al., 2006). The C-terminus, in contrast, is less structured, including an  $\alpha$ -helix ( $\alpha$ 5) that folds back against the core domain *in cis* to mediate autoinhibition (Lata et al., 2008a), a microtubule interacting and transport (MIT)-interacting motif (MIM) for Vps4 recognition (Obita et al., 2007), and an  $\alpha$ -helix ( $\alpha$ 6) for Bro1/Alix interaction (McCullough et al., 2008) (Figure 3.1A).

How is Snf7 activated to promote ESCRT-III assembly? Numerous studies indicate that ESCRT-III subunits are activated by intramolecular conformational changes that promote protein-protein interactions (Henne et al., 2012; Lata et al., 2008a; Saksena et al., 2009; Schuh et al., 2015; Shen et al., 2014), but the structural basis for this is obscure. Available X-ray crystal structures of the autoinhibited Vps24 (Muziol et al., 2006) and Ist1 (Bajorek et al., 2009b; Xiao et al., 2009) suggest that these conformational changes involve the disruption of intramolecular interactions between the basic N-terminus and the acidic C-terminus. Upon releasing this autoinhibition, Snf7 subunits assemble into higher-order protofilaments or spirals (Cashikar et al., 2014; Hanson et al., 2008; Henne et al., 2012; Shen et al., 2014) with a range of different morphologies and dimensions.

Here, I present two X-ray crystal structures that unravel the molecular mechanism governing Snf7 conformational activation and polymer assembly. By selectively removing its autoinhibitory C-terminus, I determine the first crystal structure of the Snf7 core domain in the active conformation at 1.6 $\text{\AA}$  resolution. Surprisingly, rather than adopting a rigid four-helix coiled-coil, the core domain undergoes a large-

scale conformational rearrangement to extend into a highly elongated structure. This conformational change not only extends a cationic membrane-binding surface, but also exposes hydrophobic and electrostatic protein interacting surfaces for polymerization. *In vitro* reconstitution and pulsed dipolar electron spin resonance spectroscopy (PDS) demonstrate that full-length Snf7 adopts the same active conformation and assembles into ~30Å periodic protofilaments on a near-native lipid environment. Using negative stain transmission electron microscopy (TEM) and quantitative flow cytometry, I further demonstrate that mutations on key protein interfaces halt Snf7 assembly and block ESCRT function *in vivo*. Collectively, the molecular architecture of the activated and polymeric ESCRT-III Snf7 filament provides a detailed structural explanation for the mechanism underlying ESCRT-III-mediated membrane remodeling.

## Results

### X-ray Crystal Structure of Snf7<sup>core</sup>

Despite reconstituting and visualizing ESCRT-III assembly with the resolution of TEM, it was unclear how Snf7 is conformationally activated, and how this activation coordinates the assembly of Snf7 polymers on membranes. To answer these questions, I sought to determine the structure of Snf7 at atomic resolution.

Because Snf7 intermolecular interactions rely primarily on core-core and core-membrane interactions (Figure 3.1A) (Buchkovich et al., 2013; Henne et al., 2012), I purified Snf7<sup>core</sup> to homogeneity (Figures 3.2A-B). I then crystallized and solved X-ray crystal structures of Snf7<sup>core</sup> in two conformations at 1.6Å and 2.4Å resolutions, respectively. The structures were determined by molecular replacement using

CHMP4B<sup>α1-α2</sup> (PDB: 4ABM) (Table 3.1, Figures 3.2C-D). Although two conformations were determined, they share a similar overall tertiary structure with one notable exception discussed further below.

All previous ESCRT-III X-ray crystal structures adopt a canonical four α-helical core domain fold (Bajorek et al., 2009b; Muziol et al., 2006; Xiao et al., 2009). When I superimposed my Snf7 structure with available ESCRT-III structures (Figures 3.2E-H), I was surprised to note that Snf7<sup>core</sup> does not fold into four α-helices, but instead, it contains only three α-helices that pack into a highly elongated structure (Figures 3.1B-C). Although the α1/2 hairpin is relatively unchanged, α3 and α4 undergo large-scale structural rearrangements from the proposed autoinhibited ESCRT-III fold. α2 extends into a ~90Å long α-helix combining the α2 and α3 segments that were distinct α-helices in previously defined ESCRT-III structures (Figures 3.3A-B). The angle of the flexible loop between α3 and α4 also changes, which enables α4 to position in different orientations relative to the α1-3 hairpin. Despite the conformational change, I designated this elongated α-helix as α2/3 to maintain a consistent numbering scheme for conserved ESCRT-III helices.

### **Snf7 “Opening” Coupled with Endosomal Recruitment**

Previous studies suggested that a “closed” Snf7 becomes activated by the displacement of α5 away from the core domain (Henne et al., 2012; Lata et al., 2008a). Using a homology model of closed Snf7 (Henne et al., 2012) (Figure 3.3A), I identified close proximity between conserved residues Gln90 (α2) and Met130 (α4) in the four-helix coiled-coil (Figure 3.3C).

I applied a cysteine-based crosslinking strategy to directly monitor the conformational states of Snf7 *in vivo*. I mutated both Gln90 and Met130 to cysteines, and expressed this mutant in *snf7Δ* yeast (Figures 3.4A-C). Since conformationally active Snf7 resides on endosomal membranes, I performed subcellular fractionation and collected the supernatant (S13) and the membrane-enriched pellet (P13) fractions. Western blotting analysis showed that Snf7<sup>Q90C M130C</sup> migrated to ~37kDa, comparable to cysteineless Snf7. I then oxidized both fractions using copper(II) 1,10-phenanthroline. Strikingly, in the S13 fraction, ~50% of Snf7<sup>Q90C M130C</sup> migrated faster, indicating a conformationally closed Snf7 species. Notably, in the P13 fraction, the migration shift did not occur (Figures 3.3C-E). This is indicative of distinct conformations between the cytoplasmic and the endosome-bound states, and suggests that Snf7 on endosomal membranes adopts an open conformation in which α4 is displaced away from α2.

### Polymeric Snf7 Adopts the Open Conformation

To investigate Snf7 activation at a structural level, I applied the PDS technique of double electron-electron resonance (DEER) and monitored full-length Snf7 in solution and bound to liposomes. This work was done in collaboration with Peter P. Borbat and Jack H. Freed at the National Biomedical Center for Advanced Electron Spin Resonance Technology (ACERT), Cornell University. As an approach to characterize protein conformations (Borbat and Freed, 2007; Borbat and Freed, 2014; Jeschke, 2012), PDS can provide distance constraints with a range of ~10-90Å by measuring the magnitude of the dipolar coupling between spins of unpaired electrons in nitroxide spin labels (Hubbell et al., 2000). Snf7 assembles into spiraling protofilaments on

membranes, presenting two challenges: (1) to characterize the conformational state of Snf7 building blocks; and (2) to determine the protofilament assembly from these structural elements.

To determine whether Snf7 activation induces the “open” conformation observed by X-ray crystallography, I selected two solvent-accessible residues, Glu88 ( $\alpha$ 2) and His118 ( $\alpha$ 3), predicted to be separated by a short distance of 20 $\text{\AA}$  in the closed state (Figure 3.3G), and an expected longer distance of 45 $\text{\AA}$  in the open state (Figure 3.3H). I labeled these two sites with a nitroxide spin label, MTSL (Figure 3.3F), and then obtained the distance distribution for the full length Snf7 in solution. The result showed a wide distance spread of  $\sim$ 15-50 $\text{\AA}$  (Figure 3.3I), corresponding to large amplitude motions of the spin labeled positions, but not a distinct closed or open state. Thus, soluble Snf7 is structurally heterogeneous, suggesting that it is conformationally dynamic (Figures 3.4D-H).

To map the active conformation of Snf7, I reconstituted spin-labeled full-length Snf7<sup>R52E</sup> polymers on lipid membranes, where R52E is a previously characterized activation mutant that induces Snf7 polymerization (Henne et al., 2012). I mixed the double-labeled Snf7<sup>R52E E88C H118C</sup> proteins with liposomes and collected the membrane-bound Snf7 polymers by ultracentrifugation (Figure 3.3J). Intriguingly, membrane-bound Snf7<sup>R52E E88C H118C</sup> produced a strong  $\sim$ 30 $\text{\AA}$  peak. I also observed a significant population of distances at 40-50 $\text{\AA}$ , but diminished signal at  $\sim$ 20 $\text{\AA}$  (Figure 3.3K). I postulated that both the inter- and intra-subunit interspin distances contribute these signals. To isolate the intra-subunit interspin distance, I next produced magnetically diluted samples (Borbat and Freed, 2007; Dzikovski et al., 2011) by mixing double-

labeled Snf7<sup>R52E E88C H118C</sup> with unlabeled Snf7<sup>R52E</sup> in ratios ranging from 1:1 to 1:8. I observed that the signal changed significantly up to 1:2 dilution, then less for the maximal 1:8 dilution (Figures 3.3K and 3.6C-D), showing approach to the infinite dilution limit. The data for the 1:8 dilution is characteristic of a single long distance of 45Å with a moderate distance distribution, as expected for spin labels on an α-helix separated by 29 residues.

In summary, the reconstructed distance distributions are consistent with structural rearrangements that transform α2 and α3 into one continuous α-helix in the membrane-bound active conformation. As I did not observe short distances corresponding to the closed conformation, I conclude that only the open conformation is present in Snf7 polymers assembled on membranes. Therefore, the large-scale conformational rearrangement observed in the crystal structures is fully consistent with the PDS data of the full-length Snf7 conformations on the membranes.

### **Membrane-bound Snf7 Protofilaments Exhibit A ~30Å Periodicity**

While examining the arrangement of Snf7 molecules in the crystal lattice, I noted that multiple Snf7 protomers are arrayed into polymeric lattices, reminiscent of the protofilaments previously observed by TEM (Henne et al., 2012). Each of the ~100Å long α1-3 hairpin tilts by ~27° and polymerizes into a ~45Å diameter single protofilament, with each protomer exhibiting a repeat distance of ~30Å (Figure 3.5A).

The spacing of protomers in the crystal is also in agreement with my DEER results of the full-length Snf7 protofilaments assembled on liposomes. I performed a series of DEER measurements on the single-labeled protein at several key positions.

Specifically, I selected the middle of the  $\alpha$ 1-3 hairpin (Thr20, Lys35 and Glu88), and at both ends of  $\alpha$ 2/3 (Lys60 and His118), and the end of  $\alpha$ 4 (Gly140) to spin label Snf7. This allowed us to probe the interface between adjacent Snf7 protomers to establish their mutual orientation. Importantly, these cysteine-substituted Snf7 mutants are capable of assembling into protofilaments *in vitro* and do not impair MVB sorting *in vivo* (Figures 3.6E-F).

Consistent with the extensive amount of inter-molecular contacts revealed in the Snf7 crystal, I observed moderately broad distance distributions, specifically at 28-32 $\text{\AA}$  for T20C, K35C and E88C (Figures 3B-3C), and at 32-36 $\text{\AA}$  for K60C, H118C and G140C (Figures 3D-3E). The modulation depths of the time-domain echo signals indicate a ~3-spin system, in agreement with the crystalline arrangement of Snf7, where each protomer has two neighboring protomers. The magnetic dilution (Figures 3.6A-D) readily removed the intersubunit couplings, indicating that protofilaments do not make extensive contacts homogenous with each other.

Based on this series of single-cysteine DEER scanning and the double-cysteine magnetic dilution experiments, I conclude that Snf7 packing adopts a *parallel arrangement* in a single-layer array with a period of ~30 $\text{\AA}$ , and the reconstituted full-length Snf7 spirals on liposomes adopt a packing pattern similar to the Snf7<sup>core</sup> crystals. Thus, my X-ray crystal structures provide a foundation for in-depth study of the membrane-bound Snf7 polymer.

## **Snf7 Protomer Interactions in the Protofilament Require Two Interfaces**

In the Snf7 protofilament, the protomer (i) interacts with the next protomer (i+1) through both hydrophobic and electrostatic interactions (Figures 3.7A-B), burying  $\sim 1060\text{\AA}^2$  of solvent-accessible surface area per protomer. The assembly of the extended  $\alpha 2/3$  helix exposes a hydrophobic surface on  $\alpha 3$ , which was buried in the closed state. This enables the  $\alpha 2/3$  helix of protomer (i) to interact with  $\alpha 2/3$  of its neighboring protomer (i+1) (Figure 3.7C). Notably, Gln90, which interacts with Met130 *in cis* in the closed state, interacts with Met107 *in trans* in the open state.

To validate the interactions present in this hydrophobic interface, I performed site-directed mutagenesis and tested each mutant *in vivo* by an established quantitative MVB sorting assay (Buchkovich et al., 2013; Henne et al., 2012). This assay monitors the efficiency of fluorescence quenching after internalization and MVB sorting of Mup1-pH (the plasma membrane methionine transporter, Mup1, fused to the pH-sensitive GFP-derivative, pHluorin) (Figures 3.4B and 3.7E). As a result, mutants M104E, L101E, A97K, I94E, Q90K, M87E and T83E showed severe sorting defects, with sorting efficiencies from 12% to 76%, and mutants L121D, I117E, M114E, M107E, T103E and L99K from 7% to 34% (Figures 3.7F and 3.8G-J). Correspondingly, I previously demonstrated that the L121D mutant blocks Snf7 polymerization *in vivo* and *in vitro*, and missorts the MVB cargo carboxypeptidase S, Cps1 (Saksena et al., 2009). Furthermore, recombinant Snf7<sup>R52E Q90K</sup>, Snf7<sup>R52E I94E</sup>, Snf7<sup>R52E M107E</sup>, and Snf7<sup>R52E M114E</sup> proteins were able to be purified to homogeneity, but unable to generate protofilaments visible by TEM (Figures 3.7H and 3.8D).

I also observed electrostatic interactions between  $\alpha$ 1 of protomer (i) and  $\alpha$ 2/3 of protomer (i+1) (Figure 3.7D). This interaction is also dependent upon the extension of  $\alpha$ 2/3, and appears to be important for the positioning of  $\alpha$ 1 in the protofilament. To validate whether these inter-protomer electrostatic interactions occur *in vivo*, I generated and tested charge-inversion mutations,  $snf7^{R25E\ H29E\ K36E}$  and  $snf7^{E95K\ E102K\ E109K}$ , which resulted in severe sorting defects of 16% and 44%, respectively. Strikingly, when co-expressing both mutants *in trans*, MVB sorting was restored to 91% (Figures 3.7G, 3.8A-B and 3.8E-F). Consistently, Glu95 has been previously indicated to be involved in Snf7 inter-protomer contacts (Shen et al., 2014). These results are further supported by *ex vivo* crosslinking experiments. In the Snf7 polymer-enriched P13 fraction, cysteine-substituted Lys35 ( $\alpha$ 1) can be specifically crosslinked to cysteine-substituted Glu95 ( $\alpha$ 2) or Glu102 ( $\alpha$ 3) *in trans* (Figure 3.8C). Furthermore, co-incubating recombinant  $Snf7^{R52E\ R25E\ H29E\ K36E}$  and  $Snf7^{R52E\ E95K\ E102K\ E109K}$  proteins resulted in protofilament formation, but no protofilaments were detected when each mutant was tested individually (Figure 3.7H).

Altogether, these *in vivo* and *in vitro* data provide strong evidence that the observed hydrophobic and electrostatic interfaces are required for Snf7 polymerization *in vivo*, and that the Snf7 protofilament observed in the crystal lattice is physiologically relevant.

## The Snf7 Polymer Exposes A Cationic Membrane-binding Surface

I next mapped the previously determined Snf7 membrane-interacting region (Buchkovich et al., 2013) onto the Snf7 polymer structure (Figure 3.9A). Strikingly,

several key conserved lysine residues, K60 K64 K68 K71 K79 ( $\alpha$ 2), and K112 K115 ( $\alpha$ 3), which were in distinct  $\alpha$ -helices in the closed state, are arranged on an elongated and solvent-exposed surface ideal for interacting with the acidic endosomal membrane. The electrostatic membrane-binding regions of all Snf7 protomers face the same direction in the polymer, allowing for a continuous membrane-binding interface (Figure 3.9B). Thus, the crystal structure of Snf7 polymers reveals a mechanism for coupling polymerization to stable membrane association.

Notably, ESCRT-III subunits utilize multiple hydrophobic and electrostatic interfaces to interact with endosomal membranes (Buchkovich et al., 2013). Consistent with this, I observed that  $\alpha$ 1 of Snf7 is moderately positively charged (Figure 3.1C), and cannot rule out that at some stage of vesicle biogenesis it also comes in contact with the membrane.

#### **$\alpha$ 4 Bridges Two Snf7 Protofilaments**

Comparison of my Snf7<sup>core</sup> crystal structures I determined revealed two distinct conformations. Although both structures exhibit an open conformation, I noted two different orientations of  $\alpha$ 4 with respect to the  $\alpha$ 1/2 hairpin. In open conformation A,  $\alpha$ 4 extends in the protofilament plane, whereas in open conformation B,  $\alpha$ 4 is positioned perpendicular to the protofilament plane. Superimposing the two conformations revealed that  $\alpha$ 4 can rotate by at least  $\sim 90^\circ$  along the axis of the  $\alpha$ 2/3 helix (Figures 3.10A-B). Despite the large differences in  $\alpha$ 4 positioning,  $\alpha$ 4 makes a similar interaction with the  $\alpha$ 1/2 hairpin of a Snf7 protomer in a neighboring protofilament in both structures (Figures 3.10C and 3.11D). This supports a model in which the assembly of the

extended  $\alpha$ 2/3 helix upon Snf7 activation results in two key events: (1)  $\alpha$ 4 can no longer bind *in cis* to its own protomer; (2)  $\alpha$ 5 is displaced from the  $\alpha$ 1/2 hairpin. Together, this enables  $\alpha$ 4 to contact the  $\alpha$ 1/2 hairpin of another protomer *in trans* on a neighboring protofilament.

Consistent with the DEER data that two Snf7 protofilaments do not make extensive contacts with each other and do not assemble into homogeneous arrangements, this interfilamental interface only buries  $474\text{\AA}^2$  of solvent-accessible surface area per protomer. To test whether these observed interfilamental interactions were functionally important, I mutated residues at their  $\alpha$ 1/2<sup>i</sup>- $\alpha$ 4<sup>j</sup> interface (Figures 3.10D-E). Notably, Met130, which interacts with Gln90 in the closed state, is involved in this interface in the open state. Snf7 mutants of A51E, L55E, L67E, V126E, M130E and I133E led to drastic loss-of-function, with sorting efficiencies from 9% to 55% *in vivo*, and were unable to assemble into protofilaments *in vitro* (Figures 3.10F and 3.11A-C).

To gain insights into the importance of the local rearrangement of the Snf7  $\alpha$ 3/4 loop *in vivo*, I mutated the conserved  $\alpha$ 3/4 loop residue Leu121 to Pro to constrain the rotational angle between  $\alpha$ 3 and  $\alpha$ 4. The L121P mutant exhibited a MVB sorting efficiency of 32%, compared to that of the  $\alpha$ 1/2 loop residue Asn59 mutant N59P of 75% (Figure 3.11E), suggesting that the  $\alpha$ 3/4 loop functions as an important flexible “hinge” that may facilitate different architectural stages of Snf7 polymers (Figures 3.10C and 3.11F-G).

Interestingly, studies have previously shown that the tip of the  $\alpha$ 1/2 hairpin is important for intra- and inter-molecular contacts of ESCRT-III subunits. For example, X-ray crystal structures of CHMP3 and IST1 are autoinhibited through an intramolecular

contact between the  $\alpha$ 1/2 hairpin and  $\alpha$ 5 (Figure 3.11H) (Bajorek et al., 2009b; Muziol et al., 2006); and the Ist1-Did2 co-crystal structure revealed that the MIM1 of CHMP1B forms an intermolecular contact with the  $\alpha$ 1/2 hairpin of Ist1 (Xiao et al., 2009).

### **Conserved Snf7 Protein-protein and Protein-membrane Interfaces**

To gain insights into any functionally important surfaces on the Snf7 structure, I performed CONSURF analysis (Celniker et al., 2013). As a result, I identified seven highly conserved regions in the Snf7<sup>core</sup> domain (Figures 3.12A and 3.13A). Strikingly, all of them map to regions of Snf7 assigned specific functions in either polymer assembly or membrane interaction: regions (1) and (2) are located on opposite sides of the extended  $\alpha$ 2/3 helix and stabilize intrafilamental protein-protein interactions; region (3) is located towards the amino-terminus of  $\alpha$ 1 and region (4) towards the middle of the  $\alpha$ 2/3 helix, forming the intrafilamental electrostatic interacting surfaces; region (5) corresponds to the beginning of  $\alpha$ 2, which I previously identified as a cationic membrane-binding surface; regions (6) and (7) are the tip of the  $\alpha$ 1/2 hairpin and the hydrophobic side of  $\alpha$ 4, which together stabilize interfilamental interactions. Thus, the Snf7 protein-protein interactions revealed from my X-ray crystal structures and the protein-membrane interactions previously identified (Buchkovich et al., 2013) are evolutionarily conserved.

### **A Linear Snf7 Filament Transformed into A Superhelix**

A linear Snf7 filament has a simple two-dimensional geometry, and thus is incapable of mediating the drastic three-dimensional membrane remodeling required for

membrane deformation and vesicle formation at the endosome (Figure 3.13B). Since Snf7 can form spirals on a membrane surface, I asked how a linear Snf7 filament (Figures 3.12C-D and 3.13D) could be transformed into a circular array. Due to the heterogeneity of a Snf7 double filament, I utilized a single linear Snf7 filament to determine a plausible curved Snf7 filament using normal mode analysis (NMA), a simple non-detailed simulation technique used to probe large-scale macromolecular motions by assessing flexibility intrinsic to the structure of a protein (Suhre and Sanejouand, 2004). Remarkably, without any dramatic structural rearrangement within each protomer or alterations of the protein-protein interface, a linear two-dimensional Snf7 filament can bend into a ~70nm diameter three-dimensional superhelix with turn length of ~62nm, reminiscent of the structure of the Snf7/Vps24/Vps2 co-assembly previously observed (Henne et al., 2012) (Figure 3.12D). Importantly, this 3D helical array aligns the cationic membrane-binding surfaces on the outside of the superhelix, ideal for a Snf7 polymer to stabilize a negatively curved membrane surface (Figure 3.13E).

## Discussion

The ESCRT-III machinery plays a critical role in numerous fundamental cellular processes, including MVB biogenesis, viral budding and cytokinesis, indicating an ancient and conserved membrane remodeling mechanism. The importance of understanding this mechanism is bolstered by the fact that this is so distinct from all other well characterized membrane budding processes (e.g. clathrin and COP-I/II), which invariably bud into the cytoplasm. Although the membrane-bound ESCRT-III

polymers have been reconstituted *in vitro*, the mechanisms governing the polymer assembly and how ESCRT-III coordinates membrane remodeling, remain poorly understood. Here, I focused on Snf7, the predominant ESCRT-III component, in order to fundamentally understand how it achieves membrane remodeling. Using a multi-disciplinary approach that combined X-ray crystallography, PDS, genetics, biochemistry and TEM, I reveal key structural features of Snf7 that allow its dynamic conversion from a soluble monomer to a membrane-bound polymer.

Specifically, this study provides, for the first time, atomic-resolution structures of a conformationally “open” and assembled ESCRT-III subunit, and report the first application of PDS to characterize the internal organization of protein polymers assembled on a near-native lipid environment. These Snf7 subunits assemble into remarkable linear arrays upon conformational activation, thus providing a structural explanation for the Snf7 spiraling protofilaments previously observed by TEM and mechanistic insights into the spiral-mediated membrane deformation and vesicle formation.

### **Snf7 Core Domain Rearrangement Required for Protein-membrane and Protein-protein Interactions**

A classic model of ESCRT-III activation involves the disruption of intramolecular interactions between  $\alpha 5$  and the core domain (Henne et al., 2012; Lata et al., 2008a). In the present study, I provide surprising structural evidence that this activation requires further rearrangement within the core domain itself. Consistent with the available CHMP4B $^{\alpha 1/2}$  structure (Martinelli et al., 2012),  $\alpha 1/2$  folds into a rigid ~70Å  $\alpha$ -helical

hairpin, which forms intramolecular contacts with at least three short  $\alpha$ -helices,  $\alpha$ 3,  $\alpha$ 4, and  $\alpha$ 5 in the closed state. Notably, upon activation, all of these interactions are reorganized to extend the hairpin to a  $\sim$ 90 $\text{\AA}$  structure available for intermolecular contacts. Comparison of the closed and open states reveals that  $\alpha$ 4 is displaced by  $\sim$ 60 $\text{\AA}$  as the molecule opens. Intriguingly, a recent small-angle X-ray scattering (SAXS) study showed that Vps20 exists as a 94 $\text{\AA}$  extended “open” conformation but it is incapable of homo-polymerization (Schuh et al., 2015).

Based on these structural insights, I propose a detailed “lifecycle” of Snf7 activation and polymerization: 1) In the cytoplasm, Snf7 exists in a dynamic equilibrium of mixed intermediates between the open and closed states; 2) on endosomes, Vps20  $\alpha$ 1 directly associates with the ESCRT-II subunit Vps25 (Im et al., 2009), allowing Vps20 to function as a nucleator to engage an open Snf7 from the cytoplasm (Figure 3.12B); 3) the open conformation of Snf7 with an extended  $\alpha$ 2/3 helix presents a cationic membrane-interacting surface to orient itself on endosomes; 4) the N-terminal membrane ANCHR motif further stabilizes Snf7 on the endosomal surface (Figure 3.13C); 5) the endosomal recruitment shifts the conformational equilibrium and thus triggers a “domino effect” of Snf7 opening and promotes Snf7 polymerization into a  $\sim$ 30 $\text{\AA}$  periodic array of ordered inter-protomer contacts. In agreement with this, an averaged 32.5 $\text{\AA}$  inter-subunit distance was observed in *C. elegans* Vps32 spirals (Shen et al., 2014).

Because X-ray crystal structures of both Vps24 (Muziol et al., 2006) and Ist1 (Bajorek et al., 2009b) were determined in their autoinhibitory conformations with an unresolved “linker” between the core and  $\alpha$ 5, the four-helix core domain has been

treated as a rigid body that remains unaltered between the open and closed states. However, a previous SAXS study suggested that Vps24 can adopt both a 75Å globular and a 105Å extended conformation (Lata et al., 2008a), implying that the core domain extension may be a common theme of ESCRT-III activation. Due to this unexpected conformational change, previous ESCRT-III polymer studies using the “closed” conformation as a building unit may need careful reevaluation.

### **Comparison of ESCRT-III Filaments with Other Membrane-Remodeling Polymers**

The ESCRT-III Snf7 filament-mediated membrane remodeling is conceptually reminiscent of other membrane remodeling machinery, including bacterial FtsZ (Osawa et al., 2008). Interestingly, both Snf7 and FtsZ/FtsA can drive cytokinetic abscission, and they share at least three distinct structural characteristics: electrostatic protein-membrane interactions, membrane insertion of an amphipathic helix, and oligomeric protein scaffolding.

Despite these similarities, the major difference between FtsZ and Snf7 is that FtsZ requires nucleotide hydrolysis to drive its conformational dynamics. The propagation of conformational changes in the FtsZ polymer is thus coupled with the architectural changes that promote membrane fission. In contrast, ESCRT-III does not bind nor hydrolyze nucleotides to regulate its conformation, but it recruits the AAA-ATPase Vps4 for its disassembly. Although Snf7 can be activated by specific point mutations *in vitro*, the conformational switching *in vivo* appears to be tightly regulated by other ESCRT components to prevent pre-mature polymer assembly.

During MVB biogenesis, ESCRT-II binds two copies of Vps20, which then nucleates the homo-oligomerization of Snf7. However, in enveloped viral budding and cytokinetic abscission, Bro1/Alix directly bridges ESCRT-I to ESCRT-III, by binding to the C-terminal  $\alpha$ 6 of Snf7 (McCullough et al., 2008). I speculate that this interaction may directly dissociate the C-terminal autoinhibitory region to trigger Snf7 polymer assembly. Furthermore, CHMP7 was recently shown to trigger Snf7 assembly during nuclear envelope reformation (Vietri et al., 2015), highlighting the distinct spatial and temporal regulation of Snf7 activation between different ESCRT-dependent processes.

### **A Curved ESCRT-III Filament Mediates Membrane Remodeling**

ILVs that bud into the endosomal lumen contain no outer vesicle coat, yet show consistent diameters, suggesting ESCRTs regulate vesicle size. Somewhat paradoxically, ESCRT-III cannot shape the vesicle exterior because it is segregated in the cytoplasm by the limiting membrane of the endosome. Instead, the ESCRT-III filament appears to predominantly drive membrane deformation by sculpting the neck interior of a growing vesicle. This membrane sculpting requires an intricate balance of competing curvatures. Snf7 has been shown to localize to both the curved necks of invaginations and along highly curved edges of membranes (Buchkovich et al., 2013; Fyfe et al., 2011; Wollert and Hurley, 2010) (Figure 3.13F). My study and other studies in the field on Snf7 address the balance of membrane curvatures associated with ILV formation. The ANCHR motif of Snf7 acts to sense and stabilize the positively curved rim of the invagination (Figure 3.13C). Coinciding with this positive curvature stabilization, the helical Snf7 polymer acts as a circular scaffold that triggers and

stabilizes the negatively curved circumference of the neck of the invagination (Figure 3.13E). I propose that as a two-dimensional ESCRT-III spiral elongates into a three-dimensional superhelix, the tight membrane binding of the “corkscrew” concentrates transmembrane cargoes ahead of the leading edge of the forming and narrowing filament, packaging them into the nascent ILV (Figure 3.13B).

Despite the reconstitution and high-resolution analysis of Snf7 polymers, key questions remain. The most pressing are the mechanisms governing inter-ESCRT-III subunit interactions, particularly, Vps24 and Vps2, required for the ESCRT-III architectural changes, and a precise mechanochemical role of the AAA-ATPase Vps4 complex during the final membrane constriction and scission coupled with ESCRT-III disassembly. Additional structural studies together with new assays are necessary for further addressing these challenging but exciting questions.

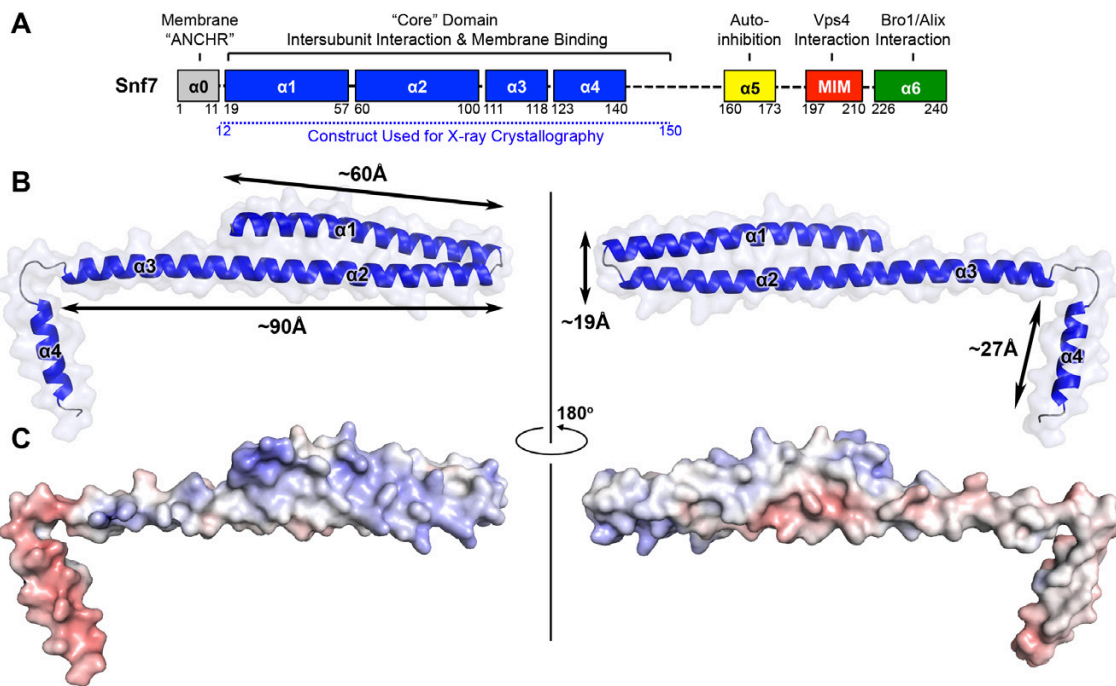


**Figure 3.1 X-ray Crystal Structure of Snf7<sup>core</sup>**

**Figure 3.1 X-ray Crystal Structure of Snf7<sup>core</sup>**

(A) The domain organization of Snf7. The core domain used for X-ray crystallography is shown in blue.

(B) Overlay of ribbon and space-filling models of the X-ray crystal structure of Snf7<sup>core</sup>.

(C) Electrostatic surface potential of Snf7<sup>core</sup> with positively charged regions in blue (+10kcal/e<sup>-</sup>) and negatively charged regions in red (-10kcal/e<sup>-</sup>).

See also Table 3.1.

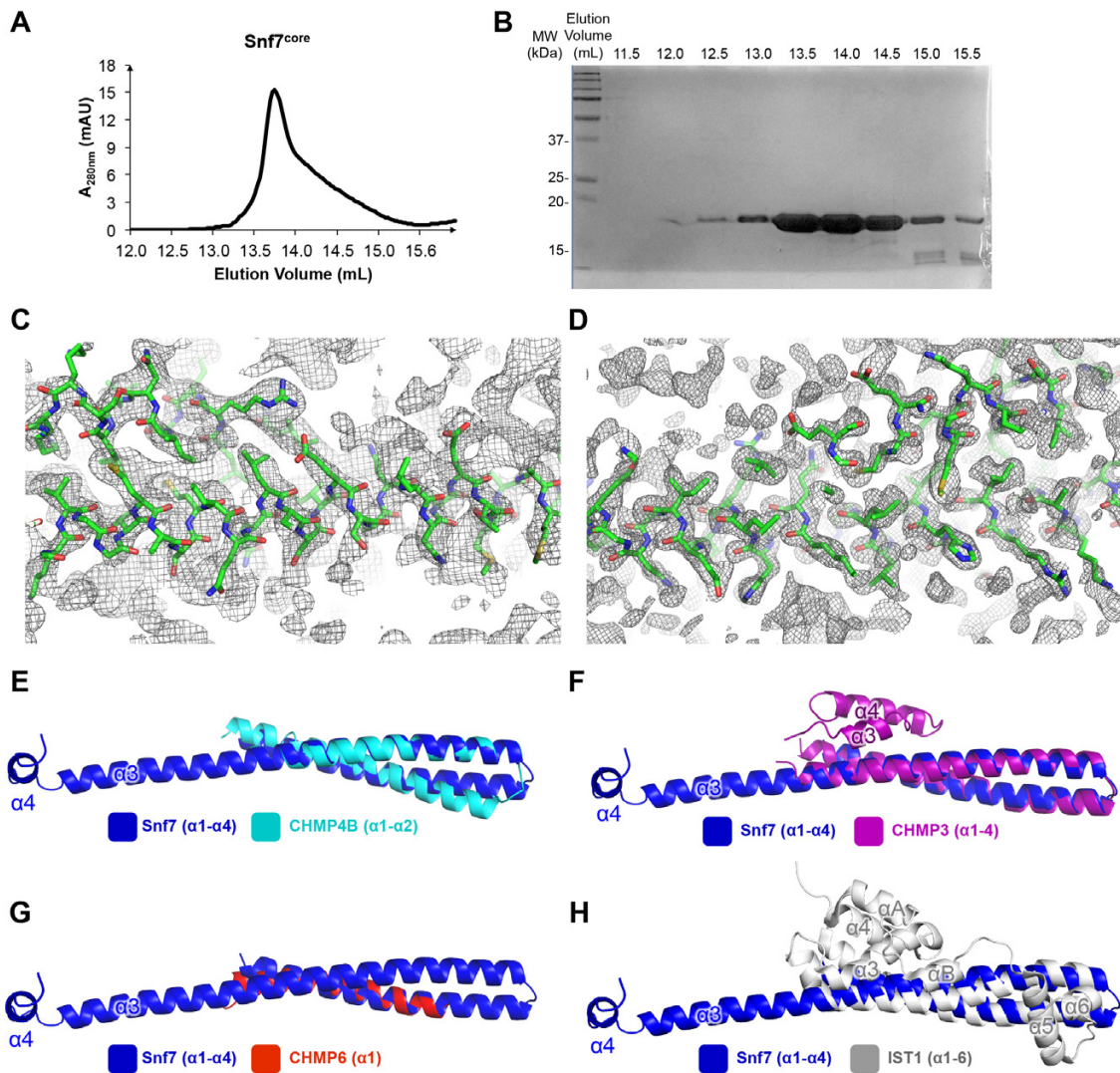


**Figure 3.2 Superimposition of Snf7<sup>core</sup> with Available ESCRT-III Structures**

**Figure 3.2 Superimposition of Snf7<sup>core</sup> with Available ESCRT-III Structures**

- (A) A superdex-200 gel filtration size exclusion chromatogram of Snf7<sup>core</sup>.  
(B) A SDS-PAGE Coomassie brilliant blue staining of the gel filtration fractions corresponding to Snf7<sup>core</sup>.  
(C-D) 2Fc-Fo simulated-annealing composite-omit electron density maps contoured at 1.0 $\sigma$  of Snf7 open conformations (C) A and (D) B.  
(E-H) Superimposing Snf7<sup>core</sup> (blue) with (E) CHMP4B <sup>$\alpha$ 1- $\alpha$ 2</sup> (cyan) (PDB: 4ABM), with (F) CHMP3 <sup>$\alpha$ 1- $\alpha$ 4</sup> (purple) (PDB: 3FRT), with (H) CHMP6 <sup>$\alpha$ 1</sup> (red) (PDB: 3HTU) Snf7<sup>core</sup>, and with (H) IST1 <sup>$\alpha$ 1- $\alpha$ 6</sup> (grey) (PDB: 3FRR).

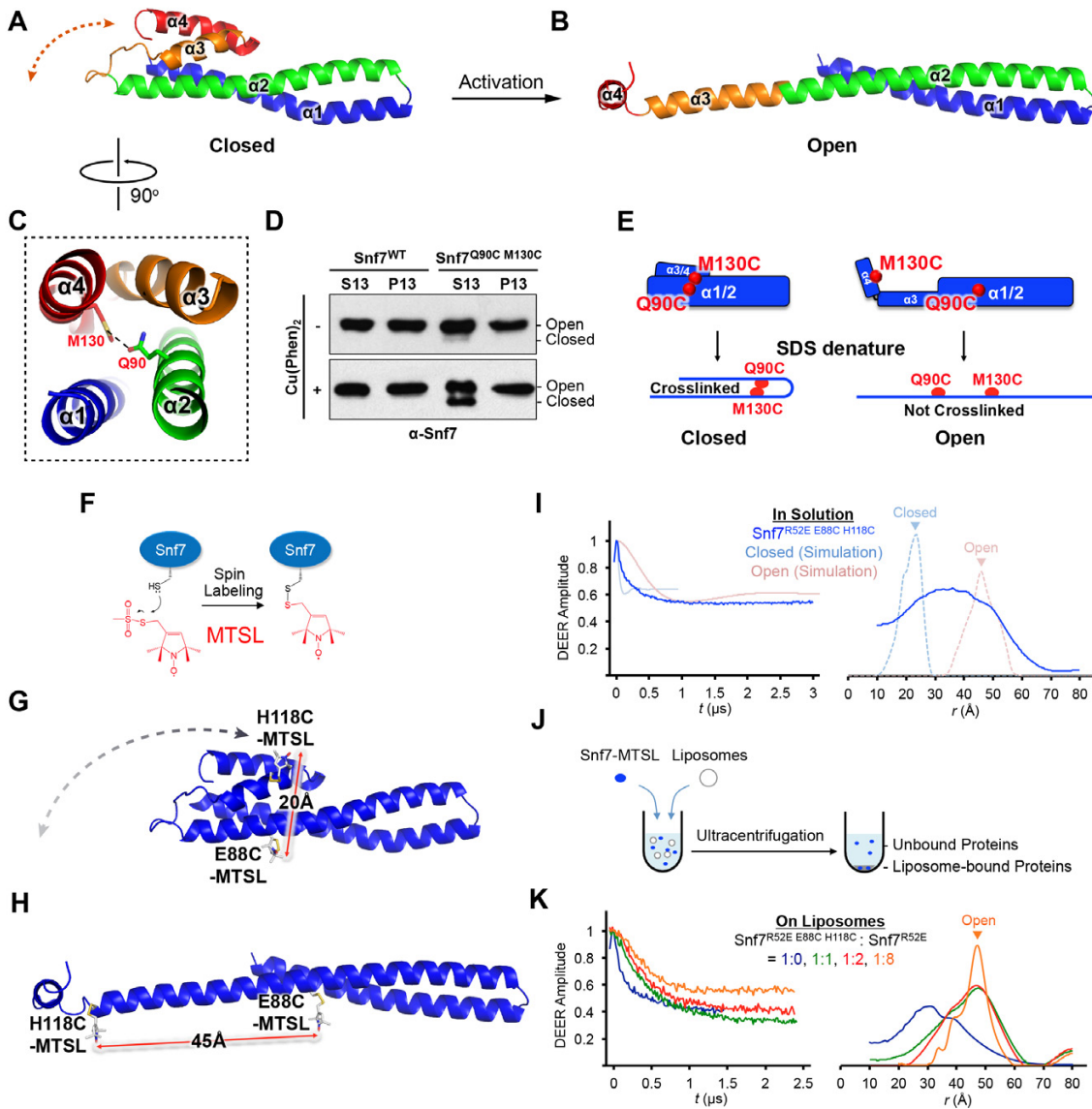


### Figure 3.3 Conformational Rearrangement of Snf7

### Figure 3.3 Conformational Rearrangement of Snf7

(A-B) Ribbon diagrams of (A) a homology model of closed Snf7<sup>core</sup> (Henne et al., 2012) and (B) the X-ray crystal structure of open Snf7<sup>core</sup>.

(C) A close-up view of the side chain interaction between Gln90 and Met130.

(D) Western blotting and subcellular fractionation of snf7Δ yeast exogenously expressing SNF7 or snf7<sup>Q90C M130C</sup> with and without copper(II) 1,10-phenanthroline.

(E) Schematic showing closed and open Snf7<sup>core</sup> with cysteines (red dots) before and after SDS-denaturing.

(F) Snf7 site-directed spin-labeling with MTSL (red).

(G-H) Distance between Glu88 and His118 of (G) closed and (H) open Snf7 shown in ribbon.

(I & K) Time domain signals and distance distributions from DEER spectroscopy of (I) Snf7<sup>R52E E88C H118C</sup> in solution, and simulated closed and open Snf7<sup>core E88C H118C</sup> using MMM, and (K) Snf7<sup>R52E E88C H118C</sup>. Snf7<sup>R52E</sup> (1:0, 1:1, 1:2, and 1:8) with liposomes.

(J) Schematic showing liposome sedimentation for DEER. MTSL-labeled Snf7 proteins (blue oval) and liposomes (grey circle).

\* Peter P. Borbat generated Cys-MTSL substituted protein data bank (PDB) files used in Figures 3.3G and H, and performed DEER simulation in Figure 3.3I. Peter P. Borbat and I together performed DEER experiments shown in Figures 3.3I and K.

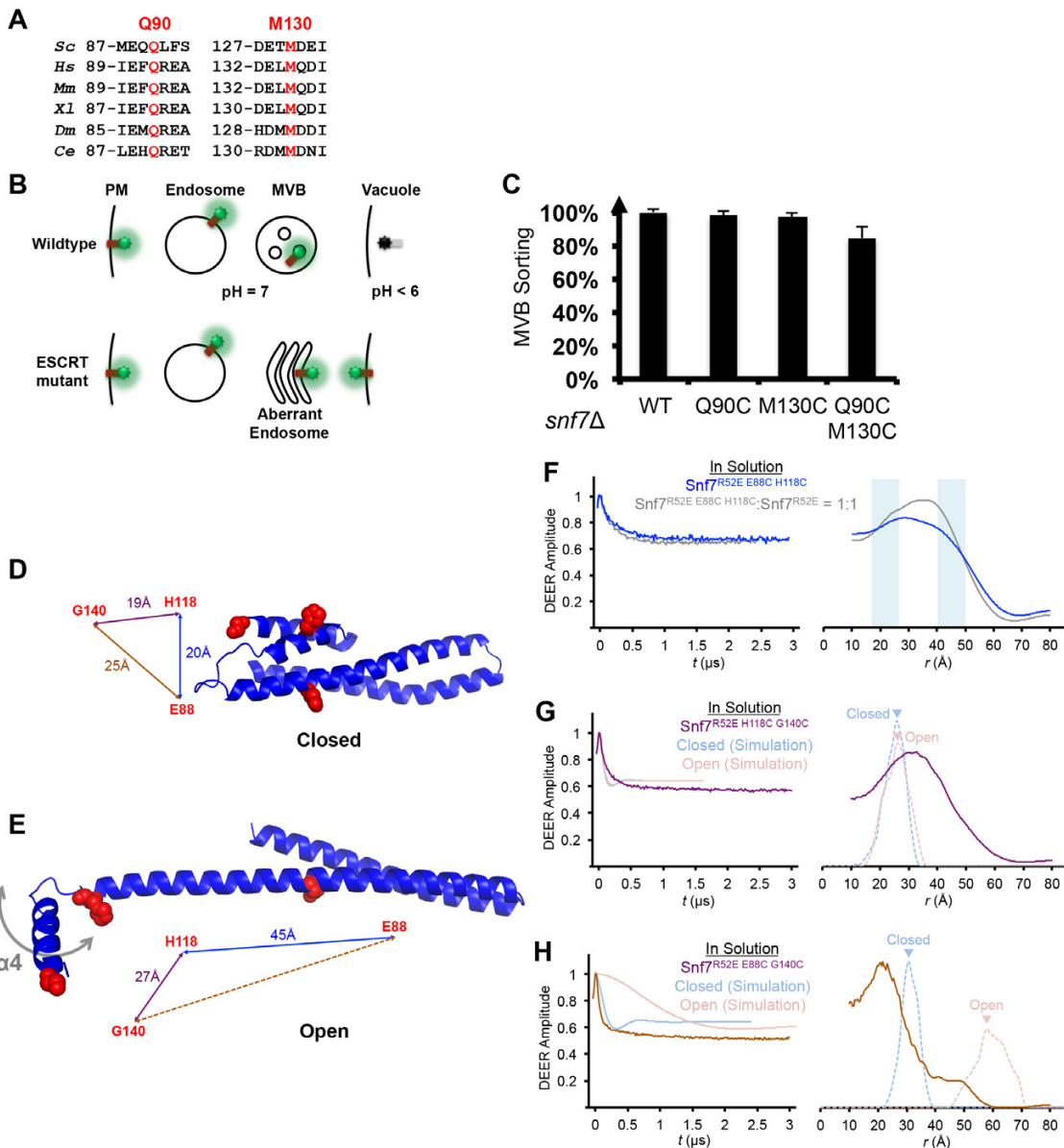
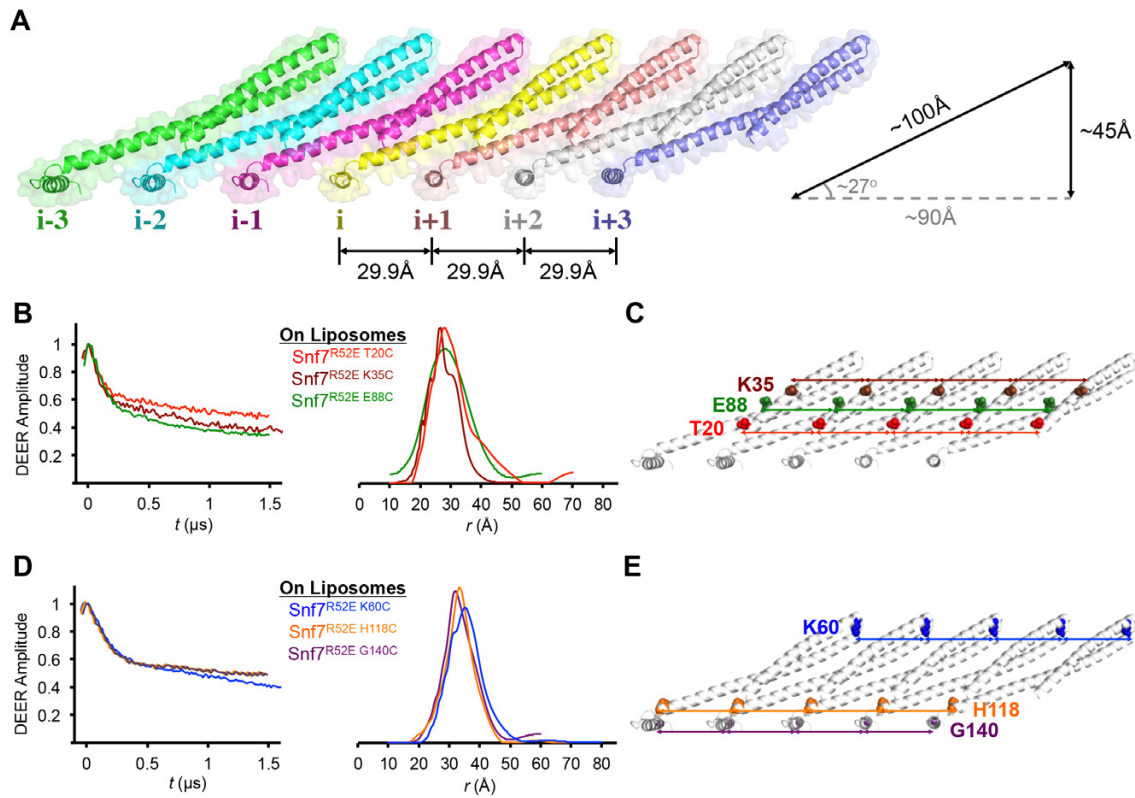


Figure 3.4 DEER Analysis of Snf7 Core Domain Rearrangement

### Figure 3.4 DEER Analysis of Snf7 Core Domain Rearrangement

- (A) Sequence alignments of Snf7  $\alpha$ 2 and  $\alpha$ 4, with conserved Gln90 and Met130 shown in red.
- (B) Conceptual model for the Mup1-pHluorin MVB sorting assay.
- (C) Quantitative MVB sorting data for  $snf7\Delta$  yeast exogenously expressing  $SNF7$ ,  $snf7^{Q90C}$ ,  $snf7^{M130C}$ , and  $snf7^{Q90C\ M130C}$ . Error bars represent standard deviations.
- (D-E) Ribbon models of (D) closed and (E) open Snf7 showing inter-residue distances between E88, H118 and G140.
- (F-H) Time domain signals and distance distributions from DEER spectroscopy of (F)  $Snf7^{R52E\ E88C\ H118C\ G140C}$ , and  $Snf7^{R52E\ E88C\ H118C}$ :  $Snf7^{R52E}$  (1:1) in solution, (G)  $Snf7^{R52E\ H118C\ G140C}$  in solution and simulated closed and open  $Snf7^{H118C\ G140C}$  using *MMM*, and (H)  $Snf7^{R52E\ E88C\ G140C}$  in solution and simulated closed and open  $Snf7^{E88C\ G140C}$  using *MMM*. Blue shaded portions of the distributions indicate distance ranges that can be attributed to open and closed conformations.

\* Peter P. Borbat performed DEER simulation in Figures 3.4F-H. Peter P. Borbat and I together performed DEER experiments shown in Figures 3.4F-H.



**Figure 3.5 Membrane-bound Snf7 Filament with ~30 Å Periodicity**

### **Figure 3.5 Membrane-bound Snf7 Filament with ~30Å Periodicity**

(A) Overlay of ribbon and space-filling models of a 7-mer Snf7 protofilament with measured dimensions.

(B & D) Time domain signals and distance distributions from DEER spectroscopy of (B) full-length Snf7<sup>R52E T20C</sup>, Snf7<sup>R52E K35C</sup>, and Snf7<sup>R52E E88C</sup> with liposomes, (D) full-length Snf7<sup>R52E K60C</sup>, Snf7<sup>R52E H118C</sup>, and Snf7<sup>R52E G140C</sup> with liposomes.

(C & E) Schematic showing the spin label positions in a Snf7 protofilament.

\* Peter P. Borbat and I together performed DEER experiments shown in Figures 3.4B and D.

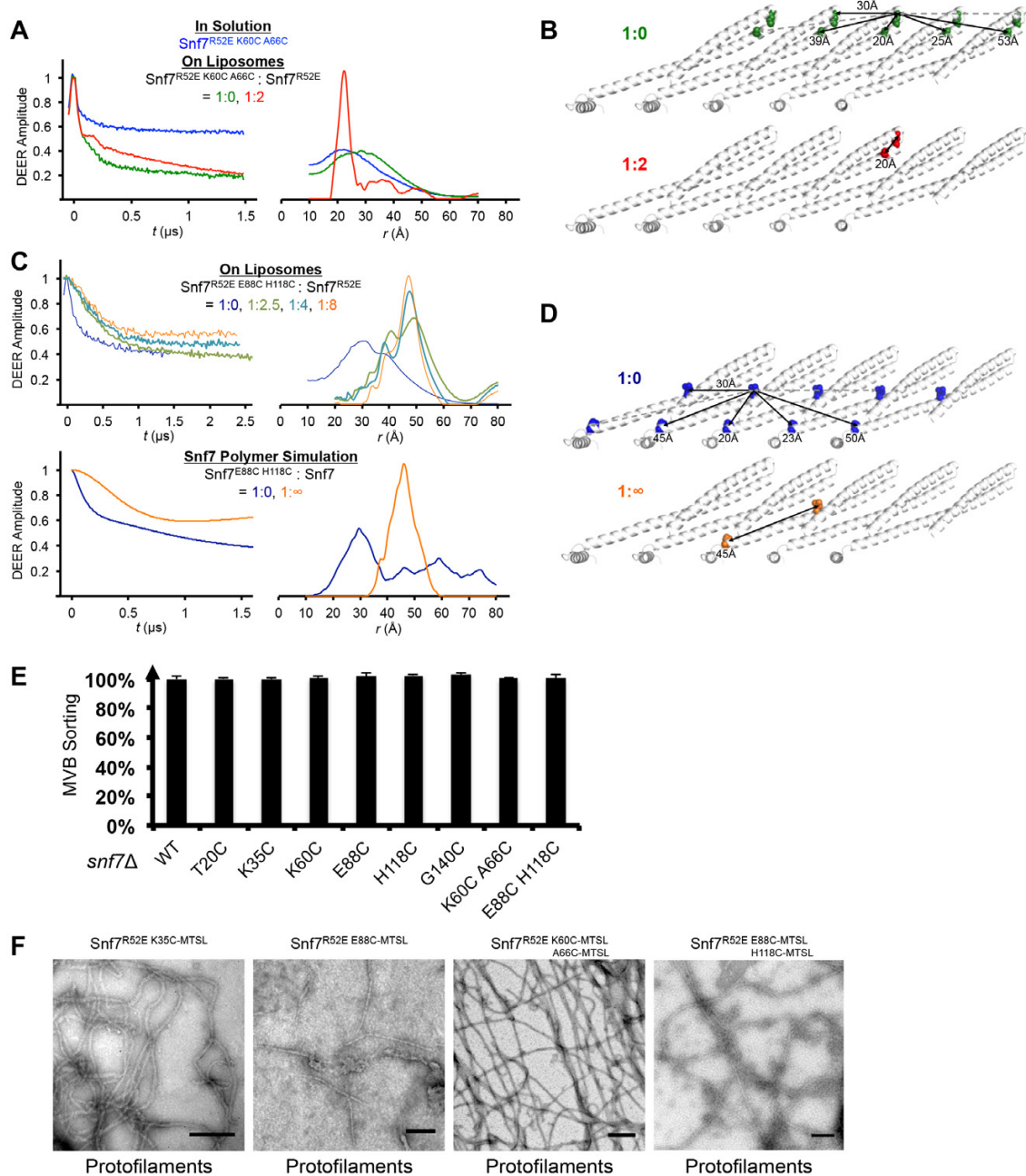


**Figure 3.6 DEER Analysis of Snf7 Filament**

### Figure 3.6 DEER Analysis of Snf7 Filament

(A & C) Time domain signals and distance distributions from DEER spectroscopy of (A) Snf7<sup>R52E K60C A66C</sup> in solution and Snf7<sup>R52E K60C A66C</sup> : Snf7<sup>R52E</sup> (1:0, 1:2) with liposomes, and (C, upper) Snf7<sup>R52E E88C H118C</sup> : Snf7<sup>R52E</sup> (1:0, 1:2.5, 1:4, 1:8) with liposomes, and (C, lower) simulated Snf7<sup>E88C H118C</sup> : Snf7 (1:0, 1:  $\infty$ ) polymers using *MMM*.

(B & D) Schematic showing the locations of the spin label positions in a Snf7 protofilament.

(E) Quantitative MVB sorting data for *snf7Δ* yeast exogenously expressing SNF7, snf7<sup>T20C</sup>, snf7<sup>K35C</sup>, snf7<sup>K60C</sup>, snf7<sup>E88C</sup>, snf7<sup>H118C</sup>, snf7<sup>G140C</sup>, snf7<sup>K60C A66C</sup> and snf7<sup>E88C H118C</sup>. Error bars represent standard deviations.

(F) Representative TEM images of recombinant Snf7<sup>R52E K35C</sup>, Snf7<sup>R52E E88C</sup>, Snf7<sup>R52E K60C A66C</sup>, and Snf7<sup>R52E E88C H118C</sup> labeled with MTSL. Scale bars, 200nm.

\* Peter P. Borbat performed DEER simulation in Figures 3.6C. Peter P. Borbat and I together performed DEER experiments shown in Figures 3.4A and C.

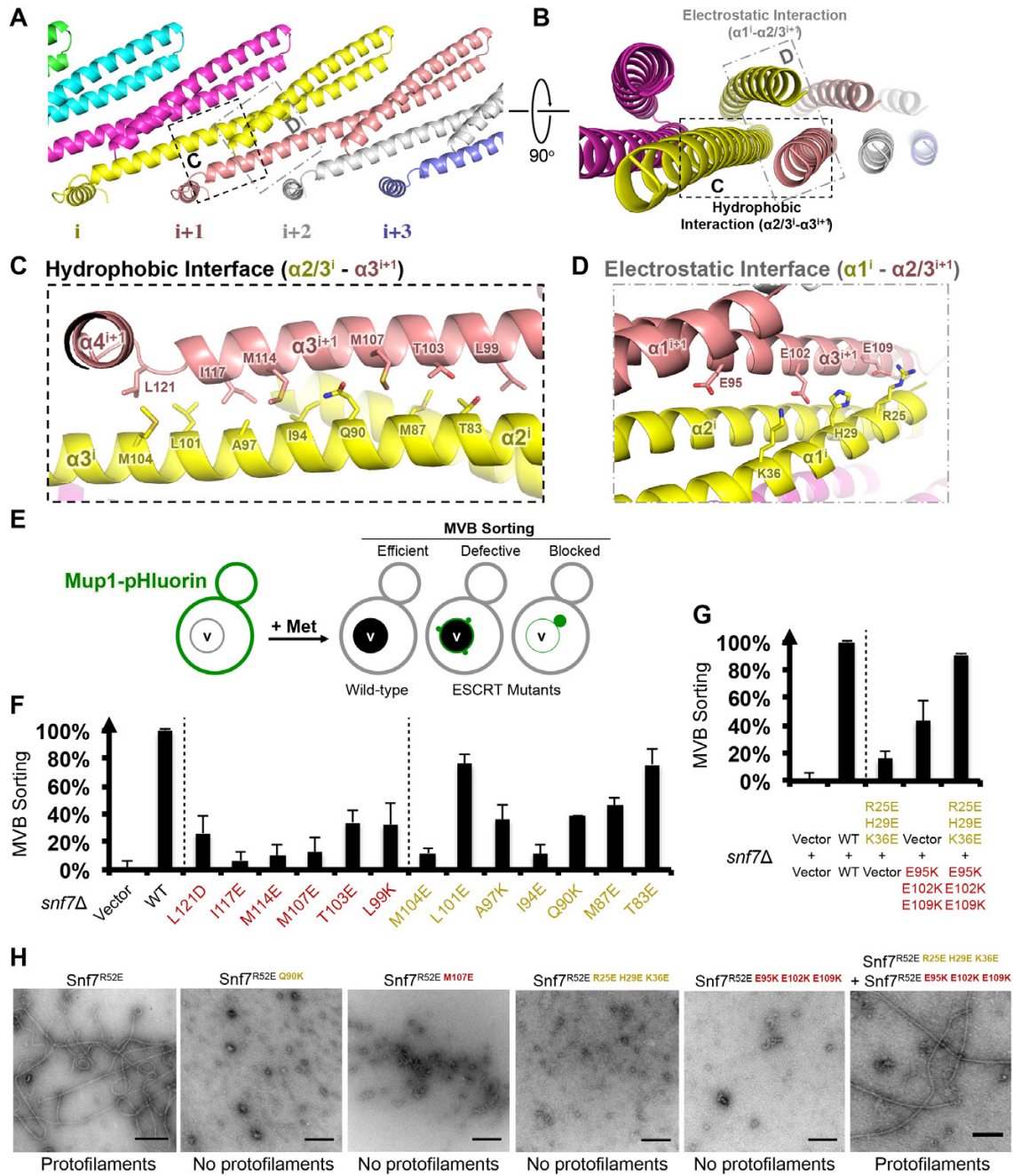


**Figure 3.7 Hydrophobic and Electrostatic Interactions in a Snf7 Filament**

### Figure 3.7 Hydrophobic and Electrostatic Interactions in a Snf7 Filament

(A-B) Ribbon models of a Snf7 protofilament. The hydrophobic protein interface is shown in black dash-line and the electrostatic interface in grey dash-dot line.

(C-D) Close-up views of the hydrophobic interface between  $\alpha_2/\alpha_3^i$  and  $\alpha_3^{i+1}$  and the electrostatic interface between  $\alpha_1^i$  and  $\alpha_2/\alpha_3^{i+1}$ . Protomer (i) shown in yellow and protomer (i+1) in red.

(E) Conceptual model for the Mup1-pHluorin MVB sorting assay. Vacuole (v).

(F) Quantitative MVB sorting data for *snf7Δ* yeast exogenously expressing empty vector, *SNF7*, *snf7<sup>L121D</sup>*, *snf7<sup>I117E</sup>*, *snf7<sup>M114E</sup>*, *snf7<sup>M107E</sup>*, *snf7<sup>T103E</sup>*, *snf7<sup>L99K</sup>*, *snf7<sup>M104E</sup>*, *snf7<sup>L101E</sup>*, *snf7<sup>A97K</sup>*, *snf7<sup>I94E</sup>*, *snf7<sup>Q90K</sup>*, *snf7<sup>M87E</sup>*, and *snf7<sup>T83E</sup>*. Error bars represent standard deviations.

(G) Quantitative MVB sorting data for *snf7Δ* yeast exogenously expressing empty vectors, *SNF7*, *snf7<sup>R25E H29E K36E</sup>* and empty vector, empty vector and *snf7<sup>E95K E102K E109K</sup>*, and *snf7<sup>R25E H29E K36E</sup>* and *snf7<sup>E95K E102K E109K</sup>*. Error bars represent standard deviations.

(H) Representative TEM images of recombinant full-length *Snf7<sup>R52E</sup>*, *Snf7<sup>R52E Q90K</sup>*, *Snf7<sup>R52E M107E</sup>*, *Snf7<sup>R52E R25E H29E K36E</sup>*, *Snf7<sup>R52E E95K E102K E109K</sup>*, and *Snf7<sup>R52E R25E H29E K36E</sup>* and *Snf7<sup>R52E E95K E102K E109K</sup>* (1:1). Scale bars, 200nm.

\* Nicholas J. Buchkovich performed the *snf7<sup>L121D</sup>*, *snf7<sup>I117E</sup>* and *snf7<sup>M114E</sup>* experiments in Figures 3.7F. W. Mike Henne performed the *Snf7<sup>R52E</sup>* experiment in Figure 3.7H.

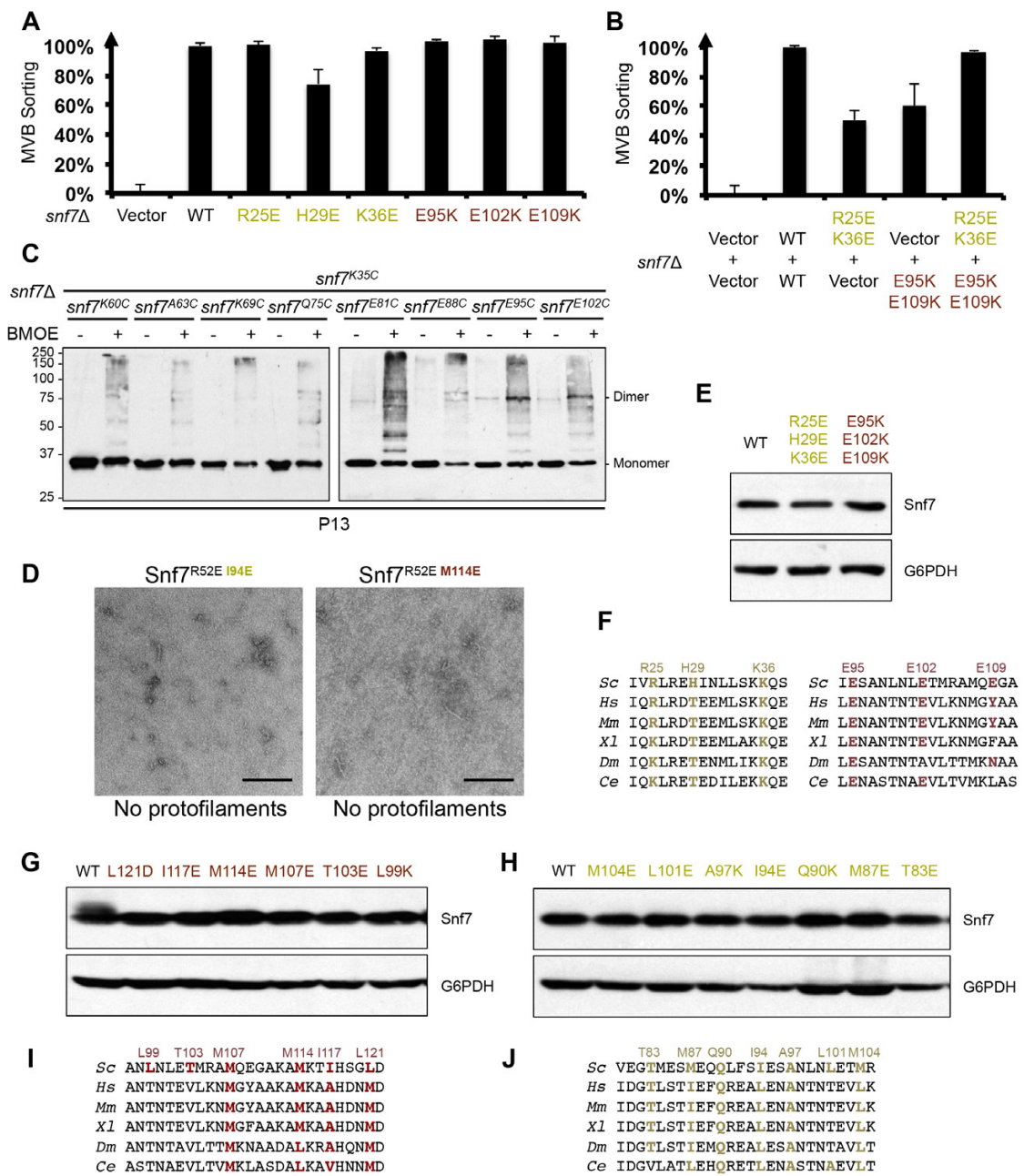


**Figure 3.8 Biochemical Analyses of Snf7 Intra-filament Interface Mutants**

### Figure 3.8 Biochemical Analyses of Snf7 Intra-filament Interface Mutants

(A) Quantitative MVB sorting data for *snf7Δ* yeast exogenously expressing empty vector, *SNF7*, *snf7<sup>R25E</sup>*, *snf7<sup>H29E</sup>*, *snf7<sup>K36E</sup>*, *snf7<sup>E95K</sup>*, *snf7<sup>E102K</sup>*, and *snf7<sup>E109K</sup>*. Error bars represent standard deviations.

(B) Quantitative MVB sorting data for *snf7Δ* yeast exogenously expressing empty vector, *SNF7*, *snf7<sup>R25E K36E</sup>* and vector, vector and *snf7<sup>E95K E109K</sup>*, *snf7<sup>R25E K36E</sup>* and *snf7<sup>E95K E109K</sup>*. Error bars represent standard deviations.

(C) Western blotting analyses of *ex vivo* P13 fractions BMOE crosslinking by *Snf7<sup>K35C</sup>* with *Snf7<sup>K60C</sup>*, *Snf7<sup>A63C</sup>*, *Snf7<sup>K69C</sup>*, *Snf7<sup>Q75C</sup>*, *Snf7<sup>E81C</sup>*, *Snf7<sup>E88C</sup>*, *Snf7<sup>E95C</sup>*, and *Snf7<sup>E102C</sup>*.

(D) Representative TEM images of recombinant *Snf7<sup>R52E I94E</sup>* and *Snf7<sup>R52E M114E</sup>*. Scale bars, 200nm.

(E, G-H) Western blotting analyses of *snf7Δ* yeast expressing (E) *SNF7*, *snf7<sup>R25E H29E K36E</sup>*, and *snf7<sup>E95K E102K E109K</sup>*, (G) *SNF7*, *snf7<sup>L121D</sup>*, *snf7<sup>I117E</sup>*, *snf7<sup>M114E</sup>*, *snf7<sup>M107E</sup>*, *snf7<sup>T103E</sup>*, and *snf7<sup>L99K</sup>*, and (H) *SNF7*, *snf7<sup>M104E</sup>*, *snf7<sup>L101E</sup>*, *snf7<sup>A97K</sup>*, *snf7<sup>I94E</sup>*, *snf7<sup>Q90K</sup>*, *snf7<sup>M87E</sup>*, and *snf7<sup>T83E</sup>*. G6PDH used as loading controls.

(F, I-J) Sequence analyses of Snf7 α2/3 with conserved residues shown in gold and dark red.

\* Nicholas J. Buchkovich performed the *snf7<sup>E102K</sup>* and *snf7<sup>E109K</sup>* experiments in Figures 3.8A.

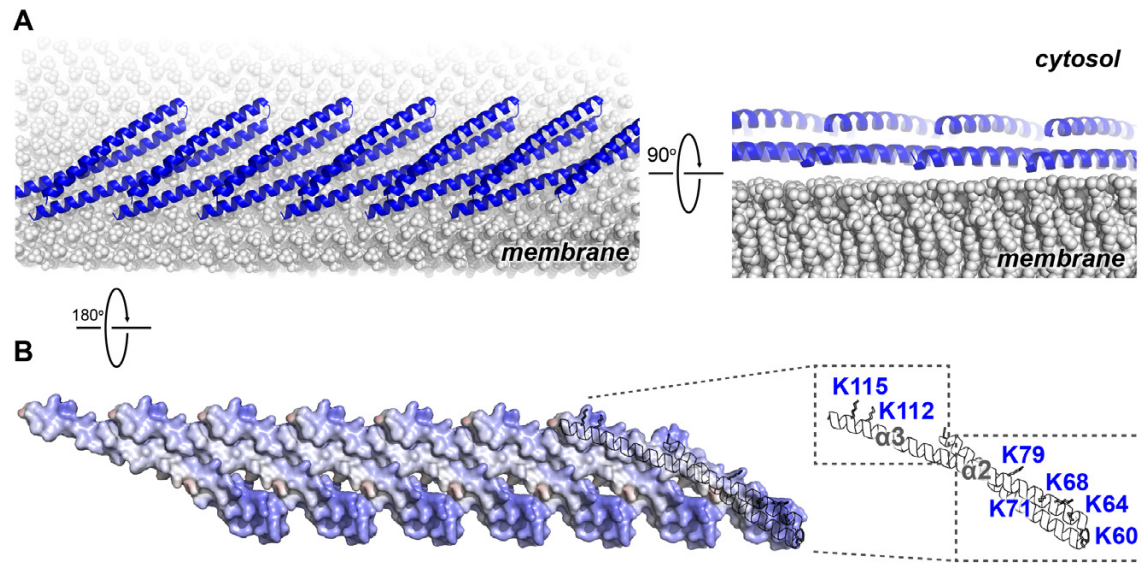


**Figure 3.9 Electrostatic Protein-membrane Interactions in a Snf7 Filament**

**Figure 3.9 Electrostatic Protein-membrane Interactions in a Snf7 Filament**

(A) A Snf7 protofilament in ribbons placed on a lipid membrane in spheres (grey) (Heller et al., 1993).

(B) Electrostatic surface potential showing the membrane interacting surface of a Snf7 protofilament with positively charged regions in blue (+10kcal/e<sup>-</sup>) and negatively charged regions in red ( -10kcal/e<sup>-</sup>).

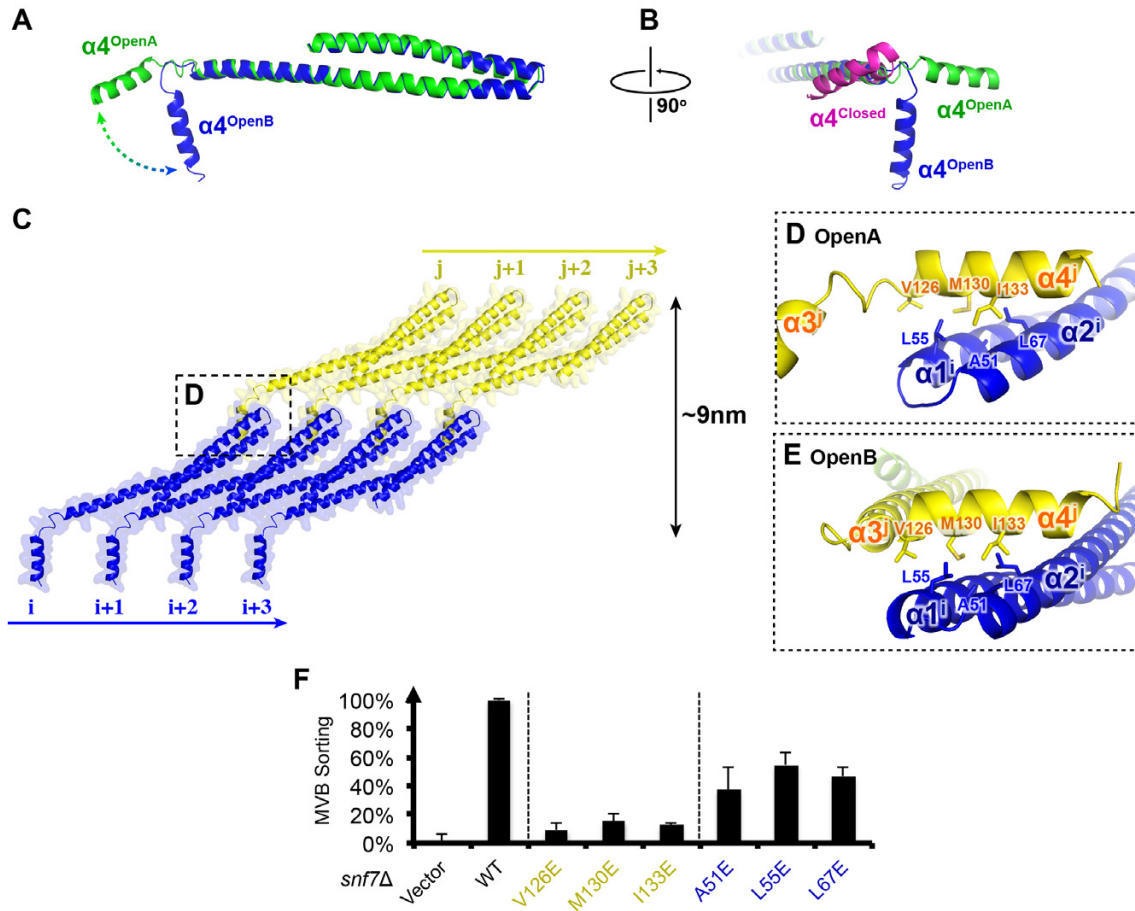


**Figure 3.10 Snf7  $\alpha$ 4 in Inter-Filament Interactions**

### Figure 3.10 Snf7 $\alpha$ 4 in Inter-Filament Interactions

- (A-B) Snf7<sup>core</sup> conformations A (green) and B (blue) superimposed.  
(B) 90° rotation and superimposing with a closed CHMP3 (purple) using its  $\alpha$ 3 as a reference.  
(C) Overlay of ribbon and space-filling models of the Snf7<sup>core</sup> crystal packing of the open conformation A. The dash-line box represents the interfilament contacts. Arrows represent inter-protofilament orientations.  
(D-E) Close-up views of the hydrophobic interface between  $\alpha$ 1/2<sup>i</sup> (blue) and  $\alpha$ 4<sup>j</sup> (yellow) of open conformations (D) A and (E) B.  
(F) Quantitative MVB sorting data for *snf7Δ* yeast exogenously expressing empty vector, *SNF7*, *snf7<sup>V126E</sup>*, *snf7<sup>M130E</sup>*, *snf7<sup>I133E</sup>*, *snf7<sup>A51E</sup>*, *snf7<sup>L55E</sup>*, and *snf7<sup>L67E</sup>*. Error bars represent standard deviations.  
See also Table 3.1.  
\* Nicholas J. Buchkovich performed the *snf7<sup>A51E</sup>* and *snf7<sup>L67E</sup>* experiments in Figures 3.10F.

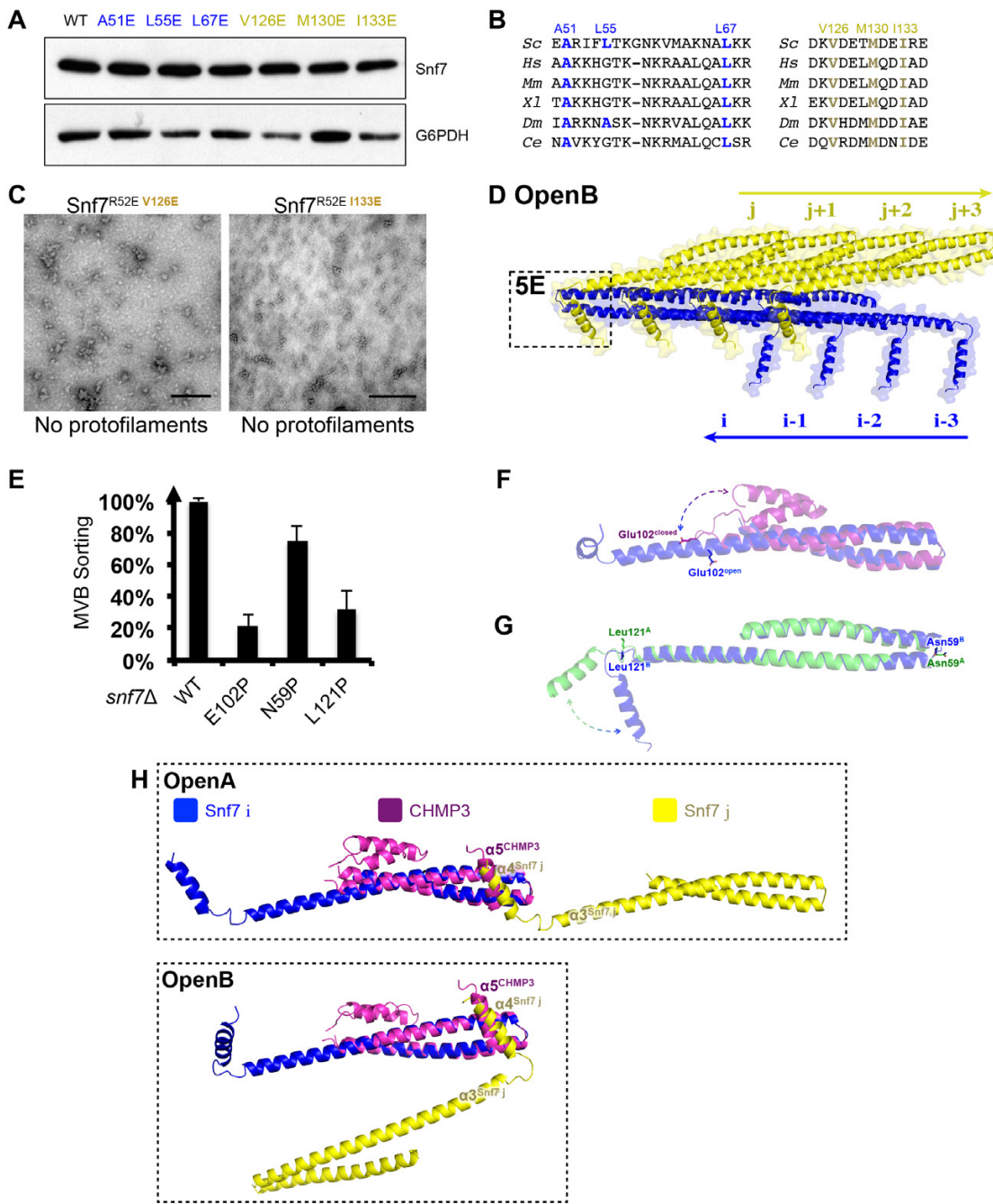
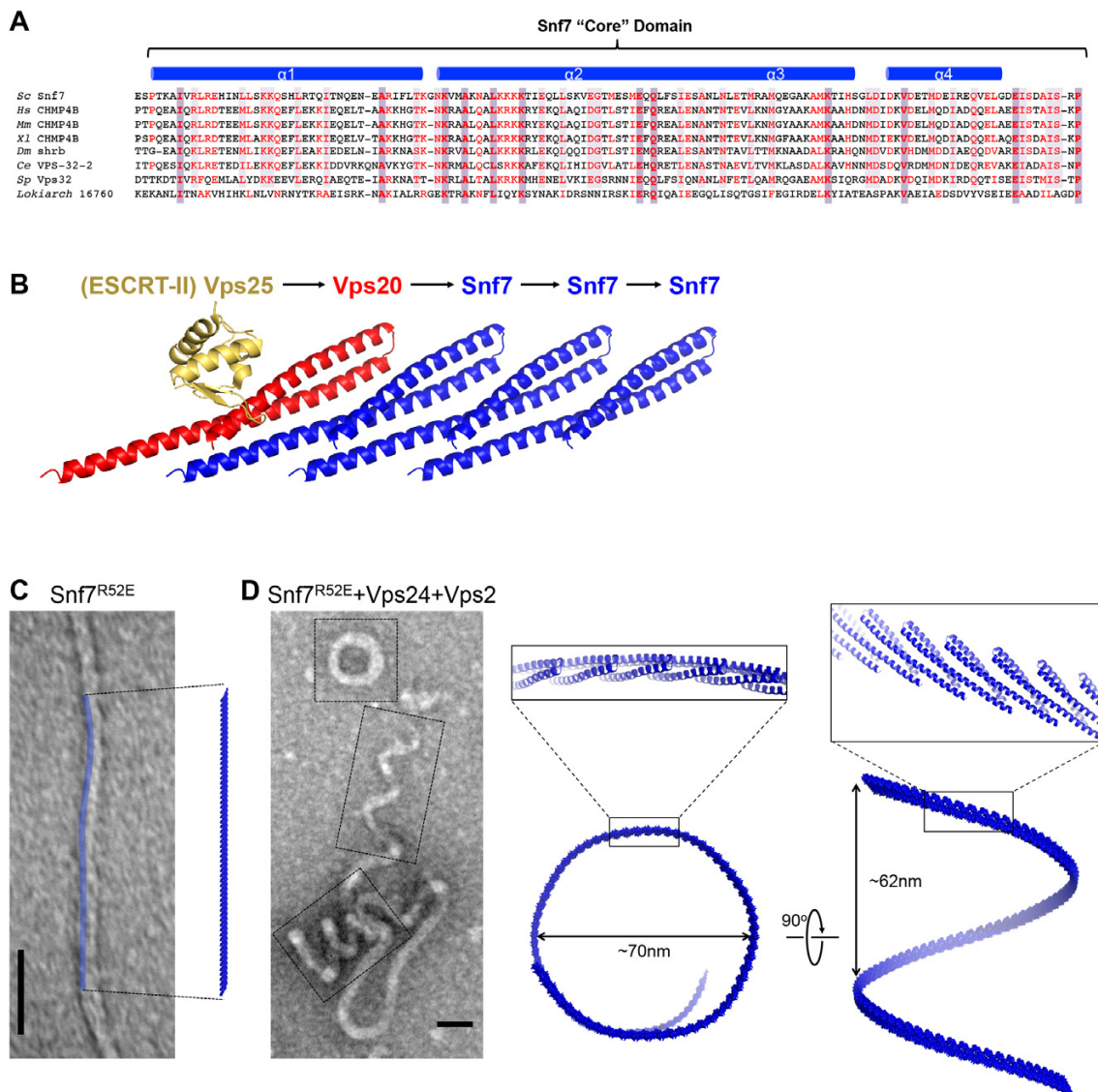


Figure 3.11 Comparison Between Snf7<sup>core</sup> Open Conformation A and B

### Figure 3.11 Comparison Between $\text{Snf7}^{\text{core}}$ Open Conformation A and B

- (A) Western blotting analyses of  $\text{snf7}\Delta$  yeast expressing  $\text{SNF7}$ ,  $\text{snf7}^{\text{A}51\text{E}}$ ,  $\text{snf7}^{\text{L}55\text{E}}$ ,  $\text{snf7}^{\text{L}67\text{E}}$ ,  $\text{snf7}^{\text{V}126\text{E}}$ ,  $\text{snf7}^{\text{M}130\text{E}}$ , and  $\text{snf7}^{\text{I}133\text{E}}$ . G6PDH as a loading control.
- (B) Sequence analyses of Snf7  $\alpha 1/2$  and  $\alpha 4$  with conserved residues shown in blue or gold.
- (C) Representative TEM images of recombinant  $\text{Snf7}^{\text{R}52\text{E V}126\text{E}}$  and  $\text{Snf7}^{\text{R}52\text{E I}133\text{E}}$ . Scale bars, 200nm.
- (D) An overlay of ribbon and space-filling models of the Snf7 crystal packing of the open conformation B. The dash-line box represent the interfilament contacts shown in Figure 5E. Arrows represent inter-protofilamental orientations.
- (E) Quantitative MVB sorting data for  $\text{snf7}\Delta$  yeast exogenously expressing  $\text{SNF7}$ ,  $\text{snf7}^{\text{E}102\text{P}}$ ,  $\text{snf7}^{\text{N}59\text{P}}$ , and  $\text{snf7}^{\text{L}121\text{P}}$ . Error bars represent standard deviations.
- (F-G) Overlay ribbon models of (F) closed (purple) and open (blue) with Glu102 shown in sticks, and (G) open conformation A (green) and B (blue) with Asn59 and Leu121 shown in sticks. Arrows represent conformational rearrangements.
- (H) Superimposing of Snf7 subunit (i) (blue), (j) (yellow) and CHMP3 (purple) of open conformations A (upper) and B (lower).



**Figure 3.12 Conservation and Normal Mode Analysis of Snf7 Filament**

### Figure 3.12 Conservation and Normal Mode Analysis of Snf7 Filament

(A) Alignment of Snf7<sup>core</sup> protein sequences from *Saccharomyces cerevisiae* (*Sc*), *Homo sapiens* (*Hs*), *Mus musculus* (*Mm*), *Xenopus laevis* (*Xl*), *Drosophila melanogaster* (*Dm*), *Caenorhabditis elegans* (*Ce*), *Schizosaccharomyces pombe* (*Sp*) and *Lokiarchaea* (*Spang et al., 2015*).

(B) A ribbon model of a supercomplex of Vps25-Vps20-Snf7. The first of Snf7's  $\alpha$ 1 was used for superimposing with the Vps20  $\alpha$ 1 (Im et al., 2009) (PDB: 3HTU) for molecular docking.

(C) A representative TEM image of recombinant Snf7<sup>R52E</sup> (left) and a space-filling model of a 61-mer Snf7 <sup>$\alpha$ 1-3</sup> straight filament shown in the same scale (right).

(D) A representative TEM image of recombinant Snf7<sup>R52E</sup>, Vps24 and Vps2 (2:1:1) (left), and space-filling and close-up view of ribbon models of a 97-mer Snf7 <sup>$\alpha$ 1-3</sup> superhelix generated by normal mode analysis with measured dimensions (right). TEM scale bars, 50nm.

\* W. Mike Henne performed the TEM experiments in Figures 3.12C-D.

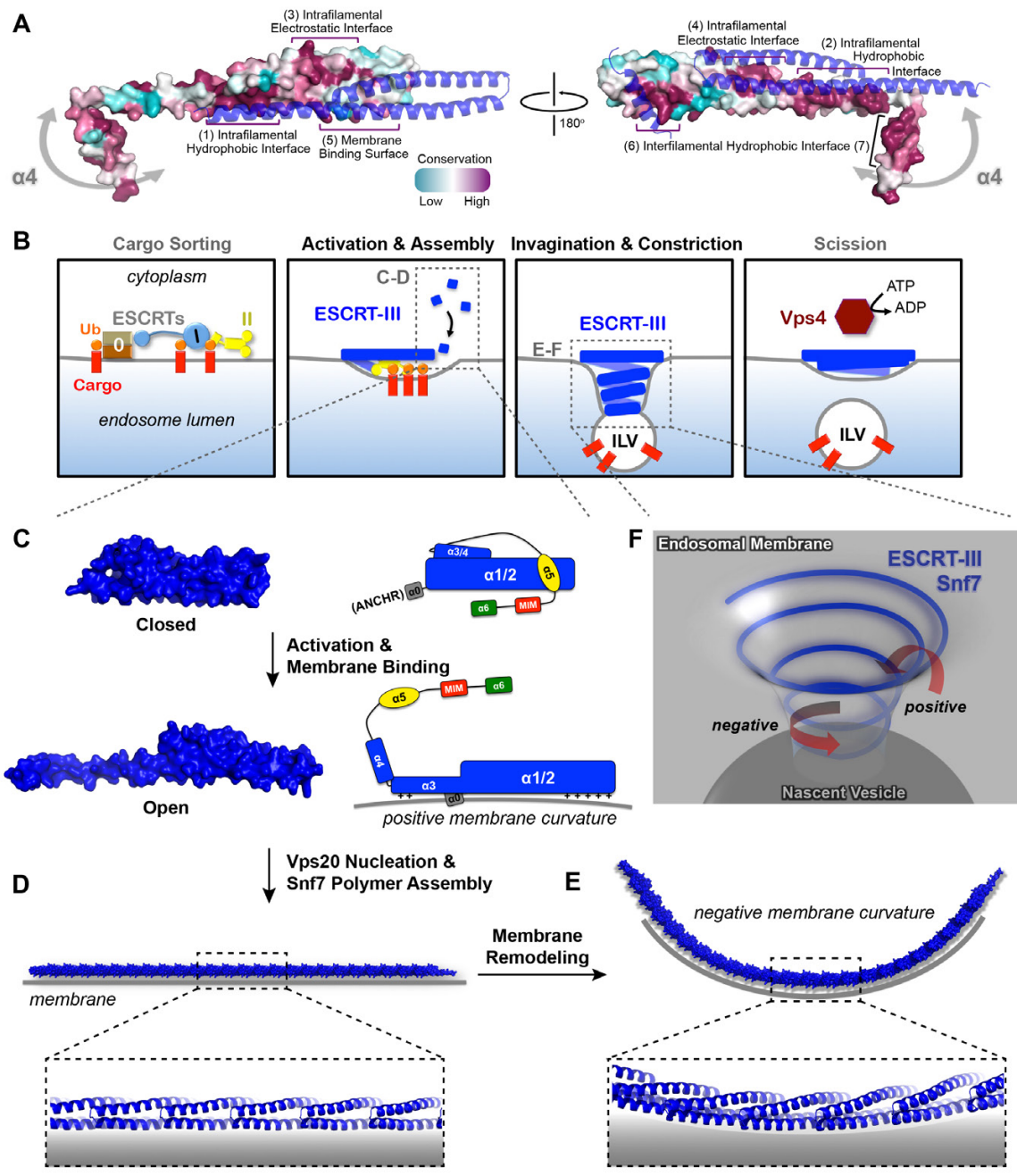


**Figure 3.13 Models of Snf7 Activation, Polymer Assembly and Membrane Remodeling**

**Figure 3.13 Models of Snf7 Activation, Polymer Assembly and Membrane Remodeling**

- (A) Space-filling CONSURF models with high conservation (purple) and low conservation (cyan). Interacting protomers shown in ribbon (blue). Seven conserved regions with assigned functions labeled. Gray arrows indicate the flexibility of  $\alpha 4$ .
- (B) Speculative cartoons illustrating four stages in ESCRT-mediated vesicle budding.
- (C) Space-filling models and schematic cartoons of Snf7<sup>core</sup> in closed and open states with membrane (grey).
- (D) Space-filling and close-up ribbon models of a 25-mer Snf7 single filament with membrane.
- (E) Space-filling and close-up ribbon models of a 23-mer Snf7 normal mode analysis filament with membrane (grey).
- (F) Schematic of a Snf7 homo-polymer in the neck of a nascent ILV with positive and negative membrane curvatures.

## Materials and Methods

### Protein Crystallization

The DNA sequence encoding *Saccharomyces cerevisiae* Snf7<sup>core</sup> (residues 12-150) was subcloned into a pET28a vector with an N-terminal His<sub>6</sub>-Sumo tag. Recombinant proteins were overexpressed in *Escherichia coli* Rosetta cells and purified by TALON metal affinity resin. The His<sub>6</sub>-Sumo tag was removed by Ulp1 protease at 4°C overnight. The mixture was further purified by Superdex-200 gel filtration. The peak corresponding to Snf7<sup>core</sup> was pooled and concentrated in a buffer of 300mM NaCl, 20mM HEPES pH7.4.

Snf7<sup>core</sup> (conformation A) was crystallized in a hanging-drop vapor diffusion system at 4°C by mixing protein (5.7mg/mL) with reservoir solution containing 100mM NaCl, 100mM MES:NaOH pH5.5, 3% PEG20,000 in 1:1 ratio (v/v). Crystals were transferred into the same solution supplemented with 30% glycerol before cooling to liquid nitrogen temperature under atmosphere pressure. Snf7<sup>core</sup> (conformation B) crystals were grown in 110mM NaCl, 70mM MES:NaOH pH5.5, 6% PEG20,000 and subject to high-pressure cryo-cooling (Kim et al., 2005a). The crystals were mounted in oil on a pin with a piece of steel piano wire attached to the base, pressurized to 200MPa and cooled to liquid nitrogen temperature. The pressure was then released while keeping the temperature unaltered.

### X-ray Crystallography

X-ray diffraction data was collected on Snf7 crystal “A” to 2.4Å at MacCHESS beam line F1 of Cornell High Energy Synchrotron Source. The crystal belonged to

space group  $P2_1$  with unit cell dimensions  $a=29.5\text{\AA}$   $b=52.2\text{\AA}$   $c=54.5\text{\AA}$   $\alpha=90^\circ$   $\beta=97.5^\circ$   $\gamma=90^\circ$ . X-ray diffraction data was collected on crystal “B” to  $1.6\text{\AA}$ . It belonged to space group  $P2_1$  with unit cell dimensions  $a=29.9\text{\AA}$   $b=46.2\text{\AA}$   $c=44.6\text{\AA}$   $\alpha=90^\circ$   $\beta=98.5^\circ$   $\gamma=90^\circ$ . Diffraction data were processed using *HKL-2000* (Otwinowski and Minor, 1997). There is one Snf7 molecule in the asymmetric unit of both crystals. The structures were solved using *Phaser* in *Phenix* (Adams et al., 2010) by molecular replacement with CHMP4B <sup>$\alpha 1$ - $\alpha 2$</sup>  (PDB: 4ABM) as a search model. Refinement and density modification were performed in *Phenix*. Model building was performed using *Coot* (Emsley and Cowtan, 2004). Throughout this study, structural images were generated with *PyMOL* using the  $1.6\text{\AA}$  structure unless otherwise noted.

## Protein Purification

All Snf7 protein purification for PDS and TEM analyses were performed as previously described (Henne et al., 2012). Briefly, Snf7 constructs were subcloned into a pET23d bacterial expression vector (Novagen) with an N-terminal His<sub>6</sub>-tag. Recombinant proteins were overexpressed by *Escherichia coli* BL21 or C41 cells, purified by TALON metal affinity resin and eluted in 150mM NaCl, 20mM HEPES pH7.4 and 400mM Imidazole. The elution fractions were pooled and further purified by Superdex-200 gel filtration in a buffer of 150mM NaCl, 20mM HEPES pH7.4.

## Site-directed Spin-labeling

Recombinant Snf7 cysteine-substituted proteins were purified and enriched on TALON resin, and spin-labeled with 1 $\mu\text{g}/\text{mL}$  S-(1-oxyl-2,2,5,5-tetramethyl-2,5-dihydro-

*1H*-pyrrol-3-yl)methyl methanesulfonothioate, MTSL (Santa Cruz Biotech) dissolved in acetonitrile at 4°C overnight. The spin-labeled proteins were eluted in 150mM NaCl, 20mM HEPES pH7.4, 400mM Imidazole and further purified by Superdex-200 gel filtration in a buffer of 150mM NaCl, 20mM HEPES pH7.4 to remove unreacted spin labels.

### **Sample Preparations for DEER Spectroscopy**

For soluble protein samples, spin-labeled proteins were buffer exchanged in a 10kDa molecular weight cutoff protein concentrator (Millipore) to ~80% deuterium buffer of 150mM NaCl, 20mM HEPES pD7.4 supplemented with 30% (v/v) glycerol-d<sub>8</sub>. For liposome-reconstituted protein samples, 1mg/mL of 800nm diameter 60% 1,2-dioleoyl-*sn*-glycero-3-phosphocholine (DOPC), 30% 1,2-dioleoyl-*sn*-glycero-3-phospho-*L*-serine (DOPS), 10% phosphatidylinositol 3-phosphate (PI(3)P) liposomes were generated as previously described (Buchkovich et al., 2013). 25μL of 10-30μM proteins and 25μL 1mg/mL liposomes were coincubated at room temperature for 15min and ultracentrifuged in a TLA-100 rotor (Beckman Coulter) for 10min at 70,000rpm at 20°C. A total of 6 liposome pellets were combined and resuspended in 20μL deuterium buffer of 150mM NaCl, 20mM HEPES pD7.4 supplemented with 15% (v/v) glycerol-d<sub>8</sub>, resulting in a sample of ~10-30μM protein : ~3mg/mL lipid for DEER measurements.

### **DEER Data Collection and Analysis**

20μL spin-labeled samples were loaded into 1.8mm inner diameter Pyrex sample tubes (Wilmad-LabGlass), shock frozen in liquid nitrogen prior to DEER measurements.

DEER measurements were performed at 60K using a home-built Ku band 17.3GHz pulse electron spin resonance spectrometer (Borbat et al., 1997; Borbat et al., 2013). A four-pulse DEER sequence (Jeschke and Polyhach, 2007) was used routinely with the detection  $\pi/2$ - and  $\pi$ -pulses having widths of 16 and 32ns and pump  $\pi$ -pulse of 16ns. The detection pulse sequence was applied at the low-field spectral position, while pumping was performed at a lower by 70MHz frequency positioned at the central maximum. A 32-step phase cycle (Gamliel and Freed, 1990) was applied to suppress unwanted contributions to the signal. Nuclear modulation effects caused by surrounding protons were suppressed by averaging the data from 4 measurements with slightly different separations of the first two pulses, *i.e.* advanced by 9.5ns for subsequent measurement. Depending on spin-labeled protein concentration, distance, and phase relaxation time, DEER data were usually acquired in less than 12h.

Time-domain DEER data,  $V(t)$ , were reconstructed into distance distributions using standard approaches (Borbat and Freed, 2007; Borbat and Freed, 2014; Jeschke, 2012; Jeschke and Polyhach, 2007). First, the signal decay due to intermolecular spin interactions was removed from  $V(t)$  by approximating the latter points (about a half of the record) of  $\ln V(t)$  with a low-order polynomial, usually nearly a straight line, and subtracting it out from  $\ln V(t)$  so that the antilog yields  $u(t)$ . Once normalized as  $V(t) = \frac{u(t)}{u(0)}$ , it serves as a typical form of DEER data presentation, while  $u(t)-1$  gives background free data, which was subsequently converted to a distance distribution between spin pairs with L-curve Tikhonov regularization (Chiang et al., 2005a) followed, when needed, by maximum entropy method refinement (Chiang et al., 2005b). The

modulation depth, defined as  $1-V(\infty)$ , where  $V(\infty)$  is the asymptotic value of  $V(t)$ , was used to report on the presence and extent of multispin effects (Bode et al., 2007).

For mapping Snf7 conformation, I employed double spin-labeled Snf7 and magnetic dilution (Borbat and Freed, 2007; Dzikovski et al., 2011; Meyer et al., 2014; Pornsuwan et al., 2013). Figure 3.6A demonstrates a benchmark magnetic dilution study of double-labeled Snf7<sup>R52E K60C A66C</sup> with unlabeled Snf7<sup>R52E</sup>. This spin pair at the tip of the  $\alpha$ 1/2 hairpin was selected as a reference for inspecting bound protein conformational variability and the conditions for isolation of intramolecular distances. The distance of this construct in solution is  $\sim 20\text{\AA}$ , in agreement with spin-label modeling into a homology structure (Figure 3.3A) using *MMM* (*molecular multiscale modeling*) software package (Polyhach et al., 2011). Generic MTSL rotamer library for 298K was used to determine conformations of attached spin labeled cysteine side chains and produce distance distributions between pairs of labeled sites. Distance distributions FWHMs were in the range of 0.4-1.2nm. Respective background free time-domain data were generated with the help of the same package.

Consistently, Snf7 was found to be structurally more heterogeneous in solution, producing broad distributions based on DEER data for a set of double-labeled Snf7 full-length constructs (Figures 3.4F-H). Intriguingly, this study revealed a distinct Snf7 conformation in the protofilaments, which manifests itself as a very narrow distance distribution already at mild magnetic dilution (1:2), thus pointing to a low extent of intermolecular contacts. In the absence of unlabeled proteins (1:0 magnetic dilution), Snf7<sup>R52E K60C A66C</sup> in liposome samples produced broad distributions, which showed a range of distances to neighbors with  $\sim 30\text{\AA}$  being dominant (Figures 3.6A-B). In addition,

the large modulation depth indicated coupling to at least two neighbors. This indicated that for isolating longer distances considerably higher dilution ratios would be desirable.

Figures 3.3I, K & 3.6C illustrate subsequent application of this method to the membrane-bound Snf7<sup>R52E E88C H118C</sup>. Note that in Figure 3.3I, the reconstructed distance distribution of soluble Snf7<sup>R52E E88C H118C</sup> is normalized at a 4x scale than the MMM simulation data to illustrate the structural heterogeneity. In Figure 3.3K, the reconstructed distance distributions have a large component of ~30Å originating from distances to immediate neighbors similar to the benchmark case, the magnetically diluted samples have a single peak at ~45Å that is dominant with only a small fraction at 30Å that could still be noticed at 1:8 dilution. A dilution factor in excess of 15 would be necessary to fully reveal the expected signal shape, however the 1:8 dilution sample already has ~5μM protein concentration, making larger ratios problematic to study.

Snf7 polymeric packing was assayed by inspecting intermolecular dipolar couplings for various single-labeled constructs assembled in protofilaments on liposome membranes. Whereas the most pronounced distance is expected to be determined by the proximal neighbors, the widths of distance distributions (Figures 3.5B-E) obtained in these scans are likely to have contributions from the couplings to more distant neighbors and in addition by the complex nature of the Snf7 polymer in a liposome-reconstituted system where Snf7 spiraling double- protofilaments are observed, and the orientation relative to each other is heterogeneous (Cashikar et al., 2014; Henne et al., 2012). Notably, while searching for “tip-to-tip” contacts possible in double protofilaments, I did not identify any spin labeled position with a distinct short proximity that is expected to occur at the contacting edge of the single filament, thus ruling out

this scenario. I also did not discern any significant distance variation as the spin labeled position is moved from one end of the  $\alpha$ 1-3 hairpin to the other, thus ruling out any alternating protomer packing in the protofilaments. So far, only parallel protomer packing in a single-layer filament is consistent with the data (see also Result).

### **Subcellular Fractionation Analysis**

Subcellular fractionation experiment was performed as previously described (Buchkovich et al., 2013). Briefly, 30OD<sub>600nm</sub>V of mid-log yeast cultures were spheroplasted in Zymolyase and lysed in 1mL of 50mM Tris pH7.4, 1mM EDTA, 200mM sorbitol with protease inhibitors (Roche). Lysates were cleared at 500xg for 5min at 4°C, and then fractionated by centrifugation at 13,000xg for 10min at 4°C. The supernatant (S13) fraction was collected. The pellet (P13) fraction was resuspended in 1mL lysis buffer. Both fractions were then precipitated by 10% trichloroacetic acid for at least 30min and washed by acetone twice.

### **Dicysteine Oxidative Crosslinking**

The oxidizing chemical copper (II) 1,10-phenanthroline was prepared freshly. 9mg copper (II) sulfate was dissolved in 250 $\mu$ L ionic buffer of 150mM postassium acetate, 5mM magnesium acetate, 250mM sorbitol, 20mM HEPES pH7.0. 20mg 1,10-phenanthroline was dissolved in 500 $\mu$ L ethanol. Both solutions were mixed creating a brilliant aqua-colored solution with white precipitate. 7 $\mu$ L copper(II) 1,10-phenanthroline solution was added into 450 $\mu$ L of S13 or P13 fractions, and incubated at 4°C for 15min.

Samples were then precipitated by 10% trichloroacetic acid, washed twice by acetone and subjected for western blotting analysis.

### ***Ex vivo* Dicysteine Crosslinking by Crosslinker**

30OD<sub>600nm</sub>V of mid-log yeast cultures were spheroplasted, lysed and fractionated. The 1mL P13 fractions were equally divided into two subfractions. Subfraction 1 was treated with 20µL DMSO and subfraction 2 with 20µL 20mM bismaleimidooethane (BMOE) (Life Technologies) in DMSO for 2hours at 4°C. Excessive BMOE was quenched by adding 0.2µL 1M dithiothreitol. Samples were then precipitated by 10% trichloroacetic acid, washed twice by acetone and subjected for western blotting analysis.

### **Flow Cytometry, Microscopy, Western Blotting, Yeast Strain and Plasmids**

The quantitative Mup1-pHluorin ESCRT cargo-sorting flow cytometry assay, negative stain TEM, and western blotting were performed as previously described (Buchkovich et al., 2013; Henne et al., 2012). See Table 3.2 for a list of plasmids and yeast strains used.

### **CONSURF Analysis**

*Saccharomyces cerevisiae* Snf7 protein sequence was input as a query sequence for a protein BLAST analysis using the algorithm of blastp (protein-protein BLAST). The top 100 sequences from the result were subjected for ClustalW sequence alignment. The multiple sequence alignment and the Snf7 conformation B structure

were then used as input for conservational analysis using the *CONSURF* server (Ashkenazy et al., 2010; Berezin et al., 2004; Celniker et al., 2013). The overall conservation scores calculated using the Bayesian method were color-coordinately mapped onto the Snf7 structure shown in Figure 3.13A.

### **Normal Mode Analysis**

Calculation of the normal modes of the Snf7 polymer was preformed on the *eNémo* server (Suhre and Sanejouand, 2004), by using a 25-mer of Snf7 of conformation B as an input structure. To model a circular structure with a diameter of ~65-70nm, perturbation parameters of DQMIN of -10000, DQMAX of 10000, and DQSTEP of 2000 were applied. This yielded 3 nontrivial normal modes numbered 7, 8 and 9. The lowest frequency nontrivial normal mode, mode 7, was used. Using *Coot*, the middle 12 protomers of the No.7 normal mode were selected and then superimposed in a head-to-tail fashion to manually generate a 23-mer and 94-mer shown in Figures 3.12D and 3.13E.

### **Accession Number**

Coordinates and structure factors for Snf7<sup>core</sup> have been deposited in the RCSB Protein Data Bank (<http://www.rcsb.org>) under accession PDB ID 5FD7 (open conformation A) and 5FD9 (open conformation B).

## Acknowledgements

I gratefully thank Scott D. Emr, Nicholas J. Buchkovich and W. Mike Henne for training, mentorship, experimental design and execution. I gratefully thank J. Christopher Fromme and Yuxin Mao for assistant with protein crystallization, X-ray crystallography and structure determination. I gratefully thank Peter P. Borbat, Jack Freed at the National Biomedical Center for Advanced Electron Spin Resonance Technology (ACERT) for assistant with pulsed dipolar electron spin resonance spectroscopy.

I thank Yun Jung Kim, Sarah T. Griffin, Yi-Chun Yeh, Leonid A. Timashev and Elka R. Georgieva for all technical expertise. I thank Cornell High Energy Synchrotron Source MacCHESS beam line F1 staff for X-ray crystallographic data collection, and Qingqiu Huang for the high-pressure cryo-cooling. I thank Joshua S. Chappie, Ming Li, Brian R. Crane, William J. Brown and Li Zhang for helpful discussion.

**Table 3.1 Crystallographic Data Collection and Refinement Statistics**

|                                     | <b>Snf7<sup>core</sup></b>   |  |
|-------------------------------------|--|--|
|                                     | <b>Conformation A</b>  | <b>Conformation B</b>  |
| <b>Wavelength (Å)</b>               | 0.978  | 0.978  |
| <b>Resolution range (Å)</b>         | 50 - 2.4 (2.49 - 2.40)   | 50 - 1.6 (1.6 - 1.55)  |
| <b>Space group</b>                  | <i>P</i> 2 <sub>1</sub>  | <i>P</i> 2 <sub>1</sub>  |
| <b>Unit cell</b>                    | <i>a</i> =29.5Å <i>b</i> =52.2Å <i>c</i> =54.5Å<br><i>α</i> =90° <i>β</i> =97.5° <i>γ</i> =90° | <i>a</i> =29.9Å <i>b</i> =46.2Å <i>c</i> =44.6Å<br><i>α</i> =90° <i>β</i> =98.5° <i>γ</i> =90° |
| <b>Total reflections</b>            | 23263 (1946)   | 73723 (6034)   |
| <b>Unique reflections</b>           | 6376 (612)   | 16849 (1581)   |
| <b>Multiplicity</b>                 | 3.6 (3.2)  | 4.4 (3.8)  |
| <b>Completeness (%)</b>             | 97.99 (93.72)  | 95.77 (90.65)  |
| <b>Mean I/sigma(I)</b>              | 8.04 (2.91)  | 8.85 (1.35)  |
| <b>Wilson B-factor</b>              | 54.03  | 25.39  |
| <b>R<sub>merge</sub></b>            | 0.0884 (0.249)   | 0.0782 (0.997)   |
| <b>CC<sub>1/2</sub></b>             | 0.988 (0.968)  | 0.995 (0.590)  |
| <b>CC*</b>                          | 0.997 (0.992)  | 0.999 (0.861)  |
| <b>R<sub>work</sub></b>             | 0.259 (0.398)  | 0.210 (0.330)  |
| <b>R<sub>free</sub></b>             | 0.263 (0.533)  | 0.225 (0.356)  |
| <b>Number of non-hydrogen atoms</b> | 982  | 1097   |
| <b>macromolecules</b>               | 975  | 992  |
| <b>water</b>                        | 7  | 105  |
| <b>Protein residues</b>             | 123  | 125  |
| <b>RMS(bonds) (Å)</b>               | 0.015  | 0.006  |
| <b>RMS(angles) (°)</b>              | 1.24   | 0.81   |
| <b>Ramachandran favored (%)</b>     | 95   | 99   |
| <b>Ramachandran outliers (%)</b>    | 1.7  | 0  |
| <b>Clashscore</b>                   | 21.56  | 9.9  |
| <b>Average B-factor</b>             | 91.1   | 39.7   |
| <b>macromolecules</b>               | 91.2   | 38.9   |
| <b>solvent</b>                      | 69.2   | 47.2   |

**Table 3.2 Plasmids and Yeast Strains Used in Chapter 3**

| <b>Plasmids for <i>Saccharomyces cerevisiae</i> Expression</b> | <b>Mutations</b> | <b>Reference</b>            |
|--|------------------|-----------------------------|
| pRS416   | N/A              | (Sikorski and Hieter, 1989) |
| pRS414   | N/A              | (Sikorski and Hieter, 1989) |
| pRS416-SNF7  | Wild-type        | (Henne et al., 2012)        |
| pRS414-SNF7  | Wild-type        | this study                  |
| pRS416-sn <sup>f</sup> 7 <sup>Q90C</sup>                       | Q90C             | this study                  |
| pRS416-sn <sup>f</sup> 7 <sup>M130C</sup>                      | M130C            | this study                  |
| pRS416-sn <sup>f</sup> 7 <sup>Q90C M130C</sup>                 | Q90C M130C       | this study                  |
| pRS416-sn <sup>f</sup> 7 <sup>T20C</sup>                       | T20C             | this study                  |
| pRS416-sn <sup>f</sup> 7 <sup>K35C</sup>                       | K35C             | this study                  |
| pRS416-sn <sup>f</sup> 7 <sup>K60C</sup>                       | K60C             | this study                  |
| pRS416-sn <sup>f</sup> 7 <sup>E88C</sup>                       | E88C             | this study                  |
| pRS416-sn <sup>f</sup> 7 <sup>H118C</sup>                      | H118C            | this study                  |
| pRS416-sn <sup>f</sup> 7 <sup>G140C</sup>                      | G140C            | this study                  |
| pRS416-sn <sup>f</sup> 7 <sup>E88C H118C</sup>                 | E88C H118C       | this study                  |
| pRS416-sn <sup>f</sup> 7 <sup>K60C A66C</sup>                  | K60C A66C        | this study                  |
| pRS416-sn <sup>f</sup> 7 <sup>T83E</sup>                       | T83E             | this study                  |
| pRS416-sn <sup>f</sup> 7 <sup>M87E</sup>                       | M87E             | this study                  |
| pRS416-sn <sup>f</sup> 7 <sup>Q90K</sup>                       | Q90K             | this study                  |
| pRS416-sn <sup>f</sup> 7 <sup>I94E</sup>                       | I94E             | this study                  |
| pRS416-sn <sup>f</sup> 7 <sup>A97K</sup>                       | A97K             | this study                  |
| pRS416-sn <sup>f</sup> 7 <sup>L99K</sup>                       | L99K             | this study                  |
| pRS416-sn <sup>f</sup> 7 <sup>L101E</sup>                      | L101E            | this study                  |
| pRS416-sn <sup>f</sup> 7 <sup>T103E</sup>                      | T103E            | this study                  |
| pRS416-sn <sup>f</sup> 7 <sup>M104E</sup>                      | M104E            | this study                  |
| pRS416-sn <sup>f</sup> 7 <sup>M107E</sup>                      | M107E            | this study                  |
| pRS416-sn <sup>f</sup> 7 <sup>M114E</sup>                      | M114E            | this study                  |
| pRS416-sn <sup>f</sup> 7 <sup>I117E</sup>                      | I117E            | this study                  |
| pRS416-sn <sup>f</sup> 7 <sup>L121D</sup>                      | L121D            | (Saksena et al., 2009)      |
| pRS416-sn <sup>f</sup> 7 <sup>R25E</sup>                       | R25E             | this study                  |
| pRS416-sn <sup>f</sup> 7 <sup>H29E</sup>                       | H29E             | this study                  |
| pRS416-sn <sup>f</sup> 7 <sup>K36E</sup>                       | K36E             | this study                  |
| pRS416-sn <sup>f</sup> 7 <sup>E95K</sup>                       | E95K             | this study                  |
| pRS416-sn <sup>f</sup> 7 <sup>E102K</sup>                      | E102K            | this study                  |
| pRS416-sn <sup>f</sup> 7 <sup>E109K</sup>                      | E109K            | this study                  |
| pRS414-sn <sup>f</sup> 7 <sup>R25E K36E</sup>                  | R25E K36E        | this study                  |
| pRS416-sn <sup>f</sup> 7 <sup>E95K E109K</sup>                 | E95K E109K       | this study                  |
| pRS414-sn <sup>f</sup> 7 <sup>R25E H29E K36E</sup>             | R25E H29E K36E   | this study                  |
| pRS416-sn <sup>f</sup> 7 <sup>E95K E102K E109K</sup>           | E95K E102K E109K | this study                  |
| pRS414-sn <sup>f</sup> 7 <sup>K35C</sup>                       | K35C             | this study                  |

|                              |       |                      |
|------------------------------|-------|----------------------|
| pRS416-snf7 <sup>A63C</sup>  | A63C  | this study           |
| pRS416-snf7 <sup>K69C</sup>  | K69C  | this study           |
| pRS416-snf7 <sup>Q75C</sup>  | Q75C  | this study           |
| pRS416-snf7 <sup>E81C</sup>  | E81C  | this study           |
| pRS416-snf7 <sup>E95C</sup>  | E95C  | this study           |
| pRS416-snf7 <sup>E102C</sup> | E102C | this study           |
| pRS416-snf7 <sup>V126E</sup> | V126E | this study           |
| pRS416-snf7 <sup>M130E</sup> | M130E | this study           |
| pRS416-snf7 <sup>I133E</sup> | I133E | this study           |
| pRS416-snf7 <sup>A51E</sup>  | A51E  | this study           |
| pRS416-snf7 <sup>L55E</sup>  | L55E  | this study           |
| pRS416-snf7 <sup>L67E</sup>  | L67E  | (Henne et al., 2012) |
| pRS416-snf7 <sup>N59P</sup>  | N59P  | this study           |
| pRS416-snf7 <sup>E102P</sup> | E102P | this study           |
| pRS416-snf7 <sup>L121P</sup> | L121P | this study           |

#### Plasmids for *Escherichia coli* Expression for Protein Purification

| Plasmid                                      | Mutations             | Reference            |
|--|-----------------------|----------------------|
| pET28a-SMT3-snf7 <sup>12-150</sup>           | SMT3-snf7N12-P150     | this study           |
| pET23d-snf7 <sup>R52E</sup>                  | R52E                  | (Henne et al., 2012) |
| pET23d-snf7 <sup>R52E E88C H118C</sup>       | R52E E88C H118C       | this study           |
| pET23d-snf7 <sup>R52E E88C G140C</sup>       | R52E E88C G140C       | this study           |
| pET23d-snf7 <sup>R52E H118C G140C</sup>      | R52E H118C G140C      | this study           |
| pET23d-snf7 <sup>R52E T20C</sup>             | R52E T20C             | this study           |
| pET23d-snf7 <sup>R52E K35C</sup>             | R52E K35C             | this study           |
| pET23d-snf7 <sup>R52E K60C</sup>             | R52E K60C             | this study           |
| pET23d-snf7 <sup>R52E E88C</sup>             | R52E E88C             | this study           |
| pET23d-snf7 <sup>R52E H118C</sup>            | R52E H118C            | this study           |
| pET23d-snf7 <sup>R52E G140C</sup>            | R52E G140C            | this study           |
| pET23d-snf7 <sup>R52E K60C A66C</sup>        | R52E K60C A66C        | this study           |
| pET23d-snf7 <sup>R52E Q90K</sup>             | R52E Q90K             | this study           |
| pET23d-snf7 <sup>R52E I94E</sup>             | R52E I94E             | this study           |
| pET23d-snf7 <sup>R52E M107E</sup>            | R52E M107E            | this study           |
| pET23d-snf7 <sup>R52E M114E</sup>            | R52E M114E            | this study           |
| pET23d-snf7 <sup>R52E R25E H29E K36E</sup>   | R52E R25E H29E K36E   | this study           |
| pET23d-snf7 <sup>R52E E95K E102K E109K</sup> | R52E E95K E102K E109K | this study           |
| pET23d-snf7 <sup>R52E V126E</sup>            | R52E V126E            | this study           |
| pET23d-snf7 <sup>R52E I133E</sup>            | R52E I133E            | this study           |
| pET23d-VPS24                                 | Wild-type             | (Henne et al., 2012) |
| pET23d-VPS2                                  | Wild-type             | (Henne et al., 2012) |

---

**Yeast Strains Used in This Study**

---

| Strain    | Genotype  | Reference               |
|-----------|---|-------------------------|
| SEY6210.1 | <i>Mat a, leu2-3, 2-112, ura3-52, his3-Δ200, trp1-Δ901, lys2-801, suc2-Δ9</i> | (Robinson et al., 1988) |
| MBY24     | SEY6210.1; <i>snf7Δ::HIS3</i>   | (Babst et al., 2002a)   |
| NBY44     | SEY6210.1; <i>snf7Δ::HIS3; MUP1-PHLOURIN::KAN</i>                             | (Henne et al., 2012)    |

---

## Reference

- Adams, P.D., Afonine, P.V., Bunkoczi, G., Chen, V.B., Davis, I.W., Echols, N., Headd, J.J., Hung, L.W., Kapral, G.J., Grosse-Kunstleve, R.W., *et al.* (2010). PHENIX: a comprehensive Python-based system for macromolecular structure solution. *Acta Crystallogr., Sect. D: Biol. Crystallogr.* **66**, 213-221.
- Ashkenazy, H., Erez, E., Martz, E., Pupko, T., and Ben-Tal, N. (2010). ConSurf 2010: calculating evolutionary conservation in sequence and structure of proteins and nucleic acids. *Nucleic Acids Res* **38**, W529-533.
- Babst, M., Katzmann, D.J., Estepa-Sabal, E.J., Meerloo, T., and Emr, S.D. (2002). ESCRT-III: an endosome-associated heterooligomeric protein complex required for mvb sorting. *Dev Cell* **3**, 271-282.
- Bajorek, M., Schubert, H.L., McCullough, J., Langelier, C., Eckert, D.M., Stubblefield, W.M., Uter, N.T., Myszka, D.G., Hill, C.P., and Sundquist, W.I. (2009). Structural basis for ESCRT-III protein autoinhibition. *Nat Struct Mol Biol* **16**, 754-762.
- Berezin, C., Glaser, F., Rosenberg, J., Paz, I., Pupko, T., Fariselli, P., Casadio, R., and Ben-Tal, N. (2004). ConSeq: the identification of functionally and structurally important residues in protein sequences. *Bioinformatics* **20**, 1322-1324.
- Bode, B.E., Margraf, D., Plackmeyer, J., Durner, G., Prisner, T.F., and Schiemann, O. (2007). Counting the monomers in nanometer-sized oligomers by pulsed electron-electron double resonance. *J Am Chem Soc* **129**, 6736-6745.
- Borbat, P.P., Crepeau, R.H., and Freed, J.H. (1997). Multifrequency two-dimensional Fourier transform ESR: an X/Ku-band spectrometer. *J Magn Reson* **127**, 155-167.
- Borbat, P.P., and Freed, J.H. (2007). Measuring distances by pulsed dipolar ESR spectroscopy: spin-labeled histidine kinases. *Methods Enzymol* **423**, 52-116.
- Borbat, P.P., and Freed, J.H. (2014). Pulse Dipolar ESR: Distance Measurements. In *Structure and Bonding* (Heidelberg Springer), pp. 1-82. .
- Borbat, P.P., Georgieva, E.R., and Freed, J.H. (2013). Improved Sensitivity for Long-Distance Measurements in Biomolecules: Five-Pulse Double Electron-Electron Resonance. *Journal of Physical Chemistry Letters* **4**, 170-175.
- Buchkovich, N.J., Henne, W.M., Tang, S., and Emr, S.D. (2013). Essential N-terminal insertion motif anchors the ESCRT-III filament during MVB vesicle formation. *Dev Cell* **27**, 201-214.

- Carlton, J.G., and Martin-Serrano, J. (2007). Parallels between cytokinesis and retroviral budding: a role for the ESCRT machinery. *Science* *316*, 1908-1912.
- Cashikar, A.G., Shim, S., Roth, R., Maldazys, M.R., Heuser, J.E., and Hanson, P.I. (2014). Structure of cellular ESCRT-III spirals and their relationship to HIV budding. *Elife* *3*.
- Celniker, G., Nimrod, G., Ashkenazy, H., Glaser, F., Martz, E., Mayrose, I., Pupko, T., and Ben-Tal, N. (2013). ConSurf: Using Evolutionary Data to Raise Testable Hypotheses about Protein Function. *Israel Journal of Chemistry* *53*, 199-206.
- Chiang, Y.W., Borbat, P.P., and Freed, J.H. (2005a). The determination of pair distance distributions by pulsed ESR using Tikhonov regularization. *J Magn Reson* *172*, 279-295.
- Chiang, Y.W., Borbat, P.P., and Freed, J.H. (2005b). Maximum entropy: a complement to Tikhonov regularization for determination of pair distance distributions by pulsed ESR. *J Magn Reson* *177*, 184-196.
- Dzikovski, B.G., Borbat, P.P., and Freed, J.H. (2011). Channel and Nonchannel Forms of Spin-Labeled Gramicidin in Membranes and Their Equilibria. *Journal of Physical Chemistry B* *115*, 176-185.
- Emsley, P., and Cowtan, K. (2004). Coot: model-building tools for molecular graphics. *Acta Crystallogr D Biol Crystallogr* *60*, 2126-2132.
- Fyfe, I., Schuh, A.L., Edwardson, J.M., and Audhya, A. (2011). Association of the endosomal sorting complex ESCRT-II with the Vps20 subunit of ESCRT-III generates a curvature-sensitive complex capable of nucleating ESCRT-III filaments. *J Biol Chem* *286*, 34262-34270.
- Gamliel, D., and Freed, J.H. (1990). Theory of 2-Dimensional ESR with Nuclear Moduation. *Journal of Magnetic Resonance* *89*, 60-93.
- Garrus, J.E., von Schwedler, U.K., Pornillos, O.W., Morham, S.G., Zavitz, K.H., Wang, H.E., Wettstein, D.A., Stray, K.M., Côté, M., Rich, R.L., et al. (2001). Tsg101 and the vacuolar protein sorting pathway are essential for HIV-1 budding. *Cell* *107*, 55-65.
- Hanson, P.I., Roth, R., Lin, Y., and Heuser, J.E. (2008). Plasma membrane deformation by circular arrays of ESCRT-III protein filaments. *J Cell Biol* *180*, 389-402.
- Heller, H., Schaefer, M., and Schulten, K. (1993). Molecular Dynamics Simulation of a Bilayer of 200 Lipids in the Gel and in the Liquid-Crystal Phases. *J. Phys. Chem.* *97*, 8343-8360.

Henne, W.M., Buchkovich, N.J., and Emr, S.D. (2011). The ESCRT pathway. *Dev Cell* 21, 77-91.

Henne, W.M., Buchkovich, N.J., Zhao, Y., and Emr, S.D. (2012). The endosomal sorting complex ESCRT-II mediates the assembly and architecture of ESCRT-III helices. *Cell* 151, 356-371.

Horii, M., Shibata, H., Kobayashi, R., Katoh, K., Yorikawa, C., Yasuda, J., and Maki, M. (2006). CHMP7, a novel ESCRT-III-related protein, associates with CHMP4b and functions in the endosomal sorting pathway. *Biochem J* 400, 23-32.

Hubbell, W.L., Cafiso, D.S., and Altenbach, C. (2000). Identifying conformational changes with site-directed spin labeling. *Nat Struct Biol* 7, 735-739.

Hurley, J.H., and Hanson, P.I. (2010). Membrane budding and scission by the ESCRT machinery: it's all in the neck. *Nat Rev Mol Cell Biol* 11, 556-566.

Im, Y.J., Wollert, T., Boura, E., and Hurley, J.H. (2009). Structure and function of the ESCRT-II-III interface in multivesicular body biogenesis. *Dev Cell* 17, 234-243.

Jeschke, G. (2012). DEER distance measurements on proteins. *Annu Rev Phys Chem* 63, 419-446.

Jeschke, G., and Polyhach, Y. (2007). Distance measurements on spin-labelled biomacromolecules by pulsed electron paramagnetic resonance. *Physical Chemistry Chemical Physics* 9, 1895-1910.

Jimenez, A.J., Maiuri, P., Lafaurie-Janvore, J., Divoux, S., Piel, M., and Perez, F. (2014). ESCRT machinery is required for plasma membrane repair. *Science* 343, 1247136.

Katzmann, D.J., Babst, M., and Emr, S.D. (2001). Ubiquitin-dependent sorting into the multivesicular body pathway requires the function of a conserved endosomal protein sorting complex, ESCRT-I. *Cell* 106, 145-155.

Kim, C.U., Kapfer, R., and Gruner, S.M. (2005). High-pressure cooling of protein crystals without cryoprotectants. *Acta Crystallogr D Biol Crystallogr* 61, 881-890.

Lata, S., Roessle, M., Solomons, J., Jamin, M., Gottlinger, H.G., Svergun, D.I., and Weissenhorn, W. (2008a). Structural basis for autoinhibition of ESCRT-III CHMP3. *J Mol Biol* 378, 818-827.

Lata, S., Schoehn, G., Jain, A., Pires, R., Piehler, J., Gottlinger, H.G., and Weissenhorn, W. (2008b). Helical structures of ESCRT-III are disassembled by VPS4. *Science* 321, 1354-1357.

Martinelli, N., Hartlieb, B., Usami, Y., Sabin, C., Dordor, A., Miguet, N., Avilov, S.V., Ribeiro, E.A., Jr., Gottlinger, H., and Weissenhorn, W. (2012). CC2D1A is a regulator of ESCRT-III CHMP4B. *J Mol Biol* 419, 75-88.

McCullough, J., Fisher, R.D., Whitby, F.G., Sundquist, W.I., and Hill, C.P. (2008). ALIX-CHMP4 interactions in the human ESCRT pathway. *Proc Natl Acad Sci U S A* 105, 7687-7691.

Meyer, V., Dinkel, P.D., Luo, Y., Yu, X., Wei, G.H., Zheng, J., Eaton, G.R., Ma, B.Y., Nussinov, R., Eaton, S.S., et al. (2014). Single Mutations in Tau Modulate the Populations of Fibril Conformers through Seed Selection. *Angewandte Chemie-International Edition* 53, 1590-1593.

Muziol, T., Pineda-Molina, E., Ravelli, R.B., Zamborlini, A., Usami, Y., Gottlinger, H., and Weissenhorn, W. (2006). Structural basis for budding by the ESCRT-III factor CHMP3. *Dev Cell* 10, 821-830.

Obita, T., Saksena, S., Ghazi-Tabatabai, S., Gill, D.J., Perisic, O., Emr, S.D., and Williams, R.L. (2007). Structural basis for selective recognition of ESCRT-III by the AAA ATPase Vps4. *Nature* 449, 735-739.

Olmos, Y., Hodgson, L., Mantell, J., Verkade, P., and Carlton, J.G. (2015). ESCRT-III controls nuclear envelope reformation. *Nature* 522, 236-239.

Osawa, M., Anderson, D.E., and Erickson, H.P. (2008). Reconstitution of contractile FtsZ rings in liposomes. *Science* 320, 792-794.

Otwinowski, Z., and Minor, W. (1997). Processing of X-ray Diffraction Data Collected in Oscillation Mode. *Methods in Enzymology*, part A 276, 307-326.

Polyhach, Y., Bordignon, E., and Jeschke, G. (2011). Rotamer libraries of spin labelled cysteines for protein studies. *Physical Chemistry Chemical Physics* 13, 2356-2366.

Pornsuwan, S., Giller, K., Riedel, D., Becker, S., Griesinger, C., and Bennati, M. (2013). Long-Range Distances in Amyloid Fibrils of alpha-Synuclein from PELDOR Spectroscopy. *Angewandte Chemie-International Edition* 52, 10290-10294.

Robinson, J., Klionsky, D., Banta, L., and Emr, S. (1988). Protein sorting in *Saccharomyces cerevisiae*: isolation of mutants defective in the delivery and processing of multiple vacuolar hydrolases. *Mol Cell Biol* 8(11), 4936-4948.

Rue, S.M., Mattei, S., Saksena, S., and Emr, S.D. (2008). Novel Ist1-Did2 complex functions at a late step in multivesicular body sorting. *Mol Biol Cell* 19, 475-484.

Saksena, S., Wahlman, J., Teis, D., Johnson, A.E., and Emr, S.D. (2009). Functional reconstitution of ESCRT-III assembly and disassembly. *Cell* 136, 97-109.

Schuh, A.L., Hanna, M., Quinney, K., Wang, L., Sarkeshik, A., Yates, J.R., 3rd, and Audhya, A. (2015). The VPS-20 subunit of the endosomal sorting complex ESCRT-III exhibits an open conformation in the absence of upstream activation. *Biochem J* 466, 625-637.

Shen, Q.T., Schuh, A.L., Zheng, Y., Quinney, K., Wang, L., Hanna, M., Mitchell, J.C., Otegui, M.S., Ahlquist, P., Cui, Q., et al. (2014). Structural analysis and modeling reveals new mechanisms governing ESCRT-III spiral filament assembly. *J Cell Biol* 206, 763-777.

Sikorski, R.S., and Hieter, P. (1989). A system of shuttle vectors and yeast host strains designed for efficient manipulation of DNA in *Saccharomyces cerevisiae*. *Genetics* 22, 19-27.

Spang, A., Saw, J.H., Jorgensen, S.L., Zaremba-Niedzwiedzka, K., Martijn, J., Lind, A.E., van Eijk, R., Schleper, C., Guy, L., and Ettema, T.J. (2015). Complex archaea that bridge the gap between prokaryotes and eukaryotes. *Nature* 521, 173-179.

Suhre, K., and Sanejouand, Y.H. (2004). ElNemo: a normal mode web server for protein movement analysis and the generation of templates for molecular replacement. *Nucleic Acids Res* 32, W610-614.

Teis, D., Saksena, S., and Emr, S.D. (2008). Ordered assembly of the ESCRT-III complex on endosomes is required to sequester cargo during MVB formation. *Dev Cell* 15, 578-589.

Teis, D., Saksena, S., Judson, B.L., and Emr, S.D. (2010). ESCRT-II coordinates the assembly of ESCRT-III filaments for cargo sorting and multivesicular body vesicle formation. *EMBO J* 29, 871-883.

Vietri, M., Schink, K.O., Campsteijn, C., Wegner, C.S., Schultz, S.W., Christ, L., Thoresen, S.B., Brech, A., Raiborg, C., and Stenmark, H. (2015). Spastin and ESCRT-

III coordinate mitotic spindle disassembly and nuclear envelope sealing. *Nature* 522, 231-235.

Webster, B.M., Colombi, P., Jager, J., and Lusk, C.P. (2014). Surveillance of nuclear pore complex assembly by ESCRT-III/Vps4. *Cell* 159, 388-401.

Wollert, T., and Hurley, J.H. (2010). Molecular mechanism of multivesicular body biogenesis by ESCRT complexes. *Nature* 464, 864-869.

Xiao, J., Chen, X.W., Davies, B.A., Saltiel, A.R., Katzmann, D.J., and Xu, Z. (2009). Structural basis of Ist1 function and Ist1-Did2 interaction in the multivesicular body pathway and cytokinesis. *Mol Biol Cell* 20, 3514-3524.

## CHAPTER IV

### ESCRT-III Activation by Parallel Action of ESCRT-I/II and ESCRT-0/Bro1 During MVB Biogenesis

Shaogeng Tang<sup>1,2</sup>, Nicholas J. Buchkovich<sup>1,2,3</sup>, W. Mike Henne<sup>1,2,4</sup>,  
Sudeep Banjade<sup>1,2</sup>, Yun Jung Kim<sup>1,2</sup>, and Scott D. Emr<sup>1,2</sup>

<sup>1</sup> Weill Institute for Cell and Molecular Biology, Cornell University, Ithaca, NY 14853,  
USA

<sup>2</sup> Department of Molecular Biology and Genetics, Cornell University, Ithaca, NY 14853,  
USA

<sup>3</sup> Present Address: Department of Microbiology and Immunology, The Pennsylvania  
State University College of Medicine, Hershey, PA 17033, USA

<sup>4</sup> Present Address: Department of Cell Biology, The University of Texas Southwestern  
Medical Center, Dallas, TX 75390, USA

Shaogeng Tang contributed significantly to all figures in this chapter (Figures 4.1A & C-G, 4.2A, 4.3A-D, 4.4A-F, 4.5A-C, 4.6A-G, 4.7A-C, 4.8A-E, 4.9A-E, 4.10A-B & E-F), and wrote and prepared the manuscript for publication.

Chapter IV was originally published in *eLife* 5, (2016)

Tang, S., Buchkovich, N.J., Henne, W.M., Banjade, S., Kim, Y.J., and Emr, S.D. (2016). ESCRT-III activation by parallel action of ESCRT-I/II and ESCRT-0/Bro1 during MVB biogenesis. *eLife* 5.

DOI: 10.7554/eLife.15507.

## **Abstract**

The endosomal sorting complexes required for transport (ESCRT) pathway facilitates multiple fundamental membrane remodeling events. Previously, I determined X-ray crystal structures of the ESCRT-III subunit Snf7, the yeast CHMP4 ortholog, in its active and polymeric state (Tang et al., 2015). However, how ESCRT-III activation is coordinated by the upstream ESCRT components at endosomes remains unclear. Here, I provide a molecular explanation for the functional divergence of structurally similar ESCRT-III subunits. I characterize novel mutations in ESCRT-III Snf7 that trigger activation, and identify a novel role of Bro1, the yeast ALIX ortholog, in Snf7 assembly. I show that upstream ESCRTs regulate Snf7 activation at both its N-terminal core domain and the C-terminus  $\alpha$ 6 helix through two parallel ubiquitin-dependent pathways: the ESCRT-I-ESCRT-II-Vps20 pathway and the ESCRT-0-Bro1 pathway. I therefore provide an enhanced understanding for the activation of the spatially unique ESCRT-III-mediated membrane remodeling.

## Introduction

The endosomal sorting complex required for transport (ESCRT) pathway mediates topologically unique membrane budding events. In multivesicular body (MVB) biogenesis, ESCRT-0, I and II sort ubiquitinated cargo by binding ubiquitin and endosomal lipids. ESCRT-III assembles into spiraling polymers for cargo sequestration, and together with the AAA-ATPase Vps4, remodels the membranes to generate cargo-laden intraluminal vesicles (ILVs).

ESCRT-III is a metastable and conformationally dynamic hetero-polymer of four “core” subunits of Vps20, Snf7/Vps32, Vps24 and Vps2 (Babst et al., 2002a). All subunits share a common domain organization of an N-terminal helical core domain and a flexible C-terminus, but provide distinct functions. ESCRT-II engages Vps20 to nucleate the polymerization of the most abundant ESCRT-III subunit, Snf7, which then recruits Vps24 and Vps2 (Teis et al., 2008). Finally, Vps2 engages Vps4 for ESCRT-III disassembly (Obita et al., 2007).

How is Snf7 activated to promote ESCRT-III assembly and cargo sequestration? Previous studies have shown that ESCRT-II and Vps20 modulate Snf7 protofilaments, emphasizing a role of the upstream ESCRTs in defining the assembly and architecture of the ESCRT-III complex (Henne et al., 2012; Teis et al., 2010). Recently, I have determined X-ray crystal structures of Snf7 protofilaments in the active conformation (Tang et al., 2015). Here, using genetics and biochemistry, I identify two parallel ubiquitin-dependent pathways that regulate Snf7 activation through both the Snf7 N-terminal core domain and the C-terminal  $\alpha$ 6 helix, providing an enhanced understanding of the activation of ESCRT-III-mediated membrane remodeling at endosomes.

## Results

### The $\alpha$ 1/2 Hairpin Confers Vps20 with a Unique Identity

Although Vps20 and Snf7 display a high degree of homology, they cannot complement each other. In order to identify regions of Vps20 essential for its function, a series of Vps20-Snf7 chimeras was designed and analyzed by an established quantitative Mup1-pHluorin MVB sorting assay (Henne et al., 2012). Although a full-length Vps20 is required for function, retaining only the  $\alpha$ 1/2 hairpin of Vps20 while replacing the remainder of Vps20 with Snf7 ( $Vps20^{1-105}$ - $Snf7^{107-240}$ ) is sufficient for sorting, albeit at ~70% efficiency (Figures 4.1A and 4.2A-D), suggesting that  $\alpha$ 1/2 is the minimal region unique to Vps20. This is consistent with the role of  $\alpha$ 1 of Vps20 in binding to the ESCRT-II subunit Vps25 (Im et al., 2009).

### Screening for Vps20-independent Snf7 Activation Mutants

To investigate the role of Vps20 in nucleating Snf7 *in vivo*, Nicholas J. Buchkovich and I next applied an unbiased random mutagenic approach. We performed error-prone polymerase chain reaction on *SNF7* and selected mutants that suppress the *vps20Δ* phenotype by growth on L-canavanine (Figure 4.1B). Two *snf7* point mutations in conserved residues, *snf7<sup>Q90L</sup>* and *snf7<sup>N100I</sup>*, showed a partial rescue of the canavanine sensitivity of *vps20Δ* (Figures 4.1C-D). Remarkably, in “closed” Snf7, Gln90 of  $\alpha$ 2 is proximal to  $\alpha$ 4 (Tang et al., 2015), and Asn100 is an asparagine cap of the  $\alpha$ 2 helix (Figure 4.1E). I propose that these mutations destabilize closed Snf7 by displacing  $\alpha$ 4 from  $\alpha$ 2 and extending the  $\alpha$ 2/3 helix.

Since conformationally active Snf7 resides on membranes, I performed liposome sedimentation assays. As predicted, Q90L enhances Snf7 membrane association from 41% to 78% (Figure 4.1F). To further identify whether these substitutions trigger “opening” in the core domain, I applied circular dichroism (CD) spectroscopy (Greenfield, 2006; Peter et al., 2004) on  $\text{Snf7}^{\alpha 1-\alpha 4}$ , a truncated Snf7 construct with reduced membrane binding compared to the full-length proteins (Buchkovich et al., 2013). In the presence of liposomes, I observed a decrease of the negative absorption band at 208 nm and an increase at 222 nm in Q90L and N100I mutants, indicating an increase of  $\alpha$ -helicity (Figure 4.1G). These data agree with the hypothesis that  $\text{Snf7}^{\text{Q90L}}$  and  $\text{Snf7}^{\text{N100I}}$  trigger structural rearrangements, where the  $\alpha 2/3$  loop becomes  $\alpha$ -helical and extends into one elongated  $\alpha$ -helix (Figures 4.3A-B) as observed in the open structures (McCullough et al., 2015; Tang et al., 2015). Notably, this structural rearrangement still occurs only upon membrane binding. Moreover,  $\text{snf7}^{\text{Q90L}}$  and  $\text{snf7}^{\text{N100I}}$  complement  $\text{snf7}\Delta$  *in vivo*, and  $\text{Snf7}^{\text{Q90L}}$  assembles into protofilaments *in vitro* (Figures 4.3C-D), confirming a functional role of the mutants in activating Snf7.

### **Auto-activated Snf7 Bypasses Vps20**

Given that  $\text{snf7}^{\text{Q90L}}$  and  $\text{snf7}^{\text{N100I}}$  only modestly suppress  $vps20\Delta$ , I hypothesized that a more stabilized “open” Snf7 on endosomal membranes would improve the suppression. I combined the activation mutations with R52E (Henne et al., 2012) to further trigger “opening”, and swapped  $\alpha 0$  of Snf7 with the N-terminal myristylation motif of Vps20 to enhance its membrane-binding affinity (Buchkovich et al., 2013). This yielded *myr-snft7*<sup>R52E Q90L</sup> and *myr-snft7*<sup>R52E Q90L N100I</sup>, hereafter denoted as  $\text{snf7}^{**}$  and

*snf7*\*\*\*, which sorted cargo with increased efficiencies, albeit not completely restoring wild-type levels (Figures 4.4A and 4.5A-C).

Consistent with these observations, the ESCRT-dependent cargo GFP-Cps1 partially localized to the vacuolar lumen in *vps20Δ* with *snf7*\*\* or *snf7*\*\*\* (Figure 4.4B), indicating a substantial level of MVB sorting. Moreover, *snf7*\*\* and *snf7*\*\*\* were also able to rescue the canavanine sensitivity of *vps20Δ* (Figure 4.4C). Thus, these *snf7* suppressors exhibit the ability to sort cargo at MVB.

To visualize whether the *snf7* suppressors could produce ILVs *in vivo*, I utilized a temperature sensitive allele of the vacuolar SNARE *vam7* to accumulate MVBs and examined yeast with thin-section TEM (Buchkovich et al., 2013; Sato et al., 1998) (Figure 4.4D). I observed that while ILVs in wild-type cells have a diameter of ~32 nm, *snf7*\*\* and *snf7*\*\*\* show a decrease in ILV number and an increase in ILV diameter to ~43 nm (Figures 4.4E-F, See Materials and Methods). Since ESCRT-II and Vps20 set the architecture of ESCRT-III, I propose that the variation in ILV size is a result of aberrant ESCRT-III architecture, although the possibility of changes in dynamics of ESCRT-III disassembly by Vps4 cannot be completely ruled out (Nickerson et al., 2010).

### **Auto-activated Snf7 Bypasses ESCRT-I and ESCRT-II**

Intrigued by the *vps20Δ* suppression, I next wanted to test if these auto-activated Snf7 mutants could also bypass the loss of other ESCRT components (Figure 4.6A). Among them, the downstream ESCRT-III subunits Vps24 and Vps2 are known to modulate Snf7 architecture (Henne et al., 2012; Teis et al., 2008) and recruit the AAA-

ATPase Vps4 via their C-terminal MIM motifs for ESCRT-III disassembly (Obita et al., 2007). I found that auto-activated Snf7 does not suppress *vps24Δ*, *vps2Δ* or *vps4Δ* (Figures 4.6B and 4.7A). This is consistent with the role of the suppressors in activating but not modulating or disassembling Snf7 filaments, reinforcing the division of labor among ESCRT-III subunits.

Previous studies showed that ESCRT-III assembly is regulated by ESCRT-II (Henne et al., 2012; Teis et al., 2010) (Figure 4.6A). ESCRT-II is a Y-shaped heterotetramer of Vps36, Vps22 and two Vps25 (arms). Vps36 GLUE domain binds ubiquitinated cargo and endosome-specific phosphatidylinositol 3-phosphate, PI3P; and each Vps25 “arm” binds one molecule of the ESCRT-III nucleator, Vps20. Since repurposing Snf7 to bind ESCRT-II does not improve the suppression (Figure 4.7B), I next tested the functionality of the suppressors in ESCRT-II single and double deletion mutants. Strikingly, *snf7\*\** and *snf7\*\*\** resulted in better suppression in ESCRT-II deletion compared to *vps20Δ*, with sorting efficiencies of ~60%-70% (Figures 4.6C, 4.7C and 4.8A).

I next tested ESCRT-I mutants. ESCRT-I is a heterotetramer of Vps23, Vps28, Vps37 and Mvb12. Vps23 UEV domain recognizes ubiquitinated cargo, Vps37 N-terminal helix binds to membranes, and Vps28 CTD engages Vps36 GLUE domain of ESCRT-II. I expressed the suppressors in ESCRT-I single and ESCRT-I/II double deletion mutants and we observed near wild-type sorting efficiencies (Figures 4.6D and 4.8B) with enlarged ILV sizes (Figures 4.8C-E). Our data suggest that ESCRT-I and ESCRT-II set up the ESCRT-III architecture to program vesicle dimension.

## Auto-activated Snf7 Does Not Bypass Bro1 and ESCRT-0

Because ESCRT-I and ESCRT-II cluster ubiquitinated cargo prior to their packaging into ILVs, the observed suppression indicated that the auto-activated Snf7 might sort cargo in a ubiquitin-independent manner. I next tested whether auto-activated Snf7 could bypass the remaining ubiquitin-binding ESCRT components, ESCRT-0 (Vps27 and Hse1) and, the yeast ALIX ortholog, Bro1/Vps31. Interestingly, the engineered *snf7* suppressors do not sort cargo in *vps27Δ* or *bro1Δ* (Figures 4.6E and 4.6G), or *hse1Δ* in combination with *vps20Δ*, *vps25Δ* (ESCRT-II) or *vps23Δ* (ESCRT-I) (Figure 4.6F). To test whether ubiquitin-binding of ESCRT-0 and Bro1 is critical, we expressed ubiquitin-binding mutants *vps27<sup>S270D S313D</sup>* (*vps27<sup>UIM</sup>*) and *bro1<sup>I377R L386R</sup>* (*bro1<sup>UBD</sup>*) (Bilodeau et al., 2002; Pashkova et al., 2013). They reduced the functionality of *snf7\*\*\** in *vps20Δ*, *vps25Δ* or *vps23Δ* (Figures 4.9D and 4.10A). These data suggest that despite the ESCRT-I/II-independence, the suppression is still ubiquitin-dependent (Figures 4.9A-C), perhaps through another subset of machinery of ESCRT-0 and Bro1. I thus propose that ESCRT-0/Bro1 are required to sort ubiquitinated cargo for ESCRT-III sequestration in parallel to ESCRT-I/II.

## Bro1 Binds to Snf7 α6 Helix and Activates Snf7

Bro1 has been shown to directly interact with Snf7, and X-ray crystal structures suggest that the C-terminal α6 helix of Snf7 binds to the Bro1 domain of Bro1 (Kim et al., 2005b; McCullough et al., 2008; Wemmer et al., 2011). To test whether this interaction is required for *snf7* suppression, I mutated residues at the Snf7-Bro1 interface. Notably, neither the Bro1-binding defective Snf7\*\*\*<sup>L231K L234K</sup> mutant (*snf7\*\*\**

*BRO1*), nor the Snf7-binding defective Bro1<sup>I144D L336D</sup> mutant (*bro1<sup>SNF7</sup>*), suppresses *vps20Δ*, *vps25Δ* or *vps23Δ* (Figures 4.9E and 4.10B). This strongly suggests that α6 of Snf7 is also auto-inhibitory, and that a physical binding between Snf7 α6 and Bro1 is a prerequisite for Snf7 activation.

I next tested if the Snf7-Bro1 interaction would release the α6 auto-inhibition. While the recombinant Snf7<sup>WT</sup> does not assemble due to auto-inhibition, coincubation with Bro1 resulted in Snf7 protofilament assembly (Figure 4.10C), indicating that Bro1 directly triggers Snf7 activation. In agreement with this, the α6 truncated Snf7 (Snf7<sup>1-225</sup>) releases auto-inhibition and assembles into protofilaments (Figure 4.10D). Therefore, my data suggest that while Snf7 N100I, Q90L, and R52E release auto-inhibition in α3, α4, and α5, respectively, α6 of Snf7 is also auto-inhibitory and its activation is Bro1-dependent (Figure 4.10E).

## Discussion

The ancient and conserved ESCRT-III membrane-remodeling machinery plays a critical role in numerous fundamental cellular processes, including MVB biogenesis, viral budding and cytokinesis. Building on my previous study (Tang et al., 2015), we focused on the predominant ESCRT-III subunit, Snf7, to understand the molecular mechanisms governing ESCRT-III for its dynamic conversion from an auto-inhibited soluble monomer to a membrane-bending polymer. Remarkably, a recent cryo-EM study on ESCRT-III IST1/CHMP1B co-polymer suggested that CHMP1B (Did2/Vps46) undergoes a similar structural rearrangement for assembly (McCullough et al., 2015), implying that the core domain extension is a common theme of ESCRT-III activation.

Here, using a mutagenic approach, I identified novel Snf7 point mutations that release the auto-inhibition of  $\alpha$ 3 and  $\alpha$ 4 as observed in the conformationally open structures. Surprisingly, this leads to Snf7 activation that functionally bypasses the ESCRT-III nucleator Vps20, as well as the ESCRT-II and ESCRT-I complexes. This suggests that Snf7, along with its downstream ESCRT components, Vps24, Vps2 and Vps4, but not ESCRT-I/II, are among the minimal machinery required for membrane remodeling.

My data suggest that ESCRT-III activation is mediated by two parallel pathways, ESCRT-I/II and ESCRT-0/Bro1 (Figure 4.10F). Bro1, directly triggers ESCRT-III assembly by binding to the C-terminal  $\alpha$ 6 of Snf7 (Figure 4.10C). Given that ESCRT-0 directly engages Bro1 (Lee et al., 2016) to recognize ubiquitinated cargo (Pashkova et al., 2013), I showed that Snf7  $\alpha$ 6 binding to Bro1 relieves autoinhibititon of Snf7. This adds to the roles for Bro1, besides its recruitment of the Doa4 deubiquitinase in the MVB pathway (Luhtala and Odorizzi, 2004).

Consistent with my observation, a very recent study suggested that ALIX and ESCRT-I/II function as parallel CHMP4B (Snf7 ortholog in human) recruiters in cytokinetic abscission (Christ et al., 2016).

While biochemical data suggest that Snf7 can be activated by specific point mutations in the core domain or truncation at the C-terminus *in vitro*, my genetic evidence indicate that the conformational equilibrium of Snf7 is tightly regulated by two pathways *in vivo* to achieve ubiquitin-dependent cargo sorting at endosomes: 1) ESCRT-I/ESCRT-II/Vps20 activates the N-terminal core domain of Snf7; 2) ESCRT-0/Bro1 activates the C-terminal  $\alpha$ 6 of Snf7 (Figures 4.10E-F). These results provide

novel insights into a two-stage activation pathway for ESCRT-III-mediated membrane remodeling.

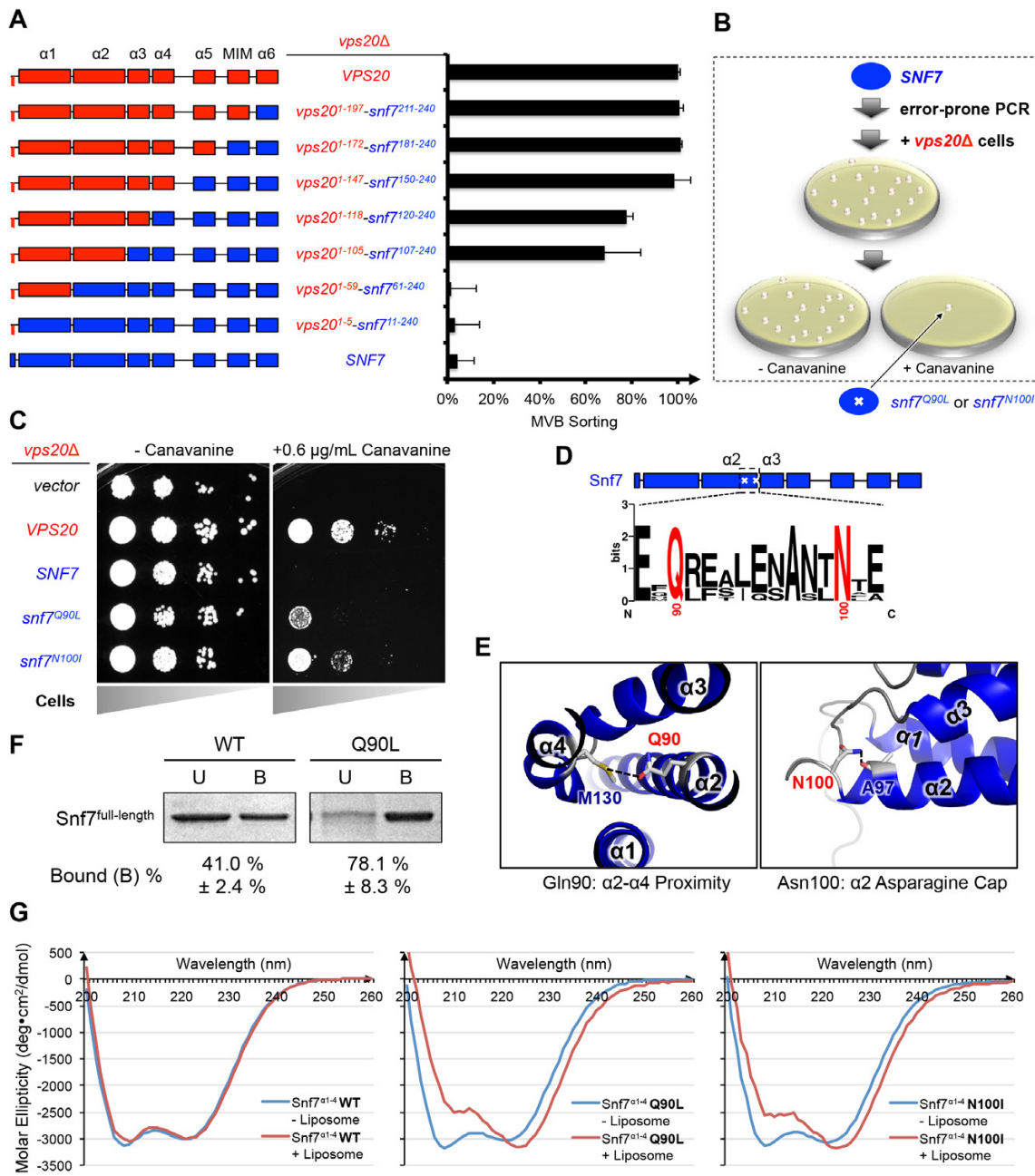


**Figure 4.1 Novel Snf7 Point Mutations Trigger Core Domain Activation**

### Figure 4.1 Novel Snf7 Point Mutations Trigger Core Domain Activation

- (A) Domain organization of Vps20(red)-Snf7(blue) chimera (left) and quantitative MVB sorting data (right) for *vps20Δ* yeast exogenously expressing *VPS20*, *vps20<sup>1-197</sup>-snf7<sup>211-240</sup>*, *vps20<sup>1-172</sup>-snf7<sup>181-240</sup>*, *vps20<sup>1-147</sup>-snf7<sup>150-240</sup>*, *vps20<sup>1-118</sup>-snf7<sup>120-240</sup>*, *vps20<sup>1-105</sup>-snf7<sup>107-240</sup>*, *vps20<sup>1-59</sup>-snf7<sup>61-240</sup>*, *vps20<sup>1-5</sup>-snf7<sup>11-240</sup>*, and *SNF7*. Error bars represent standard deviations from 3-5 independent experiments.
- (B) Screening strategy to identify *snf7* suppressors in *vps20Δ* yeast.
- (C) Canavanine sensitivity assay for *vps20Δ* yeast exogenously expressing empty vector, *VPS20*, *SNF7*, *snf7<sup>Q90L</sup>*, and *snf7<sup>N100I</sup>*.
- (D) Domain organization of Snf7, with the locations of Gln90 and Asn100. WebLogo of protein sequence analysis (Doerks et al., 2002) of Snf7 orthologs from *Saccharomyces cerevisiae*, *Homo sapiens*, *Mus musculus*, *Xenopus laevis*, *Drosophila melanogaster*, *Caenorhabditis elegans*, *Schizosaccharomyces pombe*.
- (E) Close-up view of the side chain interactions of Gln90 (left) and Asn100 (right) in a “closed” Snf7 homology model (Henne et al., 2012).
- (F) Liposome sedimentation assays of *Snf7<sup>WT</sup>* and *Snf7<sup>Q90L</sup>*. Liposome-bound (B) proteins and unbound (U) proteins.
- (G) CD scanning spectra from 200nm to 260nm of wild-type *Snf7<sup>α1-4</sup>* (left), *Snf7<sup>α1-4 Q90L</sup>* (middle), and *Snf7<sup>α1-4 N100I</sup>* proteins with (red) and without (blue) liposomes.

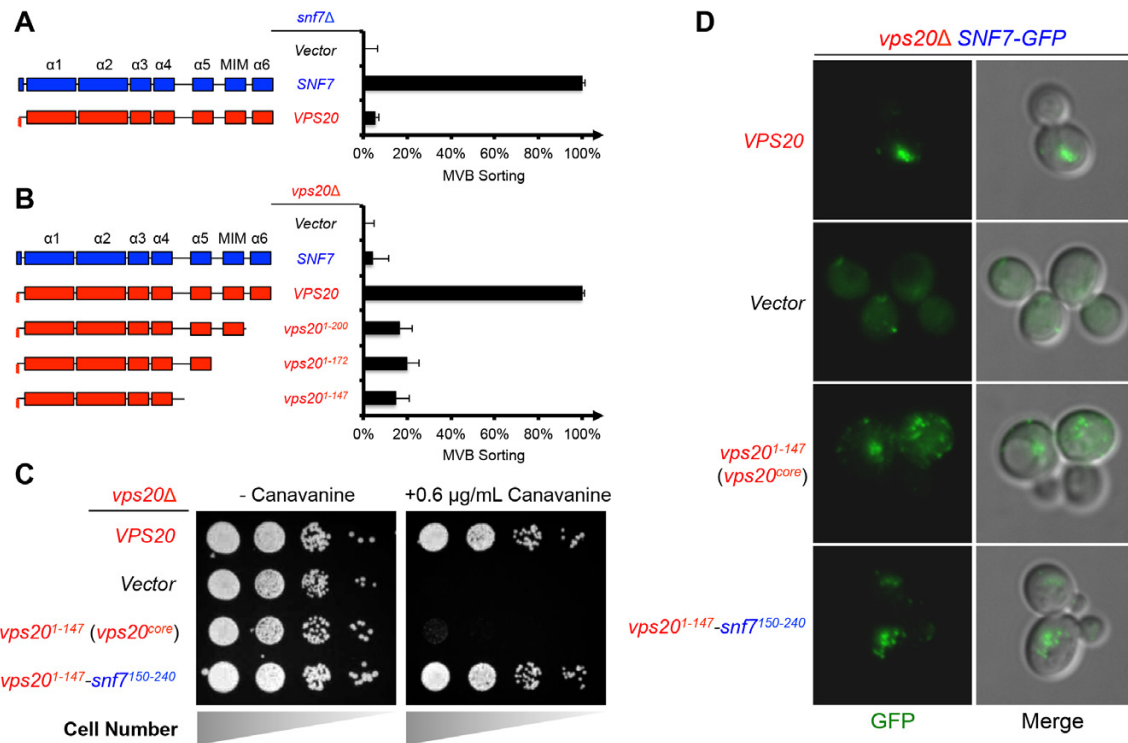


**Figure 4.2 Vps20-Snf7 Chimera Complements Vps20 Function**

### Figure 4.2. Vps20-Snf7 Chimera Complements Vps20 Function

(A-B) Domain organization (left) and quantitative MVB sorting data (right) for (A) *snf7Δ* yeast exogenously expressing empty vector, *SNF7*, and *VPS20*, and for (B) *vps20Δ* yeast exogenously expressing empty vector, *SNF7*, *VPS20*, *vps20<sup>1-200</sup>*, *vps20<sup>1-172</sup>*, and *vps20<sup>1-147</sup>*. Error bars represent standard deviations from 3-5 independent experiments.

(C) Canavanine sensitivity assay for *vps20Δ* yeast exogenously expressing *VPS20*, empty vector, *vps20<sup>1-147</sup>*, and *vps20<sup>1-147</sup>-snf7<sup>150-240</sup>*.

(D) Representative images of *vps20Δ SNF7-GFP* yeast exogenously expressing *VPS20*, empty vector, *vps20<sup>1-147</sup>*, and *vps20<sup>1-147</sup>-snf7<sup>150-240</sup>*. GFP images (left) and composite images of GFP and DIC (right).

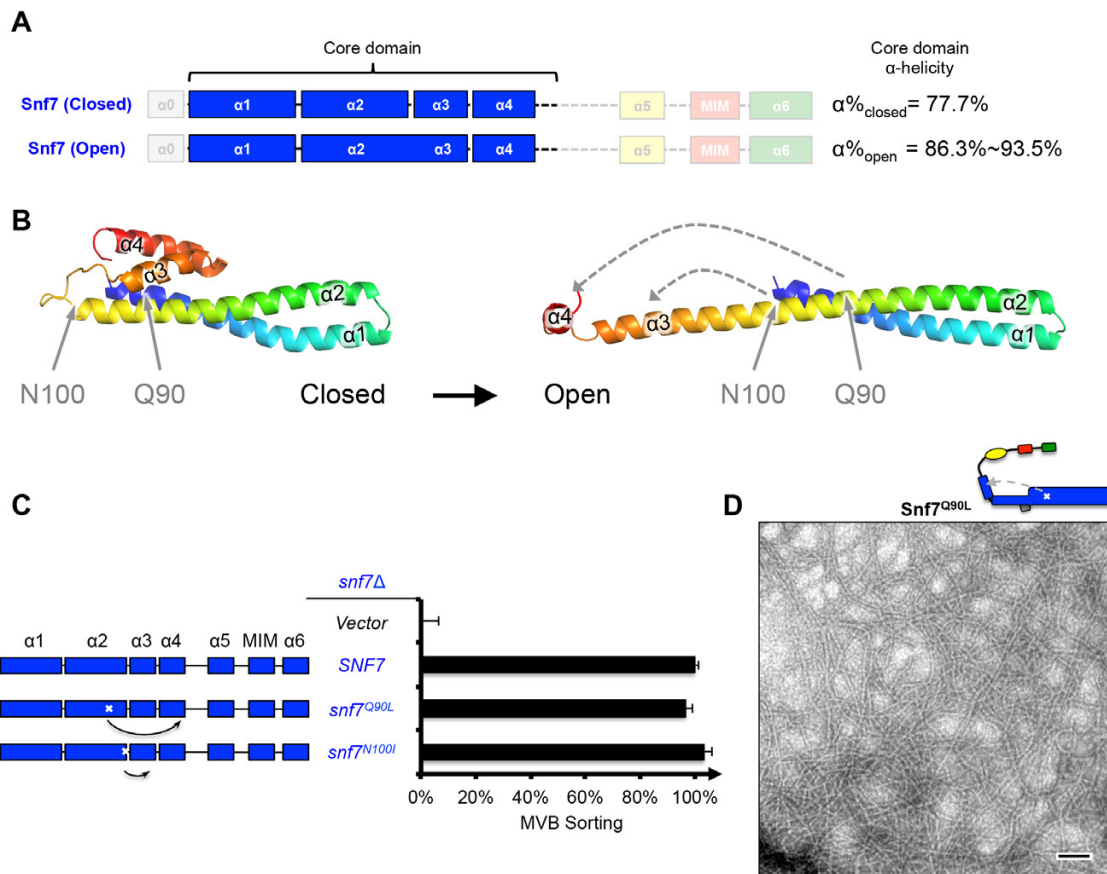


**Figure 4.3 Snf7<sup>Q90L</sup> and Snf7<sup>N100I</sup> Trigger Core Domain Activation**

### Figure 4.3 Snf7<sup>Q90L</sup> and Snf7<sup>N100I</sup> Trigger Core Domain Activation

- (A) Domain organization of Snf7 closed and open conformations, highlighting the core domain.
- (B) Ribbon models of Snf7 closed (homology) (Henne et al., 2012) and open conformations (right, PDB: 5FD9), with the locations of Gln90 and Asn100.
- (C) Domain organization and quantitative MVB sorting data (left) for *snf7Δ* yeast exogenously expressing empty vector, *SNF7*, *snf7<sup>Q90L</sup>*, and *snf7<sup>N100I</sup>*. Error bars represent standard deviations from 3-5 independent experiments.
- (D) Representative TEM images (right) of Snf7<sup>Q90L</sup>. Scale bars 100 nm.

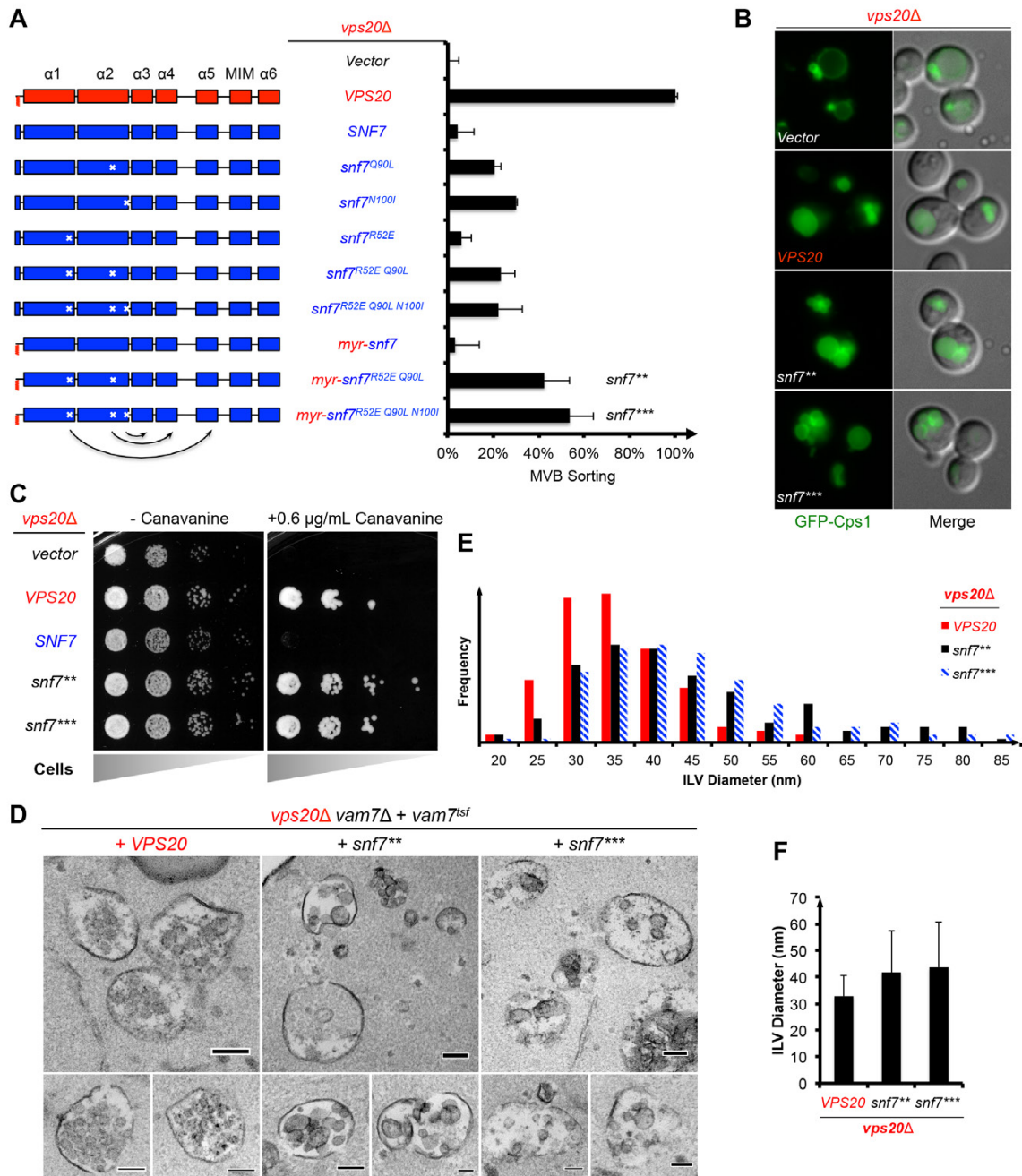


**Figure 4.4 Auto-activated Snf7 Functionally Bypasses Vps20**

#### Figure 4.4 Auto-activated Snf7 Functionally Bypasses Vps20

(A) Domain organization of Snf7 mutants (left) and quantitative MVB sorting data (right) for *vps20Δ* yeast exogenously expressing empty vector, *VPS20*, *SNF7*, *snf7<sup>Q90L</sup>*, *snf7<sup>N100I</sup>*, *snf7<sup>R52E</sup>*, *snf7<sup>R52E Q90L</sup>*, *snf7<sup>R52E Q90L N100I</sup>*, *myr-sn7*, *myr-sn7<sup>R52E Q90L</sup>*, and *myr-sn7<sup>R52E Q90L N100I</sup>*. Error bars represent standard deviations from 3-5 independent experiments. The data of *myr-sn7* (*vps20<sup>1-5</sup>-snf7<sup>11-240</sup>*) and *SNF7* were re-plotted from Figure 4.1A. Mutants *myr-sn7<sup>R52E Q90L</sup>* and *myr-sn7<sup>R52E Q90L N100I</sup>* are referred to *snf7\*\** and *snf7\*\*\**, respectively.

(B) Representative images of *vps20Δ* yeast exogenously expressing GFP-CPS1 with *VPS20*, *snf7\*\**, and *snf7\*\*\**. GFP images (left) and composite images of GFP and DIC (right).

(C) Canavanine sensitivity assay for *vps20Δ* yeast exogenously expressing empty vector, *VPS20*, *SNF7*, *snf7\*\**, and *snf7\*\*\**.

(D) Representative TEM images of ILV-containing MVBs from *vps20Δ vam7Δ* yeast exogenously expressing *vam7<sup>tsf</sup>*, with *VPS20*, *snf7\*\**, and *snf7\*\*\**. Scale bars 100 nm.

(E-F) Quantitation of ILV (N=150 ILV summed per sample) outer diameter from (D) in frequency distributions (E), and averaged measurements (F). Error bars represent standard deviations.

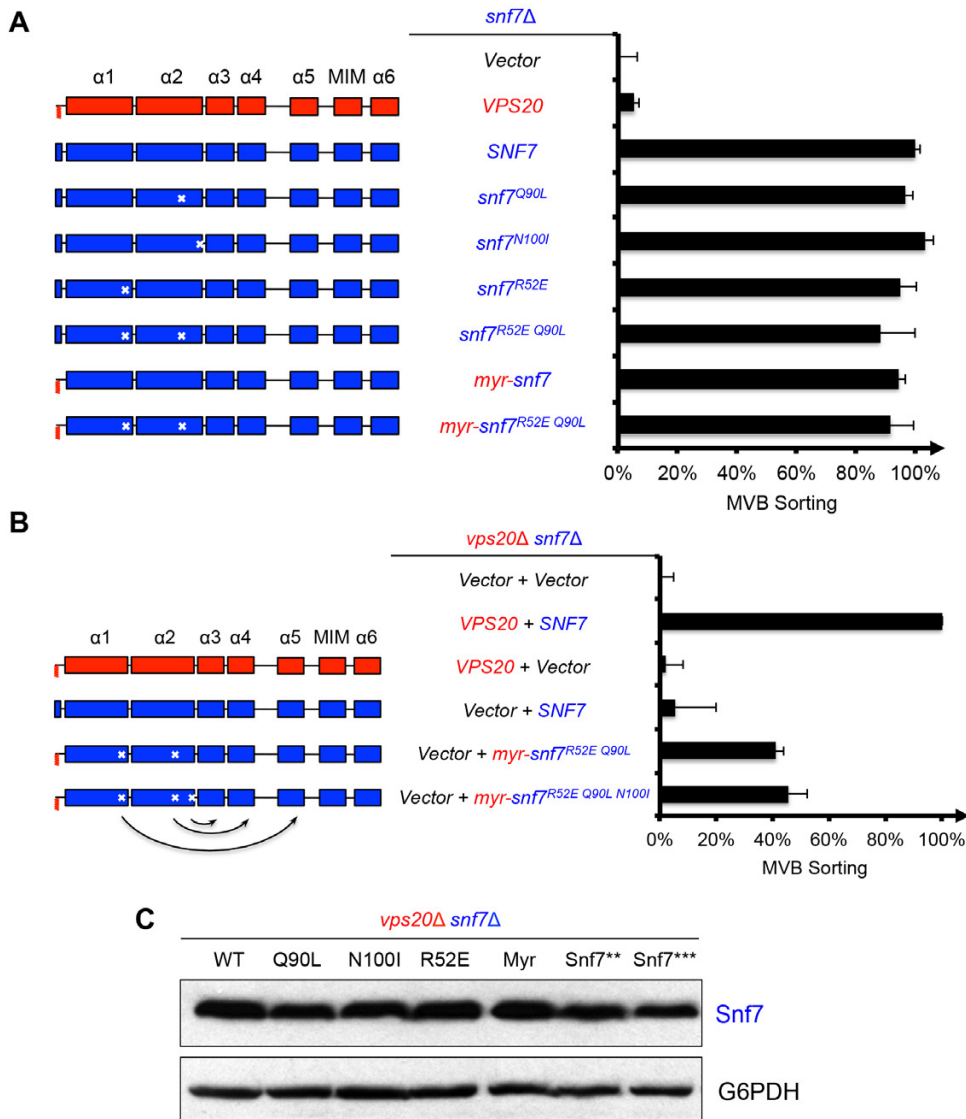


**Figure 4.5 Activation Mutants Suppress *snf7Δ* and *vps20Δ snf7Δ* *in vivo***

### Figure 4.5 Activation Mutants Suppress *snf7Δ* and *vps20Δ snf7Δ* *in vivo*

(A) Domain organization of Snf7 mutants (left) and quantitative MVB sorting data (right) for *snf7Δ* yeast exogenously expressing empty vector, *VPS20*, *SNF7*, *snf7<sup>Q90L</sup>*, *snf7<sup>N100I</sup>*, *snf7<sup>R52E</sup>*, *snf7<sup>R52E Q90L</sup>*, *myr-snf7*, and *myr-snf7<sup>R52E Q90L</sup>*. Error bars represent standard deviations from 3-5 independent experiments. The data from *snf7<sup>Q90L</sup>* and *snf7<sup>N100I</sup>* were partially re-plotted from Figure 4.4C for comparison.

(B) Domain organization of Snf7 mutants (left) and quantitative MVB sorting data (right) for *vps20Δ snf7Δ* yeast exogenously expressing empty vector and empty vector, *VPS20* and *SNF7*, *VPS20* and empty vector, empty vector and *SNF7*, empty vector and *myr-snf7<sup>R52E Q90L</sup>*, and empty vector and *myr-snf7<sup>R52E Q90L N100I</sup>*. Error bars represent standard deviations from 3-5 independent experiments.

(C) Western blotting analyses of *vps20Δ snf7Δ* yeast expressing *SNF7*, *snf7<sup>Q90L</sup>*, *snf7<sup>N100I</sup>*, *snf7<sup>R52E</sup>*, *myr-snf7*, *snf7<sup>\*\*</sup>*, and *snf7<sup>\*\*\*</sup>*. G6PDH used as loading controls.

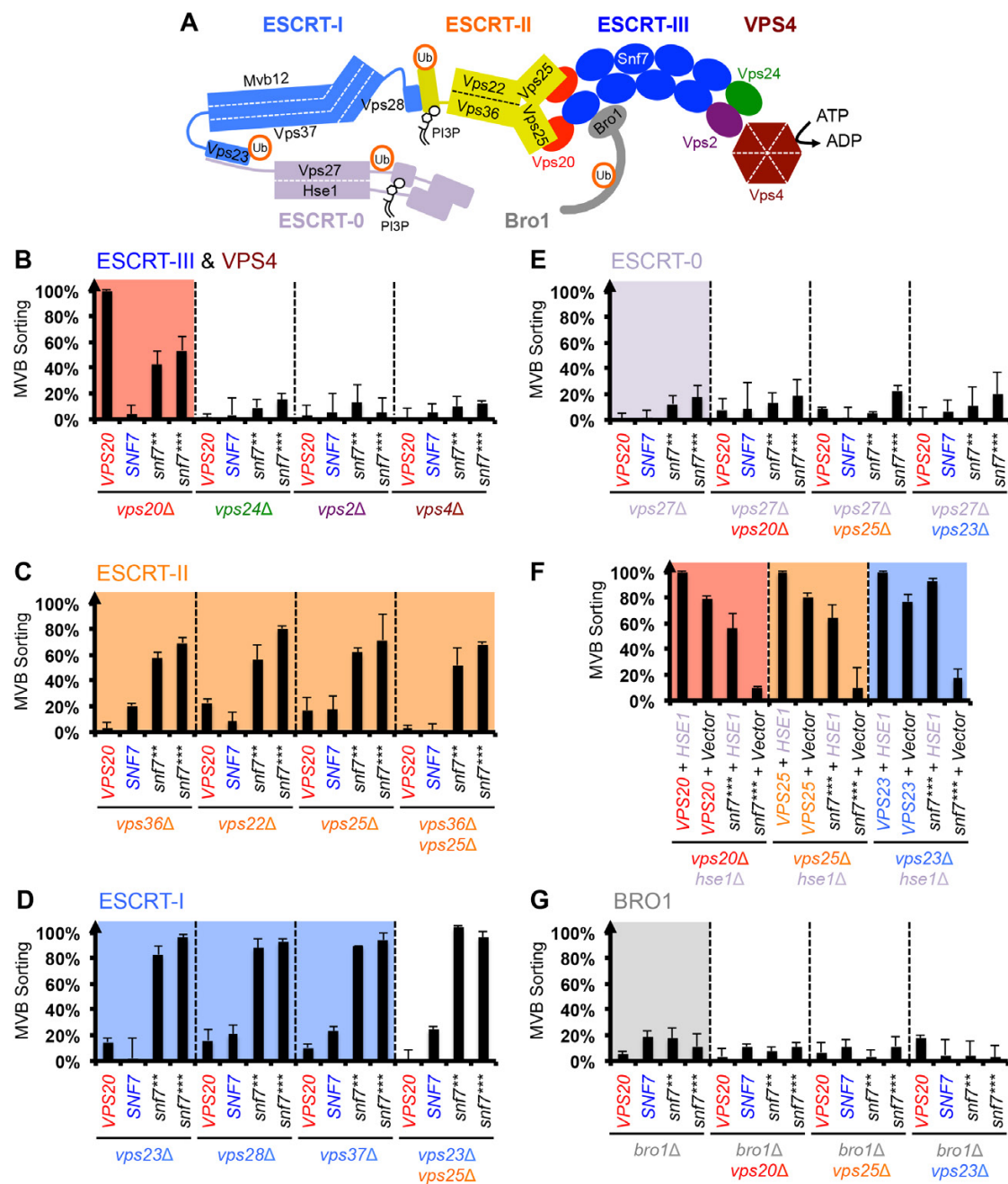


**Figure 4.6 Snf7 Core Domain Auto-activation Bypasses ESCRT-I and ESCRT-II**

## Figure 4.6 Snf7 Core Domain Auto-activation Bypasses ESCRT-I and ESCRT-II

(A) Cartoon of the ESCRT pathway in MVB Biogenesis.  
(B-D & F-G) Quantitative MVB sorting data for (B) *vps20Δ*, *vps24Δ*, *vps2Δ* and *vps4Δ* yeast, (C) *vps36Δ*, *vps22Δ*, *vps25Δ* and *vps36Δ vps25Δ* yeast, (D) *vps23Δ*, *vps28Δ*, *vps37Δ* and *vps23Δ vps25Δ* yeast, (E) *vps27Δ*, *vps27Δ vps20Δ*, *vps27Δ vps25Δ* and *vps27Δ vps23Δ* yeast, (G) *bro1Δ*, *bro1Δ vps20Δ*, *bro1Δ vps25Δ* and *bro1Δ vps23Δ* yeast exogenously expressing *VPS20*, *SNF7*, *snf7\*\**, and *snf7\*\*\**, respectively. The data from *vps20Δ* were partially re-plotted from Figure 4.4A for comparison.  
(F) Quantitative MVB sorting data for *vps20Δ hse1Δ*, *vps25Δ hse1Δ*, and *vps23Δ hse1Δ* yeast exogenously expressing *VPS20/VPS25/VPS23* and *HSE1*, and *VPS20/VPS25/VPS23* and empty vector, *snf7\*\*\** and *HSE1*, and *snf7\*\*\** and empty vector, respectively. Error bars represent standard deviations from 3-5 independent experiments.

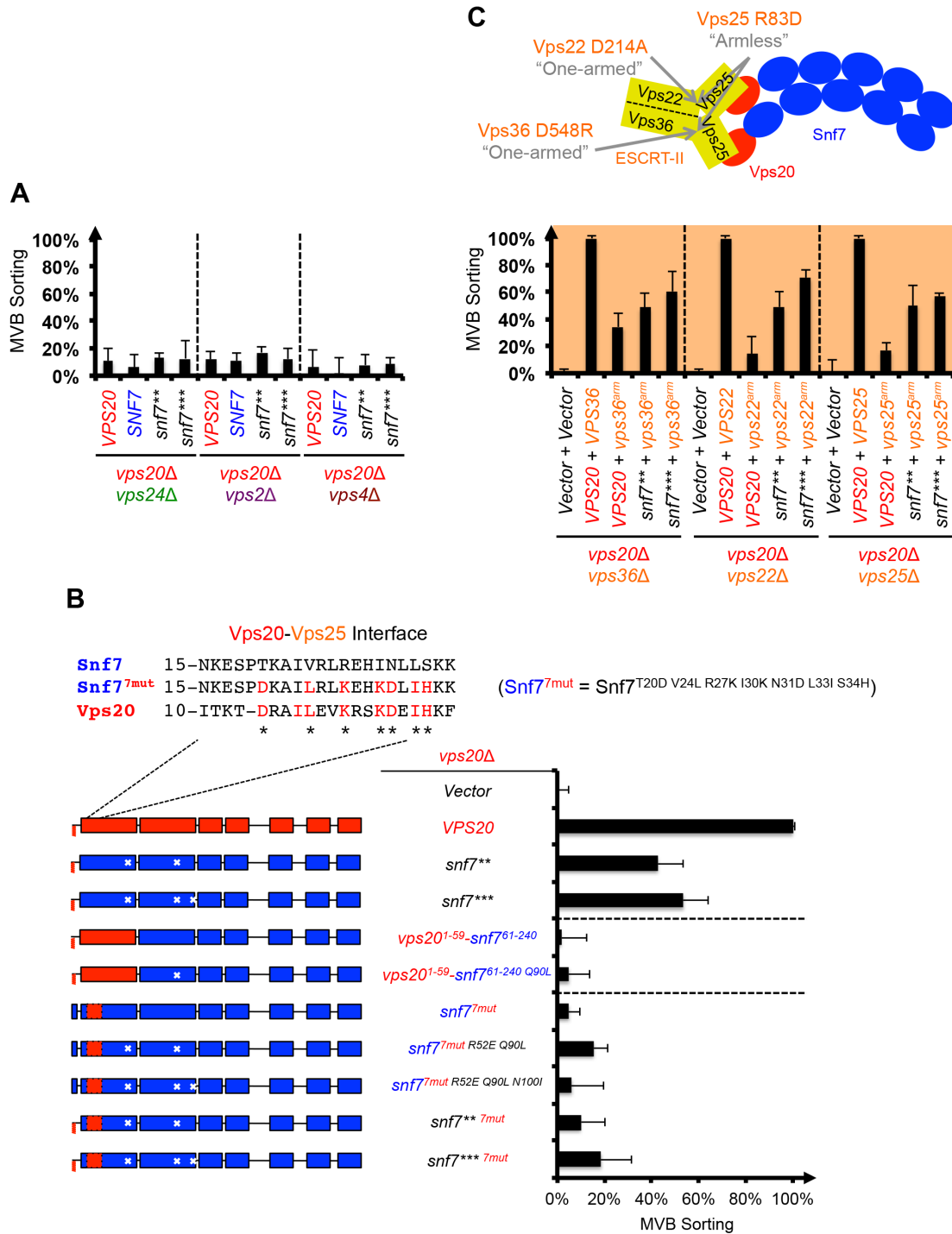


**Figure 4.7 Snf7 Core Domain Auto-activation Does Not Suppresses *vps24Δ*, *vps2Δ* and *vps4Δ* But Suppresses ESCRT-II Arm Mutants**

**Figure 4.7 Snf7 Core Domain Auto-activation Does Not Suppresses *vps24Δ*, *vps2Δ* and *vps4Δ* But Suppresses ESCRT-II Arm Mutants**

(A) Quantitative MVB sorting data for *vps20Δ vps24Δ*, *vps20Δ vps2Δ* and *vps20Δ vps4Δ* yeast exogenously expressing *VPS20*, *SNF7*, *snf7\*\**, and *snf7\*\*\**, respectively. Error bars represent standard deviations from 3-5 independent experiments.

(B) Multiple sequence alignment between *Saccharomyces cerevisiae* Snf7 and Vps20 and rational design of Snf7<sup>7mut</sup>. Quantitative MVB sorting data for *vps20Δ* yeast exogenously expressing empty vector, *VPS20*, *snf7\*\**, *snf7\*\*\**, *vps20<sup>1-59</sup>-snf7<sup>61-240</sup>*, *vps20<sup>1-59</sup>-snf7<sup>61-240 Q90L</sup>*, *snf7<sup>T20D V24L R27K I30K N31D L33I S34H</sup>* (*snf7<sup>7mut</sup>*), *snf7<sup>7mut R52E Q90L</sup>*, *snf7<sup>7mut R52E Q90L N100I</sup>*, *snf7\*\* 7mut*, and *snf7\*\*\* 7mut*. Error bars represent standard deviations from 3-5 independent experiments. The data of *snf7\*\** and *snf7\*\*\** were partially re-plotted from Figure 4.4A and *vps20<sup>1-59</sup>-snf7<sup>61-240</sup>* from Figure 4.1A for comparison.

(C) Cartoon diagram of ESCRT-II Arms. Quantitative MVB sorting data for *vps20Δ vps36Δ*, *vps20Δ vps22Δ* and *vps20Δ vps25Δ* yeast exogenously expressing empty vector and empty vector, *VPS20* and *VPS36/VPS22/VPS25*, *VPS20* and *vps36<sup>D548R</sup>* (*vps36<sup>arm</sup>*) / *vps22<sup>D214A</sup>* (*vps22<sup>arm</sup>*) / *vps25<sup>R83D</sup>* (*vps25<sup>arm</sup>*), *snf7\*\** and *vps36<sup>arm</sup>* / *vps22<sup>arm</sup>* / *vps25<sup>arm</sup>*, and *snf7\*\*\** and *vps36<sup>arm</sup>* / *vps22<sup>arm</sup>* / *vps25<sup>arm</sup>*, respectively. Error bars represent standard deviations from 3-5 independent experiments.

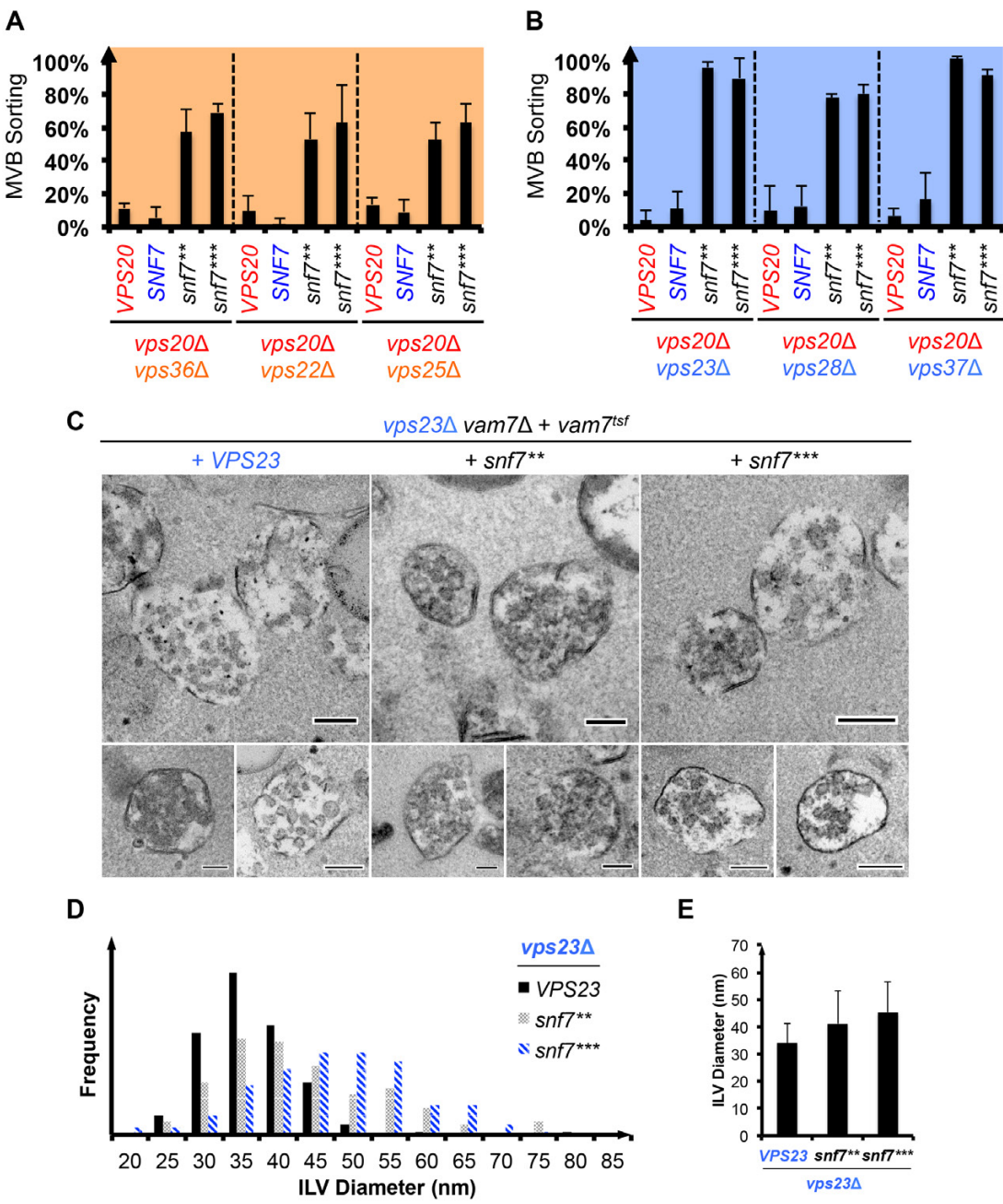
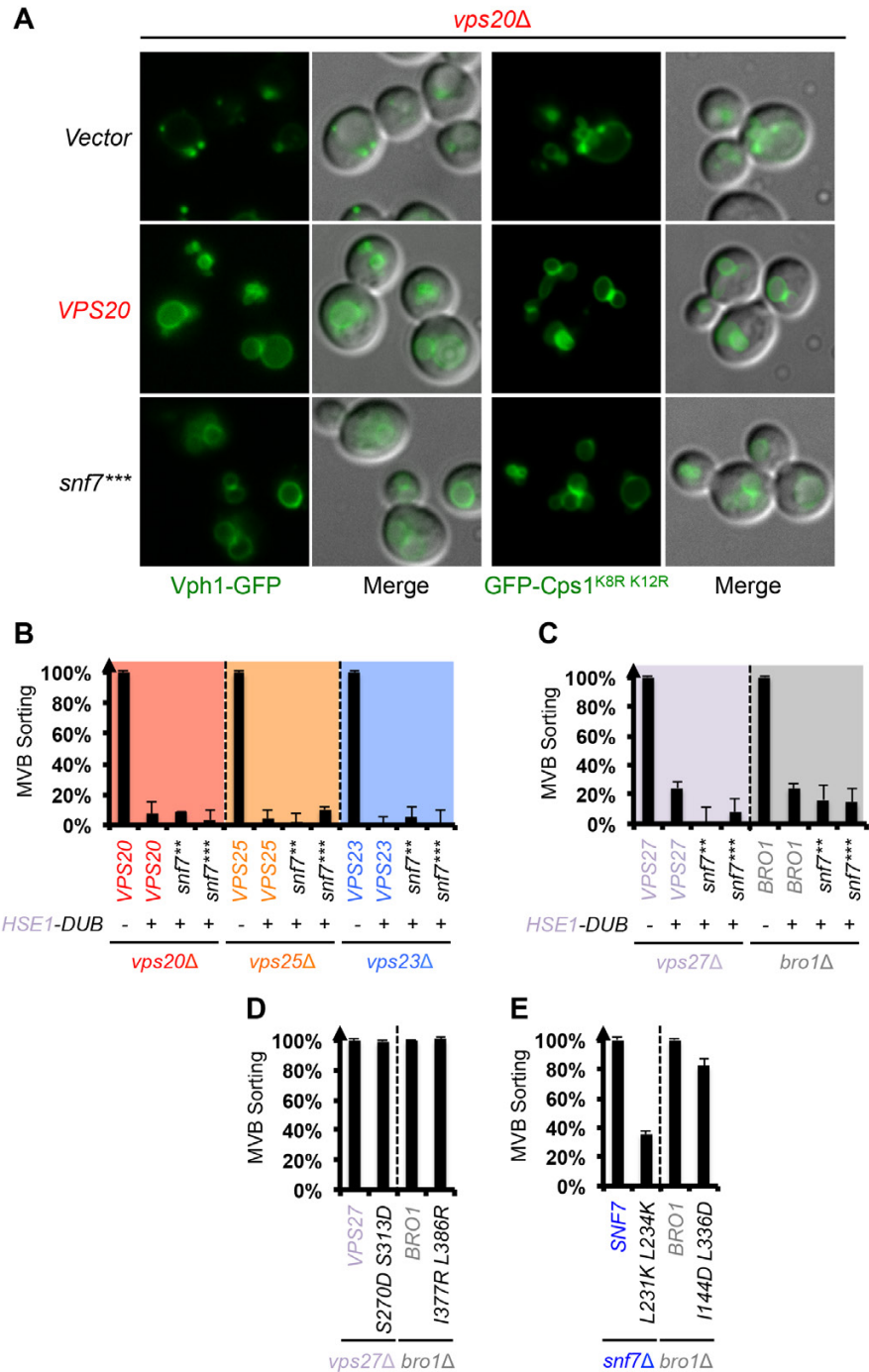


Figure 4.8 MVB Morphologies of *snf7\*\** and *snf7\*\*\** in ESCRT-I *vps23Δ*

**Figure 4.8 MVB Morphologies of *snf7*\*\* and *snf7*\*\*\* in ESCRT-I *vps23*Δ**

- (A) Quantitative MVB sorting data for *vps20*Δ *vps36*Δ, *vps20*Δ *vps22*Δ and *vps20*Δ *vps25*Δ yeast exogenously expressing VPS20, SNF7, *snf7*\*\*, and *snf7*\*\*\*, respectively. Error bars represent standard deviations from 3-5 independent experiments.
- (B) Quantitative MVB sorting data for *vps20*Δ *vps23*Δ, *vps20*Δ *vps28*Δ and *vps20*Δ *vps37*Δ yeast exogenously expressing VPS20, SNF7, *snf7*\*\*, and *snf7*\*\*\*, respectively. Error bars represent standard deviations from 3-5 independent experiments.
- (C) Representative TEM images of ILV-containing MVBs from *vps23*Δ *vam7*Δ yeast exogenously expressing *vam7*<sup>tsf</sup>, with VPS23, *snf7*\*\*, and *snf7*\*\*\*. Scale bars 100 nm.
- (D-E) Quantitation of ILV ( $N=150$  ILV summed per sample) outer diameter from (C) in frequency distributions (D), and averaged measurements (E). Error bars represent standard deviations.



**Figure 4.9 Snf7 Auto-activation Mutant Sort Cargo in a Ubiquitin-dependent Manner**

**Figure 4.9 Snf7 Auto-activation Mutant Sort Cargo in a Ubiquitin-dependent Manner**

- (A) Representative images of *vps20Δ* yeast exogenously expressing *VPH1-GFP* (left) and *GFP-CPS1<sup>K8R K12R</sup>* (right) with *VPS20*, and *snf7\*\*\**. GFP images and composite images of GFP and DIC.
- (B) Quantitative MVB sorting data for *vps20Δ*, *vps25Δ*, and *vps23Δ* yeast exogenously expressing *VPS20/VPS25/VPS23* with empty vector, and *VPS20/VPS25/VPS23, snf7\*\**, or *snf7\*\*\** with *HSE1-DUB*, respectively. Error bars represent standard deviations.
- (C) Quantitative MVB sorting data for *vps27Δ* and *bro1Δ* yeast exogenously expressing *VPS27/BRO1* with empty vector, and *VPS27/BRO1, snf7\*\**, or *snf7\*\*\** with *HSE1-DUB*, respectively. Error bars represent standard deviations.
- (D-E) Quantitative MVB sorting data for (D) *vps27Δ* yeast exogenously expressing *VPS27* and *vps27<sup>S270D S313D</sup>* and *bro1Δ* east exogenously expressing *BRO1* and *bro1<sup>I377R L386R</sup>*, and (E) *snf7Δ* yeast exogenously expressing *SNF7* and *snf7<sup>L231K L234K</sup>*, and *bro1Δ* east exogenously expressing *BRO1* and *bro1<sup>I144D L336D</sup>*. Error bars represent standard deviations from 3-5 independent experiments.

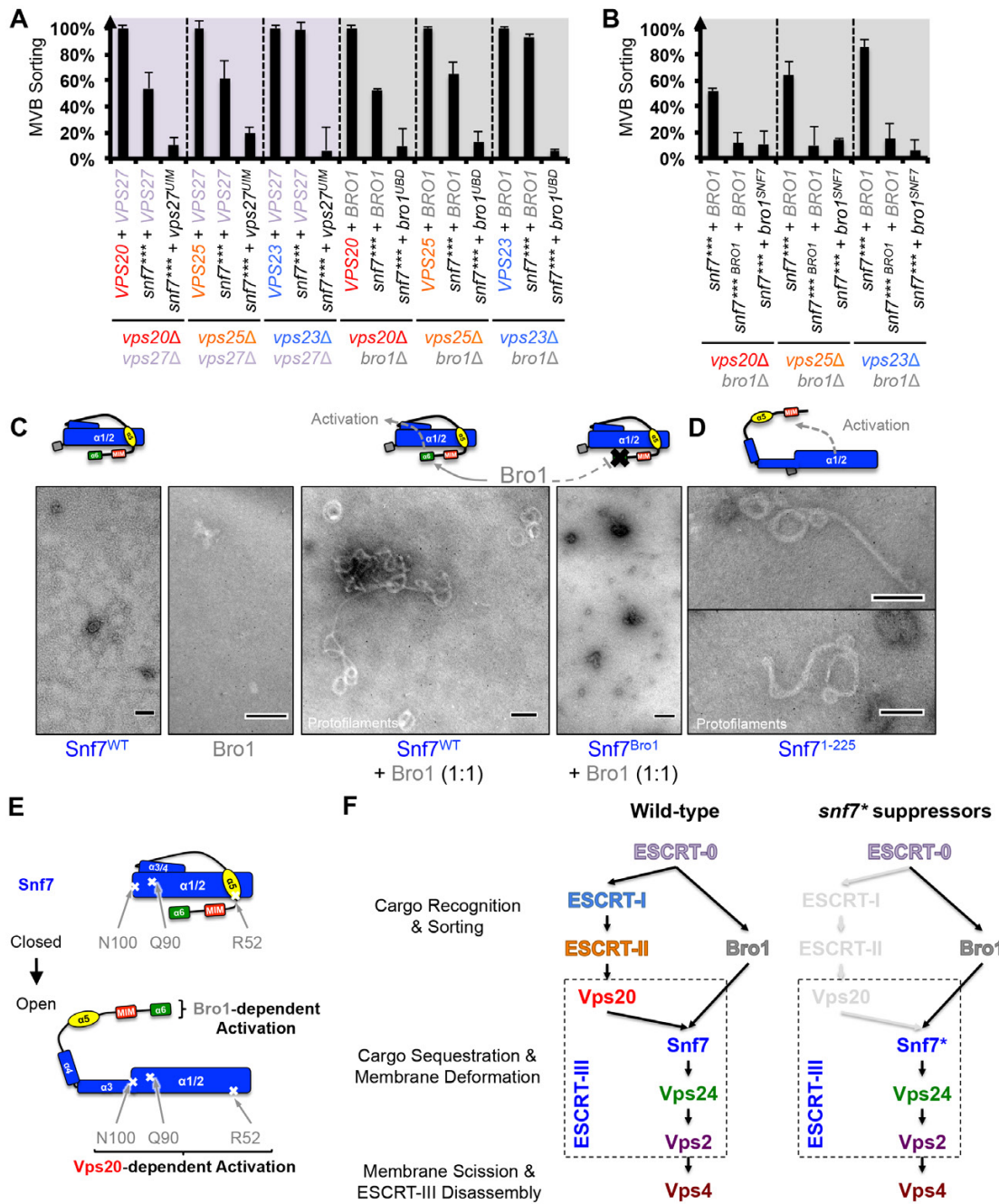


**Figure 4.10 Snf7 Activation of the Core Domain and the C-terminal α6**

### Figure 4.10 Snf7 Activation of the Core domain and the C-terminal $\alpha$ 6

(A-B) Quantitative MVB sorting data for (A)  $vps20\Delta vps27\Delta$ ,  $vps25\Delta vps27\Delta$ , and  $vps23\Delta vps27\Delta$  yeast exogenously expressing VPS20/VPS25/VPS23 and VPS27,  $snf7^{***}$  and VPS27, and  $snf7^{***}$  and  $vps27^{S270D S313D}$  ( $vps27^{UIM}$ ), and  $vps20\Delta bro1\Delta$ ,  $vps25\Delta bro1\Delta$ , and  $vps23\Delta bro1\Delta$  yeast exogenously expressing VPS20/VPS25/VPS23 and BRO1,  $snf7^{***}$  and BRO1, and  $snf7^{***}$  and  $bro1^{I377R L386R}$  ( $bro1^{UBD}$ ), respectively, and for (B)  $vps20\Delta bro1\Delta$ ,  $vps25\Delta bro1$ , and  $vps23\Delta bro1\Delta$  yeast exogenously expressing  $snf7^{***}$  and BRO1,  $snf7^{***L231K L234K}$  ( $snf7^{*** BRO1}$ ) and BRO1, and  $snf7^{***}$  and  $bro1^{I144D L336D}$  ( $bro1^{SNF7}$ ), respectively. Error bars represent standard deviations from 3-5 independent experiments.

(C-D) Representative TEM images of (C)  $Snf7^{WT}$ , Bro1, and  $Snf7^{WT}$  with Bro1 (1:1), and (D)  $Snf7^{1-225}$  and  $Snf7^{R52E}$ . Scale bars 100 nm. Cartoon diagrams of Snf7 activation.

(E) Cartoon diagrams of closed and open Snf7, with the locations of Vps20-dependent activation sites, Arg52, Gln90, and Asn100, and Bro1-dependent activation region,  $\alpha$ 6.

(F) Conceptual models of parallel ESCRT-III Snf7 activation pathways in MVB biogenesis of wild-type (left) and the core domain auto-activated Snf7 mutant,  $Snf7^*$  (right).

## **Materials and Methods**

### **Fluorescence Microscopy, Canavanine Plating Assay,**

### **Western Blotting, Protein Purification and Liposome Sedimentation**

Fluorescence microscopy, western blotting and recombinant Snf7 purification for CD, TEM and liposome sedimentation analysis were performed as described (Buchkovich et al., 2013; Henne et al., 2012; Tang et al., 2015), and canavanine plating assay as described (Lin et al., 2008).

For Bro1 purification, *Saccharomyces cerevisiae BRO1* was cloned into the pET23d vector (Novagen) with a N-terminal His<sub>6</sub>-tag, induced by 1 mM IPTG at 18°C overnight from BL21 *E. coli* cells, and purified by TALON metal affinity resin (Clontech). Protein-bound TALON resins were washed in 500 mM NaCl, 20 mM HEPES pH7.4, 20 mM imidazole, and eluted in 150 mM NaCl, 20 mM HEPES pH7.4, 400 mM imidazole.

### **Flow Cytometry**

The quantitative Mup1-pHluorin ESCRT cargo-sorting flow cytometry assay was performed as described (Buchkovich et al., 2013; Henne et al., 2012; Tang et al., 2015). Briefly, mid-log yeast cell cultures grown with the addition of 20 µg/mL *L*-methionine for 2 hours were resuspended in 1x PBS buffer. Mean green fluorescence (FL1-A channel) of 100,000 events was recorded and gated on a BD Accuri C6 flow cytometer. For single ESCRT mutants, take Figure 1A for example: NBY42 (*vps20Δ MUP1-PH*) yeast cells were transformed with 1) pRS416 empty vector, 2) pRS416 *VPS20*, or 3) different mutants, respectively. Gated mean FL1-A values, *F*, of each sample are recorded and sorting scores are calculated as:

$$MVB\ Sorting\ \% = (1 - \frac{F_{Mutant} - F_{VPS20}}{F_{empty\ vector} - F_{VPS20}}) \times 100\%$$

Sorting scores of 3 to 5 independent experiments are used to calculate standard deviation.

For double ESCRT mutants, take Figure 3D panel *vps23Δvps25Δ* for example. STY64 (*vps23Δ vps25Δ MUP1-PH*) yeast cells were co-transformed with 1) pRS415 empty vector and pRS416 empty vector, 2) pRS415 *VPS25* and pRS416 *VPS23*, 3) pRS415 empty vector and pRS416 *VPS20*, 4) pRS415 empty vector and pRS416 *SNF7*, 5) pRS415 empty vector and pRS416 *snf7\*\**, or 6) pRS415 empty vector and pRS416 *snf7\*\*\**, respectively. MVB sorting scores are calculated as:

$$MVB\ Sorting\ \% = (1 - \frac{F_{Mutant} - F_{VPS25+VPS23}}{F_{empty\ vector+empty\ vector} - F_{VPS25+VPS23}}) \times 100\%$$

Sorting scores of 3 to 5 independent experiments are used to calculate standard deviation.

## **Yeast Strain and Plasmids**

See Table 4.1 for a list of plasmids and yeast strains used in this study.

## ***SNF7* Random Mutagenesis for *vps20Δ* Suppressor Screening**

The DNA sequence of *Saccharomyces cerevisiae SNF7* with 500bp of 5'UTR and 500bp of 3'UTR was amplified by Taq DNA polymerase with 20 μM MnCl<sub>2</sub> and manipulated dNTP (N=A, T, G, or C) concentrations of 250 μM for three dNTPs and 25 μM for the other dNTP. Four individual 50 μL PCR reactions with different dNTP ratios were mixed, purified and transformed in *vps20Δ* yeast, along with a restriction enzyme

digested vector of 3'UTR-pRS416-5'UTR. Yeast cells were plated and grown on YNB-uracil for 3 days at 26°C, and replica plated on YNB-uracil with 4.0 µg/mL of L-canavanine. Canavanine-resistant yeast colonies were selected, and gap-repaired pRS416 *snf7* mutant were prepped, amplified and sequenced.

### Circular Dichroism Spectroscopy

CD experiments were carried out using an Aviv Biomedical CD spectrometer Model 202-01. 10 µM Snf7<sup>core</sup> mutants were buffer exchanged by Superdex-200 gel filtration (GE Healthcare Life Sciences) to 10 mM sodium phosphate buffer pH 7.5. For solution samples, Snf7<sup>core</sup> was mixed with an equal volume of buffer. For liposome samples, Snf7<sup>core</sup> was mixed with an equal volume of 1.0 mg/mL liposomes of 800 nm diameter, with 60% 1,2-dioleoyl-sn-glycero-3-phosphocholine (DOPC), 30% 1,2-dioleoyl-sn-glycero-3-phospho-L-serine (DOPS), 10% phosphatidylinositol 3-phosphate (PI(3)P). The preparation of liposomes was performed as previously described (Henne et al., 2012).

The degrees of ellipticity were measured at 4°C and scanned from 260 nm to 200 nm. Molar ellipticity,  $\theta$ , was then normalized using the following equation and plotted versus wavelength, where  $n=142$  is the number of peptide bonds.

$$\theta \text{ (deg} \cdot \text{cm}^2/\text{dmol}) = \frac{\text{Ellipticity (mdeg)}}{\text{Pathlength(mm)} \cdot [\text{Protein}](\mu\text{M}) \cdot n} \times 10^6$$

### Negative Stain Transmission Electron Microscopy

Visualization of ESCRT-III assembly using purified recombinant ESCRT components was performed as previously described (Henne et al., 2012).

Visualization of MVB in *vam7<sup>tsf</sup>* yeast cells was performed as previously described (Buchkovich et al., 2013). Briefly, 30 ODV of mid-log *vam7<sup>tsf</sup>* yeast cells were grown at 38°C for 3 hours, and then fixed with 2.5% (v/v) glutaraldehyde for 1 hr and spheroplasted with zymolyase and gluculase before embedding in 2% ultra-low temperature agarose. Cells were incubated in 1% osmium tetroxide/1% potassium ferrocyanide for 30 min, 1% thiocarbohydrazide for 5 min, and 1% osmium tetroxide/1% postassium ferrocyanide for 5 min. After dehydration through an ethanol series, samples were transitioned into 100% propylene oxide and embedded in Spurr's resin. Note that osmotic gradients during fixation or dehydration might account for the MVB morphological defects and the larger mean ILV diameter compared to samples prepared by high-pressure freezing and automated freeze-substitution. However, all yeast cells used in these experiments were treated equally. All TEM was performed on a Morgnani 268 transmission electron microscope (FEI) with an AMT digital camera.

## Acknowledgement

I gratefully thank Scott D. Emr, Nicholas J. Buchkovich and W. Mike Henne for training, mentorship, experimental design and execution. I gratefully thank Yun Jung Kim and Sudeep Banjade for acquisition, analysis and interpretation of experimental data.

I thank Sarah T. Griffin, Yi-Chun. Yeh, Leonid A. Timashev, Ming Li and Lu Zhu for technical expertise and sharing reagents. We thank Anthony C. Gatts VI for TEM, Nattakan Sukomon and Brian R. Crane for CD spectroscopy. We thank Yuxin Mao, J. Christopher Fromme, Peter P. Borbat and William J. Brown for helpful discussion.

**Table 4.1 Plasmids and Yeast Strains Used in Chapter 4**

| <b>Plasmids for <i>Saccharomyces cerevisiae</i> Expression</b> |  |                             |
|--|--|-----------------------------|
| <b>Plasmid</b>   | <b>Mutations</b>   | <b>Reference</b>            |
| pRS416   | N/A  | (Sikorski and Hieter, 1989) |
| pRS415   | N/A  | (Sikorski and Hieter, 1989) |
| pRS414   | N/A  | (Sikorski and Hieter, 1989) |
| pRS416-VPS20   | Wild-type  | this study                  |
| pRS416-vps20 <sup>1-197</sup> -snf7 <sup>211-240</sup>         | Vps20 <sup>1-197</sup> -Snf7 <sup>211-240</sup>              | this study                  |
| pRS416-vps20 <sup>1-172</sup> -snf7 <sup>181-240</sup>         | Vps20 <sup>1-172</sup> -Snf7 <sup>181-240</sup>              | this study                  |
| pRS416-vps20 <sup>1-147</sup> -snf7 <sup>150-240</sup>         | Vps20 <sup>1-147</sup> -Snf7 <sup>150-240</sup>              | this study                  |
| pRS416-vps20 <sup>1-118</sup> -snf7 <sup>120-240</sup>         | Vps20 <sup>1-118</sup> -Snf7 <sup>120-240</sup>              | this study                  |
| pRS416-vps20 <sup>1-105</sup> -snf7 <sup>107-240</sup>         | Vps20 <sup>1-105</sup> -Snf7 <sup>107-240</sup>              | this study                  |
| pRS416-vps20 <sup>1-59</sup> -snf7 <sup>61-240</sup>           | Vps20 <sup>1-59</sup> -Snf7 <sup>61-240</sup>                | this study                  |
| pRS416-vps20 <sup>1-5</sup> -snf7 <sup>11-240</sup>            | Vps20 <sup>1-5</sup> -Snf7 <sup>11-240</sup>                 | (Buchkovich et al., 2013)   |
| pRS416-SNF7  | Wild-type  | (Henne et al., 2012)        |
| pRS416-snf7 <sup>Q90L</sup>                                    | Q90L   | this study                  |
| pRS416-snf7 <sup>N100I</sup>                                   | N100I  | this study                  |
| pRS416-snf7 <sup>R52E</sup>                                    | R52E   | (Henne et al., 2012)        |
| pRS416-snf7 <sup>R52E Q90L</sup>                               | R52E Q90L  | this study                  |
| pRS416-snf7 <sup>R52E Q90L N100I</sup>                         | R52E Q90L N100I  | this study                  |
| pRS416-snf7 <sup>**</sup>                                      | Vps20 <sup>1-5</sup> -Snf7 <sup>11-240 R52E Q90L</sup>       | this study                  |
| pRS416-snf7 <sup>***</sup>                                     | Vps20 <sup>1-5</sup> -Snf7 <sup>11-240 R52E Q90L N100I</sup> | this study                  |
| pRS415-snf7 <sup>**</sup>                                      | Vps20 <sup>1-5</sup> -Snf7 <sup>11-240 R52E Q90L</sup>       | this study                  |
| pRS415-snf7 <sup>***</sup>                                     | Vps20 <sup>1-5</sup> -Snf7 <sup>11-240 R52E Q90L N100I</sup> | this study                  |
| pRS414-snf7 <sup>**</sup>                                      | Vps20 <sup>1-5</sup> -Snf7 <sup>11-240 R52E Q90L</sup>       | this study                  |
| pRS414-snf7 <sup>***</sup>                                     | Vps20 <sup>1-5</sup> -Snf7 <sup>11-240 R52E Q90L N100I</sup> | this study                  |
| pRS426-GFP-CPS1  | GFP  | (Odorizzi et al., 1998)     |
| pRS414-vam7 <sup>tsf</sup>                                     | L134P L287P  | (Sato et al., 1998)         |
| pRS415-VPS20   | Wild-type  | (Buchkovich et al., 2013)   |
| pRS414-SNF7  | Wild-type  | (Tang et al., 2015)         |
| pRS414-VPS24   | Wild-type  | (Buchkovich et al., 2013)   |
| pRS415-VPS2  | Wild-type  | (Buchkovich et al., 2013)   |
| pRS416-VPS4  | Wild-type  | this study                  |
| pRS416-VPS36-MYC   | Wild-type  | (Hierro et al., 2004)       |
| pRS416-VPS22-HA  | Wild-type  | (Hierro et al., 2004)       |
| pRS415-VPS25   | Wild-type  | this study                  |
| pRS416-VPS23   | Wild-type  | this study                  |
| pRS415-VPS23   | Wild-type  | this study                  |
| pRS416-VPS28   | Wild-type  | this study                  |
| pRS416-VPS37   | Wild-type  | this study                  |
| pRS416-VPS27   | Wild-type  | this study                  |
| pRS416-vps27 <sup>UIM</sup>                                    | S270D S313D  | this study                  |

|   |  |                            |
|---|--|----------------------------|
| pRS416-BRO1   | Wild-type  | (Odorizzi et al., 2003)    |
| pRS416-bro1 <sup>UBD</sup>                                | I377R L386R<br>Vps20 <sup>1-5</sup> -Snf7 <sup>11-240 R52E Q90L N100I L231K L234K</sup>    | this study                 |
| pRS415-snF7***BRO1  | I144D L336D  | this study                 |
| pRS416-bro1 <sup>SNF7</sup>                               | pCUP-HSE1-UL36 <sup>CD</sup> -HA   | this study                 |
| pRS316 HSE1-DUB   | Vps20 <sup>1-200</sup>   | (Stringer and Piper, 2011) |
| pRS415-vps20 <sup>1-200</sup>                             | Vps20 <sup>1-172</sup>   | this study                 |
| pRS415-vps20 <sup>1-172</sup>                             | Vps20 <sup>1-147</sup>   | this study                 |
| pRS415-vps20 <sup>1-147</sup>                             | Vps20 <sup>1-59</sup> -Snf7 <sup>61-240 Q90L</sup>   | this study                 |
| pRS416-vps20 <sup>1-59</sup> -snf7 <sup>61-240 Q90L</sup> | T20D V24L R27K I30K N31D L33I S34H   | this study                 |
| pRS416-snF7 <sup>7mut</sup>                               | T20D V24L R27K I30K N31D L33I S34H R52E Q90L   | this study                 |
| pRS416-snF7 <sup>7mut R52E Q90L</sup>                     | T20D V24L R27K I30K N31D L33I S34H R52E Q90L N100I   | this study                 |
| pRS416-snF7 <sup>7mut R52E Q90L N100I</sup>               | Vps20 <sup>1-5</sup> -Snf7 <sup>11-240 R52E Q90L T20D</sup>                                | this study                 |
| pRS416-snF7** <sup>7mut</sup>                             | V24L R27K I30K N31D L33I S34H Vps20 <sup>1-5</sup> -Snf7 <sup>11-240 R52E Q90L N100I</sup> | this study                 |
| pRS416-snF7*** <sup>7mut</sup>                            | T20D V24L R27K I30K N31D L33I S34H   | this study                 |
| pRS416-vps36 <sup>arm</sup> -MYC                          | D548R  | this study                 |
| pRS416-vps22 <sup>arm</sup> -HA                           | D214A  | (Hierro et al., 2004)      |
| pRS416-vps25 <sup>arm</sup> -FLAG                         | R83D   | (Hierro et al., 2004)      |
| pRS416-VPH1-GFP   | GFP  | this study                 |
| pRS426-GFP-CPS1 <sup>K8R K12R</sup>                       | GFP, K8R K12R  | this study                 |

### Plasmids for *Escherichia coli* Expression for Protein Purification

| Plasmid                            | Mutations                    | Reference                 |
|------------------------------------|------------------------------|---------------------------|
| pET23d-SNF7                        | Wild-type                    | (Henne et al., 2012)      |
| pET23d-snF7 <sup>R52E</sup>        | R52E                         | (Henne et al., 2012)      |
| pET23d-snF7 <sup>Q90L</sup>        | Q90L                         | this study                |
| pET23d-snF7 <sup>a1-a4</sup>       | Snf7 <sup>10-150</sup>       | (Buchkovich et al., 2013) |
| pET23d-snF7 <sup>a1-a4 Q90L</sup>  | Snf7 <sup>10-150 Q90L</sup>  | this study                |
| pET23d-snF7 <sup>a1-a4 N100I</sup> | Snf7 <sup>10-150 N100I</sup> | this study                |
| pET23d-BRO1                        | Wild-type                    | this study                |
| pET23d-snF7 <sup>1-225</sup>       | Snf7 <sup>1-225</sup>        | this study                |

### Yeast Strains Used in This Study

| Strain    | Genotype   | Reference                 |
|-----------|--|---------------------------|
| SEY6210   | Mat a, leu2-3, 2-112, ura3-52, his3-Δ200, trp1-Δ901, lys2-801, suc2-Δ9 | (Robinson et al., 1988)   |
| SEY6210.1 | Mat a, leu2-3, 2-112, ura3-52, his3-Δ200, trp1-Δ901, lys2-801, suc2-Δ9 | (Robinson et al., 1988)   |
| NBY42     | SEY6210.1; vps20Δ::HIS3; MUP1-PHLOURIN::KAN                            | (Buchkovich et al., 2013) |
| MBY25     | SEY6210.1; vps20Δ::HIS3  | (Babst et al., 2002a)     |

|       |  |                           |
|-------|--|---------------------------|
| NBY44 | SEY6210.1; <i>snf7Δ::HIS3; MUP1-PHLOURIN::KAN</i>                | (Henne et al., 2012)      |
| NBY80 | SEY6210.1; <i>vps20Δ::HIS3 vam7Δ::HIS3</i>                       | this study                |
| NBY47 | SEY6210.1; <i>vps24Δ::HIS3; MUP1-PHLOURIN::KAN</i>               | (Buchkovich et al., 2013) |
| NBY69 | SEY6210.1; <i>vps2Δ::HIS3; MUP1-PHLOURIN::KAN</i>                | (Buchkovich et al., 2013) |
| NBY59 | SEY6210.1; <i>vps4Δ::HIS3; MUP1-PHLOURIN::KAN</i>                | this study                |
| STY55 | SEY6210.1; <i>vps36Δ::TRP1; MUP1-PHLOURIN::KAN</i>               | this study                |
| STY56 | SEY6210.1; <i>vps22Δ::TRP1; MUP1-PHLOURIN::KAN</i>               | this study                |
| STY51 | SEY6210; <i>vps25Δ::HIS3; MUP1-PHLOURIN::KAN</i>                 | this study                |
| STY77 | SEY6210; <i>vps36Δ::TRP1; vps25Δ::HIS3; MUP1-PHLOURIN::KAN</i>   | this study                |
| NBY63 | SEY6210.1; <i>vps23Δ::HIS3; MUP1-PHLOURIN::KAN</i>               | this study                |
| SBY1  | SEY6210.1; <i>vps28Δ::TRP1; MUP1-PHLOURIN::KAN</i>               | this study                |
| STY76 | SEY6210.1; <i>vps37Δ::TRP1; MUP1-PHLOURIN::KAN</i>               | this study                |
| STY64 | SEY6210; <i>vps23Δ::TRP1; vps25Δ::HIS3; MUP1-PHLOURIN::KAN</i>   | this study                |
| STY31 | SEY6210.1; <i>vps27Δ::HIS3; MUP1-PHLOURIN::KAN</i>               | this study                |
| STY57 | SEY6210.1; <i>vps27Δ::TRP1; vps20Δ::HIS3; MUP1-PHLOURIN::KAN</i> | this study                |
| STY63 | SEY6210.1; <i>vps27Δ::TRP1; vps25Δ::HIS3; MUP1-PHLOURIN::KAN</i> | this study                |
| STY62 | SEY6210.1; <i>vps27Δ::TRP1; vps23Δ::HIS3; MUP1-PHLOURIN::KAN</i> | this study                |
| YAY16 | SEY6210; <i>bro1Δ::HIS3; MUP1-PHLOURIN::KAN</i>                  | this study                |
| YAY20 | SEY6210; <i>bro1Δ::HIS3; vps20Δ::HIS3; MUP1-PHLOURIN::KAN</i>    | this study                |
| STY65 | SEY6210; <i>bro1Δ::HIS3; vps25Δ::TRP1; MUP1-PHLOURIN::KAN</i>    | this study                |
| STY66 | SEY6210; <i>bro1Δ::HIS3; vps23Δ::TRP1; MUP1-PHLOURIN::KAN</i>    | this study                |
| DTY36 | SEY6210.1; <i>vps20Δ::HIS3; SNF7-GFP::HIS3</i>                   | (Teis et al., 2008)       |
| NBY75 | SEY6210.1; <i>vps20Δ::HIS3; snf7Δ::HIS3; MUP1-PHLOURIN::KAN</i>  | this study                |
| STY59 | SEY6210.1; <i>vps24Δ::TRP1; vps20Δ::HIS3; MUP1-PHLUORIN::KAN</i> | this study                |
| STY60 | SEY6210.1; <i>vps2Δ::TRP1; vps20Δ::HIS3; MUP1-PHLUORIN::KAN</i>  | this study                |
| STY61 | SEY6210.1; <i>vps4Δ::TRP1; vps20Δ::HIS3; MUP1-PHLUORIN::KAN</i>  | this study                |
| STY52 | SEY6210.1; <i>vps36Δ::TRP1; vps20Δ::HIS3; MUP1-PHLUORIN::KAN</i> | this study                |
| STY53 | SEY6210.1; <i>vps22Δ::TRP1; vps20Δ::HIS3; MUP1-PHLUORIN::KAN</i> | this study                |
| STY54 | SEY6210.1; <i>vps25Δ::TRP1; vps20Δ::HIS3; MUP1-PHLUORIN::KAN</i> | this study                |
| STY58 | SEY6210.1; <i>vps23Δ::TRP1; vps20Δ::HIS3; MUP1-PHLUORIN::KAN</i> | this study                |
| STY72 | SEY6210.1; <i>vps28Δ::TRP1; vps20Δ::HIS3; MUP1-PHLUORIN::KAN</i> | this study                |
| STY73 | SEY6210.1; <i>vps37Δ::TRP1; vps20Δ::HIS3; MUP1-PHLUORIN::KAN</i> | this study                |

|       |  |            |
|-------|--|------------|
| NBY55 | SEY6210.1; <i>vps23Δ::HIS3 vam7Δ::HIS3</i> | this study |
|-------|--|------------|

## Reference

- Babst, M., Katzmann, D.J., Estepa-Sabal, E.J., Meerloo, T., and Emr, S.D. (2002). ESCRT-III: an endosome-associated heterooligomeric protein complex required for mvb sorting. *Dev Cell* 3, 271-282.
- Bilodeau, P.S., Urbanowski, J.L., Winstorfer, S.C., and Piper, R.C. (2002). The Vps27p Hse1p complex binds ubiquitin and mediates endosomal protein sorting. *Nat Cell Biol* 4, 534-539.
- Buchkovich, N.J., Henne, W.M., Tang, S., and Emr, S.D. (2013). Essential N-terminal insertion motif anchors the ESCRT-III filament during MVB vesicle formation. *Dev Cell* 27, 201-214.
- Christ, L., Wenzel, E.M., Liestol, K., Raiborg, C., Campsteijn, C., and Stenmark, H. (2016). ALIX and ESCRT-I/II function as parallel ESCRT-III recruiters in cytokinetic abscission. *J Cell Biol* 212, 499-513.
- Doerks, T., Copley, R.R., Schultz, J., Ponting, C.P., and Bork, P. (2002). Systematic identification of novel protein domain families associated with nuclear functions. *Genome Research* 12, 47-56.
- Greenfield, N.J. (2006). Using circular dichroism spectra to estimate protein secondary structure. *Nat Protoc* 1, 2876-2890.
- Henne, W.M., Buchkovich, N.J., Zhao, Y., and Emr, S.D. (2012). The endosomal sorting complex ESCRT-II mediates the assembly and architecture of ESCRT-III helices. *Cell* 151, 356-371.
- Hierro, A., Sun, J., Rusnak, A.S., Kim, J., Prag, G., Emr, S.D., and Hurley, J.H. (2004). Structure of the ESCRT-II endosomal trafficking complex. *Nature* 431, 221-225.
- Im, Y.J., Wollert, T., Boura, E., and Hurley, J.H. (2009). Structure and function of the ESCRT-II-III interface in multivesicular body biogenesis. *Dev Cell* 17, 234-243.
- Kim, J., Sitaraman, S., Hierro, A., Beach, B.M., Odorizzi, G., and Hurley, J.H. (2005). Structural basis for endosomal targeting by the Bro1 domain. *Dev Cell* 8, 937-947.
- Lee, J., Oh, K.J., Lee, D., Kim, B.Y., Choi, J.S., Ku, B., and Kim, S.J. (2016). Structural Study of the HD-PTP Bro1 Domain in a Complex with the Core Region of STAM2, a Subunit of ESCRT-0. *PLoS One* 11, e0149113.

Lin, C.H., MacGurn, J.A., Chu, T., Stefan, C.J., and Emr, S.D. (2008). Arrestin-related ubiquitin-ligase adaptors regulate endocytosis and protein turnover at the cell surface. *Cell* 135, 714-725.

Luhtala, N., and Odorizzi, G. (2004). Bro1 coordinates deubiquitination in the multivesicular body pathway by recruiting Doa4 to endosomes. *J Cell Biol* 166, 717-729.

McCullough, J., Clippinger, A.K., Talledge, N., Skowyra, M.L., Saunders, M.G., Naismith, T.V., Colf, L.A., Afonine, P., Arthur, C., Sundquist, W.I., et al. (2015). Structure and membrane remodeling activity of ESCRT-III helical polymers. *Science*.

McCullough, J., Fisher, R.D., Whitby, F.G., Sundquist, W.I., and Hill, C.P. (2008). ALIX-CHMP4 interactions in the human ESCRT pathway. *Proc Natl Acad Sci U S A* 105, 7687-7691.

Nickerson, D.P., West, M., Henry, R., and Odorizzi, G. (2010). Regulators of Vps4 ATPase activity at endosomes differentially influence the size and rate of formation of intraluminal vesicles. *Mol Biol Cell* 21, 1023-1032.

Obita, T., Saksena, S., Ghazi-Tabatabai, S., Gill, D.J., Perisic, O., Emr, S.D., and Williams, R.L. (2007). Structural basis for selective recognition of ESCRT-III by the AAA ATPase Vps4. *Nature* 449, 735-739.

Odorizzi, G., Babst, M., and Emr, S.D. (1998). Fab1p PtdIns(3)P 5-Kinase Function Essential for Protein Sorting in the Multivesicular Body. *Cell* 95, 847-858.

Odorizzi, G., Katzmann, D.J., Babst, M., Audhya, A., and Emr, S.D. (2003). Bro1 is an endosome-associated protein that functions in the MVB pathway in *Saccharomyces cerevisiae*. *J Cell Sci* 116, 1893-1903.

Pashkova, N., Gakhar, L., Winistorfer, S.C., Sunshine, A.B., Rich, M., Dunham, M.J., Yu, L., and Piper, R.C. (2013). The yeast alix homolog bro1 functions as a ubiquitin receptor for protein sorting into multivesicular endosomes. *Dev Cell* 25, 520-533.

Peter, B.J., Kent, H.M., Mills, I.G., Vallis, Y., Butler, P.J., Evans, P.R., and McMahon, H.T. (2004). BAR domains as sensors of membrane curvature: the amphiphysin BAR structure. *Science* 303, 495-499.

Robinson, J., Klionsky, D., Banta, L., and Emr, S. (1988). Protein sorting in *Saccharomyces cerevisiae*: isolation of mutants defective in the delivery and processing of multiple vacuolar hydrolases. *Mol Cell Biol* 8(11), 4936-4948.

Sato, T.K., Darsow, T., and Emr, S.D. (1998). Vam7p, a SNAP-25-like molecule, and Vam3p, a syntaxin homolog, function together in yeast vacuolar protein trafficking. *Mol Cell Biol* 18, 5308-5319.

Sikorski, R.S., and Hieter, P. (1989). A system of shuttle vectors and yeast host strains designed for efficient manipulation of DNA in *Saccharomyces cerevisiae*. *Genetics* 22, 19-27.

Stringer, D.K., and Piper, R.C. (2011). A single ubiquitin is sufficient for cargo protein entry into MVBs in the absence of ESCRT ubiquitination. *J Cell Biol* 192, 229-242.

Tang, S., Henne, W.M., Borbat, P.P., Buchkovich, N.J., Freed, J.H., Mao, Y., Fromme, J.C., and Emr, S.D. (2015). Structural basis for activation, assembly and membrane binding of ESCRT-III Snf7 filaments. *Elife* 4.

Teis, D., Saksena, S., and Emr, S.D. (2008). Ordered assembly of the ESCRT-III complex on endosomes is required to sequester cargo during MVB formation. *Dev Cell* 15, 578-589.

Teis, D., Saksena, S., Judson, B.L., and Emr, S.D. (2010). ESCRT-II coordinates the assembly of ESCRT-III filaments for cargo sorting and multivesicular body vesicle formation. *EMBO J* 29, 871-883.

Wemmer, M., Azmi, I., West, M., Davies, B., Katzmann, D., and Odorizzi, G. (2011). Bro1 binding to Snf7 regulates ESCRT-III membrane scission activity in yeast. *J Cell Biol* 192, 295-306.

## CHAPTER V

### Conclusion, Discussion and Future Directions

#### Conclusion

The endosomal sorting complex required for transport-III (ESCRT-III) catalyzes numerous topologically equivalent cellular membrane remodeling events by generating membrane curvature away from the cell cytoplasm. Although the class E *VPS* genes were originally identified in the 1980s, the functional characterization of the ESCRT-III complex as a multi-subunit polymeric machine did not begin until the early 2000s. Since the first structural determination of an ESCRT-III subunit in 2006, research on the function and architecture of the ESCRT-III machinery has quickly expanded, yet the molecular mechanisms governing ESCRT-III activation and assembly to mediate membrane deformation and vesicle biogenesis largely remained a mystery.

Through the work presented in my dissertation focusing on the predominant ESCRT-III subunit, Snf7 (CHMP4), I determined the first atomic resolution structure of the Snf7 protofilament, revealing for the first time the molecular mechanisms underlying the ESCRT-III conformational dynamics in activation, assembly and membrane binding. The Snf7 “core” domain, which was long believed to be a rigid structural fold, undergoes a global conformational rearrangement to expose new interacting surfaces for ESCRT-III polymerization and membrane association. I demonstrated that ESCRT-III conformational dynamics are tightly regulated through the parallel action of two ubiquitin-

dependent pathways: the ESCRT-I – ESCRT-II pathway and the ESCRT-0 – Bro1 pathway, during multivesicular endosome biogenesis *in vivo*. Together with the identification of a novel membrane insertion motif that anchors the ESCRT-III circular polymer to the membranes, my dissertation provides a fundamental advance in understanding the molecular mechanisms of ESCRT-mediated membrane remodeling. Hopefully, my studies will serve as a foundation for future work on the ESCRT pathway.

Since I started the investigations on the structure and function of the ESCRT-III Snf7 filament, the ESCRT field has dramatically expanded, with a large amount of exciting research being published. These new studies, together with my work, have revolutionized the understanding of the ESCRT-III pathway. However, new questions have arisen that will drive future research. In the following section, I highlight the culmination of these exciting recent studies and discuss key remaining mysteries in the field.

## **Discussion**

### **Diversity of ESCRT Function**

Since its original discovery in 2001, remarkable progress has been made toward the molecular understanding of ESCRT structure and function. Significant achievements have been completed in ESCRT genetic characterization, protein purification, structural determination, and functional reconstitution. In parallel with this, the ESCRTs have emerged as key players in diverse physiological and pathological processes. Functional characterization of the ESCRTs has

dominated the field with the perspectives of three cellular processes since their discovery in 2001: MVB biogenesis in the endolysosomal pathway, the budding of HIV-1 and other viruses at the plasma membrane, and the abscission of cytokinesis.

Notably, the observation of the ESCRTs necessary for cytokinesis in unicellular organisms suggests a potential ancestral purpose of ESCRT proteins. It is notable that ESCRT-III and Vps4 are involved in cytokinesis both in archaea and metazoans. ESCRTs -0, -I, -II and ALIX may represent a further specialization on this theme, coupling ubiquitin and PI(3)P binding with scission to form a cargo-sorting pathway conserved from yeast to human. The ability to isolate and characterize distinct ESCRT complexes also underlines the “division of labor” between complexes necessary to carry out cargo sorting in a tightly regulated manner.

The past five years, however, have seen an explosion of novel ESCRT functions: the formation of shedding microvesicles and exosomes, autophagy, plasma membrane wound repair, neuron pruning, surveillance of defective nuclear pore complex intermediates, nuclear envelope reformation, plus-stranded RNA virus replication compartment formation. All of the ESCRT functions involve the conserved membrane bending topology, revealing a remarkably widespread role for this membrane-remodeling machinery.

## **Theme of ESCRT-III Recruitment**

From the perspectives of the ESCRT complexes, lipid membrane, and ubiquitinated cargo, the ESCRT pathway can be viewed as a cargo-recognition and membrane-sculpting macromolecular machine conserved from archaea to yeast to human (Spang et al., 2015). However, numerous recent studies highlight an emerging divergence in ESCRT function. Despite the fact that ESCRT-III and Vps4 are ubiquitously involved, the requirement of upstream ESCRTs is different among the ESCRT-dependent biological contexts. For HIV-1 budding, ESCRT-I and ESCRT-III appear to be essential. ESCRT-I Tsg101 (Vps23) and ALIX (Bro1) bind directly to the viral L-domain. ALIX recruits CHMP4B (Snf7) for ESCRT-III assembly. ESCRT-0 and ESCRT-II appear to be dispensable (Langelier et al., 2006), although a recent study suggested a functional role of ESCRT-II in HIV budding (Meng et al., 2015). Similarly, ESCRT-I and -III are important for cytokinesis, and their loss impairs abscission (Carlton and Martin-Serrano, 2007). ESCRT-II and ESCRT-III CHMP6 (Vps20) were recently shown to be essential to cytokinesis, forming a parallel recruitment arm with ALIX for ESCRT-III CHMP4B (Snf7) (Christ et al., 2016). Thus, ESCRT-0 appears to be unnecessary in both processes, consistent with the observation that ESCRT-0 only appears present in fungi and metazoan (Leung et al., 2008), where intracellular endomembrane systems exist. In HIV budding and cytokinesis, the HIV Gag and the microtubule bundling CEP55 proteins mimic ESCRT-0 for the engagement of ESCRT-I.

Another significant divergence in ESCRT function is the difference in cargo between processes. MVB sorting requires ubiquitinated cargo, however, ubiquitination of an enveloped virus is not essential for its budding, although studies have shown that ubiquitination of Gag proteins increases viral budding efficiency (Strack et al., 2000; VerPlank et al., 2001). ESCRTs do not appear to utilize ubiquitin for cytokinesis either, where the “cargo” can be viewed as the entire daughter cell interior. This underscores the relative independence of each of the two chief ESCRT functions as a cargo-recognition and membrane-sculpting machine.

### **ESCRTs and New Membrane Topology**

A very recent cryo-EM reconstruction of the IST1-CHMP1B (Ist1-Did2) structure revealed a remarkable internal organization of a double-stranded ESCRT-III co-polymer and a surprising membrane binding topology. The inner strand comprises “open” CHMP1B subunits that interlock in an elaborate core domain rearranged architecture, reminiscent of the open conformation in the Snf7 filament crystal structure (Tang et al., 2015). CHMP1B is encircled by an outer strand of “closed” IST1 subunits (McCullough et al., 2015). The conformational rearrangement observed in the core domain of two different ESCRT-III subunits implies that the core domain activation is a common theme for ESCRT-III activation and assembly.

Strikingly, the CHMP1B polymer exerts its  $\alpha 1$  membrane interacting surface from each protomer interior, which forms external coats on positively

curved membranes *in vitro* and in cells when overexpressed. This is an inverted membrane topology as observed by the canonical ESCRT-III CHMP4B (Snf7) polymers (McCullough et al., 2015). Nevertheless, CHMP1B and IST1 play atypical roles in ESCRT biology. They appear to be dispensable for HIV-1 budding, and depletion of either gene resulted in mild MVB sorting defects (Rue et al., 2008). IST1 has been suggested to function in the scission of recycling carriers leaving endosomes (Allison et al., 2013). However, both CHMP1B and IST1 function in cytokinesis (Agromayor et al., 2009; Bajorek et al., 2009a) and nuclear envelope reformation during the recruitment of the AAA ATPase Spastin for microtubule severing (Vietri et al., 2015). Future work will continue to explore this exciting non-canonical ESCRT-III membrane topology.

## Future Directions

### Remaining Mysteries

Despite the amazing recent progress with ESCRTs, key questions still remain. In general, a complete elucidation of the ESCRT pathway will require a temporal and spatial understanding of: (1) cargo recognition and recruitment of the ESCRT-0, -I, and -II complexes, (2) activation and assembly of ESCRT-III at the membrane surface for cargo sequestration, (3) membrane deformation and scission, and (4) Vps4-mediated ESCRT-III disassembly.

For stages (1) and (2), a greater understanding of the upstream ESCRT stoichiometry for a single round of MVB sorting is needed. ESCRT-I and ESCRT-II form a supercomplex of 1:1 ratio *in vitro* (Gill et al., 2007). The ESCRT-

0/ESCRT-I stoichiometry is less certain and may not be fixed for MVB sorting. Whether there is an exact stoichiometry to a budding event remains a major challenge to determine. Notably, recent studies suggest a novel role of Bro1 as an upstream ESCRT component in ubiquitin recognition (Pashkova et al., 2013; Tang et al., 2016) and ESCRT-III recruitment (Christ et al., 2016; Tang et al., 2016), however, the molecular mechanism and detailed stoichiometry remain unclear.

Moreover, stages (3) and (4) will continue to require intense study to fully elucidate, although my studies and recent studies in the field have already made substantial advances in these stages. The most pressing is the mechanisms of ESCRT-III and Vps4-mediated membrane scission. Intertwined with this mystery is a strong urgency for the determination of an intact ESCRT-III structure, which would provide insight into its mechanism of action. The mechanochemical role of Vps4 in ESCRT-III disassembly and membrane scission also remains a key question in the field. Numerous electron micrographs exist for ESCRT-III assemblies, but most cannot reveal atomic resolution details like subunit connectivity and protein interfaces. Recent advances in structural determination by cryo-electron microscopy would provide an intriguing approach to tackle these challenging questions through the characterization of ESCRT-III assemblies under different subunit composition, stoichiometry and conformational intermediates.

A final big question is whether additional cellular processes involve ESCRT proteins. No doubt future studies will continue to reveal new and exciting properties of this remarkable membrane sculpting machinery.

## Reference

- Agromayor, M., Carlton, J.G., Phelan, J.P., Matthews, D.R., Carlin, L.M., Ameer-Beg, S., Bowers, K., and Martin-Serrano, J. (2009). Essential Role of hIST1 in Cytokinesis. *Mol Biol Cell* 20, 1374-1387.
- Allison, R., Lumb, J.H., Fassier, C., Connell, J.W., Ten Martin, D., Seaman, M.N.J., Hazan, J., and Reid, E. (2013). An ESCRT-spastin interaction promotes fission of recycling tubules from the endosome. *Journal of Cell Biology* 202, 527-543.
- Bajorek, M., Morita, E., Skalicky, J.J., Morham, S.G., Babst, M., and Sundquist, W.I. (2009). Biochemical Analyses of Human IST1 and Its Function in Cytokinesis. *Mol Biol Cell* 20, 1360-1373.
- Carlton, J.G., and Martin-Serrano, J. (2007). Parallels between cytokinesis and retroviral budding: a role for the ESCRT machinery. *Science* 316, 1908-1912.
- Christ, L., Wenzel, E.M., Liestol, K., Raiborg, C., Campsteijn, C., and Stenmark, H. (2016). ALIX and ESCRT-I/II function as parallel ESCRT-III recruiters in cytokinetic abscission. *J Cell Biol* 212, 499-513.
- Gill, D.J., Teo, H., Sun, J., Perisic, O., Veprintsev, D.B., Emr, S.D., and Williams, R.L. (2007). Structural insight into the ESCRT-I-II link and its role in MVB trafficking. *EMBO J* 26, 600-612.
- Langelier, C., von Schwedler, U.K., Fisher, R.D., De Domenico, I., White, P.L., Hill, C.P., Kaplan, J., Ward, D., and Sundquist, W.I. (2006). Human ESCRT-II complex and its role in human immunodeficiency virus type 1 release. *Journal of Virology* 80, 9465-9480.
- Leung, K.F., Dacks, J.B., and Field, M.C. (2008). Evolution of the multivesicular body ESCRT machinery; retention across the eukaryotic lineage. *Traffic* 9, 1698-1716.
- McCullough, J., Clippinger, A.K., Talledge, N., Skowyra, M.L., Saunders, M.G., Naismith, T.V., Colf, L.A., Afonine, P., Arthur, C., Sundquist, W.I., et al. (2015). Structure and membrane remodeling activity of ESCRT-III helical polymers. *Science*.
- Meng, B., Ip, N.C., Prestwood, L.J., Abbink, T.E., and Lever, A.M. (2015). Evidence that the endosomal sorting complex required for transport-II (ESCRT-II)

is required for efficient human immunodeficiency virus-1 (HIV-1) production. *Retrovirology* 12, 72.

Pashkova, N., Gakhar, L., Winstorfer, S.C., Sunshine, A.B., Rich, M., Dunham, M.J., Yu, L., and Piper, R.C. (2013). The yeast alix homolog bro1 functions as a ubiquitin receptor for protein sorting into multivesicular endosomes. *Dev Cell* 25, 520-533.

Rue, S.M., Mattei, S., Saksena, S., and Emr, S.D. (2008). Novel Ist1-Did2 complex functions at a late step in multivesicular body sorting. *Mol Biol Cell* 19, 475-484.

Spang, A., Saw, J.H., Jorgensen, S.L., Zaremba-Niedzwiedzka, K., Martijn, J., Lind, A.E., van Eijk, R., Schleper, C., Guy, L., and Ettema, T.J. (2015). Complex archaea that bridge the gap between prokaryotes and eukaryotes. *Nature* 521, 173-179.

Strack, B., Calistri, A., Accola, M.A., Palu, G., and Gottlinger, H.G. (2000). A role for ubiquitin ligase recruitment in retrovirus release. *Proc Natl Acad Sci U S A* 97, 13063-13068.

Tang, S., Buchkovich, N.J., Henne, W.M., Banjade, S., Kim, Y.J., and Emr, S.D. (2016). ESCRT-III activation by parallel action of ESCRT-I/II and ESCRT-0/Bro1 during MVB biogenesis. *Elife* 5.

Tang, S., Henne, W.M., Borbat, P.P., Buchkovich, N.J., Freed, J.H., Mao, Y., Fromme, J.C., and Emr, S.D. (2015). Structural basis for activation, assembly and membrane binding of ESCRT-III Snf7 filaments. *Elife* 4.

VerPlank, L., Bouamr, F., LaGrassa, T.J., Agresta, B., Kikonyogo, A., Leis, J., and Carter, C.A. (2001). Tsg101, a homologue of ubiquitin-conjugating (E2) enzymes, binds the L domain in HIV type 1 Pr55(Gag). *Proc Natl Acad Sci U S A* 98, 7724-7729.

Vietri, M., Schink, K.O., Campsteijn, C., Wegner, C.S., Schultz, S.W., Christ, L., Thoresen, S.B., Brech, A., Raiborg, C., and Stenmark, H. (2015). Spastin and ESCRT-III coordinate mitotic spindle disassembly and nuclear envelope sealing. *Nature* 522, 231-235.

## APPENDIX I

### Characterizing the Role of the Snf7 $\alpha$ 4 Helix in ESCRT-III Assembly

#### Summary

The Endosomal Sorting Complex Required for Transport-III (ESCRT-III) is cellular membrane remodeling machinery that induces membrane budding that occurs away from the cytoplasm. ESCRT-III is comprised of structurally and biochemically similar subunits. Since Snf7 is the most abundant ESCRT-III subunit and is able to homo-polymerize to deform membranes, it is essential to understand the assembly and architecture of Snf7 homo-polymer and ESCRT-III hetero-polymer.

#### The Snf7 $\alpha$ 4 Helix is Important for ESCRT-III Function

Conservation and structure-based mutagenesis analysis in the Snf7 N-terminal core domain (Figure A1.1A) suggest that an electrostatic charged surface (denoted as surface “A”) in the  $\alpha$ 4 helix is functionally important (Figure A1.1B). Mutations on negatively charged residues Asp127, Asp131, Glu138 and Glu142, and positively charged residues Arg134 and Arg149 severely impaired the MVB sorting function of Snf7 (Figure A1.1C). C-terminally GFP-tagged Snf7  $\alpha$ 4 mutants localized to the vacuolar membranes in the presence of wild-type Snf7, and to the aberrant endosomal class E compartments in the absence of wild-type Snf7. Notably, a fraction of  $\alpha$ 4 mutant Snf7-GFP localized to the punctate structure peripheral to the plasma membranes (Figures A1.1D-E). Moreover, *snf7*  $\alpha$ 4 mutants, D127K, D131K, exhibited canavanine sensitive phenotype (Lin et al., 2008) (Figures A1.1F-G). Strikingly, the *snf7* double

mutant D127K D131K showed dominant negative phenotype (Figures A1.1I-J), indicating that  $\text{Snf7}^{\text{D127K D131K}}$  could integrate into Snf7 polymer and impair the ESCRT-III function (Figures A1.1H and K). By far,  $\text{snf7}^{\text{D127K D131K}}$  is known to be the only dominant negative mutant, after testing hundreds of  $\text{snf7}$  mutants.

### **Identification of a Snf7 α4-α4 Interface Required for Polymer Assembly**

To investigate whether  $\text{snf7}$  α4 is involved in Snf7 polymer assembly, I performed an unbiased random mutagenesis screening using  $\text{snf7}^{\text{D127K}}$  or  $\text{snf7}^{\text{D131K}}$  as a template, and selected suppressor alleles by canavanine (Figure A1.2). Charge inversion mutations on Snf7 α3 residue His118, α4 residues Arg134 and Arg149 (Figure A1.2B) are able to functionally rescue the phenotypes caused by  $\text{snf7}^{\text{D127K}}$ ,  $\text{snf7}^{\text{D131K}}$  or  $\text{snf7}^{\text{E142K}}$  *in cis* (Figures A1.2C-D, F). To test whether these oppositely charged residues form an electrostatic interface between two Snf7 subunits in an ESCRT-III polymer, I co-expressed both charge-inversion mutants *in trans*. Remarkably, this resulted in functional rescue to near wild-type MVB sorting levels (Figure A1.2E).

The Snf7 α4 residue Leu121 has been previously shown important for Snf7 self-assembly both *in vitro* and *in vivo* (Saksena et al., 2009; Tang et al., 2015). Notably, despite mutations on Leu121 to Lys (L121K) or Asp (L121D) caused severe MVB sorting defects, co-expressing both mutants *in trans* restored function to near wild-type level (Figure A1.2G). Moreover, a significant portion of purified recombinant  $\text{Snf7}^{\text{R52E L121C}}$  proteins crosslinked to a dimer through a disulfide bond (Figure A1.2H), indicating that Leu121 is also involved in the proposed Snf7 α4-α4 interface.

To test whether these *snf7* α4 suppressors are functionally important, I performed further analyses of these charge inversion mutations on His118, Arg134 and Arg149. Although the single charge inversion does not exhibit canavanine sensitivity (Figure A1.3A), when mutations are combined, MVB sorting efficiencies were further decreased from 40-60% to below 20% (Figure A1.3C). Interestingly, when the double mutants, D127K D131K, cannot be fully rescued by H118D R134D R149D (Figure A1.3B). H118D R134D R149D is not dominant negative (Figure A1.3D), but it was able to rescue the dominant negative phenotype of D127K D131K (Figure A1.3F).

### **Snf7 α4 Mutants with Increased Membrane Binding and Polymer Assembly Capabilities**

I next asked if *snf7* α4 surface “A” is involved in the interaction between Snf7 and Vps24, since previous studies suggested the functional importance of Snf7 α4 in Vps24 recruitment (Sciskala and Kolling, 2013). I performed subcellular fractionation using *snf7Δ* yeast cells, yeast cells chromosomally expressing *SNF7-FLAG*, or *vps4Δ* yeast cells chromosomally expressing *SNF7-FLAG*, and ectopically expressing *SNF7*, *snf7<sup>D127K</sup>*, *snf7<sup>D131K</sup>* or *snf7<sup>D127K D131K</sup>*. Surprisingly, Snf7 α4 mutants were increasingly enriched in the membrane-bound P13 fractions compared to the wild-type Snf7 (Figures A1.4A-C). Western blotting analyses on Vps24 indicate that the Vps24 was reduced in the P13 fractions in the presence of Vps4, which disassembles and recycles ESCRT-III polymer to cytosol (Babst et al., 1997) (Figures A1.4A-C). Co-immunoprecipitation between Snf7 α4 mutants and Snf7<sup>WT</sup>-FLAG, and glycerol gradient analyses further suggest that Snf7 α4 mutants D127K or D131K increased the interaction with Snf7 and

generated high molecular weight assemblies (Figures A1.4D-E). This may explain the dominant-negative effect, as this mutant incorporates into wild-type Snf7 filaments but blocks the recruitment of Vps24.

I took advantage of the observation that Vps24-GFP normally localizes to aberrant endosomal class E compartments but is redistributed to the cytoplasm in *snf7Δ* cells (Teis et al., 2008). It has been shown previously that Snf7<sup>core</sup> is sufficient to recruit Vps24-GFP to class E compartments, but Snf7<sup>a0-3</sup> mislocalizes Vps24-GFP to the cytoplasm (Henne et al., 2012). Using this assay, I found that Snf7<sup>D131K</sup> partially mislocalizes Vps24-GFP, and Snf7<sup>D127K D131K</sup> quantitatively redistributes Vps24-GFP to the cytoplasm (Figure 6G). These observations indicated that the conserved surface “A” of Snf7 α4 is necessary for the recruitment of Vps24.

### **Identification of the Role of the Snf7 α4 Helix in Vps24 Recruitment**

Given that all ESCRT-III subunits show similar domain organization, I performed mutagenesis on the α4 helix of Vps20, Vps24, Vps2 based on sequence alignment. Interestingly, mutations on Vps20, Vps24, Vps2 did not show significant functional defects (Figure A1.5A). Since modestly overexpressing *VPS24* can also partially restore the functional defect of *snf7<sup>D131K</sup>* (Figure A1.5B), I hypothesized that the Snf7 α4 helix may have additional roles than previously proposed as Snf7-Snf7 interface. Perhaps a functional Snf7 α4-α4 interface is a perquisite for generating a novel surface for Vps24 recruitment (Figure A1.5C).

To identify potential regions on Vps24 required for its recruitment, I performed random mutagenesis on *VPS24*, and screened for suppressor mutants in *snf7<sup>D127K D131K</sup>*

VPS24 or *snf7*<sup>D127K D131K</sup> *vps24Δ* cells (Figure A1.5D). Interestingly, I identified several suppressor mutants in VPS24 that partially rescued the loss of function by *snf7*<sup>D131K</sup> (Figure A1.5F). Unexpectedly, these suppressor mutants (Figure A1.5E) do not locate to one particular region of Vps24. Because of the lack of additional atomic resolution structural information of Snf7-Vps24 hetero-polymer, it is currently unclear how a Snf7 homopolymer recruits Vps24 to the membranes, and how Vps24 remodel Snf7 polymer to generate a membrane sculpting superhelix. Ordered assembly of the ESCRT-III complex highlights the unique division of labor between ESCRT-III subunits, with every subunit contributing to a unique function. Although Snf7, Vps24 and Vps2 are all capable of self-assembly, Snf7-dependent recruitment of Vps24 and Vps2 causes Snf7 spirals to reorganize into superhelices to drive membrane invaginations (Henne et al., 2012). Thus, characterizing inter-ESCRT-III subunit interactions is critical for the understanding of distinct architectural states of ESCRT-III. Intriguingly, I found that the Snf7 interfilamentary binding site in α4 and the surface “A” of Snf7 that has a role in either Snf7-Snf7 or Snf7-Vps24 interaction, are distinct but very close to each other. Because of this, I propose that the recruitment of Vps24 may sterically hinder further inter-filament Snf7 interactions, which would result in the formation of a Snf7-Vps24 co-polymer that alters the overall ESCRT-III architecture. This may induce the structural changes necessary for the formation of a ESCRT-III superhelix. However, to fully understand this architectural change, future work is needed.

## Vps20 and Vps24 are More Tolerant to Mutations than Snf7

Despite the absence of structural information of ESCRT-III hetero-polymer of core subunits, sequence alignment analysis of Snf7, Vps20, and Vps24 suggest that all ESCRT-III subunits show high degree of homology, especially at key residues important for Snf7 self-assembly (Figures A1.6A, D) (Tang et al., 2015). We hypothesized that the Vps20 and Vps24 may utilize their equivalent residues to interact with Snf7 or themselves. To test this hypothesis, we perform sequence alignment-based site-directed mutagenesis (Figures A1.6B, E, G and J) and tested each *vps20* or *vps24* mutants in *vps20Δ* or *vps24Δ* yeast by the Mup1-pH MVB sorting assay. Surprisingly, although these point mutants on the  $\alpha 2/3^i-\alpha 3^{i+1}$  hydrophobic or  $\alpha 1^i-\alpha 2/3^{i+1}$  electrostatic interfaces severely block the function of Snf7 *in vivo*, the equivalent mutations showed only modest MVB sorting defects on Vps24 (I92E, M105E and M112E of 60-80% MVB sorting efficiencies), and wild-type level sorting on Vps20. Selected double mutants on Vps20 showed MVB sorting defects. It is unclear, however, which surface ("i" or "i+1") of Vps20 is utilized to nucleate a Snf7 filament.

Since Snf7 is major component of the ESCRT-III complex, the interaction between Snf7 are repeated many times in a polymer and, thus, mutations on the interface would have "additive" effect, which resulted in a quantifiable phenotype. Vps20, a minor component of ESCRT-III, is more tolerant to mutations, likely because the Vps20-Snf7 interaction is only present once in a Snf7 polymerization event.

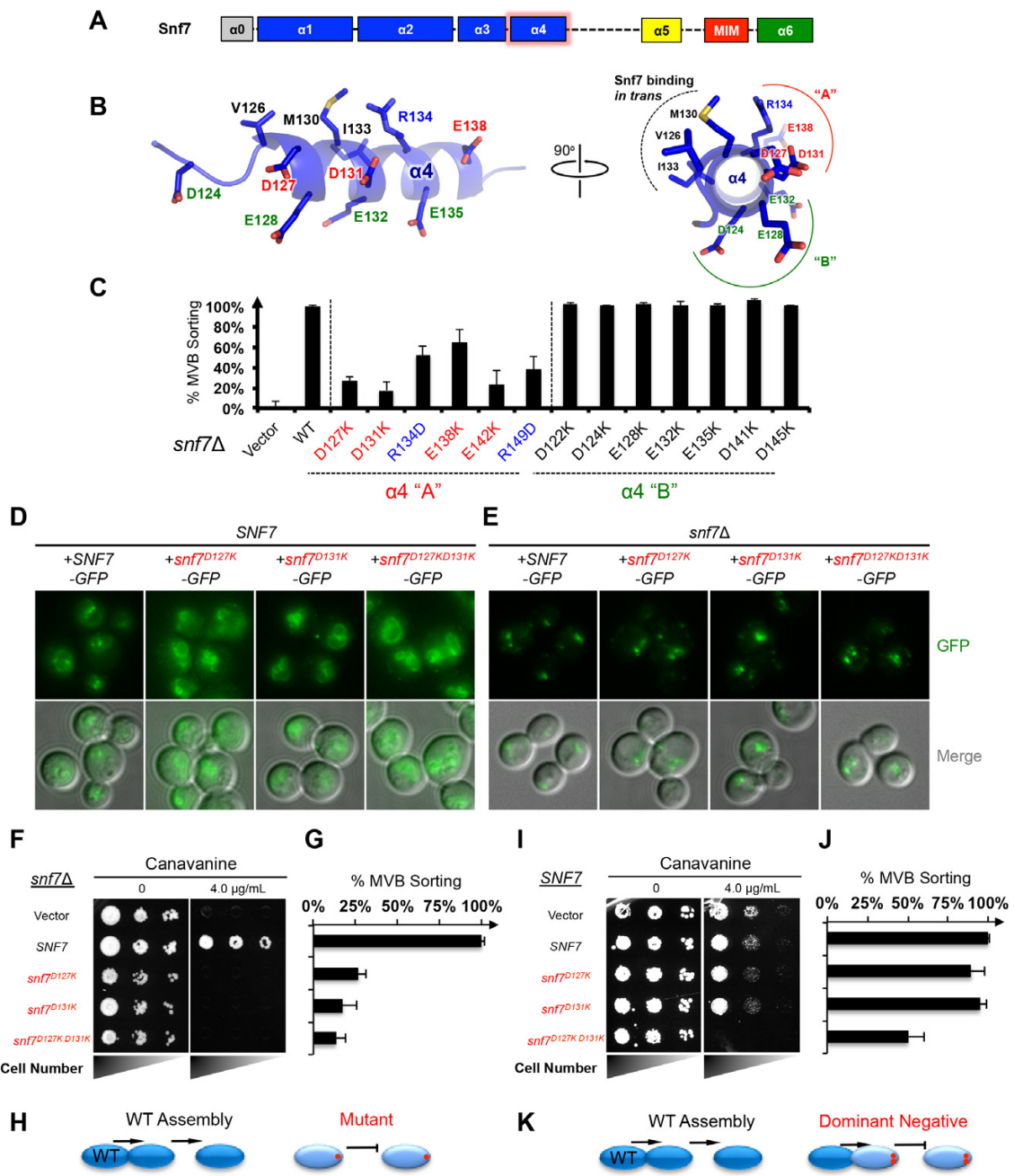


**Figure A1.1 Charged Residues in Snf7 $\alpha^4$  are Critical for Function *in vivo***

## Figure A1.1 Charged Residues in Snf7<sup>α4</sup> are Critical for Function *in vivo*

- (A) Domain organization of Snf7. The α4 helix is boxed in red.
- (B) Ribbon diagrams of Snf7 α4 (PDB: 5FD9) with side chains shown in sticks. Residues for Snf7 binding *in trans* (Tang et al., 2015) are labeled in black, for surface “A” in red and “B” in green.
- (C) Quantitative MVB sorting data for *snf7Δ* yeast exogenously expressing empty vector, *SNF7*, *snf7*<sup>D127K</sup>, *snf7*<sup>D131K</sup>, *snf7*<sup>R134D</sup>, *snf7*<sup>E138K</sup>, *snf7*<sup>E142K</sup>, *snf7*<sup>R149D</sup>, *snf7*<sup>D122K</sup>, *snf7*<sup>D124K</sup>, *snf7*<sup>D128K</sup>, *snf7*<sup>E132K</sup>, *snf7*<sup>E135K</sup>, *snf7*<sup>D141K</sup> and *snf7*<sup>D145K</sup>. Error bars represent standard deviations from 3-5 independent experiments.
- (D) Representative images of mid-log wild-type yeast exogenously expressing *SNF7-GFP*, *snf7*<sup>D127K</sup>-*GFP*, *snf7*<sup>D131K</sup>-*GFP* and *snf7*<sup>D127KD131K</sup>-*GFP*. GFP images (upper row); composite images of GFP and DIC (bottom row).
- (E) Representative images of mid-log *snf7Δ* yeast exogenously expressing *SNF7-GFP*, *snf7*<sup>D127K</sup>-*GFP*, *snf7*<sup>D131K</sup>-*GFP* and *snf7*<sup>D127KD131K</sup>-*GFP*. GFP images (upper row); composite images of GFP and DIC (bottom row).
- (F) Canavanine sensitivity assay of *snf7Δ* yeast exogenously expressing empty vector, *SNF7*, *snf7*<sup>D127K</sup>, *snf7*<sup>D131K</sup>, and *snf7*<sup>D127K D131K</sup> grown under 0 or 4.0 µg/mL canavanine.
- (G) Quantitative MVB sorting data for *snf7Δ* yeast exogenously expressing *SNF7*, *snf7*<sup>D127K</sup>, *snf7*<sup>D131K</sup> and *snf7*<sup>D127K D131K</sup>. Error bars represent standard deviations from 3-5 independent experiments. Data for *SNF7*, *snf7*<sup>D127K</sup> and *snf7*<sup>D131K</sup> are replotted from Figure A1.1C for comparison.
- (H) Schematic of wild-type and mutant Snf7 assembly.
- (I) Canavanine sensitivity assay of wild-type yeast exogenously expressing empty vector, *SNF7*, *snf7*<sup>D127K</sup>, *snf7*<sup>D131K</sup>, and *snf7*<sup>D127K D131K</sup> grown under 0 or 4.0 µg/mL canavanine.
- (J) Quantitative MVB sorting data for *snf7Δ* yeast exogenously expressing *SNF7* and *SNF7*, *SNF7* and *snf7*<sup>D127K</sup>, *SNF7* and *snf7*<sup>D131K</sup>, and *SNF7* and *snf7*<sup>D127K D131K</sup>. Error bars represent standard deviations from 3-5 independent experiments.
- (K) Schematic of wild-type and dominant negative mutant Snf7 assembly.

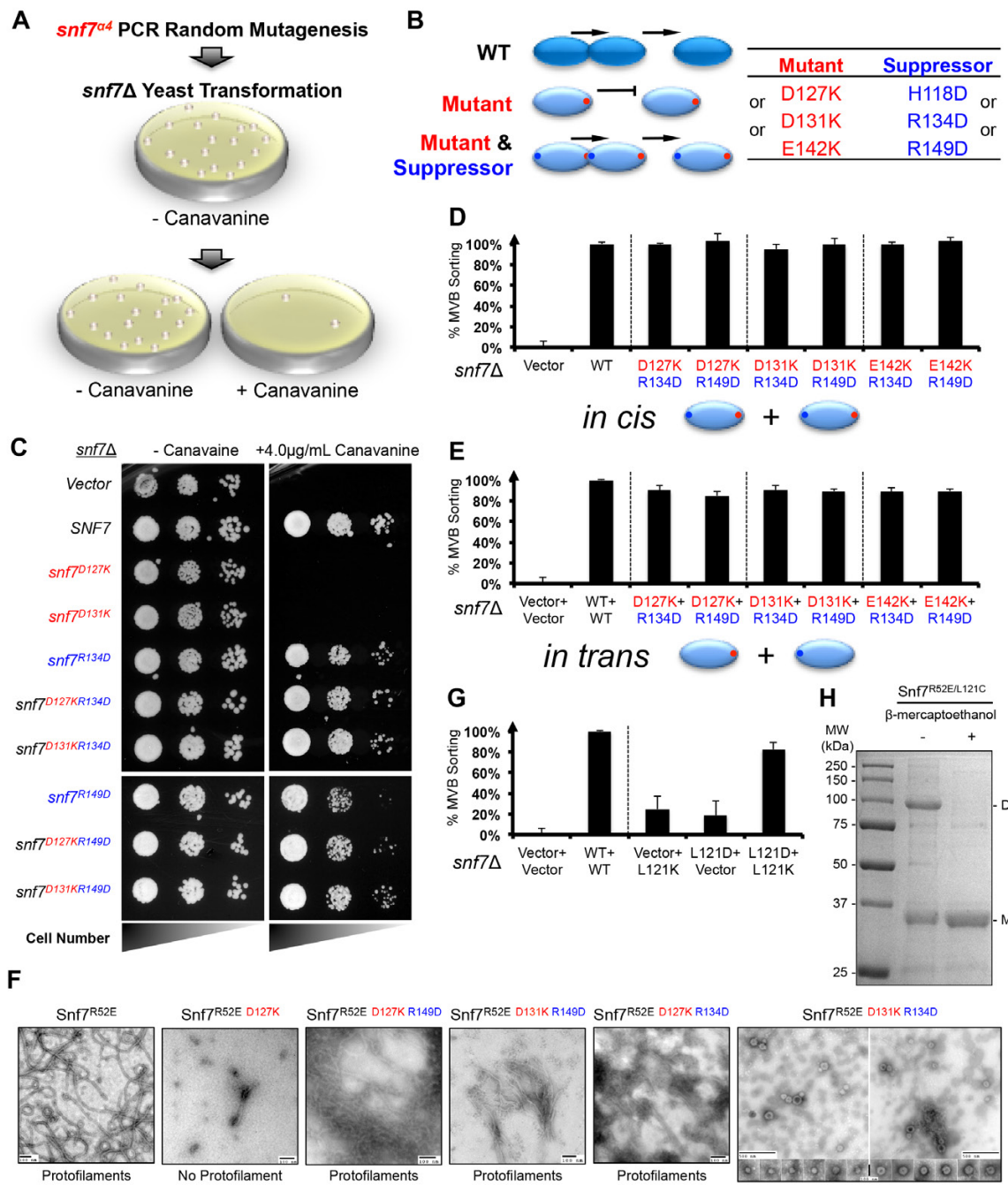


**Figure A1.2 Electrostatically Charged Residues in Snf7<sup>a4</sup> Form a Snf7 Binding Interface**

**Figure A1.2 Electrostatically Charged Residues in Snf7<sup>a4</sup> Form a Snf7 Binding Interface**

- (A) Cartoon schematic of the screening strategy to identify  $snf7^{D127K}$  or  $snf7^{D131K}$  suppressors in  $snf7\Delta$  yeast.
- (B) Schematic of Snf7 assembly and summary of the genetic screening results.
- (C) Canavanine sensitivity assay of  $snf7\Delta$  yeast exogenously expressing empty vector,  $SNF7$ ,  $snf7^{D127K}$ ,  $snf7^{D131K}$ ,  $snf7^{R134D}$ ,  $snf7^{D127K R134D}$ ,  $snf7^{D131K R134D}$ ,  $snf7^{R149D}$ ,  $snf7^{D127K R149D}$  and  $snf7^{D131K R149D}$  grown under 0 or 4.0 µg/mL canavanine.
- (D) Quantitative MVB sorting data for  $snf7\Delta$  yeast exogenously expressing empty vector,  $SNF7$ ,  $snf7^{D127K R134D}$ ,  $snf7^{D127K R149D}$ ,  $snf7^{D131K R134D}$ ,  $snf7^{D131K R149D}$ ,  $snf7^{E142K R134D}$  and  $snf7^{E142K R149D}$ . Error bars represent standard deviations from 3-5 independent experiments.
- (E) Quantitative MVB sorting data for  $snf7\Delta$  yeast exogenously expressing empty vector and empty vector,  $SNF7$  and  $SNF7$ ,  $snf7^{D127K}$  and  $snf7^{R134D}$ ,  $snf7^{D127K}$  and  $snf7^{R149D}$ ,  $snf7^{D131K}$  and  $snf7^{R134D}$ ,  $snf7^{D131K}$  and  $snf7^{R149D}$ ,  $snf7^{E142K}$  and  $snf7^{R134D}$ , and  $snf7^{E142K}$  and  $snf7^{R149D}$ . Error bars represent standard deviations from 3-5 independent experiments.
- (F) Representative TEM images of recombinant  $Snf7^{R52E}$ ,  $Snf7^{R52E D127K}$ ,  $Snf7^{R52E D127K R149D}$ ,  $Snf7^{R52E D131K R149D}$ ,  $Snf7^{R52E D127K R134D}$  and  $Snf7^{R52E D131K R134D}$ . Scale bars 100 nm or 500 nm as indicated in the panel.
- (G) Quantitative MVB sorting data for  $snf7\Delta$  yeast exogenously expressing empty vector and empty vector,  $SNF7$  and  $SNF7$ , empty vector and  $snf7^{L121K}$ ,  $snf7^{L121D}$  and empty vector, and  $snf7^{L121D}$  and  $snf7^{L121K}$ . Error bars represent standard deviations from 3-5 independent experiments.
- (H) SDS-PAGE coomassie brilliant blue staining of purified recombinant  $Snf7^{R52E L121C}$  in the absence or presence of β-mercaptoethanol.

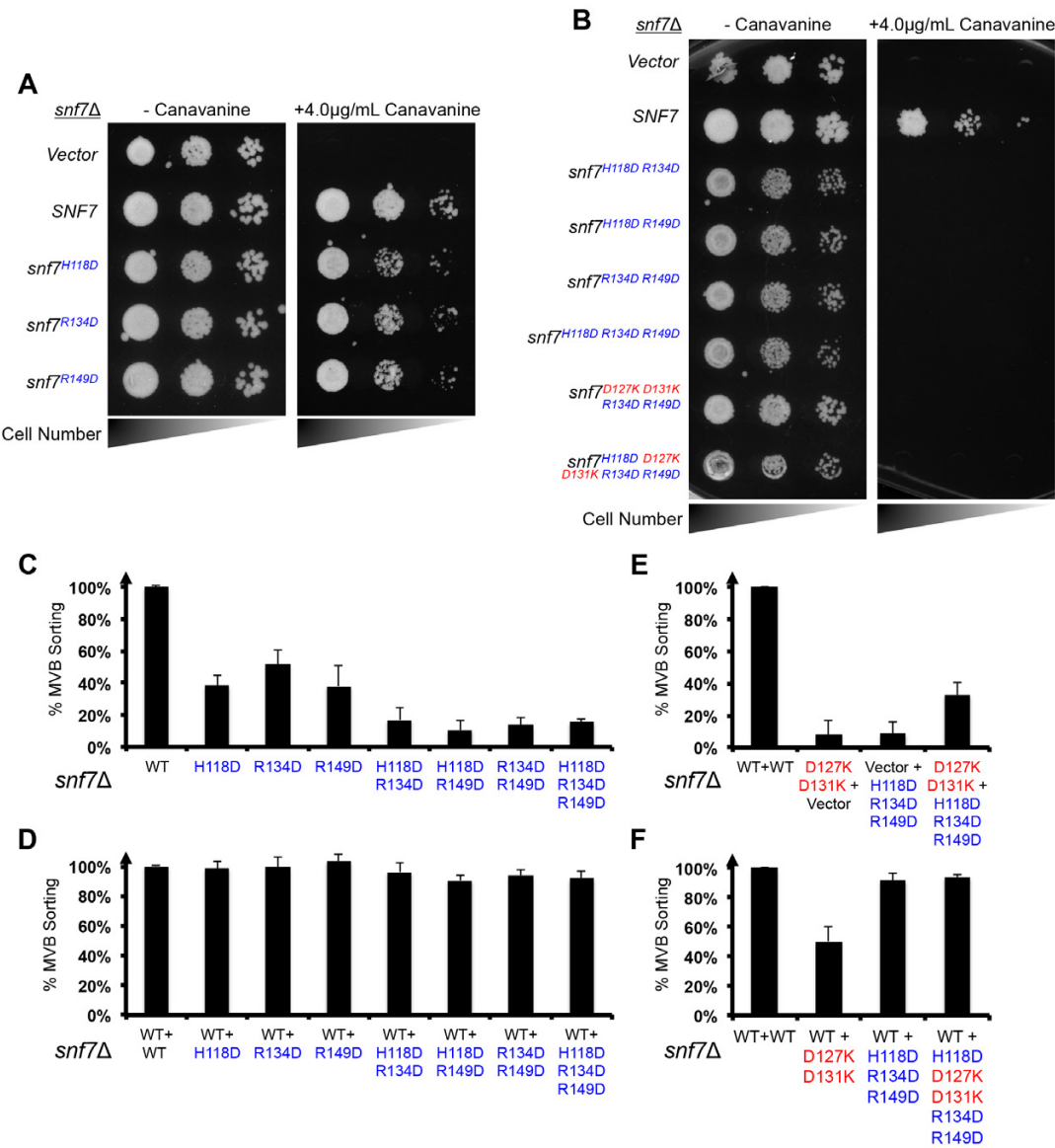


**Figure A1.3 The Snf7<sup>α4</sup> Interface is Sensitive to Multiple Mutations**

### Figure A1.3 The Snf7<sup>a4</sup> Interface is Sensitive to Multiple Mutations

- (A) Canavanine sensitivity assay of *snf7Δ* yeast exogenously expressing empty vector, *SNF7*, *snf7*<sup>H118D</sup>, *snf7*<sup>R134D</sup> and *snf7*<sup>R149D</sup> grown under 0 or 4.0 µg/mL canavanine.
- (B) Canavanine sensitivity assay of *snf7Δ* yeast exogenously expressing empty vector, *SNF7*, *snf7*<sup>H118D R134D</sup>, *snf7*<sup>H118D R149D</sup>, *snf7*<sup>R134D R149D</sup>, *snf7*<sup>H118D R134D R149D</sup>, *snf7*<sup>D127K D131K R134D R149D</sup> and *snf7*<sup>H118D D127K D131K R134D R149D</sup> grown under 0 or 4.0 µg/mL canavanine.
- (C) Quantitative MVB sorting data for *snf7Δ* yeast exogenously expressing *SNF7*, *snf7*<sup>H118D</sup>, *snf7*<sup>R134D</sup>, *snf7*<sup>R149D</sup>, *snf7*<sup>H118D R134D</sup>, *snf7*<sup>H118D R149D</sup>, *snf7*<sup>R134D R149D</sup> and *snf7*<sup>H118D R134D R149D</sup>. Error bars represent standard deviations from 3-5 independent experiments.
- (D) Quantitative MVB sorting data for *snf7Δ* yeast exogenously expressing *SNF7* and *SNF7*, *SNF7* and *snf7*<sup>H118D</sup>, *SNF7* and *snf7*<sup>R134D</sup>, *SNF7* and *snf7*<sup>R149D</sup>, *SNF7* and *snf7*<sup>H118D R134D</sup>, *SNF7* and *snf7*<sup>H118D R149D</sup>, *SNF7* and *snf7*<sup>R134D R149D</sup>, and *SNF7* and *snf7*<sup>H118D R134D R149D</sup>. Error bars represent standard deviations from 3-5 independent experiments.
- (E) Quantitative MVB sorting data for *snf7Δ* yeast exogenously expressing *SNF7* and *SNF7*, *snf7*<sup>D127K D131K</sup> and empty vector, empty vector and *snf7*<sup>H118D R134D R149D</sup>, *snf7*<sup>D127K D131K</sup> and *snf7*<sup>H118D R134D R149D</sup>. Error bars represent standard deviations from 3-5 independent experiments.
- (F) Quantitative MVB sorting data for *snf7Δ* yeast exogenously expressing *SNF7* and *SNF7*, *SNF7* and *snf7*<sup>D127K D131K</sup>, *SNF7* and *snf7*<sup>H118D R134D R149D</sup>, and *SNF7* and *snf7*<sup>H118D D127K D131K R134D R149D</sup>. Error bars represent standard deviations from 3-5 independent experiments.

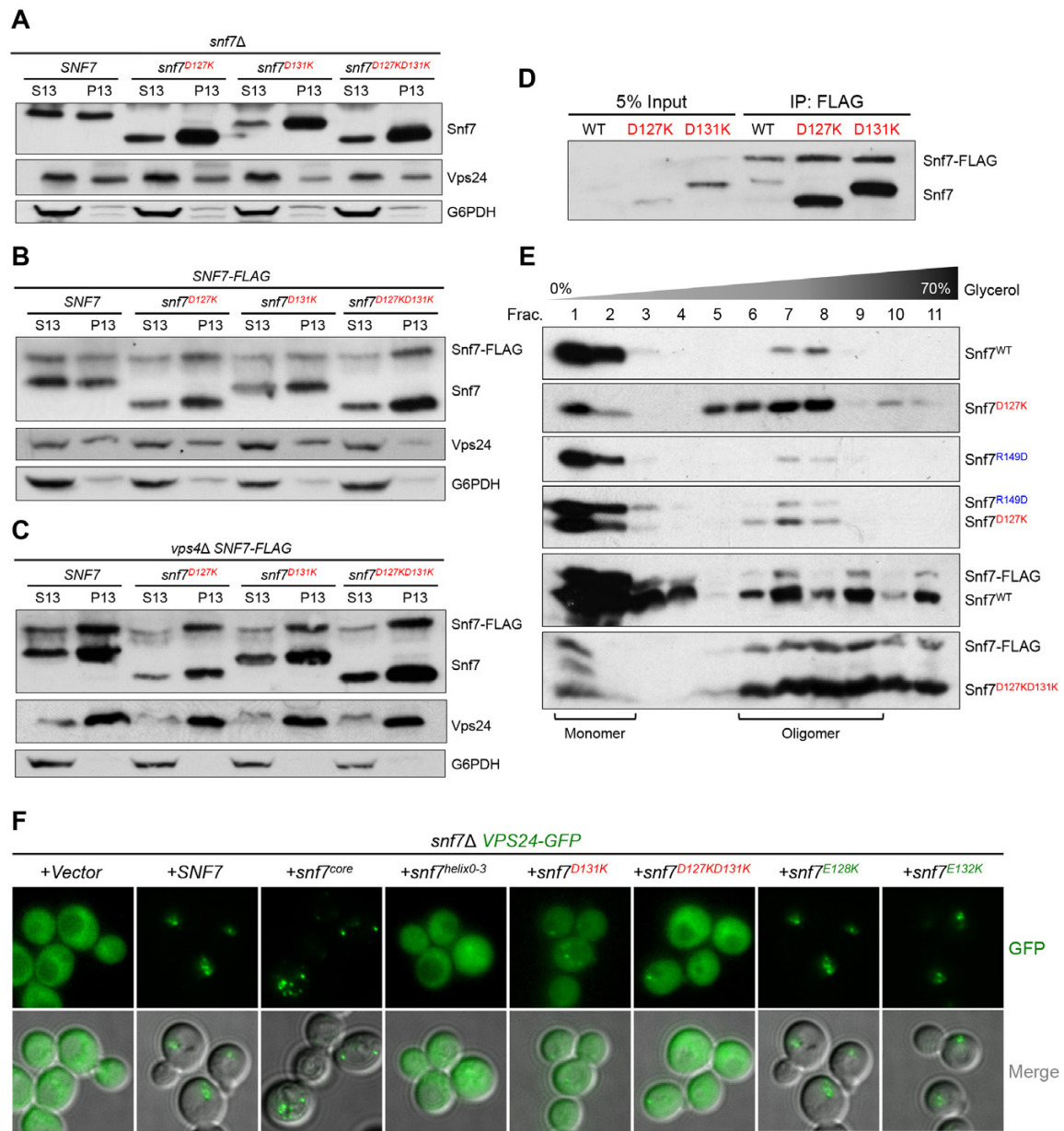


**Figure A1.4 The Snf7<sup>a4</sup> Interface is Critical in Vps24 Endosomal Recruitment**

**Figure A1.4 The Snf7<sup>a4</sup> Interface is Critical in Vps24 Endosomal Recruitment**

- (A) Subcellular fractionation and western blotting analysis of *snf7Δ* yeast exogenously expressing *SNF7*, *snf7*<sup>D127K</sup>, *snf7*<sup>D131K</sup> and *snf7*<sup>D127K D131K</sup>. Anti-Snf7 and anti-Vps24. G6PDH as a loading control.
- (B) Subcellular fractionation and western blotting analysis of *SNF7-3FLAG* yeast exogenously expressing *SNF7*, *snf7*<sup>D127K</sup>, *snf7*<sup>D131K</sup> and *snf7*<sup>D127K D131K</sup>. Anti-Snf7 and anti-Vps24. G6PDH as a loading control.
- (C) Subcellular fractionation and western blotting analysis of *vps4Δ SNF7-3FLAG* yeast exogenously expressing *SNF7*, *snf7*<sup>D127K</sup>, *snf7*<sup>D131K</sup> and *snf7*<sup>D127K D131K</sup>. Anti-Snf7 and anti-Vps24. G6PDH as a loading control.
- (D) Co-immunoprecipitation and western blotting analysis of *SNF7-3FLAG* yeast exogenously expressing *SNF7*, *snf7*<sup>D127K</sup> and *snf7*<sup>D131K</sup>. Anti-Snf7.
- (E) Glycerol gradient (10%-70%) analysis of *snf7Δ* yeast exogenously expressing *SNF7*, *snf7*<sup>D127K</sup>, *snf7*<sup>R149D</sup>, and *snf7*<sup>D127K</sup> and *snf7*<sup>R149D</sup>, *SNF7-3FLAG* yeast exogenously expressing *SNF7*, and *snf7*<sup>D127K D131K</sup>.
- (F) Representative images of mid-log *snf7Δ VPS24-GFP* yeast exogenously expressing empty vector, *SNF7*, *snf7*<sup>1-150</sup>, *snf7*<sup>1-120</sup>, *snf7*<sup>D127K</sup>, *snf7*<sup>D127K D131K</sup>, *snf7*<sup>E128K</sup> and *snf7*<sup>E132K</sup>. GFP images (upper row); composite images of GFP and DIC (bottom row).

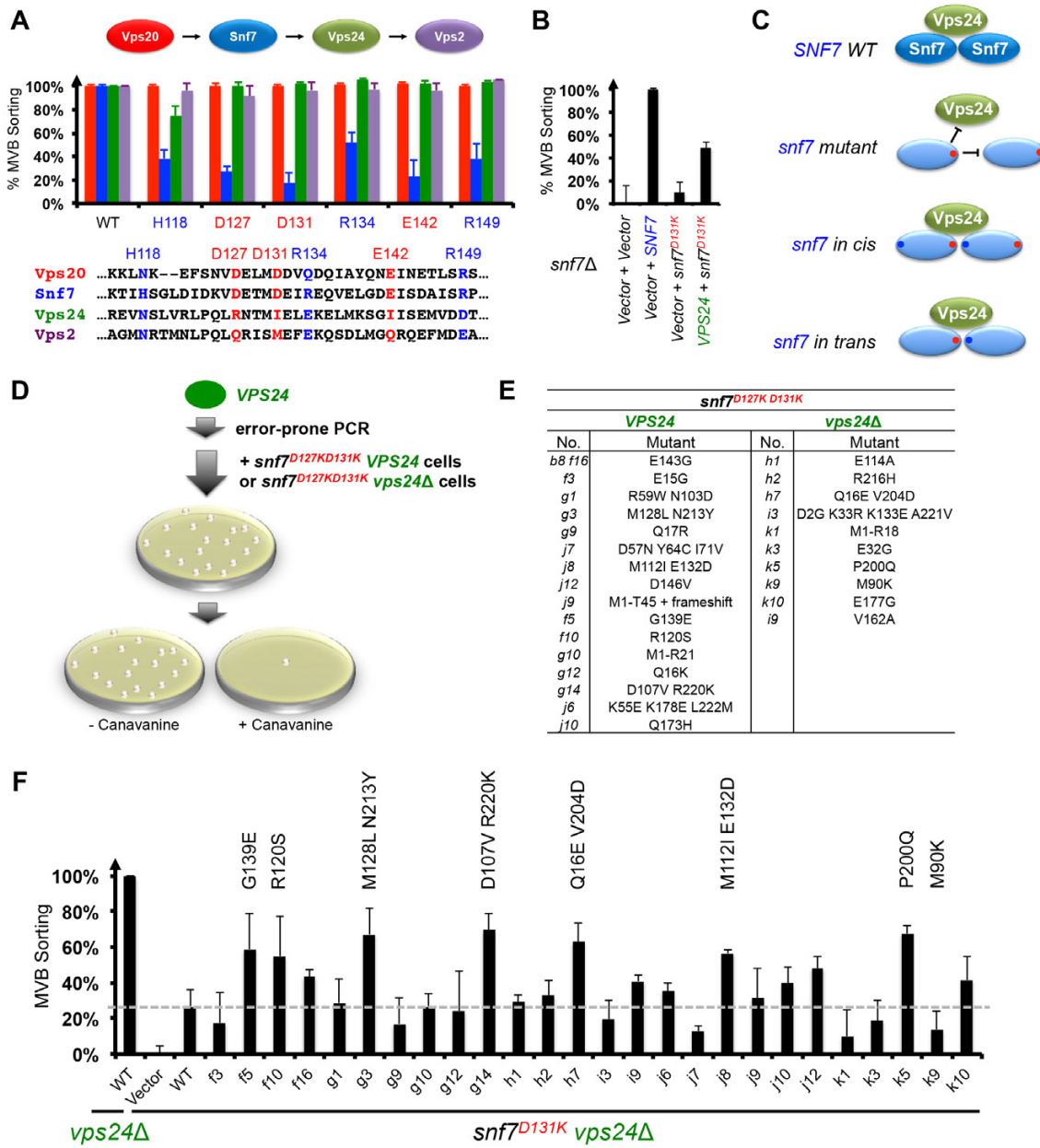


**Figure A1 5 Genetic Screening for Snf7-Vps24 Interface Mutants**

### Figure A1.5 Genetic Screening for Snf7-Vps24 Interface Mutants

(A) Schematic of ESCRT-III ordered assembly: Vps20-Snf7-Vps24-Vps2. Quantitative MVB sorting data for *vps20Δ* yeast (red) exogenously expressing *VPS20*, *vps20<sup>N117D</sup>*, *vps20<sup>D124K</sup>*, *vps20<sup>D128K</sup>*, *vps20<sup>Q131D</sup>*, *vps20<sup>E139K</sup>* and *vps20<sup>R146D</sup>*, *snf7Δ* yeast (blue) exogenously expressing *SNF7*, *snf7<sup>H118D</sup>*, *snf7<sup>D127K</sup>*, *snf7<sup>D131K</sup>*, *snf7<sup>R134D</sup>*, *snf7<sup>E142K</sup>* and *snf7<sup>R149D</sup>*, *vps24Δ* yeast (green) exogenously expressing *VPS24*, *vps24<sup>N116R</sup>*, *vps24<sup>R125D</sup>*, *vps24<sup>I129D</sup>*, *vps24<sup>E132R</sup>*, *vps24<sup>I140D</sup>* and *vps24<sup>D147R</sup>*, *vps2Δ* yeast (purple) exogenously expressing *VPS2*, *vps2<sup>N117R</sup>*, *vps2<sup>Q126D</sup>*, *vps2<sup>M130D</sup>*, *vps2<sup>E133R</sup>*, *vps2<sup>Q141D</sup>* and *vps2<sup>E148R</sup>*. Error bars represent standard deviations from 3-5 independent experiments. α4 sequence alignment of Vps20, Snf7, Vps24 and Vps2. Snf7's key α4 residues are labeled on the top.

(B) Quantitative MVB sorting data for *snf7Δ* yeast exogenously expressing empty vector and empty vector, empty vector and *SNF7*, empty vector and *snf7<sup>D131K</sup>*, and *VPS24* and *snf7<sup>D131K</sup>*. Error bars represent standard deviations from 3-5 independent experiments.

(C) Schematic of the role of α4 residues in the Snf7-Vps24 interaction.

(D) Cartoon schematic of the screening strategy to identify *vps24* suppressors in *snf7<sup>D127K D131K</sup>* *vps24Δ* or *snf7<sup>D127K D131K</sup>* *VPS24* yeast.

(E) Summary of *vps24* suppressor screening results.

(F) Quantitative MVB sorting data for *vps24Δ* yeast exogenously expressing *VPS24* and empty vector, *snf7<sup>D131K</sup>* *vps24Δ* yeast exogenously expressing *VPS24* and each candidate *vps24* suppressor listed in (E). Error bars represent standard deviations from 3-5 independent experiments.

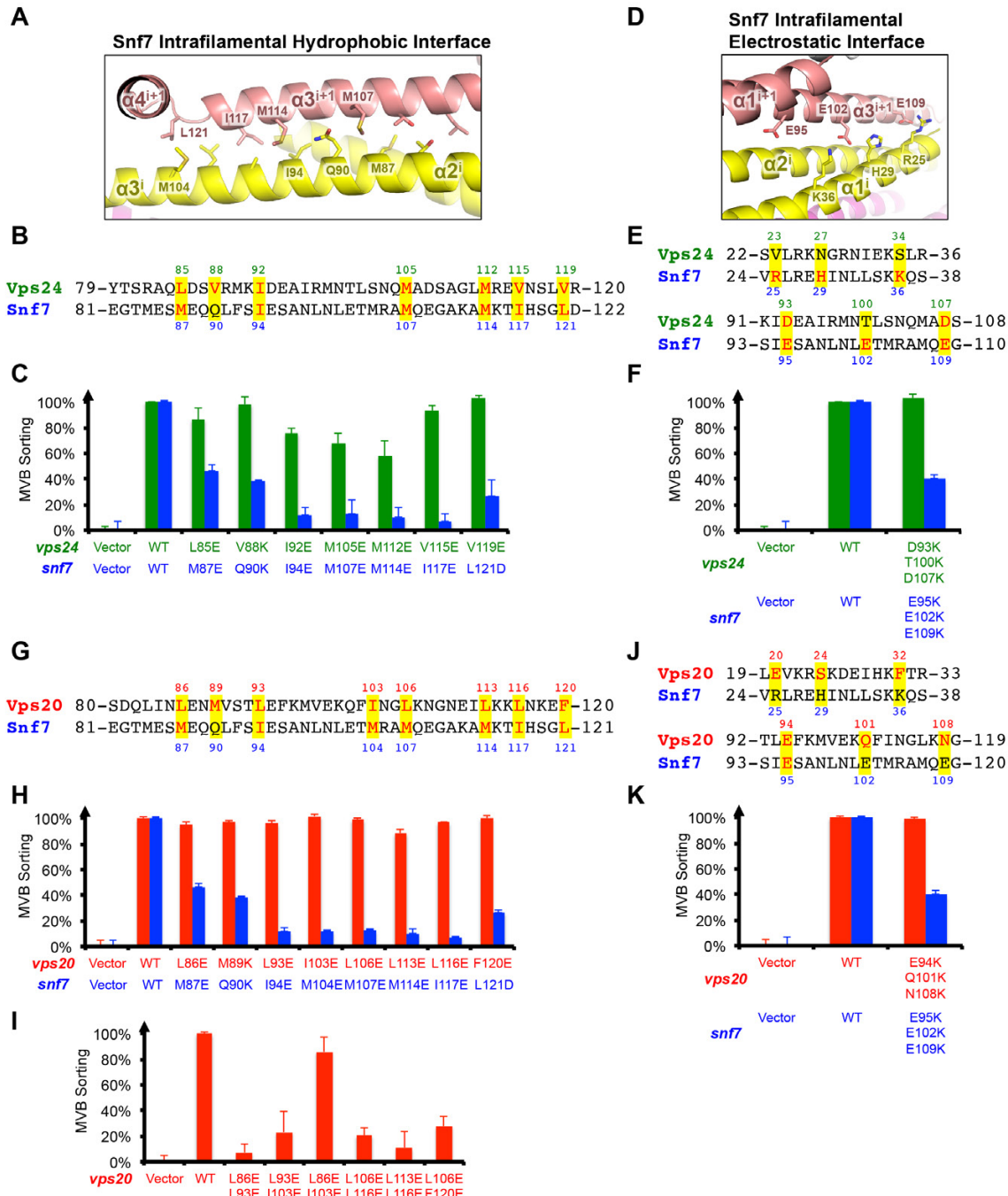


**Figure A1.6 Vps24 and Vps20 are Tolerant to Mutations in the Proposed Inter-Subunit Interfaces**

## Figure A1.6 Vps24 and Vps20 are Tolerant to Mutations in the Proposed Inter-Subunit Interfaces

(A) Ribbon diagram of Snf7 intrafilamental hydrophobic interface (PDB: 5FD9) with key residue side chains shown in sticks.

(B)  $\alpha$ 2/3 sequence alignment between Vps24 and Snf7, with residues subjected for mutagenesis in (C) highlighted.

(C) Quantitative MVB sorting data for *vps24 $\Delta$*  (green) yeast exogenously expressing empty vector, *VPS24*, *vps24<sup>L85E</sup>*, *vps24<sup>V88K</sup>*, *vps24<sup>I92E</sup>*, *vps24<sup>M105E</sup>*, *vps24<sup>M112E</sup>*, *vps24<sup>V115E</sup>* and *vps24<sup>V119E</sup>*, *snf7 $\Delta$*  (blue) yeast exogenously expressing empty vector, *SNF7*, *snf7<sup>M87E</sup>*, *snf7<sup>Q90K</sup>*, *snf7<sup>I94E</sup>*, *snf7<sup>M107E</sup>*, *snf7<sup>M114E</sup>*, *snf7<sup>I117E</sup>* and *snf7<sup>L121D</sup>* (Tang et al., 2015). Error bars represent standard deviations from 3-5 independent experiments.

(D) Ribbon diagram of Snf7 intrafilamental electrostatic interface (PDB: 5FD9) with key residue side chains shown in sticks.

(E)  $\alpha$ 1 and  $\alpha$ 2/3 sequence alignment between Vps24 and Snf7, with residues subjected for mutagenesis in (F) highlighted.

(F) Quantitative MVB sorting data for *vps24 $\Delta$*  (green) yeast exogenously expressing empty vector, *VPS24* and *vps24<sup>D93K T100K D107K</sup>*, *snf7 $\Delta$*  (blue) yeast exogenously expressing empty vector, *SNF7* and *snf7<sup>E95K E102K E109K</sup>* (Tang et al., 2015). Error bars represent standard deviations from 3-5 independent experiments.

(G)  $\alpha$ 2/3 sequence alignment between Vps20 and Snf7, with residues subjected for mutagenesis in (H) and (I) highlighted.

(H) Quantitative MVB sorting data for *vps20 $\Delta$*  (red) yeast exogenously expressing empty vector, *VPS20*, *vps20<sup>L86E</sup>*, *vps20<sup>M89K</sup>*, *vps20<sup>L93E</sup>*, *vps20<sup>I103E</sup>*, *vps20<sup>L106E</sup>*, *vps20<sup>L113E</sup>*, *vps24<sup>L116E</sup>* and *vps24<sup>F120E</sup>*, *snf7 $\Delta$*  (blue) yeast exogenously expressing empty vector, *SNF7*, *snf7<sup>M87E</sup>*, *snf7<sup>Q90K</sup>*, *snf7<sup>I94E</sup>*, *snf7<sup>M104E</sup>*, *snf7<sup>M107E</sup>*, *snf7<sup>M114E</sup>*, *snf7<sup>I117E</sup>* and *snf7<sup>L121D</sup>* (Tang et al., 2015). Error bars represent standard deviations from 3-5 independent experiments.

(I) Quantitative MVB sorting data for *vps20 $\Delta$*  (red) yeast exogenously expressing empty vector, *VPS20*, *vps20<sup>L86E L93E</sup>*, *vps20<sup>L93E I103E</sup>*, *vps20<sup>L86E I103E</sup>*, *vps20<sup>L106E L116E</sup>*, *vps20<sup>L113E</sup>* and *vps20<sup>L106E F120E</sup>*. Error bars represent standard deviations from 3-5 independent experiments.

(J)  $\alpha$ 1  $\alpha$ 2/3 sequence alignment between Vps20 and Snf7, with residues subjected for mutagenesis in (K) highlighted.

(K) Quantitative MVB sorting data for *vps20 $\Delta$*  (red) yeast exogenously expressing empty vector, *VPS20* and *vps20<sup>E94K Q101K N108K</sup>*, *snf7 $\Delta$*  (blue) yeast exogenously expressing empty vector, *SNF7* and *snf7<sup>E95K E102K E109K</sup>* (Tang et al., 2015). Error bars represent standard deviations from 3-5 independent experiments.

**Table A1.1 Plasmids and Yeast Strains Used in Appendix 1**

| <b>Plasmids for <i>Saccharomyces cerevisiae</i> Expression</b> |                         |                             |
|--|-------------------------|-----------------------------|
| <b>Plasmid</b>   | <b>Mutations</b>        | <b>Reference</b>            |
| pRS416   |                         | (Sikorski and Hieter, 1989) |
| pRS416-SNF7  | Wild-type               | (Henne et al., 2012)        |
| pRS416-sn $\text{f}^{\text{D127K}}$                            | D127K                   | this study                  |
| pRS416-sn $\text{f}^{\text{D131K}}$                            | D131K                   | this study                  |
| pRS416-sn $\text{f}^{\text{R134D}}$                            | R134D                   | this study                  |
| pRS416-sn $\text{f}^{\text{E138K}}$                            | E138K                   | this study                  |
| pRS416-sn $\text{f}^{\text{E142K}}$                            | E142K                   | this study                  |
| pRS416-sn $\text{f}^{\text{R149D}}$                            | R149D                   | this study                  |
| pRS416-sn $\text{f}^{\text{D122K}}$                            | D122K                   | this study                  |
| pRS416-sn $\text{f}^{\text{D124K}}$                            | D124K                   | this study                  |
| pRS416-sn $\text{f}^{\text{E128K}}$                            | E128K                   | this study                  |
| pRS416-sn $\text{f}^{\text{E132K}}$                            | E132K                   | this study                  |
| pRS416-sn $\text{f}^{\text{E135K}}$                            | E135K                   | this study                  |
| pRS416-sn $\text{f}^{\text{D141K}}$                            | D141K                   | this study                  |
| pRS416-sn $\text{f}^{\text{D145K}}$                            | D145K                   | this study                  |
| pRS416-SNF7-GFP  | GFP                     | this study                  |
| pRS416-sn $\text{f}^{\text{D127K}}\text{-GFP}$                 | D127K; GFP              | this study                  |
| pRS416-sn $\text{f}^{\text{D131K}}\text{-GFP}$                 | D131K; GFP              | this study                  |
| pRS416-sn $\text{f}^{\text{D127K D131K}}\text{-GFP}$           | D127K D131K; GFP        | this study                  |
| pRS416-sn $\text{f}^{\text{D127K D131K}}$                      | D127K D131K             | this study                  |
| pRS416-sn $\text{f}^{\text{D127K R134D}}$                      | D127K R134D             | this study                  |
| pRS416-sn $\text{f}^{\text{D131K R134D}}$                      | D131K R134D             | this study                  |
| pRS416-sn $\text{f}^{\text{D127K R149D}}$                      | D127K R149D             | this study                  |
| pRS416-sn $\text{f}^{\text{D131K R149D}}$                      | D131K R149D             | this study                  |
| pRS416-sn $\text{f}^{\text{E142K R134D}}$                      | E142K R134D             | this study                  |
| pRS416-sn $\text{f}^{\text{E142K R149D}}$                      | E142K R149D             | this study                  |
| pRS414   |                         | (Sikorski and Hieter, 1989) |
| pRS414-SNF7  | Wild-type               | (Tang et al., 2015)         |
| pRS414-sn $\text{f}^{\text{D127K}}$                            | D127K                   | this study                  |
| pRS414-sn $\text{f}^{\text{D131K}}$                            | D131K                   | this study                  |
| pRS414-sn $\text{f}^{\text{E142K}}$                            | E142K                   | this study                  |
| pRS414-sn $\text{f}^{\text{L121D}}$                            | L121D                   | this study                  |
| pRS416-sn $\text{f}^{\text{L121K}}$                            | L121K                   | this study                  |
| pRS416-sn $\text{f}^{\text{H118D}}$                            | H118D                   | this study                  |
| pRS416-sn $\text{f}^{\text{H118D R134D}}$                      | H118D R134D             | this study                  |
| pRS416-sn $\text{f}^{\text{H118D R149D}}$                      | H118D R149D             | this study                  |
| pRS416-sn $\text{f}^{\text{R134D R149D}}$                      | R134D R149D             | this study                  |
| pRS416-sn $\text{f}^{\text{H118D R134D R149D}}$                | H118D R134D R149D       | this study                  |
| pRS416-sn $\text{f}^{\text{D127K D131K R134D R149D}}$          | D127K D131K R134D R149D | this study                  |

|  |                                  |                           |
|--|----------------------------------|---------------------------|
| pRS416- <i>snf7</i> <sup>H118D D127K D131K R134D<br/>R149D</sup> | H118D D127K D131K R134D<br>R149D | this study                |
| pRS414- <i>snf7</i> <sup>D127K D131K</sup>                       | D127K D131K                      | this study                |
| pRS416- <i>snf7</i> <sup>core</sup>                              | 1-150, 3xFLAG                    | (Henne et al., 2012)      |
| pRS416- <i>snf7</i> <sup>helix0-3</sup>                          | 1-120, 3xFLAG                    | (Henne et al., 2012)      |
| pRS415-VPS20   | Wild-type                        | (Buchkovich et al., 2013) |
| pRS415-vps20 <sup>N117D</sup>                                    | N117D                            | this study                |
| pRS415-vps20 <sup>D124K</sup>                                    | D124K                            | (Sato et al., 1998)       |
| pRS415-vps20 <sup>D128K</sup>                                    | D128K                            | this study                |
| pRS415-vps20 <sup>Q131D</sup>                                    | Q131D                            | this study                |
| pRS415-vps20 <sup>E139K</sup>                                    | E139K                            | this study                |
| pRS415-vps20 <sup>R146D</sup>                                    | R146D                            | this study                |
| pRS414-VPS24   | Wild-type                        | (Buchkovich et al., 2013) |
| pRS414-vps24 <sup>N116R</sup>                                    | N116R                            | this study                |
| pRS414-vps24 <sup>R125D</sup>                                    | R125D                            | this study                |
| pRS414-vps24 <sup>I129D</sup>                                    | I129D                            | this study                |
| pRS414-vps24 <sup>E132R</sup>                                    | E132R                            | this study                |
| pRS414-vps24 <sup>I140D</sup>                                    | I140D                            | this study                |
| pRS414-vps24 <sup>D147R</sup>                                    | D147R                            | this study                |
| pRS415-VPS2  | Wild-type                        | (Buchkovich et al., 2013) |
| pRS415-vps2 <sup>N117R</sup>                                     | N117R                            | this study                |
| pRS415-vps2 <sup>Q126D</sup>                                     | Q126D                            | this study                |
| pRS415-vps2 <sup>M130D</sup>                                     | M130D                            | this study                |
| pRS415-vps2 <sup>E133R</sup>                                     | E133R                            | this study                |
| pRS415-vps2 <sup>Q141D</sup>                                     | Q141D                            | this study                |
| pRS415-vps2 <sup>E148R</sup>                                     | E148R                            | this study                |
| pRS305- <i>snf7</i> <sup>D131K</sup>                             | D131K                            | this study                |
| pRS305- <i>snf7</i> <sup>D127K D131K</sup>                       | D127K D131K                      | this study                |
| pRS414-vps24 <sup>E143G</sup>                                    | (b8) E143G                       | this study                |
| pRS414-vps24 <sup>E15G</sup>                                     | (f3) E15G                        | this study                |
| pRS414-vps24 <sup>R59W N103D</sup>                               | (g1) R59W N103D                  | this study                |
| pRS414-vps24 <sup>M128L N213Y</sup>                              | (g3) M128L N213Y                 | this study                |
| pRS414-vps24 <sup>Q17R</sup>                                     | (g9) Q17R                        | this study                |
| pRS414-vps24 <sup>E114A</sup>                                    | (h1) E114A                       | this study                |
| pRS414-vps24 <sup>R216H</sup>                                    | (h2) R216H                       | this study                |
| pRS414-vps24 <sup>Q16E V204D</sup>                               | (h7) Q16E V204D                  | this study                |
| pRS414-vps24 <sup>D2G K33R K133E A221V</sup>                     | (i3) D2G K33R K133E A221V        | this study                |
| pRS414-vps24 <sup>D57N Y64C I71V</sup>                           | (j7) D57N Y64C I71V              | this study                |
| pRS414-vps24 <sup>M112I E132D</sup>                              | (j8) M112I E132D                 | this study                |
| pRS414-vps24 <sup>D146V</sup>                                    | (j12) D146V                      | this study                |
| pRS414-vps24 <sup>I-18</sup>                                     | (k1) I-18                        | this study                |
| pRS414-vps24 <sup>E32G</sup>                                     | (k3) E32G                        | this study                |

|  |                       |            |
|--|-----------------------|------------|
| pRS414-vps24 <sup>P200Q</sup>            | (k5) P200Q            | this study |
| pRS414-vps24 <sup>M90K</sup>             | (k9) M90K             | this study |
| pRS414-vps24 <sup>E177G</sup>            | (k10) E177G           | this study |
| pRS414-vps24 <sup>1-45+frameshift</sup>  | (j9) 1-45+frameshift  | this study |
| pRS414-vps24 <sup>G139E</sup>            | (f5) G139E            | this study |
| pRS414-vps24 <sup>R120S</sup>            | (f10) R120S           | this study |
| pRS414-vps24 <sup>1-21</sup>             | (g10) 1-21            | this study |
| pRS414-vps24 <sup>Q16K</sup>             | (g12) Q16K            | this study |
| pRS414-vps24 <sup>D107V R220K</sup>      | (g14) D107V R220K     | this study |
| pRS414-vps24 <sup>V162A</sup>            | (i9) V162A            | this study |
| pRS414-vps24 <sup>K55E K178E L222M</sup> | (j6) K55E K178E L222M | this study |
| pRS414-vps24 <sup>Q173H</sup>            | (j10) Q173H           | this study |
| pRS414-vps24 <sup>L85E</sup>             | L85E                  | this study |
| pRS414-vps24 <sup>V88E</sup>             | V88E                  | this study |
| pRS414-vps24 <sup>I92E</sup>             | I92E                  | this study |
| pRS414-vps24 <sup>M105E</sup>            | M105E                 | this study |
| pRS414-vps24 <sup>M112E</sup>            | M112E                 | this study |
| pRS414-vps24 <sup>V115E</sup>            | V115E                 | this study |
| pRS414-vps24 <sup>V119E</sup>            | V119E                 | this study |
| pRS414-vps24 <sup>D93K T100K D107K</sup> | D93K T100K D107K      | this study |
| pRS415-vps20 <sup>L86E</sup>             | L86E                  | this study |
| pRS415-vps20 <sup>M89K</sup>             | M89K                  | this study |
| pRS415-vps20 <sup>L93E</sup>             | L93E                  | this study |
| pRS415-vps20 <sup>I103E</sup>            | I103E                 | this study |
| pRS415-vps20 <sup>L106E</sup>            | L106E                 | this study |
| pRS415-vps20 <sup>L113E</sup>            | L113E                 | this study |
| pRS415-vps20 <sup>L116E</sup>            | L116E                 | this study |
| pRS415-vps20 <sup>F120E</sup>            | F120E                 | this study |
| pRS415-vps20 <sup>L86E L93E</sup>        | L86E L93E             | this study |
| pRS415-vps20 <sup>L93E I103E</sup>       | L93E I103E            | this study |
| pRS415-vps20 <sup>L86E I103E</sup>       | L86E I103E            | this study |
| pRS415-vps20 <sup>L106E L116E</sup>      | L106E L116E           | this study |
| pRS415-vps20 <sup>L113E L116E</sup>      | L113E L116E           | this study |
| pRS415-vps20 <sup>L106E F120E</sup>      | L106E F120E           | this study |
| pRS415-vps20 <sup>E94K Q101K N108K</sup> | E94K Q101K N108K      | this study |

#### Plasmids for *Escherichia coli* Expression for Protein Purification

| Plasmid                                 | Mutations        | Reference            |
|---|------------------|----------------------|
| pET23d-snfr <sup>R52E</sup>             | R52E             | (Henne et al., 2012) |
| pET23d-snfr <sup>R52E D127K</sup>       | R52E D127K       | this study           |
| pET23d-snfr <sup>R52E D127K R149D</sup> | R52E D127K R149D | this study           |

|   |                  |            |
|---|------------------|------------|
| pET23d- <i>snf7</i> <sup>R52E D131K R149D</sup> | R52E D131K R149D | this study |
| pET23d- <i>snf7</i> <sup>R52E D127K R134D</sup> | R52E D127K R134D | this study |
| pET23d- <i>snf7</i> <sup>R52E D131K R134D</sup> | R52E D131K R134D | this study |
| pET23d- <i>snf7</i> <sup>R52E L121C</sup>       | R52E L121C       | this study |

### Yeast Strains Used in This Study

| Strain    | Genotype  | Reference                 |
|-----------|---|---------------------------|
| SEY6210   | <i>Mat a, leu2-3, 2-112, ura3-52, his3-Δ200, trp1-Δ901, lys2-801, suc2-Δ9</i>                   | (Robinson et al., 1988)   |
| SEY6210.1 | <i>Mat a, leu2-3, 2-112, ura3-52, his3-Δ200, trp1-Δ901, lys2-801, suc2-Δ9</i>                   | (Robinson et al., 1988)   |
| NBY44     | SEY6210.1; <i>snf7Δ::HIS3; MUP1-PHLOURIN::KAN</i>   | (Henne et al., 2012)      |
| MBY24     | SEY6210.1; <i>snf7Δ::HIS3</i>   | (Babst et al., 2002a)     |
| DTY11     | SEY6210.1; <i>SNF7-3xFLAG::HIS3</i>   | (Teis et al., 2008)       |
| STY50     | SEY6210.1; <i>pep4Δ::LEU2; SNF7-3xFLAG::HIS3</i>  | this study                |
| STY48     | SEY6210.1; <i>vps4Δ::TRP1; SNF7-3xFLAG::HIS3</i>  | this study                |
| DTY25     | SEY6210.1; <i>snf7Δ::HIS3; VPS24-GFP::HIS3</i>  | (Teis et al., 2008)       |
| NBY42     | SEY6210.1; <i>vps20Δ::HIS3; MUP1-PHLOURIN::KAN</i>  | (Buchkovich et al., 2013) |
| NBY47     | SEY6210.1; <i>vps24Δ::HIS3; MUP1-PHLOURIN::KAN</i>  | (Buchkovich et al., 2013) |
| NBY69     | SEY6210.1; <i>vps2Δ::HIS3; MUP1-PHLOURIN::KAN</i>   | (Buchkovich et al., 2013) |
| STY69     | SEY6210.1; <i>snf7Δ::HIS3; snf7<sup>D127K D131K</sup>::LEU2; MUP1-PHLOURIN::KAN</i>             | this study                |
| STY71     | SEY6210; <i>snf7Δ::HIS3; vps24Δ::HIS3; snf7<sup>D127K D131K</sup>::LEU2; MUP1-PHLOURIN::KAN</i> | this study                |
| STY70     | SEY6210; <i>snf7Δ::HIS3; vps24Δ::HIS3; snf7<sup>D131K</sup>::LEU2; MUP1-PHLOURIN::KAN</i>       | this study                |

## Reference

- Babst, M., Katzmann, D.J., Estepa-Sabal, E.J., Meerloo, T., and Emr, S.D. (2002). ESCRT-III: an endosome-associated heterooligomeric protein complex required for mvb sorting. *Dev Cell* 3, 271-282.
- Babst, M., Sato, T.K., Banta, L.M., and Emr, S.D. (1997). Endosomal transport function in yeast requires a novel AAA-type ATPase, Vps4p. *EMBO J* 16, 1820-1831.
- Buchkovich, N.J., Henne, W.M., Tang, S., and Emr, S.D. (2013). Essential N-terminal insertion motif anchors the ESCRT-III filament during MVB vesicle formation. *Dev Cell* 27, 201-214.
- Henne, W.M., Buchkovich, N.J., Zhao, Y., and Emr, S.D. (2012). The endosomal sorting complex ESCRT-II mediates the assembly and architecture of ESCRT-III helices. *Cell* 151, 356-371.
- Lin, C.H., MacGurn, J.A., Chu, T., Stefan, C.J., and Emr, S.D. (2008). Arrestin-related ubiquitin-ligase adaptors regulate endocytosis and protein turnover at the cell surface. *Cell* 135, 714-725.
- Robinson, J., Klionsky, D., Banta, L., and Emr, S. (1988). Protein sorting in *Saccharomyces cerevisiae*: isolation of mutants defective in the delivery and processing of multiple vacuolar hydrolases. *Mol Cell Biol* 8(11), 4936-4948.
- Saksena, S., Wahlman, J., Teis, D., Johnson, A.E., and Emr, S.D. (2009). Functional reconstitution of ESCRT-III assembly and disassembly. *Cell* 136, 97-109.
- Sato, T.K., Darsow, T., and Emr, S.D. (1998). Vam7p, a SNAP-25-like molecule, and Vam3p, a syntaxin homolog, function together in yeast vacuolar protein trafficking. *Mol Cell Biol* 18, 5308-5319.
- Sciskala, B., and Kolling, R. (2013). Interaction maps of the *Saccharomyces cerevisiae* ESCRT-III protein Snf7. *Eukaryot Cell* 12, 1538-1546.
- Sikorski, R.S., and Hieter, P. (1989). A system of shuttle vectors and yeast host strains designed for efficient manipulation of DNA in *Saccharomyces cerevisiae*. *Genetics* 22, 19-27.
- Tang, S., Henne, W.M., Borbat, P.P., Buchkovich, N.J., Freed, J.H., Mao, Y., Fromme, J.C., and Emr, S.D. (2015). Structural basis for activation, assembly and membrane binding of ESCRT-III Snf7 filaments. *Elife* 4.

Teis, D., Saksena, S., and Emr, S.D. (2008). Ordered assembly of the ESCRT-III complex on endosomes is required to sequester cargo during MVB formation. *Dev Cell* 15, 578-589.

## APPENDIX II

### Functional Design of ESCRT-III Tandem Fusion Proteins

#### Summary

The endosomal sorting complex required for transport-III (ESCRT-III) mediates topologically unique cellular membrane remodeling events. Here, I focus on the most abundant ESCRT-III subunit, Snf7, design ESCRT-III tandem fusion dimers and characterize that both units in the dimers are functionally important.

#### Design and Characterization of Snf7 Tandem Fusion Proteins

To characterize the internal organization of Snf7 homo-polymer, I designed a tandem fusion dimer of two Snf7. I utilized an EcoRI restriction enzyme site, GAATCC, to connect two SNF7 open reading frames. This EcoRI site encodes a two-amino acid residue linker, Glu-Phe. When expressed this construct in *snf7Δ*, it restored MVB sorting back to ~80% efficiencies, indicating that a tandem fusion dimer is functional (Figure A2.1A). To test whether both components are functional in the dimer, we introduced single point substitution that is known to cause MVB sorting defects and tested their functionality *in vivo*. D127K, which causes severe MVB sorting defect, significantly reduced the functionality of the Snf7 tandem fusion dimer in MVB sorting. Interestingly, R134D, which restores the loss of function of *snf7<sup>D127K</sup>* *in cis* and *in trans*, is unable to restore the loss of function of *snf7<sup>D127K</sup>* in the tandem fusion dimer (Figures A2.1A, D-E). Western blotting analyses indicated that most of the tandem fusion dimers are properly expressed as a dimer *in vivo*, with an exception of Snf7<sup>D127K</sup>-Snf7<sup>R134D</sup>,

which is substantially degraded into two fragments that migrating to ~50 kDa and ~30kDa on a SDS-PAGE (Figures A2.1B-C).

Since both units in the tandem fusion dimer is involved in ESCRT-III polymer assembly, I next tested whether both units are required to bind membranes. To do that, I mutated the key residues, Trp2, Phe6 and Trp8 required for membrane insertion in the N-terminal amphipathic ANCHR motif. Interestingly, although mutating the ANCHR motif in the first unit in the dimer reduced its functionality, mutating the second unit remained the MVB sorting efficiencies as a tandem fusion dimer (Figures A2.2F-H). These data suggested that only the first Snf7 unit anchors the tandem fusion dimer to the endosomal membranes.

### **Design and Characterization of Vps20-Vps20 and Vps20-Snf7 Tandem Fusion Proteins**

To characterize the Vps20-dependent Snf7 nucleation and polymerization, I designed a tandem fusion Vps20-Vps20, Vps20-Snf7 and Snf7-Vps20 dimer proteins. *VPS20-VPS20* fusion was able to completely complement *VPS20*. *VPS20-SNF7* fusion rescues the loss of *VPS20* to a decent ~70% sorting efficiency. However, *SNF7-VPS20* fusion failed to restore function. To test whether the Snf7 unit in the Vps20-Snf7 fusion is functional, I introduced well-characterized *snf7* C-terminal truncation or point mutations, and found that they failed to restore the functionality (Figure A2.2A). As expected, none of the Vps20-Snf7 fusion constructs are functional in *snf7Δ* (Figures A2.2B-D), indicating that these fusion dimers function as a Snf7 nucleator, upstream of the Snf7 homo-polymerization.

To further understand the ESCRT-II and Vps20-mediated ESCRT-III assembly, I designed fusion construct of Vps25 and Snf7 and tested it in *vps20Δ*, *snf7Δ* and *vps25Δ*. Remarkably, the *VPS25-SNF7* fusion construct is unable to bypass the loss of *VPS20* or *SNF7* (Figures A2.2A-B), indicating a unique architecture of ESCRT-II-Vps20-Snf7 hetero-polymer. *VPS25-SNF7* restores the loss of *VPS25* to 65%. Well-characterized *vps25* mutations, V148E and T150K, that impair the interaction with Vps20 (Im et al., 2009), showed severe loss of function in the *VPS25-SNF7* fusion dimer construct (Figure A2.2E). The ESCRT-II Vps36 binding defective Vps25 mutants, R83D (“armless” ESCRT-II) (Hierro et al., 2004; Teis et al., 2010) also resulted in a dramatic reduced function in the fusion construct. Moreover, I showed previously that Q90L mutations on Snf7 would able to trigger autoactivation in the Snf7 core domain for assembly (Tang et al., 2016). However, the addition of Q90L to Snf7 does not significantly improve the fusion’s function in sorting MVB cargo (Figure A2.2E). Altogether, these data indicate that Vps25-Snf7 fusion dimer is functional in a pathway that involves the classic ESCRT-II and Vps20 components.

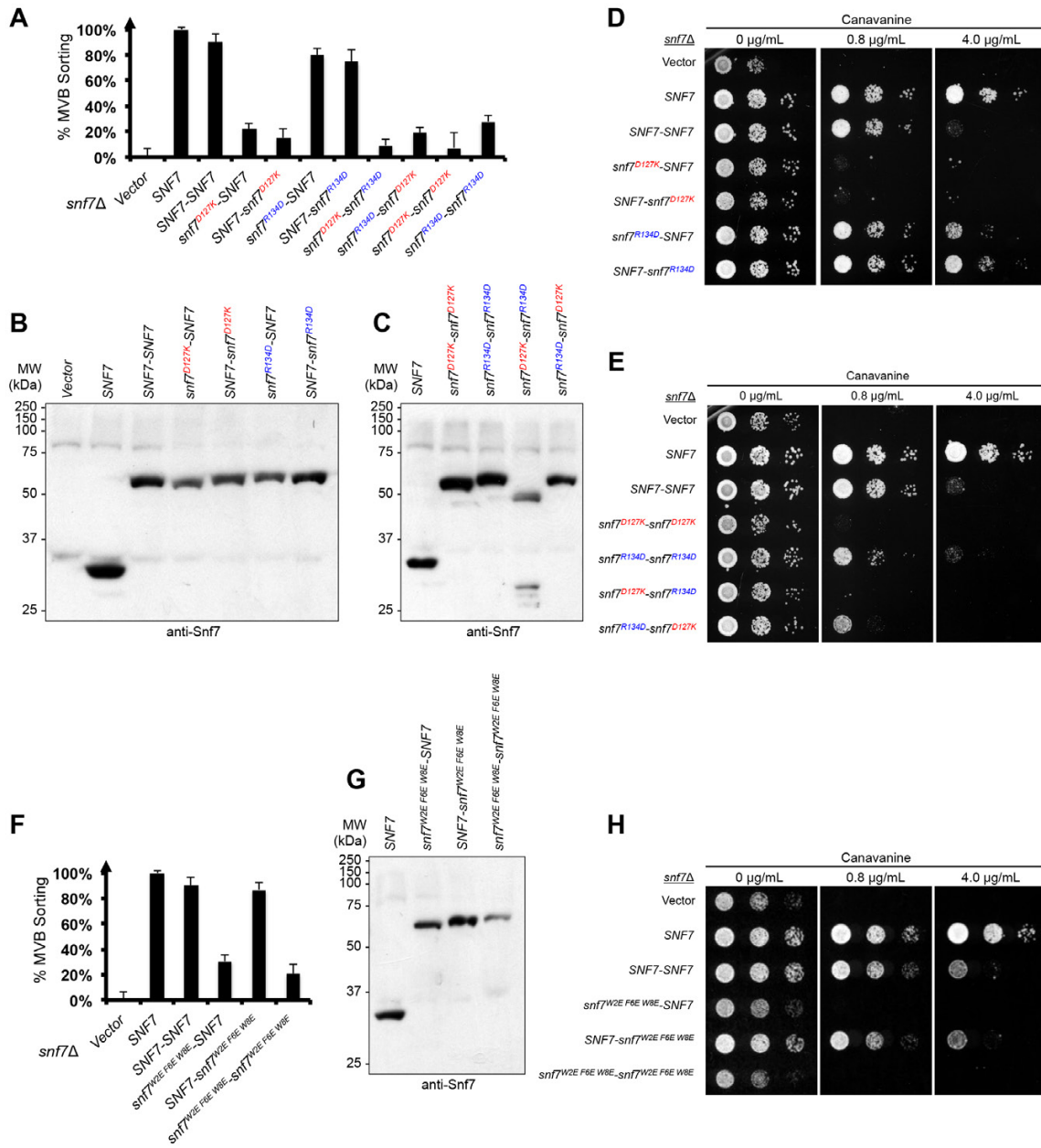


**Figure A2.1 Snf7 Tandem Fusion Dimer is Functional *in vivo***

### Figure A2.1 Snf7 Tandem Fusion Dimer is Functional *in vivo*

(A) Quantitative MVB sorting data for *snf7Δ* yeast exogenously expressing empty vector, *SNF7*, *SNF7-SNF7*, *snf7<sup>D127K</sup>-SNF7*, *SNF7-snf7<sup>D127K</sup>*, *snf7<sup>R134D</sup>-SNF7*, *SNF7-snf7<sup>R134D</sup>*, *snf7<sup>D127K</sup>-snf7<sup>R134D</sup>*, *snf7<sup>R134D</sup>-snf7<sup>D127K</sup>*, *snf7<sup>D127K</sup>-snf7<sup>D127K</sup>* and *snf7<sup>R134D</sup>-snf7<sup>R134D</sup>*. Error bars represent standard deviations from 3-5 independent experiments.

(B) Western blotting analyses of *snf7Δ* yeast expressing empty vector, *SNF7*, *SNF7-SNF7*, *snf7<sup>D127K</sup>-SNF7*, *SNF7-snf7<sup>D127K</sup>*, *snf7<sup>R134D</sup>-SNF7* and *SNF7-snf7<sup>R134D</sup>*. Anti-Snf7.

(C) Western blotting analyses of *snf7Δ* yeast expressing *SNF7*, *snf7<sup>D127K</sup>-snf7<sup>D127K</sup>*, *snf7<sup>R134D</sup>-snf7<sup>R134D</sup>*, *snf7<sup>D127K</sup>-snf7<sup>R134D</sup>* and *snf7<sup>R134D</sup>-snf7<sup>D127K</sup>*. Anti-Snf7.

(D) Canavanine sensitivity assay for *snf7Δ* yeast exogenously expressing empty vector, *SNF7*, *SNF7-SNF7*, *snf7<sup>D127K</sup>-SNF7*, *SNF7-snf7<sup>D127K</sup>*, *snf7<sup>R134D</sup>-SNF7* and *SNF7-snf7<sup>R134D</sup>* grown under no, 0.8 µg/mL, or 4.0 µg/mL Canavanine.

(E) Canavanine sensitivity assay for *snf7Δ* yeast exogenously expressing empty vector, *SNF7*, *SNF7-SNF7*, *snf7<sup>D127K</sup>-snf7<sup>D127K</sup>*, *snf7<sup>R134D</sup>-snf7<sup>R134D</sup>*, *snf7<sup>D127K</sup>-snf7<sup>R134D</sup>* and *snf7<sup>R134D</sup>-snf7<sup>D127K</sup>* grown under no, 0.8 µg/mL, or 4.0 µg/mL Canavanine.

(F) Quantitative MVB sorting data for *snf7Δ* yeast exogenously expressing empty vector, *SNF7*, *SNF7-SNF7*, *snf7<sup>W2E F6E W8E</sup>-SNF7*, *SNF7-snf7<sup>W2E F6E W8E</sup>* and *snf7<sup>W2E F6E W8E</sup>-snf7<sup>W2E F6E W8E</sup>*. Error bars represent standard deviations from 3-5 independent experiments.

(G) Western blotting analyses of *snf7Δ* yeast *SNF7*, *snf7<sup>W2E F6E W8E</sup>-SNF7*, *SNF7-snf7<sup>W2E F6E W8E</sup>* and *snf7<sup>W2E F6E W8E</sup>-snf7<sup>W2E F6E W8E</sup>*. Anti-Snf7.

(H) Canavanine sensitivity assay for *snf7Δ* yeast exogenously expressing empty vector, *SNF7*, *SNF7-SNF7*, *snf7<sup>W2E F6E W8E</sup>-SNF7*, *SNF7-snf7<sup>W2E F6E W8E</sup>* and *snf7<sup>W2E F6E W8E</sup>-snf7<sup>W2E F6E W8E</sup>* grown under no, 0.8 µg/mL, or 4.0 µg/mL Canavanine.

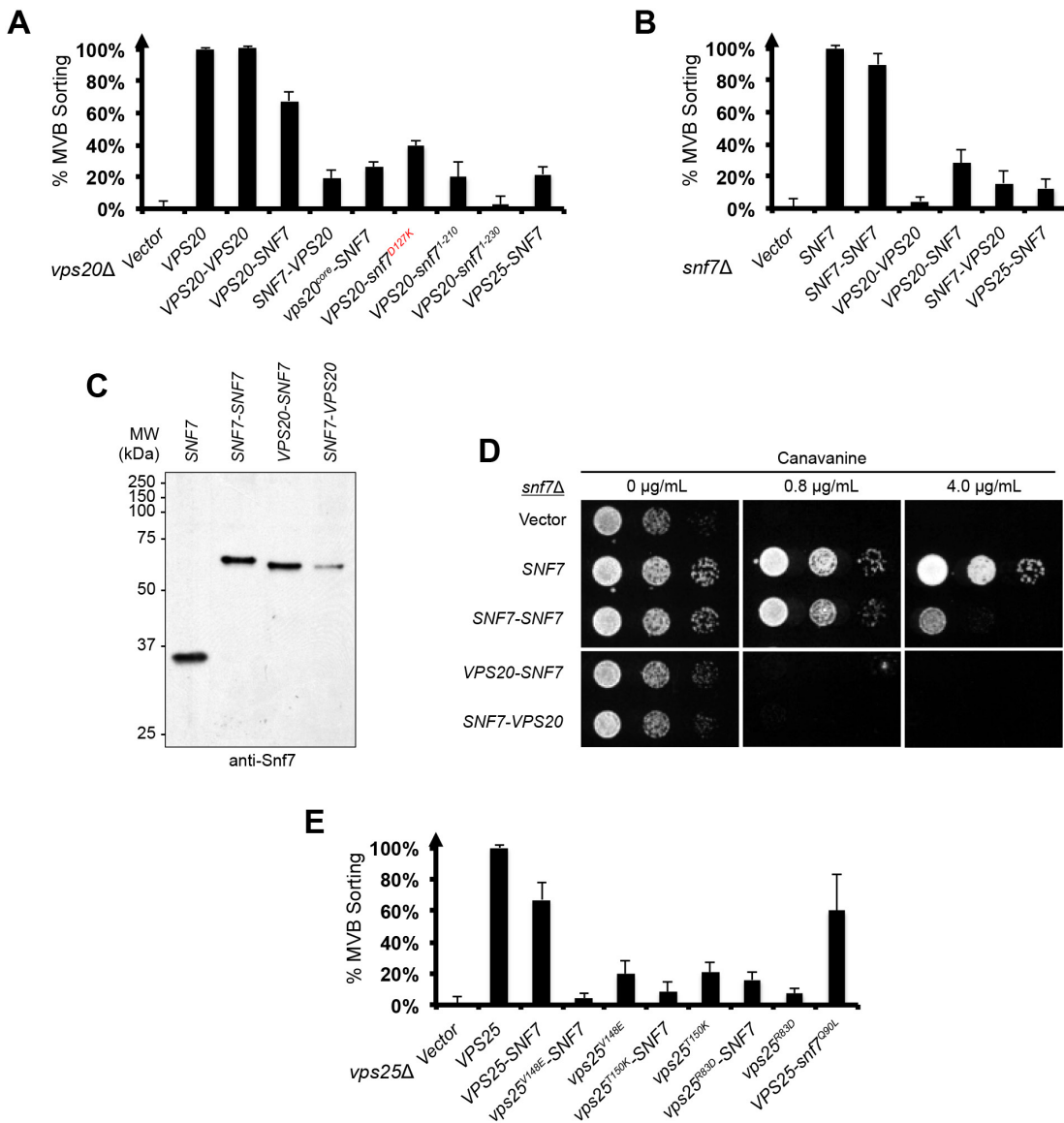


**Figure A2.2 Vps20 Tandem Fusion Dimer and Vps20-Snf7 Fusion is Functional *in vivo***

**Figure A2.2 Vps20 Tandem Fusion Dimer and Vps20-Snf7 Fusion is Functional *in vivo***

- (A) Quantitative MVB sorting data for *vps20Δ* yeast exogenously expressing empty vector, *VPS20*, *VPS20-VPS20*, *VPS20-SNF7*, *SNF7-VPS20*, *vps20<sup>core</sup>-SNF7*, *VPS20-snf7<sup>D127K</sup>*, *VPS20-snf7<sup>1-230</sup>*, *VPS20-snf7<sup>1-210</sup>* and *VPS25-SNF7*. Error bars represent standard deviations from 3-5 independent experiments.
- (B) Quantitative MVB sorting data for *snf7Δ* yeast exogenously expressing empty vector, *SNF7*, *SNF7-SNF7*, *VPS20-VPS20*, *VPS20-SNF7*, *SNF7-VPS20* and *VPS25-SNF7*. Error bars represent standard deviations from 3-5 independent experiments.
- (C) Western blotting analyses of *snf7Δ* yeast *SNF7*, *SNF7-SNF7*, *VPS20-SNF7* and *SNF7-VPS20*. Anti-Snf7.
- (D) Canavanine sensitivity assay for *snf7Δ* yeast exogenously expressing empty vector, *SNF7*, *SNF7-SNF7*, *VPS20-SNF7* and *SNF7-VPS20* grown under no, 0.8 µg/mL, or 4.0 µg/mL Canavanine.
- (E) Quantitative MVB sorting data for *vps25Δ* yeast exogenously expressing empty vector, *VPS25*, *VPS25-SNF7*, *vps25<sup>V148E</sup>-SNF7*, *vps25<sup>V148E</sup>*, *vps25<sup>T150K</sup>-SNF7*, *vps25<sup>T150K</sup>*, *vps25<sup>R83D</sup>-SNF7*, *vps25<sup>R83D</sup>* and *VPS25-snf7<sup>Q90L</sup>*. Error bars represent standard deviations from 3-5 independent experiments.

**Table A2 1 Plasmids and Yeast Strains Used in Appendix 2**

| <b>Plasmids for <i>Saccharomyces cerevisiae</i> Expression</b> |                                      |                             |
|--|--------------------------------------|-----------------------------|
| <b>Plasmid</b>   | <b>Mutations</b>                     | <b>Reference</b>            |
| pRS416   |                                      | (Sikorski and Hieter, 1989) |
| pRS416-SNF7  | Wild-type                            | (Henne et al., 2012)        |
| pRS416-SNF7-SNF7   | Linker: EF (EcoRI site)              | this study                  |
| pRS416-sn <sup>D127K</sup> 7-SNF7                              | D127K, Linker: EF                    | this study                  |
| pRS416-SNF7-sn <sup>D127K</sup> 7                              | Linker: EF, D127K                    | this study                  |
| pRS416-sn <sup>R134D</sup> 7-SNF7                              | R134D, Linker: EF,                   | this study                  |
| pRS416-SNF7-sn <sup>R134D</sup> 7                              | Linker: EF, R134D                    | this study                  |
| pRS416-sn <sup>D127K</sup> 7-sn <sup>R134D</sup> 7             | D127K, Linker: EF, R134D             | this study                  |
| pRS416-sn <sup>R134D</sup> 7-sn <sup>D127K</sup> 7             | R134D, Linker: EF, D127K             | this study                  |
| pRS416-sn <sup>D127K</sup> 7-sn <sup>D127K</sup> 7             | D127K, Linker: EF, D127K             | this study                  |
| pRS416-sn <sup>R134D</sup> 7-sn <sup>D127K</sup> 7             | R134D, Linker: EF, R134D             | this study                  |
| pRS416-sn <sup>D2E F6E W8E</sup> 7-SNF7                        | W2E F6E W8E, Linker: EF              | this study                  |
| pRS416-SNF7-sn <sup>D2E F6E W8E</sup> 7                        | Linker: EF, W2E F6E W8E,             | this study                  |
| pRS416-sn <sup>D2E F6E W8E</sup> 7-sn <sup>D2E F6E W8E</sup> 7 | W2E F6E W8E, Linker: EF, W2E F6E W8E | this study                  |
| pRS416-VPS20   | Wild-type                            | (Tang et al., 2016)         |
| pRS416-VPS20-VPS20   | Linker: EF                           | this study                  |
| pRS416-VPS20-SNF7  | Linker: EF,                          | this study                  |
| pRS416-vps20 <sup>core</sup> -SNF7                             | Vps20 1-147, Linker: EF              | this study                  |
| pRS416-VPS20-sn <sup>D127K</sup> 7                             | Linker: EF, Snf7 D127K               | this study                  |
| pRS416-VPS20-sn <sup>1-210</sup> 7                             | Linker: EF, Snf7 1-210               | this study                  |
| pRS416-VPS20-sn <sup>1-230</sup> 7                             | Linker: EF, Snf7 1-230               | this study                  |
| pRS415   |                                      | (Sikorski and Hieter, 1989) |
| pRS415-VPS25   | Wild-type                            | (Tang et al., 2016)         |
| pRS416-VPS25-FLAG  | 3xFLAG                               | (Hierro et al., 2004)       |
| pRS416-VPS25-SNF7  | Linker: GT (KpnI site)               | this study                  |
| pRS416-vps25 <sup>V148E</sup> -SNF7                            | Vps25 V148E, Linker: GT              | this study                  |
| pRS415-vps25 <sup>V148E</sup>                                  | V148E                                | this study                  |
| pRS416-vps25 <sup>T150K</sup> -SNF7                            | Vps25 T150K, Linker: GT              | this study                  |
| pRS415-vps25 <sup>T150K</sup>                                  | T150K                                | this study                  |
| pRS416-vps25 <sup>R83D</sup> -SNF7                             | Vps25 R83D, Linker: GT               | (Sikorski and Hieter, 1989) |
| pRS416-vps25 <sup>R83D</sup> -FLAG                             | Vps25R83D, 3xFLAG                    | (Tang et al., 2015)         |
| pRS416-VPS25-sn <sup>Q90L</sup> 7                              | Linker: GT, Snf7 Q90L                | this study                  |

**Yeast Strains Used in This Study**

| <b>Strain</b> | <b>Genotype</b>   | <b>Reference</b>        |
|---------------|---|-------------------------|
| SEY6210       | <i>Mat a, leu2-3, 2-112, ura3-52, his3-Δ200, trp1-Δ901, lys2-801, suc2-Δ9</i> | (Robinson et al., 1988) |
| SEY6210.1     | <i>Mat a, leu2-3, 2-112, ura3-52, his3-Δ200, trp1-Δ901, lys2-801, suc2-Δ9</i> | (Robinson et al., 1988) |

|       |  |                           |
|-------|--|---------------------------|
| NBY44 | SEY6210.1; <i>snf7Δ::HIS3; MUP1-PHLOURIN::KAN</i>  | (Henne et al., 2012)      |
| MBY24 | SEY6210.1; <i>snf7Δ::HIS3</i>                      | (Babst et al., 2002a)     |
| NBY42 | SEY6210.1; <i>vps20Δ::HIS3; MUP1-PHLOURIN::KAN</i> | (Buchkovich et al., 2013) |
| STY51 | SEY6210; <i>vps25Δ::HIS3; MUP1-PHLOURIN::KAN</i>   | (Tang et al., 2015)       |

## Reference

- Babst, M., Katzmann, D.J., Estepa-Sabal, E.J., Meerloo, T., and Emr, S.D. (2002). ESCRT-III: an endosome-associated heterooligomeric protein complex required for mvb sorting. *Dev Cell* 3, 271-282.
- Buchkovich, N.J., Henne, W.M., Tang, S., and Emr, S.D. (2013). Essential N-terminal insertion motif anchors the ESCRT-III filament during MVB vesicle formation. *Dev Cell* 27, 201-214.
- Henne, W.M., Buchkovich, N.J., Zhao, Y., and Emr, S.D. (2012). The endosomal sorting complex ESCRT-II mediates the assembly and architecture of ESCRT-III helices. *Cell* 151, 356-371.
- Hierro, A., Sun, J., Rusnak, A.S., Kim, J., Prag, G., Emr, S.D., and Hurley, J.H. (2004). Structure of the ESCRT-II endosomal trafficking complex. *Nature* 431, 221-225.
- Im, Y.J., Wollert, T., Boura, E., and Hurley, J.H. (2009). Structure and function of the ESCRT-II-III interface in multivesicular body biogenesis. *Dev Cell* 17, 234-243.
- Robinson, J., Klionsky, D., Banta, L., and Emr, S. (1988). Protein sorting in *Saccharomyces cerevisiae*: isolation of mutants defective in the delivery and processing of multiple vacuolar hydrolases. *Mol Cell Biol* 8(11), 4936-4948.
- Sikorski, R.S., and Hieter, P. (1989). A system of shuttle vectors and yeast host strains designed for efficient manipulation of DNA in *Saccharomyces cerevisiae*. *Genetics* 22, 19-27.
- Tang, S., Buchkovich, N.J., Henne, W.M., Banjade, S., Kim, Y.J., and Emr, S.D. (2016). ESCRT-III activation by parallel action of ESCRT-I/II and ESCRT-0/Bro1 during MVB biogenesis. *Elife* 5.
- Tang, S., Henne, W.M., Borbat, P.P., Buchkovich, N.J., Freed, J.H., Mao, Y., Fromme, J.C., and Emr, S.D. (2015). Structural basis for activation, assembly and membrane binding of ESCRT-III Snf7 filaments. *Elife* 4.
- Teis, D., Saksena, S., Judson, B.L., and Emr, S.D. (2010). ESCRT-II coordinates the assembly of ESCRT-III filaments for cargo sorting and multivesicular body vesicle formation. *EMBO J* 29, 871-883.

## APPENDIX III

### Functional Dissection of Novel ESCRT-III Snf7 Interactor, Chm7

#### Summary

The Endosomal Sorting Complexes Required for Transport (ESCRT) constitute hetero-oligomeric membrane remodeling machines. The ESCRT-III machinery plays a critical role in numerous fundamental cellular processes, including MVB biogenesis, viral budding, cytokinesis, nuclear envelope reformation, and etc, indicating an ancient and conserved membrane remodeling mechanism. Snf7 is the predominant ESCRT-III component. Using a proteomic approach, Snf7 interacting proteins were identified. The yeast open reading frame (ORF), *YJL049W*, which encodes the human CHMP7 ortholog, a protein of unknown function (in 2012), was found as a novel Snf7 interactor. Here, I aimed to characterize the role of *YJL049W* or Chm7 in the multivesicular body pathway.

#### **Snf7 SILAC Identified a Novel Interacting Protein, Chm7**

In the wild-type condition, ~60% Snf7 localizes to the cytoplasm, but under *vps4Δ*, ~90% Snf7 are recruited to the endosomal membranes (Babst et al., 2002a). To identify Snf7 interactors and characterize the differences between soluble monomeric inactive conformation and membrane-bound polymeric active conformation, Nicholas J. Buchkovich and Jason A. MacGurn performed Snf7 stable isotope labeling with amino acids in cell culture (SILAC) coupled with liquid chromatography-tandem mass spectrometry (LC-MS/MS) using an Orbitrap XL mass spectrometer in the laboratory of

Marcus Smolka. SILAC experiments using wild-type Snf7-FLAG yeast and *vps4Δ* Snf7-FLAG yeast were performed (Figure A3.1A). Among the Snf7 interactors, we identified ESCRT-II (Vps36, Vps25 and Vps22), ESCRT-III (Vps20, Snf7 Vps24, Vps2, Did2 and Vps60) and Bro1 family proteins (Bro1 and Rim20). We also identified endosomal and vacuolar cargo (Bap2, Cps1, Ycf1, Sit1, Vma10, Vph1, Vps10 and Vth1). Interestingly, we also identified two proteins of unknown function (in 2012), yeast open reading frames, YJL049W and YDL089W (Figure A3.2A, Tables A3.1-3.3).

YJL049W (Chm7) encodes a protein of human CHMP7 ortholog in yeast. Sequence analysis on Chm7 indicates that Chm7 has two domains, both of which have high degree of homology to ESCRT-III subunits (Horii et al., 2006) (Figure A3.1C). I next performed sequence alignment analysis between the N-terminal or the C-terminal domain domains of Chm7 with all core ESCRT-III subunits. The N-terminal domain of Chm7 (37.1% to Vps20, 35.7% to Snf7, 32.2% to Vps24, 34.8% to Vps2) is less conserved than the C-terminal domain (46.2% to Vps20, 46.5% to Snf7, 45.9% to Vps24 and 46.9% to Vps2) (Figure A3.1D).

### **Chm7 Localizes to Cytoplasm and Intracellular Puncta**

Chm7 is ubiquitously expressed in all eukaryotes like all ESCRT-III subunits. However, the function of Chm7 was poorly understood. To characterize the function of Chm7, I examined the intracellular localization of Chm7. Chm7-GFP localizes to the cytoplasm, and its localization remains in the cytoplasm in upstream ESCRT mutant, ESCRT-0 (*vps27Δ*), ESCRT-I (*vps23Δ*) and ESCRT-II (*vps36Δ*) (Figure A3.2A). I next tested the localization in ESCRT-III and Vps4 mutants, although Chm7-GFP localizes to

the cytoplasm in *vps20Δ*, Chm7-GFP localizes to intracellular puncta structures in downstream ESCRT-III mutants, *snf7Δ*, *vps24Δ*, *vps2Δ* and *vps4Δ* (Figure A3.2B).

To characterize whether these intracellular puncta structures are aberrant endosomal class E compartment, I co-localized these structures with the lipophilic probe, FM4-64. However, CHM7-GFP puncta do not co-localize with early endosomes or aberrant endosomal class E compartments (Figure A3.2C). It remains unknown the identity of these puncta structures.

### **Chm7 Does Not Play a Role in Endosomal Cargo Sorting**

We next tested whether Chm7 has role in endosomal sorting. Many ESCRT-III subunits are functionally defective when C-terminally tagged with GFP. We first tested the heat sensitivity. Although ESCRT-III *snf7Δ* showed modest heat sensitivity under 38°C, *chm7Δ* and *CHM7-GFP* did not show heat sensitivity (Figure A3.3A). We next tested the canavanine sensitivity. Although ESCRT-III *snf7Δ* is canavanine sensitive, *chm7Δ* and *CHM7-GFP* did not show canavanine sensitivity (Figure A3.3B).

Next, we assayed the role of Chm7 in sorting well-characterized ESCRT-dependent cargo. Mup1-GFP, Can1-GFP, Lyp1-GFP and GFP-Cps1 are properly sorted to the vacuolar lumen in *chm7Δ* (Figure A3.3C). Since ESCRT-III accessory proteins Ist1, Did2 and Vta1, whose deletions also have mild MVB sorting phenotypes (Rue et al., 2008), I asked if multiple deletions with *chm7Δ* would result in a stronger MVB sorting defects. However, *vta1Δchm7Δ*, *ist1Δchm7Δ*, *did2Δchm7Δ* and *ist1Δdid2Δchm7Δ* do not exhibit a stronger GFP-CPS1 sorting defect compared to *vta1Δ*, *ist1Δ*, *did2Δ*, and *ist1Δdid2Δ* (Figure A3.3D).

Recently, I determined the parallel ESCRT-III Snf7 activation pathway that involved both ESCRT-II/Vps20 and Bro1. To test whether Chm7 plays a role in the Bro1-dependent Snf7 activation pathway, I tested the functionalities of *snf7* suppressor (*myr-snf7<sup>R52E Q90L N100I</sup>*) in *vps20Δchm7Δ*, *vps25Δchm7Δ* and *vps23Δchm7Δ*. However, the deletion of *CHM7* does not affect the functionalities of *snf7* suppressor (Figure A3.3E), indicating that Chm7 has no direct role in the Bro1-dependent Snf7 activation pathway.

To characterize whether Chm7 can activate Snf7, I overexpressed Chm7 in *vps20Δ* (Figure A3F). I observed that overexpressed Chm7-GFP localizes to both the cytoplasm and intracellular puncta in wild-type cells (Figure A3.3G). However, overexpressed Chm7 does not significantly restore the loss of Vps20, which made its role in the endosomal sorting pathway remained unclear.

## A Functional Role of Chm7 as a Nuclear ESCRT?

Recently, CHMP7 was identified as a nucleator of CHMP4B polymerization during nuclear envelope reformation (Vietri et al., 2015). Also, a report also showed that Chm7 is not involved in endosomal sorting but rather seems to play a role at the ER membrane, presumably as part of a novel ESCRT-III complex (Bauer et al., 2015). It was reported that *chm7Δ* shows a synthetic growth defect with *apq12Δ*, indicating a role of Chm7 in nuclear pore complex (NPC) assembly (Bauer et al., 2015; Webster et al., 2014). *Saccharomyces cerevisiae* has a closed mitosis, which is considered to be the most ancient form of mitosis. Remarkably, Chm7 is an ancient protein already present in the “last common eukaryotic ancestor,” which did not have a nucleus (Leung et al.,

2008). Therefore, Chm7 may have a fundamental function that remains to be elucidated.

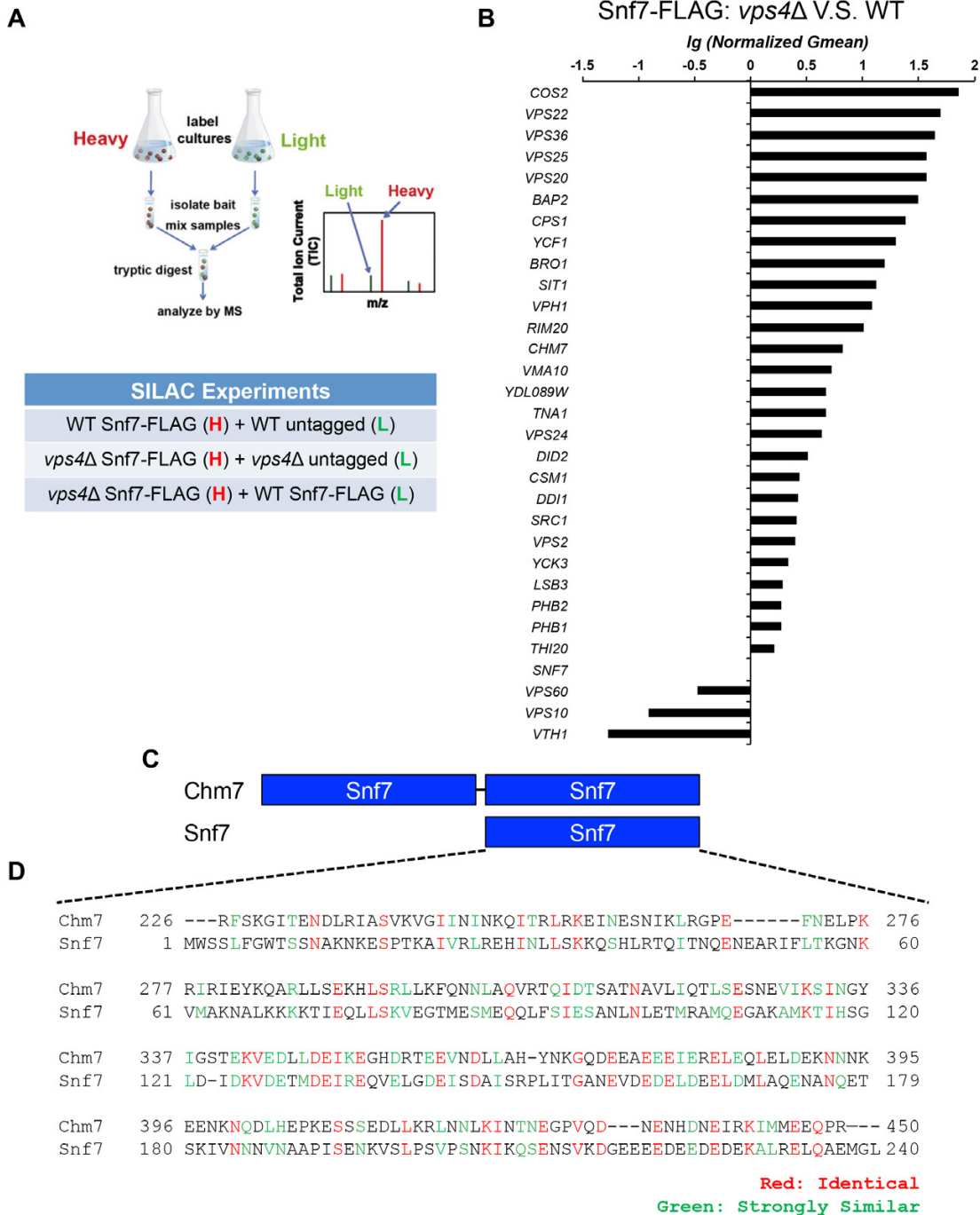


**Figure A3.1 ESCRT-III like Protein Chm7 as a Novel Snf7 Interactor**

### **Figure A3.1 ESCRT-III like Protein Chm7 as a Novel Snf7 Interactor**

- (A) Schematic of stable isotope labeling by amino acids in cell culture (SILAC)-quantitative mass spectrometry analysis to determine Snf7 interactome in wild-type (WT) and *vps4Δ* cells. Diagram adopted from (MacGurn et al., 2011)
- (B) Snf7 interactome comparison between WT and *vps4Δ* cells. Genes are listed as decreasing  $Ig(G_{mean})$  ( $G_{mean}>1$  means enriched in *vps4Δ* cells;  $G_{mean}=1$  means no difference between WT and *vps4Δ* cells;  $G_{mean}<1$  means enriched in WT cells). YJL049W, previously a protein of unknown function, is listed as Chm7 (Bauer et al., 2015).
- (C) Domain organization diagram of Chm7 and Snf7 (Horii et al., 2006).
- (D) Sequence alignment analysis using the *NPS@CLUSTALW* server between the C-terminal Snf7 domain of Chm7 and Snf7. Strongly similar residues are labeled in green and identical residue in red.

\* SILAC experiments were performed by Nicholas J. Buchkovich and Jason A. MacGurn in Marcus B. Smolka's laboratory at Cornell University.

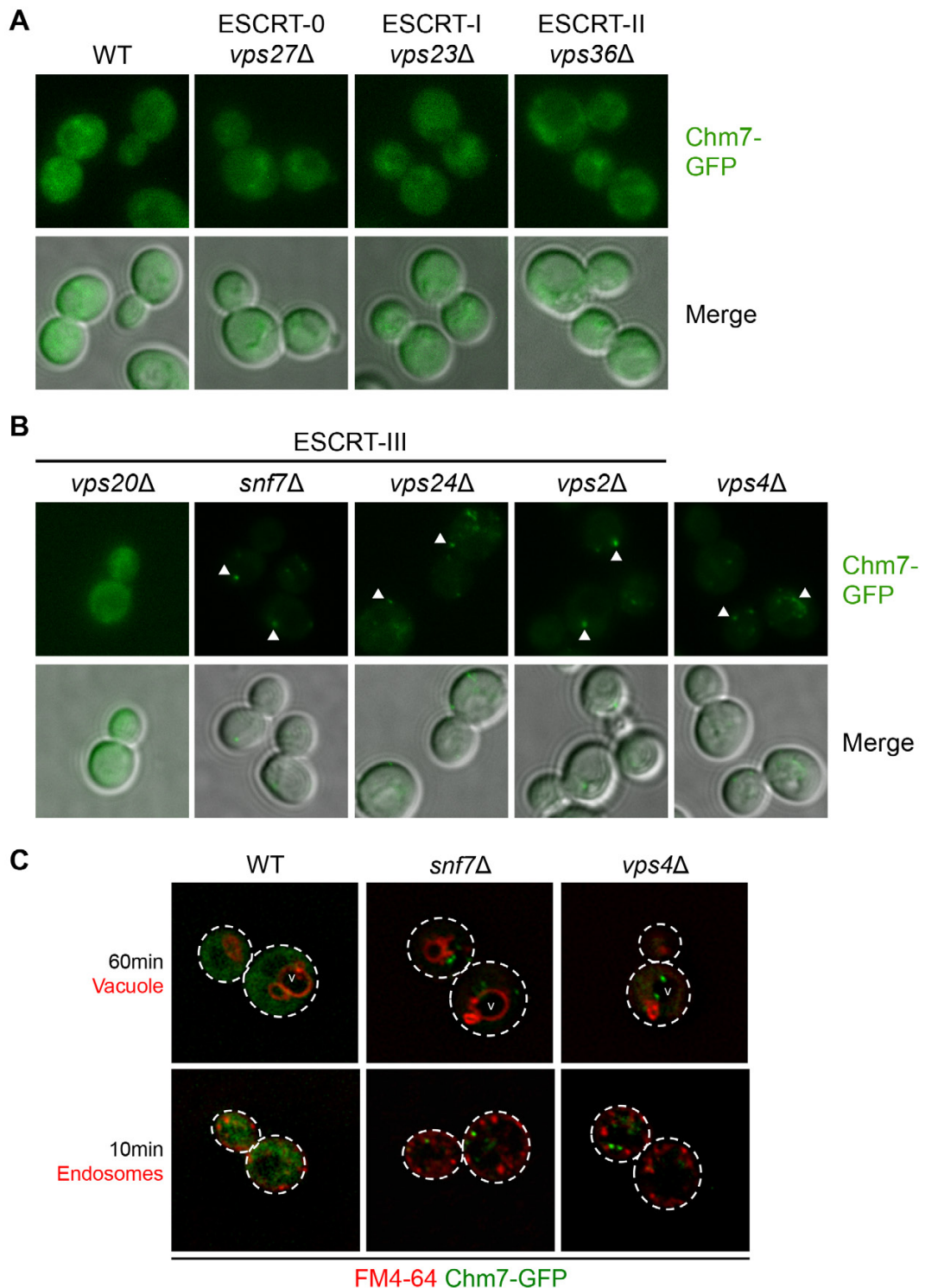


**Figure A3.2 Chm7 Localizes to Cytoplasm or Intracellular Punctate Structures**

**Figure A3.2 Chm7 Localizes to Cytoplasm or Intracellular Punctate Structures**

- (A) Representative images of mid-log wild-type, *vps27Δ* (ESCRT-0 subunit), *vps23Δ* (ESCRT-I subunit) and *vps36Δ* (ESCRT-II subunit) yeast, exogenously expressing Chm7-GFP. GFP images (upper row); composite images of GFP and DIC (bottom row).
- (B) Representative images of mid-log *vps20Δ*, *snf7Δ*, *vps24Δ* and *vps2Δ* yeast, expressing Chm7-GFP. GFP images (upper row); composite images of GFP and DIC (bottom row). White arrows denote intracellular punctate structures.
- (C) Representative colocalization images of mid-log wild-type, *snf7Δ* and *vps4Δ* yeast, expressing Chm7-GFP and labeled with FM4-64 (Vida and Emr, 1995) for 60 min (upper row) and 10 min (bottom row). Vacuole (v).

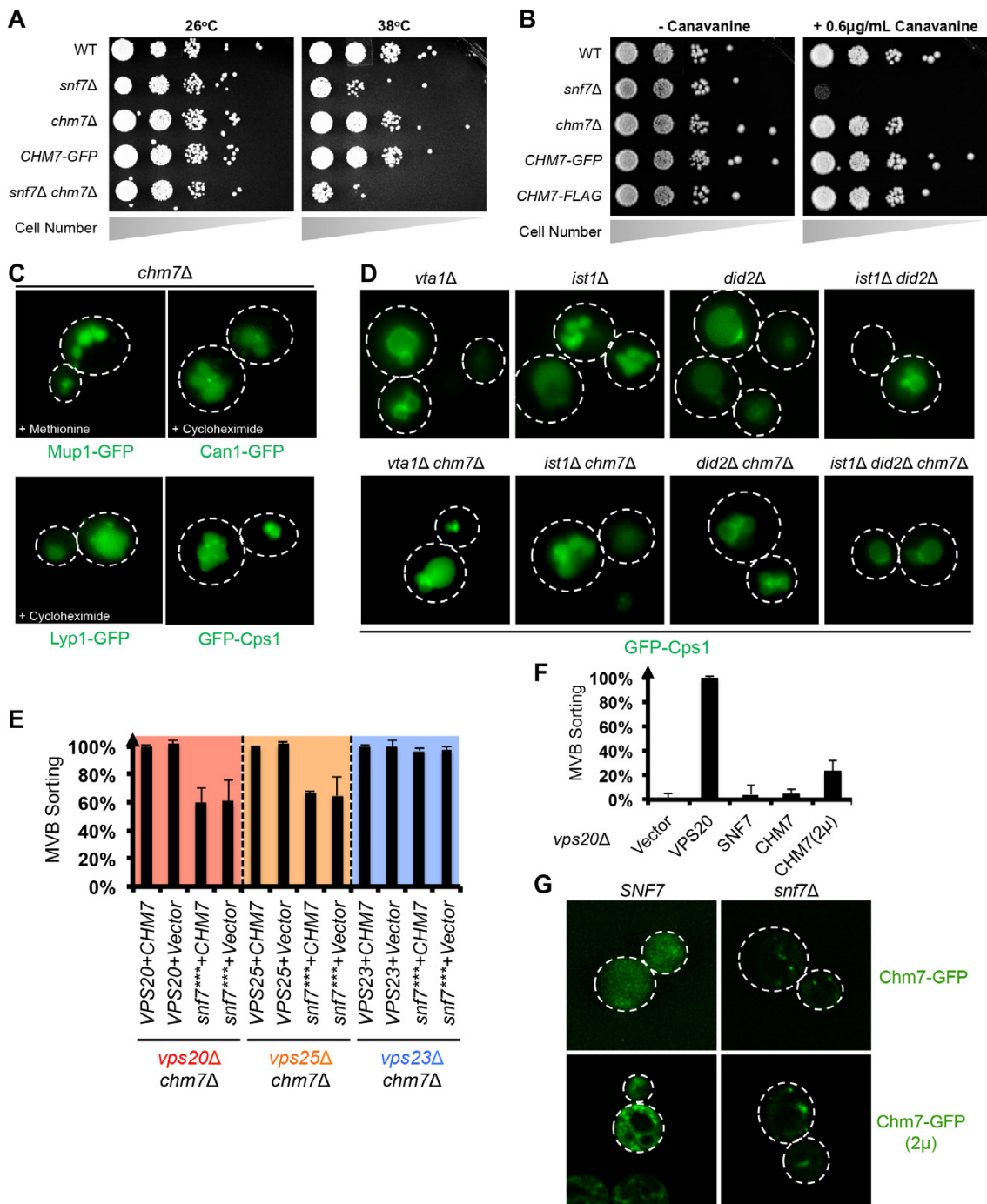


**Figure A3.3 *chm7Δ* Does Not Affect Endosomal Cargo Sorting *in vivo***

### Figure A3.3 *chm7Δ* Does Not Affect Endosomal Cargo Sorting *in vivo*

- (A) Temperature sensitivity assay for wild-type, *snf7Δ*, *chm7Δ*, *CHM7-GFP* and *snf7Δchm7Δ* yeast grown under 26°C and 38°C (3 days).
- (B) Canavanine sensitivity assay for wild-type, *snf7Δ*, *chm7Δ*, *CHM7-GFP* and *CHM7-FLAG* yeast grown under no or 0.6 µg/mL Canavanine.
- (C) Representative images of mid-log *chm7Δ* yeast exogenously expressing *MUP1-GFP* (2 hours post 20 µg/mL methionine treatment), *CAN1-GFP* (2 hours post cycloheximide treatment), *LYP1-GFP* (2 hours post 50 mg/mL cycloheximide treatment) (Lin et al., 2008), *GFP-CPS1*.
- (D) Representative images of mid-log *vta1Δ*, *ist1Δ*, *did2Δ*, *ist1Δdid2Δ* (upper), *vta1Δchm7Δ*, *ist1Δchm7Δ*, *did2Δchm7Δ* and *ist1Δdid2Δchm7Δ* (lower) yeast exogenously expressing *GFP-CPS1*.
- (E) Quantitative MVB sorting data for *vps20Δchm7Δ*, *vps25Δchm7Δ* and *vps23Δchm7Δ* yeast exogenously expressing *VPS20/VPS25/VPS23* and *CHM7*, *VPS20/VPS25/VPS23* and vector, *snf7\*\*\** and *CHM7*, and *snf7\*\*\** and vector. Error bars represent standard deviations from 3-5 independent experiments. *snf7\*\*\** = *myr-snf7<sup>R52E Q90L N100I</sup>*.
- (F) Quantitative MVB sorting data for *vps20Δ* yeast exogenously expressing vector, *VPS20*, *SNF7*, *CHM7* (*centromeric*), and *CHM7* (2µ). Error bars represent standard deviations from 3-5 independent experiments.
- (G) Representative images of mid-log wildtype and *snf7Δ* yeast exogenously expressing *CHM7-GFP* (*centromeric*) or *CHM7-GFP* (2µ).

**Table A3.1 Snf7 SILAC: WT Snf7-FLAG (Heavy) V.S. WT Untagged (Light)**

| protein | count | count_h | count_l | gmean  | aa   | pept/aa  |
|---------|-------|---------|---------|--------|------|----------|
| SNF7    | 119   | 117     | 2       | 204.04 | 240  | 0.495833 |
| DID2    | 30    | 27      | 3       | 67.06  | 204  | 0.147059 |
| VPS2    | 18    | 18      | 0       | 53.92  | 232  | 0.077586 |
| VPS24   | 11    | 11      | 0       | 143.64 | 224  | 0.049107 |
| PHB1    | 8     | 8       | 0       | 15.23  | 287  | 0.027875 |
| PHB2    | 7     | 7       | 0       | 8.32   | 310  | 0.022581 |
| YJL049W | 8     | 8       | 0       | 75.78  | 450  | 0.017778 |
| CSM1    | 3     | 3       | 0       | 36.42  | 190  | 0.015789 |
| VPS20   | 3     | 3       | 0       | 42.22  | 221  | 0.013575 |
| YDL089W | 5     | 5       | 0       | 77.82  | 484  | 0.010331 |
| SRC1    | 8     | 8       | 0       | 9.8    | 834  | 0.009592 |
| VTH1    | 11    | 11      | 0       | 13.56  | 1549 | 0.007101 |
| TMS1    | 3     | 3       | 0       | 19.34  | 473  | 0.006342 |
| LSB3    | 2     | 1       | 1       | 9.75   | 459  | 0.004357 |
| VPS36   | 2     | 2       | 0       | 17.15  | 566  | 0.003534 |
| PEP1    | 2     | 2       | 0       | 109.52 | 1579 | 0.001267 |

Hits shown: any protein with Gmean > 5 (ie, 5-fold enrichment over background)

Table is organized by stoichiometry

**Table A3.2 Snf7 SILAC: *vps4Δ* Snf7-FLAG (Heavy) V.S. *vps4Δ* Untagged (Light)**

| gene    | count | count_h | count_l | gmean  | aa   | pept/aa  |
|---------|-------|---------|---------|--------|------|----------|
| DID2    | 41    | 40      | 1       | 182.86 | 204  | 0.20098  |
| SNF7    | 43    | 42      | 1       | 222.18 | 240  | 0.179167 |
| VPS2    | 23    | 22      | 1       | 174.8  | 232  | 0.099138 |
| VPS24   | 20    | 20      | 0       | 167.15 | 224  | 0.089286 |
| VPS36   | 50    | 50      | 0       | 263.27 | 566  | 0.088339 |
| VPS22   | 20    | 20      | 0       | 340.03 | 233  | 0.085837 |
| VPS25   | 13    | 13      | 0       | 134.01 | 202  | 0.064356 |
| VPS20   | 11    | 11      | 0       | 290.75 | 221  | 0.049774 |
| YJL049W | 19    | 19      | 0       | 52.42  | 450  | 0.042222 |
| VPH1    | 25    | 21      | 4       | 10.48  | 840  | 0.029762 |
| CPS1    | 13    | 9       | 4       | 5.2    | 576  | 0.022569 |
| VMA10   | 2     | 2       | 0       | 4.98   | 114  | 0.017544 |
| VPS60   | 4     | 4       | 0       | 231.52 | 229  | 0.017467 |
| BRO1    | 13    | 13      | 0       | 53.42  | 844  | 0.015403 |
| SRC1    | 10    | 10      | 0       | 6.83   | 834  | 0.01199  |
| TNA1    | 6     | 5       | 1       | 8.81   | 534  | 0.011236 |
| COS2    | 2     | 2       | 0       | 16.17  | 379  | 0.005277 |
| BAP2    | 3     | 3       | 0       | 5.86   | 609  | 0.004926 |
| SIT1    | 3     | 3       | 0       | 10.63  | 628  | 0.004777 |
| DDI1    | 2     | 2       | 0       | 8.28   | 428  | 0.004673 |
| RIM20   | 3     | 3       | 0       | 233.4  | 661  | 0.004539 |
| YCK3    | 2     | 1       | 1       | 5.96   | 524  | 0.003817 |
| THI20   | 2     | 2       | 0       | 8.6    | 551  | 0.00363  |
| YCF1    | 2     | 2       | 0       | 44.32  | 1515 | 0.00132  |

Hits shown: any protein with Gmean > 5 (ie, 5-fold enrichment over background)

Table is organized by stoichiometry

**Table A3.3 Snf7 SILAC: *vps4Δ* Snf7-FLAG (Heavy) V.S. WT Snf7-FLAG (Light)**

| gene    | expt | count | count_h | count_l | gmean | norm_gmean | description              |
|---------|------|-------|---------|---------|-------|------------|--------------------------|
| COS2    | 2    | 3     | 3       | 0       | 40.6  | 72.5       |                          |
| VPS22   | 2    | 28    | 22      | 6       | 27.47 | 49.05357   | ESCRT-II                 |
| VPS36   | both | 70    | 58      | 12      | 24.68 | 44.07143   | ESCRT-II                 |
| VPS25   | 2    | 19    | 18      | 1       | 21.03 | 37.55357   | ESCRT-II                 |
| VPS20   | both | 17    | 14      | 3       | 20.54 | 36.67857   | ESCRT-III                |
| BAP2    | 2    | 2     | 2       | 0       | 17.33 | 30.94643   | cargo                    |
| CPS1    | 2    | 3     | 3       | 0       | 13.39 | 23.91071   | cargo                    |
| YCF1    | 2    | 16    | 16      | 0       | 11.16 | 19.92857   | cargo                    |
| BRO1    | 2    | 14    | 14      | 0       | 8.86  | 15.82143   | ESCRT-accessory          |
| SIT1    | 2    | 2     | 2       | 0       | 7.44  | 13.28571   | cargo                    |
| VPH1    | 2    | 45    | 31      | 14      | 6.77  | 12.08929   | V-ATPase                 |
| RIM20   | 2    | 5     | 5       | 0       | 5.71  | 10.19643   | Bro1-like                |
| YJL049W | both | 28    | 20      | 8       | 3.67  | 6.553571   |                          |
| VMA10   | 2    | 3     | 3       | 0       | 2.93  | 5.232143   | v-ATPase                 |
| YDL089W | 1    | 5     | 3       | 2       | 2.64  | 4.714286   |                          |
| TNA1    | 2    | 7     | 6       | 1       | 2.61  | 4.660714   | cargo                    |
| VPS24   | both | 38    | 22      | 16      | 2.39  | 4.267857   | ESCRT-III                |
| DID2    | both | 81    | 47      | 34      | 1.81  | 3.232143   | ESCRT-accessory          |
| CSM1    | 1    | 1     | 1       | 0       | 1.53  | 2.732143   |                          |
| DDI1    | 2    | 3     | 2       | 1       | 1.49  | 2.660714   | v-SNARE                  |
| SRC1    | both | 15    | 10      | 5       | 1.45  | 2.589286   |                          |
| VPS2    | both | 37    | 19      | 18      | 1.42  | 2.535714   | ESCRT-III                |
| YCK3    | 2    | 2     | 1       | 1       | 1.22  | 2.178571   | vacuolar kinase          |
| LSB3    | 1    | 3     | 2       | 1       | 1.09  | 1.946429   | binds Las17              |
| PHB2    | 1    | 10    | 5       | 5       | 1.06  | 1.892857   | prohibitin               |
| PHB1    | 1    | 7     | 3       | 4       | 1.04  | 1.857143   | prohibitin               |
| THI20   | 2    | 2     | 1       | 1       | 0.92  | 1.642857   | thiamine biosynthesis    |
| SNF7    | both | 120   | 49      | 71      | 0.56  | 1          | BAIT                     |
| VPS60   | 2    | 12    | 4       | 8       | 0.19  | 0.339286   | ESCRT-accessory          |
| VPS10   | 1    | 5     | 0       | 5       | 0.07  | 0.125      | Golgi-endosome transport |
| VTH1    | 1    | 17    | 0       | 17      | 0.03  | 0.053571   | similar to Vps10         |

Extracted data for every hit in tables A1.1 and A1.2 (*i.e.*, all proteins that interact specifically with Snf7). Data is organized by decreasing Gmean (Gmean>1 means enriched in *vps4Δ* cells, Gmean=1 means no difference between WT and *vps4Δ* cells, Gmean<1 means enriched in WT cells)

**Table A3.4 Plasmids and Yeast Strains Used in Appendix 3**

| <b>Plasmids for <i>Saccharomyces cerevisiae</i> Expression</b> |  |                             |
|--|--|-----------------------------|
| <b>Plasmid</b>   | <b>Mutations</b>   | <b>Reference</b>            |
| pRS416-CHM7-GFP  | GFP  | this study                  |
| pRS415-CHM7-GFP  | GFP  | this study                  |
| pRS416-MUP1-GFP  | GFP  | (Lin et al., 2008)          |
| pRS416-CAN1-GFP  | GFP  | (Lin et al., 2008)          |
| pRS416-LYP1-GFP  | GFP  | (Lin et al., 2008)          |
| pRS426-GFP-CPS1  | GFP  | (Odorizzi et al., 1998)     |
| pRS416   |  | (Sikorski and Hieter, 1989) |
| pRS415   |  | (Sikorski and Hieter, 1989) |
| pRS415-VPS20   | Wild-type  | (Buchkovich et al., 2013)   |
| pRS416-CHM7  | Wild-type  | this study                  |
| pRS416-snf7***   | Vps20 <sup>1-5</sup> -Snf7 <sup>11-240 R52E Q90L N100I</sup> | (Tang et al., 2016)         |
| pRS415-VPS25   | Wild-type  | (Tang et al., 2016)         |
| pRS415-VPS23   | Wild-type  | (Tang et al., 2016)         |
| pRS426-CHM7  | Wild-type  | this study                  |
| pRS426-CHM7-GFP  | GFP  | this study                  |

**Yeast Strains Used in This Study**

| <b>Strain</b> | <b>Genotype</b>   | <b>Reference</b>        |
|---------------|---|-------------------------|
| SEY6210       | <i>Mat a, leu2-3, 2-112, ura3-52, his3-Δ200, trp1-Δ901, lys2-801, suc2-Δ9</i> | (Robinson et al., 1988) |
| SEY6210.1     | <i>Mat a, leu2-3, 2-112, ura3-52, his3-Δ200, trp1-Δ901, lys2-801, suc2-Δ9</i> | (Robinson et al., 1988) |
| MBY21         | SEY6210; <i>vps27Δ::HIS3</i>  | (Katzmann et al., 2003) |
| MBY23         | SEY6210.1; <i>vps23Δ::HIS3</i>  | (Katzmann et al., 2001) |
| MBY13         | SEY6210.1; <i>vps36Δ::HIS3</i>  | (Babst et al., 2002b)   |
| MBY25         | SEY6210.1; <i>vps20Δ::HIS3</i>  | (Babst et al., 2002a)   |
| MBY24         | SEY6210.1; <i>snf7Δ::HIS3</i>   | (Babst et al., 2002a)   |
| MBY24         | SEY6210.1; <i>snf7Δ::HIS3</i>   | (Babst et al., 2002a)   |
| BWY102        | SEY6210; <i>vps24Δ::HIS3</i>  | (Babst et al., 1998)    |
| MBY28         | SEY6210; <i>vps2Δ::HIS3</i>   | (Babst et al., 2002a)   |
| MBY3          | SEY6210; <i>vps4Δ::HIS3</i>   | (Babst et al., 1997)    |
| SJ053         | SEY6210; <i>CHM7-GFP::HIS3</i>  | this study              |
| STY5          | SEY6210.1; <i>vps4Δ::TRP1; CHM7-GFP::HIS3</i>                                 | this study              |
| STY1          | SEY6210; <i>snf7Δ::HIS3; CHM7-GFP::HIS3</i>                                   | this study              |
| STY10         | SEY6210.1; <i>vps20Δ::HIS3; CHM7-GFP::HIS3</i>                                | this study              |
| SJ054         | SEY6210; <i>chm7Δ::HIS3</i>   | this study              |
| SJ052         | SEY6210; <i>CHM7-FLAG::HIS3</i>   | this study              |
| STY4          | SEY6210.1; <i>snf7Δ::HIS3; chm7Δ::HIS3</i>                                    | this study              |
| SRY558        | SEY6210; <i>vta1Δ::TRP1</i>   | (Rue et al., 2008)      |

|        |   |                           |
|--------|---|---------------------------|
| SRY403 | SEY6210; <i>ist1Δ::TRP1</i>                                     | (Rue et al., 2008)        |
| SMY60  | SEY6210; <i>did2Δ::TRP1</i>                                     | (Rue et al., 2008)        |
| SRY686 | SEY6210; <i>ist1Δ::TRP1; did2Δ::TRP1</i>                        | (Rue et al., 2008)        |
| STY26  | SEY6210.1; <i>chm7Δ::HIS3; vta1Δ::TRP1</i>                      | this study                |
| STY27  | SEY6210; <i>chm7Δ::HIS3; ist1Δ::TRP1</i>                        | this study                |
| STY28  | SEY6210.1; <i>chm7Δ::HIS3; did2Δ::TRP1</i>                      | this study                |
| STY29  | SEY6210; <i>chm7Δ::HIS3; ist1Δ::TRP1; did2Δ::TRP1</i>           | this study                |
| STY82  | SEY6210.1; <i>vps20Δ::HIS3; chm7Δ::TRP1; MUP1-PHLOURIN::KAN</i> | this study                |
| STY83  | SEY6210; <i>vps25Δ::HIS3; chm7Δ::TRP1; MUP1-PHLOURIN::KAN</i>   | this study                |
| STY84  | SEY6210.1; <i>vps24Δ::HIS3; chm7Δ::TRP1; MUP1-PHLOURIN::KAN</i> | this study                |
| NBY42  | SEY6210.1; <i>vps20Δ::HIS3; MUP1-PHLOURIN::KAN</i>              | (Buchkovich et al., 2013) |

## Reference

- Babst, M., Katzmann, D.J., Estepa-Sabal, E.J., Meerloo, T., and Emr, S.D. (2002a). ESCRT-III: an endosome-associated heterooligomeric protein complex required for mvb sorting. *Dev Cell* 3, 271-282.
- Babst, M., Katzmann, D.J., Snyder, W.B., Wendland, B., and Emr, S.D. (2002b). Endosome-associated complex, ESCRT-II, recruits transport machinery for protein sorting at the multivesicular body. *Dev Cell* 3, 283-289.
- Babst, M., Sato, T.K., Banta, L.M., and Emr, S.D. (1997). Endosomal transport function in yeast requires a novel AAA-type ATPase, Vps4p. *EMBO J* 16, 1820-1831.
- Babst, M., Wendland, B., Estepa, E.J., and Emr, S.D. (1998). The Vps4p AAA ATPase regulates membrane association of a Vps protein complex required for normal endosome function. *EMBO J* 17, 2982-2993.
- Bauer, I., Brune, T., Preiss, R., and Kolling, R. (2015). Evidence for a Nonendosomal Function of the *Saccharomyces cerevisiae* ESCRT-III-Like Protein Chm7. *Genetics* 201, 1439-1452.
- Buchkovich, N.J., Henne, W.M., Tang, S., and Emr, S.D. (2013). Essential N-terminal insertion motif anchors the ESCRT-III filament during MVB vesicle formation. *Dev Cell* 27, 201-214.
- Horii, M., Shibata, H., Kobayashi, R., Katoh, K., Yorikawa, C., Yasuda, J., and Maki, M. (2006). CHMP7, a novel ESCRT-III-related protein, associates with CHMP4b and functions in the endosomal sorting pathway. *Biochem J* 400, 23-32.
- Katzmann, D.J., Babst, M., and Emr, S.D. (2001). Ubiquitin-dependent sorting into the multivesicular body pathway requires the function of a conserved endosomal protein sorting complex, ESCRT-I. *Cell* 106, 145-155.
- Katzmann, D.J., Stefan, C.J., Babst, M., and Emr, S.D. (2003). Vps27 recruits ESCRT machinery to endosomes during MVB sorting. *J Cell Biol* 162, 413-423.
- Leung, K.F., Dacks, J.B., and Field, M.C. (2008). Evolution of the multivesicular body ESCRT machinery; retention across the eukaryotic lineage. *Traffic* 9, 1698-1716.
- Lin, C.H., MacGurn, J.A., Chu, T., Stefan, C.J., and Emr, S.D. (2008). Arrestin-related ubiquitin-ligase adaptors regulate endocytosis and protein turnover at the cell surface. *Cell* 135, 714-725.

MacGurn, J.A., Hsu, P.C., Smolka, M.B., and Emr, S.D. (2011). TORC1 regulates endocytosis via Npr1-mediated phosphoinhibition of a ubiquitin ligase adaptor. *Cell* 147, 1104-1117.

Odorizzi, G., Babst, M., and Emr, S.D. (1998). Fab1p PtdIns(3)P 5-Kinase Function Essential for Protein Sorting in the Multivesicular Body. *Cell* 95, 847-858.

Robinson, J., Klionsky, D., Banta, L., and Emr, S. (1988). Protein sorting in *Saccharomyces cerevisiae*: isolation of mutants defective in the delivery and processing of multiple vacuolar hydrolases. *Mol Cell Biol* 8(11), 4936-4948.

Rue, S.M., Mattei, S., Saksena, S., and Emr, S.D. (2008). Novel Ist1-Did2 complex functions at a late step in multivesicular body sorting. *Mol Biol Cell* 19, 475-484.

Sikorski, R.S., and Hieter, P. (1989). A system of shuttle vectors and yeast host strains designed for efficient manipulation of DNA in *Saccharomyces cerevisiae*. *Genetics* 22, 19-27.

Tang, S., Buchkovich, N.J., Henne, W.M., Banjade, S., Kim, Y.J., and Emr, S.D. (2016). ESCRT-III activation by parallel action of ESCRT-I/II and ESCRT-0/Bro1 during MVB biogenesis. *Elife* 5.

Vida, T.A., and Emr, S.D. (1995). A new vital stain for visualizing vacuolar membrane dynamics and endocytosis in yeast. *J Cell Biol* 128, 779-792.

Vietri, M., Schink, K.O., Campsteijn, C., Wegner, C.S., Schultz, S.W., Christ, L., Thoresen, S.B., Brech, A., Raiborg, C., and Stenmark, H. (2015). Spastin and ESCRT-III coordinate mitotic spindle disassembly and nuclear envelope sealing. *Nature* 522, 231-235.

Webster, B.M., Colombi, P., Jager, J., and Lusk, C.P. (2014). Surveillance of nuclear pore complex assembly by ESCRT-III/Vps4. *Cell* 159, 388-401.

## APPENDIX IV

### Summary of the Quantitative MVB Sorting Data

#### Summary

This appendix summarized the results from the quantitative Mup1-pHluorin ESCRT cargo-sorting assay. For the flow cytometry assay, 1.5-3.0 mL of overnight yeast cell cultures were cut back to OD=0.3 and grown to mid-log phase the addition of 20 µg/mL L-methionine at 26°C for 2 hours. Mid-log cultures were resuspended in 50-100 µL 1x PBS buffer.

Mean green fluorescence (FL1-A channel) of 100,000 events was recorded and gated on a BD Accuri C6 flow cytometer (located and maintained by in the Jan Lammerding Lab). Each sample was gated and the gated mean FL1-A values,  $F$ , were recorded. For each experimental setup, two “empty vector” and two “wild-type” samples were included for data quantification:

$$F_{empty\ vector} = \frac{F_{empty\ vector\ 1} + F_{empty\ vector\ 2}}{2} \text{ and } F_{WT} = \frac{F_{WT\ 1} + F_{WT\ 2}}{2}.$$

For single ESCRT mutants, MVB sorting scores were calculated as:

$$MVB\ Sorting\ \% = \left( 1 - \frac{F_{Mutant} - F_{WT}}{F_{empty\ vector} - F_{WT}} \right) \times 100\%$$

For double ESCRT mutants, MVB sorting scores were calculated as:

$$MVB\ Sorting\ \% = \left( 1 - \frac{F_{Mutant} - F_{WT+WT}}{F_{empty\ vector+empty\ vector} - F_{WT+WT}} \right) \times 100\%$$

Sorting scores of 3 to 5 independent experiments are used to calculate standard deviation.

**Table A4.1 Summary of Mup1-pHluorin MVB Sorting in *snf7Δ* Yeast**

| Mutants expressed in<br><i>snf7Δ</i> | MVB<br>Sorting | STD    | Mutants expressed in<br><i>snf7Δ</i> | MVB<br>Sorting | STD    |
|--------------------------------------|----------------|--------|--------------------------------------|----------------|--------|
| Vector                               | 0.00%          | 6.40%  | <b>α3</b>                            |                |        |
| <i>SNF7</i>                          | 100.00%        | 1.57%  | <i>L101K</i>                         | 97.30%         | 4.56%  |
|                                      |                |        | <i>L101E</i>                         | 75.74%         | 6.67%  |
| <b>α0</b>                            |                |        | <i>E102C</i>                         | 101.56%        | 2.55%  |
| <i>ΔN</i> *                          | 13.3%          | 6.4%   | <i>E102P</i>                         | 21.43%         | 6.90%  |
| <i>N(BAR)</i> *                      | 78.6%          | 6.4%   | <i>E102A T103A M104A R105A</i>       | 59.03%         | 5.52%  |
| <i>N(Rvs161) F6E</i> *               | 1.3%           | 2.2%   | <i>E102P R105P</i>                   | 7.68%          | 5.94%  |
| <i>N(ALPS)</i> *                     | 89.6%          | 4.0%   | <i>E102K</i>                         | 104.18%        | 1.95%  |
| <i>N(ALPS) W5E</i> *                 | 17.2%          | 14.7%  | <i>E102K E109K</i>                   | 100.85%        | 0.42%  |
| <i>N(Rvs167)</i> *                   | 26.7%          | 6.8%   | <i>T103R</i>                         | 88.24%         | 2.08%  |
| <i>N(Rvs167) F6E</i> *               | 6.1%           | 9.0%   | <i>T103E</i>                         | 34.00%         | 8.77%  |
| <i>N(Ent1)</i> *                     | 59.5%          | 3.6%   | <i>M104E</i>                         | 11.80%         | 3.97%  |
| <i>N(ABBA)</i> *                     | 24.6%          | 10.3%  | <i>M107E</i>                         | 13.11%         | 9.21%  |
| <i>N(MIM)</i> *                      | 28.7%          | 9.8%   | <i>E109K</i>                         | 102.56%        | 4.13%  |
| <i>N(Arf1)</i> *                     | 21.1%          | 9.4%   | <i>G110A</i>                         | 98.88%         | 1.88%  |
| <i>N(Arf1) G2A</i> *                 | 98.5%          | 1.1%   | <i>G110W</i>                         | 99.06%         | 1.15%  |
| <i>myr (N(Vps20))</i> *              | 94.4%          | 2.3%   | <i>K112E K115E</i> *                 | 60.3%          | 5.7%   |
| <i>myr (N(Vps20)) G2A</i> *          | 20.7%          | 12.7%  | <i>M114E</i>                         | 10.23%         | 7.66%  |
| <i>N(Vps24)</i> *                    | 31.0%          | 5.8%   | <i>I117E</i> *                       | 6.7%           | 0.73%  |
| <i>N(Vps2)</i> *                     | 53.6%          | 7.0%   | <i>H118S</i>                         | 98.47%         | 6.3%   |
| <i>N(Vps2) E5G</i> *                 | 93.3%          | 5.7%   | <i>H118A</i>                         | 99.89%         | 1.03%  |
| <i>N(Gpa1)</i>                       | 82.65%         | 10.41% | <i>H118F</i>                         | 102.11%        | 1.09%  |
| <i>N(Gpa1) C3A</i>                   | 101.74%        | 3.98%  | <i>H118N</i>                         | 101.73%        | 1.23%  |
| <i>N(Gpa1) G2A</i>                   | 1.14%          | 21.84% | <i>H118Q</i>                         | 102.82%        | 3.74%  |
| <i>N(Gpa1) G2A C3A</i>               | 26.92%         | 6.87%  | <i>H118K</i>                         | 101.42%        | 0.30%  |
| <i>N(Rho3)</i>                       | 22.55%         | 13.04% | <i>H118D</i>                         | 38.32%         | 6.76%  |
| <i>N(Rho3) C5A</i>                   | 28.47%         | 12.09% | <i>H118E</i>                         | 100.21%        | 1.67%  |
| <i>N(Sna4)</i>                       | 7.11%          | N.D.   | <i>H118C</i>                         | 102.41%        | 1.23%  |
| <i>2xN</i> *                         | 26.6%          | 4.6%   | <i>H118D R134D</i>                   | 16.99%         | 7.90%  |
| <i>StoK</i> *                        | 97.8%          | 1.8%   | <i>H118D R149D</i>                   | 10.63%         | 5.64%  |
| <i>8A</i> *                          | 13.8%          | 8.6%   | <i>H118D R134D R149D</i>             | 15.32%         | 2.34%  |
| <i>6K</i> *                          | 19.0%          | 8.7%   | <i>G120P</i>                         | 98.29%         | 4.39%  |
| <i>TDH3Promoter 6K</i> *             | 9.9%           | 18.7%  |                                      |                |        |
| <i>6E</i> *                          | 5.6%           | 9.5%   | <b>α4</b>                            |                |        |
| <i>6W</i> *                          | 71.4%          | 8.3%   | <i>L121P</i>                         | 31.71%         | 11.82% |
| <i>6WK</i> *                         | 98.6%          | 1.5%   | <i>L121K</i>                         | 51.83%         | 11.10% |
| <i>10WK</i> *                        | 54.7%          | 9.2%   | <i>L121C</i>                         | 99.82%         | 1.36%  |
| <i>14WK</i> *                        | 0.0%           | 5.8%   | <i>R52E L121C</i>                    | 61.06%         | 5.14%  |

|                     |         |        |  |                         |         |        |
|---------------------|---------|--------|--|-------------------------|---------|--------|
| 18WS *              | 18.2%   | 8.3%   |  | L121W                   | 102.10% | 1.40%  |
| Δ2-6                | 35.97%  | 6.00%  |  | L121F                   | 104.20% | 0.84%  |
| Δ2-6 G7A            | 19.77%  | 6.43%  |  | L121D                   | 26.24%  | 12.77% |
| Δ2-5                | 80.74%  | 6.07%  |  | L121P                   | 32.70%  | 13.10% |
| Δ2-7                | 23.61%  | 9.31%  |  | D122K                   | 101.96% | 2.26%  |
| W2E *               | 41.6%   | 13.5%  |  | D124K                   | 101.15% | 0.32%  |
| S4P *               | 90.6%   | 8.6%   |  | K125E                   | 103.97% | 1.74%  |
| L5P *               | 82.8%   | 10.0%  |  | V126E                   | 9.26%   | 5.11%  |
| F6E *               | 39.6%   | 14.7%  |  | D127K                   | 26.74%  | 4.42%  |
| F6W *               | 101.3%  | 6.7%   |  | D127K D131K             | 18.30%  | 5.76%  |
| F6A *               | 91.2%   | 5.5%   |  | D127K E128K D131K E132K | 23.68%  | 9.75%  |
| F6C                 | 95.93%  | 6.22%  |  | D127E                   | 102.44% | 2.85%  |
| F6S *               | 91.9%   | 4.6%   |  | D127A                   | 101.77% | 1.60%  |
| G7W *               | 102.5%  | 3.5%   |  | D127W                   | 103.71% | 1.97%  |
| W8E *               | 63.6%   | 2.5%   |  | E128K                   | 101.85% | 1.52%  |
| α1                  |         |        |  | M130E                   | 15.21%  | 5.49%  |
| T20E                | 100.60% | 3.48%  |  | M130C                   | 97.17%  | 1.82%  |
| T20E I30K *         | 102.6%  | 5.4%   |  | D131K                   | 17.46%  | 8.18%  |
| T20C                | 100.14% | 1.20%  |  | D131E                   | 99.90%  | 1.47%  |
| T20D I30K N31Q *    | 103.3%  | 0.3%   |  | D131A                   | 102.41% | 2.14%  |
| T20E I30K R52E *    | 39.7%   | 11.4%  |  | D131W                   | 103.51% | 2.26%  |
| T20E I30K L67E *    | 6.0%    | 2.8%   |  | E132K                   | 101.15% | 4.10%  |
| K21E                | 18.63%  | 4.13%  |  | E132C R52E              | 87.87%  | 7.03%  |
| K21E E50K           | 102.48% | 3.04%  |  | I133E                   | 12.39%  | 1.81%  |
| R25E                | 100.83% | 2.16%  |  | D131K R149G             | 83.58%  | 2.05%  |
| R25E H29E           | 24.47%  | 5.71%  |  | R134D                   | 51.80%  | 9.25%  |
| R25E K36E           | 39.95%  | 6.53%  |  | D127K R134D             | 99.75%  | 0.62%  |
| R25E H29E K36E      | 17.54%  | 6.84%  |  | D131K R134D             | 95.14%  | 4.20%  |
| R25D                | 101.98% | 4.15%  |  | R134E                   | 99.33%  | 4.42%  |
| R25C                | 100.98% | 2.30%  |  | E135K                   | 101.24% | 0.97%  |
| R27E                | 101.34% | 2.03%  |  | Q136E *                 | 97.2%   | 1.22%  |
| R27E R52E           | 94.66%  | 1.53%  |  | Q136A                   | 98.01%  | 3.2%   |
| R27E K57E           | 99.60%  | 4.07%  |  | E138K                   | 64.69%  | 12.07% |
| R27E K35E K36E      | 31.69%  | 13.31% |  | D141K                   | 106.17% | 1.64%  |
| R27E K35E R52E      | 46.31%  | 16.84% |  | E142K                   | 22.62%  | 14.68% |
| R27E K35E R52E K57E | 17.64%  | 21.05% |  | E142K S144A             | 26.94%  | 18.49% |
| E28K Q136E *        | 98.1%   | 7.3%   |  | S144A                   | 106.28% | 1.70%  |
| H29E                | 74.28%  | 9.19%  |  | D145K                   | 100.94% | 0.53%  |
| H29E K36E           | 7.27%   | 5.87%  |  | S148A                   | 103.82% | 4.58%  |
| H29C                | 101.11% | 1.94%  |  | R149D                   | 38.12%  | 12.55% |
|                     |         |        |  | R149E                   | 93.10%  | 9.78%  |

|   |         |        |
|---|---------|--------|
| <i>I30K</i> *                                   | 105.0%  | 6.9%   |
| <i>I30K N31Q</i> *                              | 101.5%  | 1.8%   |
| <i>S34A</i> *                                   | 96.9%   | 0.3%   |
| <i>S34E</i> *                                   | 97.9%   | 1.0%   |
| <i>S34H</i> *                                   | 96.4%   | 2.4%   |
| <i>K35E K36E</i>                                | 86.16%  | 9.27%  |
| <i>K35E R52E</i>                                | 88.38%  | 3.86%  |
| <i>K35E K36E R52E</i>                           | 25.32%  | 17.53% |
| <i>K35E R52E K57E</i>                           | 73.47%  | 9.13%  |
| <i>K35E K36E E85R E88R</i>                      | 38.40%  | 8.71%  |
| <i>K35C</i>                                     | 99.92%  | 1.44%  |
| <i>K35C R52E</i>                                | 51.23%  | 5.35%  |
| <i>R27E K35E K36E</i>                           | 43.74%  | 13.55% |
| <i>R27E K35E K36E E85R E88R E95R</i>            | 68.77%  | 9.12%  |
| <i>K35E</i>                                     | 99.88%  | 1.71%  |
| <i>K36E</i>                                     | 96.79%  | 2.24%  |
| <i>S38C</i>                                     | 102.05% | 0.81%  |
| <i>H39E</i>                                     | 94.15%  | 4.44%  |
| <i>R41D</i>                                     | 92.96%  | 3.47%  |
| <i>Q43C</i>                                     | 99.23%  | 1.70%  |
| <i>E48K</i>                                     | 101.05% | 1.51%  |
| <i>E50K</i>                                     | 98.79%  | 0.90%  |
| <i>A51E</i> *                                   | 37.1%   | 15.6%  |
| <i>A51C</i>                                     | 100.55% | 0.37%  |
| <i>R52E</i>                                     | 94.98%  | 5.36%  |
| <i>R52C</i>                                     | 103.28% | 1.36%  |
| <i>I53E</i>                                     | 99.24%  | 2.24%  |
| <i>L55E</i>                                     | 54.71%  | 8.85%  |
| <i>K57E</i>                                     | 100.05% | 2.56%  |
| <i>K57E K60E</i>                                | 97.63%  | 6.51%  |
| <i>K57E K60E K64E</i>                           | 31.05%  | 11.63% |
| <i>K57C</i>                                     | 100.64% | 1.38%  |
| <i>G58P</i>                                     | 55.07%  | 7.54%  |
| <i>G58C</i>                                     | 100.54% | 1.98%  |
| <i>N59P</i>                                     | 74.81%  | 9.36%  |
| <b>α2</b>                                       |         |        |
| <i>K60E</i> *                                   | 102.7%  | 2.7%   |
| <i>K60C</i>                                     | 100.82% | 1.47%  |
| <i>K60C A66C</i>                                | 100.49% | 0.40%  |
| <i>M62E</i>                                     | 100.72% | 1.77%  |
| <i>R149K</i>                                    | 101.11% | 3.02%  |
| <i>R149G</i>                                    | 106.42% | 1.02%  |
| <i>R149A</i>                                    | 103.04% | 2.65%  |
| <i>R149W</i>                                    | 85.97%  | 10.09% |
| <i>D127K R149D</i>                              | 103.21% | 6.37%  |
| <i>D131K R149D</i>                              | 99.38%  | 5.73%  |
| <i>D127K D131K R149D</i>                        | 13.44%  | 12.48% |
| <i>D127K R134D R149D</i>                        | 12.36%  | 9.70%  |
| <i>D127K D131K R134D R149D</i>                  | 44.01%  | 17.20% |
| <i>D127K D131K H118D R134D R149D</i>            | 13.96%  | 1.05%  |
| <i>D131K R134D R149D</i>                        | 14.79%  | 9.78%  |
| <i>R134D R149D</i>                              | 13.60%  | 4.44%  |
| <i>R134D E142K</i>                              | 99.35%  | 2.78%  |
| <i>G140P</i>                                    | 24.91%  | 2.79%  |
| <i>G140C</i>                                    | 103.27% | 1.28%  |
| <i>E142K R149D</i>                              | 102.90% | 3.48%  |
| <b>α5</b>                                       |         |        |
| <i>D159Y I192A</i>                              | 109.06% | 5.46%  |
| <i>L167E</i> *                                  | 26.7%   | 9.5%   |
| <i>A171E</i>                                    | 101.97% | 0.35%  |
| <i>E173R</i>                                    | 101.66% | 1.63%  |
| <i>E173C R52E</i>                               | 95.62%  | 5.34%  |
| <i>N174K</i>                                    | 101.53% | 0.78%  |
| <i>A175K</i>                                    | 102.25% | 2.58%  |
| <i>E178K</i>                                    | 103.49% | 1.57%  |
| <i>T179K</i>                                    | 105.24% | 1.17%  |
| <i>V183K</i>                                    | 97.60%  | N.D.   |
| <i>V187C R52E</i>                               | 95.06%  | 7.64%  |
| <b>C-terminus</b>                               |         |        |
| <i>Δ185-195</i>                                 | 101.46% | 3.23%  |
| <i>E218-228A</i>                                | 73.10%  | 4.28%  |
| <i>Δ218-228</i>                                 | 57.63%  | 13.21% |
| <i>L231K</i>                                    | 69.44%  | 6.66%  |
| <i>L234K</i>                                    | 106.30% | 3.86%  |
| <i>L231K L234K</i>                              | 35.39%  | 2.63%  |
| <b>Vps20-Snf7 chimera</b>                       |         |        |
| <i>VPS20</i>                                    | 5.52%   | 1.46%  |
| <i>vps20<sup>59-61</sup>snf7<sup>Q90L</sup></i> | 19.70%  | 3.02%  |

|  |         |        |  |        |        |
|--|---------|--------|--|--------|--------|
| <i>M62E N65E</i>                         | 100.86% | 1.96%  | <i>vps20<sup>118-120</sup>snf7</i>               | 9.11%  | 6.30%  |
| <i>A63C</i>                              | 101.89% | 1.67%  | <i>vps20<sup>147-151</sup>snf7 *</i>             | 13.0%  | 13.6%  |
| <i>K64E *</i>                            | 59.2%   | 1.3%   | <i>VPS20-snF7<sup>1-150</sup> *</i>              | 3.1%   | 5.4%   |
| <i>N65L</i>                              | 98.02%  | 2.64%  | <i>SNF7-vps20<sup>1-150</sup> *</i>              | 6.4%   | 5.9%   |
| <i>N65E</i>                              | 102.03% | 0.27%  |  |        |        |
| <i>L67E *</i>                            | 46.8%   | 5.9%   | <b><i>vps20Δ suppressor</i></b>                  |        |        |
| <i>K68E *</i>                            | 75.3%   | 2.7%   | <i>5mut *</i>                                    | 66.7%  | 13.9%  |
| <i>K68E K69E</i>                         | 13.90%  | 15.05% | <i>5mut Q90L *</i>                               | 55.3%  | 11.1%  |
| <i>K68E K69E D127K E128K D131K E132K</i> | 9.03%   | 6.00%  | <i>7mut *</i>                                    | 39.5%  | 9.1%   |
| <i>K68E K71E *</i>                       | 5.4%    | 3.8%   | <i>Q90L</i>                                      | 96.65% | 2.49%  |
| <i>K68E K112E K115E *</i>                | 1.1%    | 0.9%   | <i>R52E Q90L</i>                                 | 88.08% | 11.79% |
| <i>K68E K71E K112E K115E *</i>           | 3.6%    | 3.1%   | <i>R52E Q90L N100I</i>                           | 7.84%  | 14.67% |
| <i>K69E</i>                              | 40.75%  | 6.39%  | <i>myr R52E Q90L</i>                             | 91.74% | 7.87%  |
| <i>K69E E173R</i>                        | 91.53%  | 8.61%  | <i>myr R52E Q90L N100I</i>                       | 17.42% | 6.28%  |
| <i>K69E D131K</i>                        | 13.24%  | 2.88%  | <i>myr Q90L N100I</i>                            | 13.04% | 17.61% |
| <i>K69E E132K</i>                        | 98.03%  | 2.33%  | <i>RM#7 *</i>                                    | 96.9%  | 4.4%   |
| <i>K69C</i>                              | 101.60% | 0.99%  | <i>RM#9 *</i>                                    | 38.9%  | 5.2%   |
| <i>K70E *</i>                            | 46.1%   | N.D.   | <i>RM#9 R52E</i>                                 | 15.47% | 5.91%  |
| <i>K71E *</i>                            | 58.9%   | 0.52%  | <i>myr RM#9 R52E</i>                             | 9.88%  | 10.39% |
| <i>K71E K79E *</i>                       | 32.3%   | 8.8%   | <i>RM#9 R52E N100I</i>                           | 6.19%  | 13.59% |
| <i>K71E K112E K115E *</i>                | 13.4%   | 5.8%   | <i>myr RM#9 R52E N100I</i>                       | 18.72% | 12.92% |
| <i>T72A</i>                              | 99.58%  | 6.0%   | <i>myr RM#9</i>                                  | 14.98% | 12.91% |
| <i>T72E</i>                              | 101.76% | 0.46%  | <i>7mut R52E</i>                                 | 14.61% | 2.71%  |
| <i>T72K</i>                              | 101.26% | 0.53%  | <i>myr 7mut R52E</i>                             | 11.71% | 10.71% |
| <i>E74K</i>                              | 100.70% | 1.39%  | <i>myr R52E Q90L N100I I73V I123V</i>            | 20.97% | 21.01% |
| <i>Q75C</i>                              | 100.97% | 0.84%  | <i>myr R52E Q90L N100I N212D</i>                 | 10.17% | 8.13%  |
| <i>L76E *</i>                            | 42.4%   | 1.62%  | <i>myr R52E Q90L N100I E81G K112E T129A</i>      | 12.76% | 2.16%  |
| <i>K79E *</i>                            | 97.8%   | 22.5%  | <i>myr R52E Q90L 1-225</i>                       | 28.57% | 15.48% |
| <i>K79E K112E K115E *</i>                | 2.3%    | 2.3%   | <i>myr R52E Q90L N100I 1-225</i>                 | 23.42% | 13.74% |
| <i>V80E</i>                              | 64.81%  | 3.9%   |  |        |        |
| <i>E81R</i>                              | 99.33%  | 3.43%  | <b><i>Snf7 tandem fusion</i></b>                 |        |        |
| <i>E81C</i>                              | 99.97%  | 0.74%  | <i>SNF7-SNF7 (Linker: -E-F-)</i>                 | 89.97% | 6.57%  |
| <i>T83R</i>                              | 98.41%  | 0.61%  | <i>SNF7-SNF7-SNF7</i>                            | 77.82% | 4.07%  |
| <i>T83E</i>                              | 72.11%  | 8.08%  | <i>snf7<sup>D127K</sup>-SNF7</i>                 | 21.96% | 4.98%  |
| <i>T83W</i>                              | 100.00% | 1.41%  | <i>SNF7-snF7<sup>D127K</sup></i>                 | 15.32% | 6.72%  |
| <i>E85R</i>                              | 99.07%  | 2.96%  | <i>snf7<sup>R134D</sup>-SNF7</i>                 | 80.02% | 4.84%  |
| <i>M87R</i>                              | 43.34%  | 3.64%  | <i>SNF7-snF7<sup>R134D</sup></i>                 | 74.53% | 9.52%  |
| <i>M87E</i>                              | 42.36%  | 8.23%  | <i>snf7<sup>D127K</sup>-snf7<sup>R134D</sup></i> | 9.28%  | 5.13%  |
| <i>E88R</i>                              | 100.19% | 2.57%  | <i>snf7<sup>R134D</sup>-snf7<sup>D127K</sup></i> | 19.21% | 4.62%  |
| <i>E88C</i>                              | 101.88% | 1.94%  | <i>snf7<sup>D127K</sup>-snf7<sup>D127K</sup></i> | 7.35%  | 12.10% |

|                         |         |        |   |        |        |
|-------------------------|---------|--------|---|--------|--------|
| <i>E88C H118C</i>       | 100.61% | 2.51%  | <i>snf7</i> <sup>R134D</sup> - <i>snf7</i> <sup>R134D</sup>             | 27.86% | 4.40%  |
| <i>E95R</i>             | 86.80%  | 4.46%  | <i>snf7</i> <sup>W2E F6E W8E</sup> - <i>Snf7</i>                        | 30.56% | 4.52%  |
| <i>E81R E85R E88R</i>   | 22.30%  | 9.65%  | <i>SNF7-snf7</i> <sup>W2E F6E W8E</sup>                                 | 86.69% | 5.94%  |
| <i>E85R E88R</i>        | 94.13%  | 6.07%  | <i>snf7</i> <sup>W2E F6E W8E</sup> - <i>snf7</i> <sup>W2E F6E W8E</sup> | 20.49% | 7.30%  |
| <i>E85R E88R E95R</i>   | 18.64%  | 16.49% | <i>VPS25-SNF7</i>   | 12.61% | 5.67%  |
| <i>E88R E95R</i>        | 68.65%  | 16.25% | <i>VPS20-VPS20</i> *  | 4.5%   | 2.7%   |
| <i>E88C R52E</i>        | 47.36%  | 2.72%  | <i>VPS20-SNF7</i> *   | 28.6%  | 7.7%   |
| <i>Q90K</i>             | 38.22%  | 0.60%  | <i>SNF7-VPS20</i> *   | 15.8%  | 7.4%   |
| <i>Q90C M130C</i>       | 84.44%  | 6.59%  | <i>VPS20-VPS20</i> *  | -20.7% | 18.8%  |
| <i>Q90C</i>             | 98.25%  | 2.68%  | <i>snf7</i> <sup>RM#7</sup> - <i>SNF7</i> *                             | 85.2%  | 4.9%   |
| <i>F92A</i>             | 104.05% | 1.70%  | <i>snf7</i> <sup>RM#9</sup> - <i>SNF7</i> *                             | 13.2%  | 10.3%  |
| <i>F92E</i>             | 103.59% | 1.25%  |   |        |        |
| <i>F92R</i>             | 102.84% | 0.39%  | <b>Truncation &amp; deletion</b>  |        |        |
| <i>F92R L99K</i>        | 4.17%   | 6.88%  | <i>1-150</i> *  | 340.0% | 2.0%   |
| <i>I94E</i>             | 11.44%  | 6.46%  | <i>1-225</i>  | 15.36% | 10.41% |
| <i>E95K</i>             | 103.52% | 0.91%  | <i>1-230</i> *  | 11.8%  | 8.7%   |
| <i>E95K E102K</i>       | 99.35%  | 3.45%  | $\Delta$ 188-211 *  | 36.9%  | 15.3%  |
| <i>E95K E109K</i>       | 86.50%  | 8.96%  | 188-197 10Ala *   | 103.7% | 1.7%   |
| <i>E95K E102K E109K</i> | 39.86%  | 3.54%  | 198-210 13Ala *   | 102.9% | 1.2%   |
| <i>E95C</i>             | 101.41% | 1.03%  | $\Delta$ a5 *   | 23.4%  | 6.5%   |
| <i>A97E</i>             | 63.65%  | 12.84% | $\Delta$ a4/5 linker *  | 8.6%   | 5.0%   |
| <i>A97K</i>             | 29.70%  | 15.02% | $\alpha$ 4/5 linker E to K *  | 7.4%   | 8.0%   |
| <i>N98Q N100Q</i>       | 100.22% | 1.98%  |   |        |        |
| <i>L99K</i>             | 20.94%  | 13.16% | <b>Others</b>   |        |        |
| <i>L99E</i>             | 89.93%  | 7.85%  | <i>ESCRT-II</i> (2 $\mu$ ) *  | 7.5%   | 6.5%   |
| <i>N100I</i>            | 103.32% | 2.88%  | <i>VPS20Promotor</i> *  | 98.8%  | 1.5%   |
| <i>N100A</i>            | 101.32% | 0.75%  | <i>ART1Promotor</i> *   | 98.0%  | 2.4%   |
| <i>N100Q</i>            | 100.84% | 1.65%  | <i>TDH3Promotor</i> *   | 63.2%  | 6.6%   |
|                         |         |        | <i>SNF7PromotorADH1Terminator</i> *                                     | 101.6% | 2.1%   |
|                         |         |        | <i>VPS20PromotorADH1Terminator</i> *                                    | 101.0% | 0.3%   |
|                         |         |        | <i>ART1PromotorADH1Terminator</i> *                                     | 94.4%  | 3.4%   |

| Mutants co-expressed in <i>snf7</i> $\Delta$ | MVB Sorting | STD   | Mutants co-expressed in <i>snf7</i> $\Delta$ | MVB Sorting | STD    |
|--|-------------|-------|--|-------------|--------|
| <i>Vector+Vector</i>                         | 0.00%       | 6.18% | <b><math>\alpha</math>3/4</b>                |             |        |
| <i>SNF7+SNF7</i>                             | 100.00%     | 0.64% | <i>D127K+Vector</i>                          | 16.27%      | 2.64%  |
| <b><math>\alpha</math>1/2</b>                |             |       | <i>Vector+R149D</i>                          | 39.76%      | 13.24% |
| <i>R25E H29E K35E+Vector</i>                 | 15.88%      | 6.18% | <i>D127K+R149D</i>                           | 84.94%      | 4.07%  |
| <i>Vector+E95K E102K E109K</i>               | 43.96%      | 6.64% | <i>E135K+Vector</i>                          | 91.20%      | 3.17%  |
| <i>R25E H29E K35E+E95K E102KE109K</i>        | 90.94%      | 0.47% | <i>E135K+R149D</i>                           | 99.46%      | 0.90%  |
|  |             |       | <i>Vector+R134D</i>                          | 50.83%      | 6.36%  |

|   |         |       |   |         |        |
|---|---------|-------|---|---------|--------|
| <i>R25E H29E+Vector</i>                   | 28.27%  | 3.14% | <i>Vector+H118D</i>                                 | 34.58%  | 9.53%  |
| <i>Vector+E102K E109K</i>                 | 89.68%  | 2.17% | <i>D127K+R134D</i>                                  | 89.80%  | 4.61%  |
| <i>R25E H29E+<br/>E102K E109K</i>         | 97.41%  | 1.55% | <i>D127K+H118D</i>                                  | 89.50%  | 3.52%  |
| <i>R25E K36E+Vector</i>                   | 50.63%  | 6.44% | <i>D127K D131K+WT</i>                               | 50.24%  | 9.91%  |
| <i>Vector+E95K E109K</i>                  | 60.52%  | 4.69% | <i>D131K+Vector</i>                                 | 5.80%   | 5.10%  |
| <i>R25E K36E+<br/>E95K E109K</i>          | 96.86%  | 1.84% | <i>D131K+H118D</i>                                  | 90.52%  | 3.37%  |
| <i>Vector+<br/>E81R E85R E88R</i>         | 23.14%  | 3.00% | <i>D131K+R134D</i>                                  | 90.50%  | 3.97%  |
| <i>R25E H29E K36E+<br/>E81R E85R E88R</i> | 21.74%  | 5.10% | <i>D131K+R149D</i>                                  | 89.58%  | 2.45%  |
| <i>Vector+<br/>E85R E88R E95R</i>         | 32.94%  | 6.05% | <i>D127K+WT</i>                                     | 89.65%  | 8.02%  |
| <i>R25E H29E K36E+<br/>E85R E88R E95R</i> | 28.95%  | 5.30% | <i>D131K+WT</i>                                     | 94.85%  | 4.44%  |
| <i>K35C+F6C</i>                           | 99.70%  | 2.68% | <i>WT+H118D</i>                                     | 98.65%  | 4.87%  |
| <i>K35C+T20C</i>                          | 99.44%  | 0.77% | <i>WT+R134D</i>                                     | 99.24%  | 6.62%  |
| <i>K35C+R25C</i>                          | 99.88%  | 4.81% | <i>WT+R149D</i>                                     | 103.19% | 5.18%  |
| <i>K35C+H29C</i>                          | 101.53% | 1.46% | <i>Vector+<br/>H118D R134D R149D</i>                | 8.66%   | 7.39%  |
| <i>K35C+K35C</i>                          | 101.19% | 3.75% | <i>D127K D131K+Vector</i>                           | 8.08%   | 9.01%  |
| <i>K35C+S38C</i>                          | 101.90% | 0.90% | <i>D127K D131K+<br/>R134D R149D</i>                 | 26.34%  | 5.42%  |
| <i>K35C+Q43C</i>                          | 98.66%  | 2.34% | <i>D127K D131K+H118D R134D<br/>R149D</i>            | 32.75%  | 7.67%  |
| <i>K35C+A51C</i>                          | 102.58% | 1.24% | <i>WT+H118D R134D</i>                               | 96.19%  | 6.64%  |
| <i>K35C+R52C</i>                          | 97.11%  | 4.38% | <i>WT+R134D R149D</i>                               | 94.00%  | 3.57%  |
| <i>K35C+K57C</i>                          | 97.26%  | 4.26% | <i>WT+H118D R149D</i>                               | 90.53%  | 3.76%  |
| <i>K35C+G58C</i>                          | 102.51% | 0.36% | <i>WT+H118D R134D R149D</i>                         | 91.59%  | 4.92%  |
| <i>K35C+K60C</i>                          | 99.33%  | 3.35% | <i>WT+H118D D127K D131K<br/>R134D R149D</i>         | 93.76%  | 1.58%  |
| <i>K35C+A63C</i>                          | 103.23% | 0.91% | <i>E142K+Vector</i>                                 | 19.09%  | 5.06%  |
| <i>K35C+K69C</i>                          | 103.79% | 2.51% | <i>E142K+H118D</i>                                  | 86.75%  | 3.65%  |
| <i>K35C+Q75C</i>                          | 102.94% | 0.05% | <i>E142K+R134D</i>                                  | 88.74%  | 3.61%  |
| <i>K35C+E81C</i>                          | 101.13% | 1.56% | <i>E142K+R149D</i>                                  | 89.64%  | 1.94%  |
| <i>K35C+E88C</i>                          | 101.97% | 2.12% | <i>Vector+L121K</i>                                 | 24.87%  | 12.51% |
| <i>K35C+E95C</i>                          | 100.78% | 2.47% | <i>L121D+Vector</i>                                 | 18.84%  | 14.21% |
| <i>K35C+E102C</i>                         | 100.61% | 3.19% | <i>L121D+L121K</i>                                  | 82.47%  | 7.28%  |
| <i>Q75C+F6C</i>                           | 97.98%  | 0.92% | <b>Tandem fusion</b>                                |         |        |
| <i>Q75C+T20C</i>                          | 100.16% | 0.07% | <i>WT+snf7<sup>D127K</sup>-SNF7</i>                 | 85.54%  | 4.10%  |
| <i>Q75C+R25C</i>                          | 100.22% | 0.71% | <i>WT+snf7<sup>R134D</sup>-SNF7</i>                 | 98.47%  | 1.52%  |
| <i>Q75C+H29C</i>                          | 101.88% | 0.90% | <i>WT+SNF7-snft<sup>D127K</sup></i>                 | 93.18%  | 2.04%  |
| <i>Q75C+K35C</i>                          | 102.48% | 0.20% | <i>WT+snf7<sup>D127K</sup>-snf7<sup>D127K</sup></i> | 77.00%  | 2.06%  |
| <i>Q75C+S38C</i>                          | 98.36%  | 0.16% | <i>WT+snf7<sup>D127K</sup>-snf7<sup>R134D</sup></i> | 92.90%  | 0.76%  |
| <i>Q75C+Q43C</i>                          | 98.38%  | 0.05% | <i>WT+VPS20-SNF7</i>                                | 76.22%  | 4.48%  |
| <i>Q75C+A51C</i>                          | 99.08%  | 0.30% | <i>WT+SNF7-VPS20</i>                                | 94.17%  | 1.57%  |
| <i>Q75C+R52C</i>                          | 104.17% | 1.94% |   |         |        |

|            |         |       |  |  |  |
|------------|---------|-------|--|--|--|
| Q75C+K57C  | 101.77% | 0.89% |  |  |  |
| Q75C+G58C  | 101.35% | 0.99% |  |  |  |
| Q75C+K60C  | 97.23%  | 0.66% |  |  |  |
| Q75C+A63C  | 101.61% | 1.98% |  |  |  |
| Q75C+K69C  | 101.67% | 0.23% |  |  |  |
| Q75C+Q75C  | 100.62% | 0.88% |  |  |  |
| Q75C+E81C  | 101.56% | 1.07% |  |  |  |
| Q75C+E88C  | 101.39% | 1.00% |  |  |  |
| Q75C+E95C  | 100.47% | 1.92% |  |  |  |
| Q75C+E102C | 100.97% | 0.76% |  |  |  |
|            |         |       |  |  |  |
|            |         |       |  |  |  |
|            |         |       |  |  |  |

Notes:

- 1) “\*\*” representing data provided by Nicholas J. Buchkovich
- 2)  $3mut = snf7^{T20D\ I30K\ N31D}$
- 3)  $5mut = snf7^{T20D\ V24L\ K27R\ I30K\ N31D}$
- 4)  $7mut = snf7^{T20D\ V24L\ K27R\ I30K\ N31D\ L33I\ S34H}$
- 5)  $RM\#3 = snf7^{Q90L}$
- 6)  $RM\#7 = snf7^{F54L\ N100I\ N212I}$
- 7)  $RM\#9 = snf7^{7mut\ I44V\ Q90L}$
- 8)  $RM\#13 = snf7^{7mut\ N59D\ Q90L}$
- 9)  $myr = N(Vps20)$

**Table A4.2 Summary of Mup1-pHluorin MVB Sorting in *vps20Δ* Yeast**

| Mutants expressed in <i>vps20Δ</i> | MVB Sorting | STD    | Mutants expressed in <i>vps20Δ</i>                    | MVB Sorting | STD    |
|------------------------------------|-------------|--------|---|-------------|--------|
| Vector                             | 0.00%       | 4.81%  | <b>α5</b>   |             |        |
| <i>VPS20</i>                       | 100.00%     | 1.06%  | <i>L162E</i> *  | 94.8%       | 3.6%   |
|                                    |             |        | <i>N170H</i> *  | 102.7%      | 0.4%   |
| <b>α1</b>                          |             |        | <b>Snf7 mutants</b>                                   |             |        |
| <i>G2A</i> *                       | 84.5%       | 2.8%   | <i>SNF7</i>   | 4.28%       | 7.22%  |
| <i>ΔN</i> *                        | 70.9%       | 5.1%   | <i>snf7</i> <sup>I30K N31Q</sup> *                    | -9.3%       | 4.9%   |
| <i>N(Snf7)</i> *                   | 96.7%       | 1.4%   | <i>snf7</i> <sup>T20E I30K N30Q</sup> *               | -2.2%       | 14.7%  |
| <i>R15E</i> *                      | 98.9%       | 2.8%   | <i>snf7</i> <sup>5mut</sup> *                         | 2.1%        | 1.4%   |
| <i>R15E K29E</i> *                 | 90.4%       | 5.8%   | <i>snf7</i> <sup>5mut Q90L</sup> *                    | 14.0%       | 8.9%   |
| <i>K29E</i> *                      | 94.2%       | 1.5%   | <i>snf7</i> <sup>7mut</sup> *                         | 0.0%        | 4.8%   |
| <i>K29E L116W</i> *                | 91.3%       | 3.2%   | <i>snf7</i> <sup>RM#7</sup> *                         | 31.7%       | 10.2%  |
| <i>R32E</i> *                      | 95.3%       | 0.5%   | <i>snf7</i> <sup>RM#9</sup> *                         | 33.6%       | 7.4%   |
| <i>R33E</i> *                      | 99.0%       | 0.6%   | <i>snf7</i> <sup>RM#13</sup> *                        | 43.6%       | 6.4%   |
| <i>R32E R33E</i> *                 | 91.9%       | 3.3%   | <i>myrsnf7</i>  | 3.44%       | 10.50% |
| <i>K42E</i> *                      | 99.6%       | 0.2%   | <i>snf7</i> <sup>R52E</sup>                           | 5.86%       | 4.49%  |
| <i>L45E</i> *                      | 42.5%       | 6.3%   | <i>snf7</i> <sup>Q90L</sup>                           | 20.43%      | 3.07%  |
| <i>K46E</i> *                      | 101.3%      | 0.3%   | <i>snf7</i> <sup>N100I</sup>                          | 29.89%      | 0.65%  |
| <i>R50E</i> *                      | 101.5%      | 0.8%   | <i>snf7</i> <sup>R52E Q90L</sup>                      | 13.09%      | 6.40%  |
| <i>K51E</i> *                      | 102.4%      | 1.2%   | <i>snf7</i> <sup>R52E Q90L N100I</sup>                | 12.26%      | 10.51% |
| <i>R50E K51E</i> *                 | 101.8%      | 1.9%   | <i>myrsnf7</i> <sup>R52E Q90L</sup>                   | 42.69%      | 10.87% |
| <i>K29E R50E</i> *                 | 99.2%       | 1.8%   | <i>myrsnf7</i> <sup>R52E Q90L N100I</sup>             | 53.65%      | 10.38% |
| <b>α2</b>                          |             |        | <i>myrsnf7</i> <sup>Q90L N100I</sup>                  | 54.16%      | 15.61% |
| <i>K57E</i> *                      | 95.7%       | 2.9%   | <i>snf7</i> <sup>RM#9 R52E</sup>                      | 19.33%      | 11.00% |
| <i>N59E V62E</i>                   | 66.59%      | 2.78%  | <i>snf7</i> <sup>RM#9 R52E N100I</sup>                | 13.25%      | 1.72%  |
| <i>K61E</i> *                      | 100.6%      | 0.7%   | <i>myrsnf7</i> <sup>RM#9 R52E</sup>                   | 13.28%      | 10.90% |
| <i>V62E L65D</i>                   | 3.13%       | 7.72%  | <i>myrsnf7</i> <sup>RM#9 R52E N100I</sup>             | 21.15%      | 8.97%  |
| <i>L66E</i>                        | 92.31%      | 4.15%  | <i>myrsnf7</i> <sup>RM#9</sup>                        | 8.70%       | 8.69%  |
| <i>L66E M127E</i>                  | 69.03%      | 12.06% | <i>snf7</i> <sup>7mut R52E</sup>                      | 16.84%      | 3.19%  |
| <i>K67E</i> *                      | 97.6%       | 0.1%   | <i>myrsnf7</i> <sup>7mut R52E</sup>                   | 6.08%       | 3.84%  |
| <i>R68E</i> *                      | 97.2%       | 1.8%   | <i>myrsnf7</i> <sup>R52E Q90L N100I L231K L234K</sup> | 8.94%       | 2.57%  |
| <i>K67R R68E</i> *                 | 75.9%       | 6.9%   | <i>myrsnf7</i> <sup>R52E Q90L N100I L234K</sup>       | 20.34%      | 4.68%  |
| <i>L76E</i> *                      | 92.7%       | 7.2%   | <i>snf7</i> <sup>L234K</sup>                          | 7.99%       | 7.49%  |
| <i>S80W I84K</i>                   | 99.02%      | 2.31%  | <i>snf7</i> <sup>L231K L234K</sup>                    | 20.42%      | 6.19%  |
| <i>L86E</i>                        | 94.80%      | 2.85%  |   |             |        |
| <i>L86E L93E</i>                   | 7.17%       | 6.59%  |   |             |        |
| <i>L86E I103E</i>                  | 85.83%      | 11.37% |   |             |        |
| <i>E87R E94R</i>                   | 13.03%      | 4.18%  |   |             |        |
|                                    |             |        | <b>Tandem fusion</b>                                  |             |        |
|                                    |             |        | <i>VPS25-SNF7</i>                                     | 21.62%      | 4.62%  |
|                                    |             |        | <i>VPS20-SNF7</i>                                     | 67.61%      | 5.91%  |

|  |                    |            |  |                    |            |
|--|--------------------|------------|--|--------------------|------------|
| <i>M89K</i>                                  | 97.19%             | 1.05%      | <i>VPS20-snf7<sup>D127K</sup></i>                  | 39.65%             | 2.92%      |
| <i>M89L</i> *                                | 101.4%             | 0.3%       | <i>VPS20-snf7<sup>1-210</sup></i>                  | 20.10%             | 9.36%      |
| <i>M89Q</i> *                                | 93.0%              | 13.1%      | <i>VPS20-snf7<sup>1-230</sup></i>                  | 2.73%              | 5.03%      |
| <i>M89C</i>                                  | 98.91%             | 1.70%      | <i>VPS20-VPS20</i> *                               | 100.5%             | 1.4%       |
| <i>M89C M127C</i>                            | 100.43%            | 1.50%      | <i>vps20<sup>core</sup>-SNF7</i> *                 | 25.9%              | 3.9%       |
| <i>L93E</i>                                  | 95.83%             | 2.86%      | <i>SNF7-VPS20</i> *                                | 18.9%              | 5.6%       |
| <i>L93E/I103E</i>                            | 22.99%             | 16.63%     | <i>snf7<sup>RM#7</sup>-SNF7</i> *                  | 12.6%              | 5.1%       |
| <i>E94K</i>                                  | 99.44%             | 1.24%      | <i>snf7<sup>RM#9</sup>-SNF7</i> *                  | 18.8%              | 8.9%       |
| <i>E94K Q101K</i>                            | 94.90%             | 0.73%      |  |                    |            |
| <i>E94K N108K</i>                            | 98.15%             | 2.36%      |  |                    |            |
| <i>E94K Q101K N108K</i>                      | 98.81%             | 1.06%      |  |                    |            |
|  |                    |            |  |                    |            |
| <b>α3</b>                                    |                    |            |  |                    |            |
| <i>Q101K</i>                                 | 101.75%            | 0.72%      | <b>Vps20-Snf7 Chimera</b>                          |                    |            |
| <i>Q101K N108K</i>                           | 99.77%             | 0.66%      | <i>vps20<sup>197-211</sup>snf7</i> *               | 100.6%             | 2.0%       |
| <i>I103E</i>                                 | 101.62%            | 1.31%      | <i>vps20<sup>172-181</sup>snf7</i> *               | 101.4%             | 0.5%       |
| <i>G105W</i> *                               | 98.6%              | 3.0%       | <i>vps20<sup>147-151</sup>snf7</i> *               | 98.5%              | 7.1%       |
| <i>L106E</i>                                 | 98.82%             | 1.02%      | <i>vps20<sup>118-120</sup>snf7</i>                 | 77.68%             | 2.90%      |
| <i>L106EL116E</i>                            | 20.58%             | 5.90%      | <i>vps20<sup>105-107</sup>snf7</i> *               | 68.4%              | 15.6%      |
| <i>L106EF120E</i>                            | 27.63%             | 7.77%      | <i>vps20<sup>107-150</sup>snf7</i> *               | 88.7%              | 1.7%       |
| <i>N108K</i>                                 | 102.12%            | 0.62%      | <i>vps20<sup>59-61</sup>snf7</i> *                 | -0.6%              | 10.9%      |
| <i>L113E</i>                                 | 88.48%             | 3.10%      | <i>vps20<sup>59-61</sup>snf7<sup>Q90L</sup></i>    | 15.02%             | 2.96%      |
| <i>L113E L116E</i>                           | 10.88%             | 12.82%     | <i>vps20<sup>52-60</sup>snf7</i> *                 | 95.7%              | 4.8%       |
| <i>L116W</i> *                               | 96.7%              | 0.9%       |  |                    |            |
| <i>L116E</i> *                               | 96.8%              | 0.8%       |  |                    |            |
| <i>N117D</i>                                 | 98.82%             | 0.81%      |  |                    |            |
|  |                    |            |  |                    |            |
| <b>α4</b>                                    |                    |            |  |                    |            |
| <i>F120E</i> *                               | 100.2%             | 2.1%       | <b>Truncation &amp; deletion</b>                   |                    |            |
| <i>D124K</i>                                 | 100.25%            | 2.06%      | <i>1-147</i> *                                     | 14.7%              | 6.2%       |
| <i>D128K</i>                                 | 99.80%             | 1.41%      | <i>1-172</i> *                                     | 20.3%              | 5.1%       |
| <i>D124K D128K</i>                           | 98.85%             | 2.28%      | <i>1-178</i> *                                     | 22.5%              | 3.8%       |
| <i>Q131D</i>                                 | 101.84%            | 0.61%      | <i>1-183</i> *                                     | -2.1%              | 12.2%      |
| <i>R146D</i>                                 | 102.00%            | 1.17%      | <i>1-200</i> *                                     | 16.6%              | 5.8%       |
| <i>E139K</i>                                 | 100.33%            | 1.18%      | <i>1-214</i> *                                     | 74.2%              | 13.9%      |
| <i>M127C</i>                                 | 100.84%            | 1.00%      | <i>1-172 H29N</i> *                                | 20.4%              | 3.2%       |
| <i>M127E</i>                                 | 98.47%             | 1.55%      | <i>1-183 H29N</i> *                                | 20.8%              | 7.2%       |
|  |                    |            | <i>Vps25 binding</i> *                             | 15.8%              | 2.1%       |
|  |                    |            | <i>148-154 7Ala</i> *                              | 102.6%             | 1.6%       |
|  |                    |            | <i>155-163 9Ala</i> *                              | 93.9%              | 5.5%       |
|  |                    |            | <i>164-172 9Ala</i> *                              | 97.3%              | 4.6%       |
|  |                    |            |  |                    |            |
|  |                    |            |  |                    |            |
|  |                    |            |  |                    |            |
| <b>Mutants co-expressed in <i>vps20Δ</i></b> | <b>MVB Sorting</b> | <b>STD</b> | <b>Others</b>                                      |                    |            |
| <i>Vector+Vector</i>                         | 0.00%              | 2.28%      | <i>CHM7</i> ( $2\mu$ )                             | 23.45%             | 8.88%      |
| <i>VPS20+Vector</i>                          | 100.00%            | 0.93%      | <i>CHMP6 (human)</i> *                             | 7.4%               | 6.3%       |
|  |                    |            |  |                    |            |
|  |                    |            |  |                    |            |
|  |                    |            |  |                    |            |
|  |                    |            | <b>Mutants co-expressed in <i>vps20Δ snf7Δ</i></b> | <b>MVB Sorting</b> | <b>STD</b> |
| <i>Vector+Vector</i>                         | 0.00%              | 4.97%      | <i>VPS20+SNF7</i>                                  | 100.00%            | 0.42%      |

|  |                        |            |   |        |        |
|--|------------------------|------------|---|--------|--------|
| <i>VPS20+HSE1-DUB</i>  | 7.37%                  | 8.40%      | <i>Vector+snf7<sup>R52E Q90L</sup></i>          | 6.89%  | 4.88%  |
| <i>myrsnf7<sup>R52E Q90L</sup>+</i><br><i>HSE1-DUB</i>                           | 8.23%                  | 0.42%      | <i>Vector+snf7<sup>R52E Q90L N100I</sup></i>    | 24.17% | 10.22% |
| <i>myrsnf7<sup>R52E Q90L N100I</sup>+</i><br><i>HSE1-DUB</i>                     | 3.29%                  | 6.85%      | <i>VPS20+Vector</i>                             | 2.06%  | 6.35%  |
| <i>vps20<sup>E94K Q101K N108K</sup>+</i><br><i>Vector</i>                        | 88.49%                 | 3.02%      | <i>Vector+SNF7</i>                              | 5.57%  | 14.45% |
| <i>Vector+snf7<sup>R25E H29E K36E</sup></i>                                      | 0.25%                  | 1.19%      | <i>Vector+myrsnf7<sup>R52E Q90L</sup></i>       | 41.26% | 2.90%  |
| <i>vps20<sup>E94K Q101K N108K</sup>+</i><br><i>snf7<sup>R25E H29E K36E</sup></i> | 89.17%                 | 3.13%      | <i>Vector+myrsnf7<sup>R52E Q90L N100I</sup></i> | 40.75% | 6.79%  |
| <i>vps20<sup>E87R E94R</sup>+</i><br><i>Vector</i>                               | 0.20%                  | 3.14%      | <i>Vector+snf7<sup>RM#3 *</sup></i>             | 0.83%  | 5.20%  |
| <i>vps20<sup>E87R E94R</sup>+</i><br><i>snf7<sup>R25E H29E K36E</sup></i>        | -12.30%                | 13.32%     | <i>Vector+snf7<sup>RM#7 *</sup></i>             | 34.68% | 6.08%  |
| <b>Mutants co-expressed<br/>in <i>vps20Δ chm7Δ</i></b>                           | <b>MVB<br/>Sorting</b> | <b>STD</b> | <i>Vector+snf7<sup>RM#9 *</sup></i>             | 10.13% | 7.22%  |
| <i>Vector+Vector</i>   | 0.00%                  | 1.57%      | <i>Vector+snf7<sup>RM#13 *</sup></i>            | 4.10%  | 23.30% |
| <i>VPS20+CHM7</i>  | 100.00%                | 0.87%      | <i>Vector+VPS20-SNF7 *</i>                      | 12.90% | 5.52%  |
| <i>VPS20+Vector</i>  | 101.91%                | 1.88%      | <i>Vector+SNF7-VPS20 *</i>                      | 0.34%  | 6.63%  |
| <i>Vector+CHM7</i>   | 4.71%                  | 3.29%      | <i>Vector+snf7<sup>RM#7</sup>-SNF7 *</i>        | 10.59% | 9.76%  |
| <i>VPS20+myrsnf7<sup>R52E Q90L N100I</sup></i>                                   | 105.40%                | 2.05%      | <i>Vector+snf7<sup>RM#9</sup>-SNF7 *</i>        | 20.25% | 1.57%  |
| <i>myrsnf7<sup>R52E Q90L N100I</sup>+</i><br><i>CHM7</i>                         | 60.27%                 | 10.15%     |   |        |        |
| <i>myrsnf7<sup>R52E Q90L N100I</sup>+</i><br><i>Vector</i>                       | 60.69%                 | 15.10%     |   |        |        |
| <i>SNF7+Vector</i>   | 3.04%                  | 9.75%      |   |        |        |

Notes:

- 1) “\*” representing data provided by Nicholas J. Buchkovich
- 2) *3mut = snf7<sup>T20D I30K N31D</sup>*
- 3) *5mut = snf7<sup>T20D V24L K27R I30K N31D</sup>*
- 4) *7mut = snf7<sup>T20D V24L K27R I30K N31D L33I S34H</sup>*
- 5) *RM#3 = snf7<sup>Q90L</sup>*
- 6) *RM#7 = snf7<sup>F54L N100I N212I</sup>*
- 7) *RM#9 = snf7<sup>7mut I44V Q90L</sup>*
- 8) *RM#13 = snf7<sup>7mut N59D Q90L</sup>*
- 9) *myr = N(Vps20)*

**Table A4.3 Summary of Mup1-pHluorin MVB Sorting in *vps24Δ* Yeast**

| Mutants expressed in<br><i>vps24Δ</i> | MVB<br>Sorting | STD    | Mutants expressed in<br><i>vps24Δ</i>             | MVB<br>Sorting | STD    |
|---------------------------------------|----------------|--------|---|----------------|--------|
| Vector                                | 0.00%          | 2.63%  | <b><i>vps24</i> Random<br/>Mutagenesis Screen</b> |                |        |
| VPS24                                 | 100.00%        | 0.42%  | K26E  | 100.10%        | 7.99%  |
|                                       |                |        | T60A  | 102.87%        | 2.41%  |
| <b>α0</b>                             |                |        | E143G   | 103.55%        | 3.92%  |
| ΔN *                                  | 24.91%         | 17.07% | K137R   | 99.32%         | 3.92%  |
| N(Snf7) *                             | 98.8%          | 4.4%   | D160G   | 100.49%        | 1.05%  |
| N(Vps2) *                             | -2.1%          | 22.0%  | D107N   | 98.92%         | 1.22%  |
| I4E *                                 | 55.2%          | 8.0%   | K205E   | 99.79%         | 1.21%  |
| K5E K6E *                             | 81.9%          | 10.0%  | I141V   | 96.36%         | 4.88%  |
|                                       |                |        | Y69F  | 97.76%         | 0.73%  |
| <b>α1</b>                             |                |        | f3  | 98.62%         | 1.69%  |
| Q16E                                  | 103.12%        | 0.89%  | g1  | 103.41%        | 2.53%  |
| Q17E                                  | 100.73%        | 1.46%  | g3  | 100.91%        | 1.21%  |
| Q16E Q17E                             | 50.80%         | 17.75% | g9  | 105.15%        | 0.90%  |
| Q16E Q17E R17E R18E                   | 7.74%          | 11.91% | h1  | 101.52%        | 1.73%  |
| R25E R26E *                           | 78.7%          | 1.5%   | h2  | 101.15%        | 0.69%  |
| R25E K26E K50E *                      | 8.4%           | 3.0%   | h7  | 104.37%        | 2.89%  |
| R25E K26E K54E K55E *                 | 13.3%          | 2.2%   | i3  | 104.00%        | 1.64%  |
| K50E *                                | 55.2%          | 2.1%   | f5  | 101.13%        | 3.45%  |
| K54E K55E *                           | 98.0%          | 2.3%   | f10   | 101.07%        | 2.94%  |
|                                       |                |        | f16   | 100.95%        | 2.42%  |
| <b>α2</b>                             |                |        | g10   | 6.41%          | 12.95% |
| L85E                                  | 86.32%         | 8.83%  | g12   | 102.29%        | 0.92%  |
| V88K                                  | 98.30%         | 5.77%  | g14   | 99.81%         | 2.20%  |
| I92E                                  | 75.63%         | 3.71%  | i9  | 96.88%         | 3.34%  |
| D93K                                  | 99.77%         | 1.40%  | j6  | 100.62%        | 2.17%  |
| D93K T100K                            | 100.92%        | 0.70%  | j10   | 101.60%        | 0.33%  |
| D93K D107K                            | 101.09%        | 1.55%  | j7  | 83.45%         | 5.14%  |
| D93K T100K D107K                      | 102.99%        | 2.61%  | j8  | 95.88%         | 1.31%  |
|                                       |                |        | j9  | 3.25%          | 12.24% |
| <b>α3</b>                             |                |        | j12   | 102.29%        | 1.49%  |
| T100K                                 | 99.70%         | 2.29%  | k1  | 11.77%         | 12.06% |
| T100K D107K                           | 101.94%        | 0.79%  | k3  | 95.18%         | 2.01%  |
| M105E                                 | 67.72%         | 7.90%  | k5  | 102.25%        | 6.22%  |
| D107K                                 | 100.03%        | 0.34%  | k9  | 94.36%         | 5.59%  |
| M112E                                 | 57.70%         | 11.72% | k10   | 101.39%        | 2.33%  |
| V115E                                 | 93.17%         | 3.66%  |   |                |        |

|   |                        |            | <b>Mutants expressed in<br/><i>snf7</i><sup>D131K</sup> <i>vps24Δ</i></b> | <b>MVB<br/>Sorting</b> | <b>STD</b> |
|---|------------------------|------------|---|------------------------|------------|
| <i>N116R</i>  | 74.67%                 | 8.67%      |   |                        |            |
| <i>V119E</i>  | 102.72%                | 2.54%      |   |                        |            |
| <i>R120E</i>  | 63.05%                 | 14.68%     |   |                        |            |
| <b>α4</b>   |                        |            |   |                        |            |
| <i>R125D</i>  | 100.05%                | 3.46%      |   |                        |            |
| <i>I129D</i>  | 102.58%                | 0.65%      |   |                        |            |
| <i>E132R</i>  | 105.64%                | 1.64%      |   |                        |            |
| <i>I140D</i>  | 102.29%                | 1.99%      |   |                        |            |
| <i>E143K</i>  | 35.13%                 | 4.51%      |   |                        |            |
| <i>D147R</i>  | 103.98%                | 0.53%      |   |                        |            |
| <b>Snf7 Mutants</b>   |                        |            |   |                        |            |
| <i>VPS20</i>  | 1.97%                  | 2.43%      |   |                        |            |
| <i>SNF7</i>   | 3.51%                  | 12.63%     |   |                        |            |
| <i>myrsnf7</i> <sup>R52E Q90L</sup>                           | 19.21%                 | 5.77%      |   |                        |            |
| <i>myrsnf7</i> <sup>R52E Q90L N100I</sup>                     | 25.40%                 | 5.00%      |   |                        |            |
| <b>Snf7-Vps24 Chimera</b>                                     |                        |            |   |                        |            |
| <i>vps24</i> <sup>147-151</sup> * <i>snf7</i> *               | 45.5%                  | 8.4%       |   |                        |            |
| <b>Mutants co-expressed in<br/><i>vps20Δ vps24Δ</i></b>       | <b>MVB<br/>Sorting</b> | <b>STD</b> |   |                        |            |
| <i>VPS24+Vector</i>   | 7.64%                  | 19.56%     |   |                        |            |
| <i>Vector+VPS20</i>   | 10.74%                 | 9.21%      |   |                        |            |
| <i>Vector+SNF7</i>  | 5.92%                  | 10.06%     |   |                        |            |
| <i>Vector+myrsnf7</i> <sup>R52E Q90L</sup>                    | 19.25%                 | 2.93%      |   |                        |            |
| <i>Vector+myrsnf7</i> <sup>R52E Q90L N100I</sup>              | 18.59%                 | 13.28%     |   |                        |            |
| <b>Mutants co-expressed in<br/><i>snf7Δ vps24Δ</i></b>        | <b>MVB<br/>Sorting</b> | <b>STD</b> |   |                        |            |
| <i>Vector+Vector</i>  | 0.00%                  | 3.23%      |   |                        |            |
| <i>VPS24+SNF7</i>   | 100.00%                | 1.32%      |   |                        |            |
| <i>VPS24+snf7</i> <sup>D131K</sup>                            | 19.65%                 | 3.88%      |   |                        |            |
| <i>vps24</i> <sup>K26E</sup> + <i>snf7</i> <sup>D131K</sup>   | 7.71%                  | 6.03%      |   |                        |            |
| <i>vps24</i> <sup>T60A</sup> + <i>snf7</i> <sup>D131K</sup>   | 47.21%                 | 25.64%     |   |                        |            |
| <i>vps24</i> <sup>E143G</sup> + <i>snf7</i> <sup>D131K</sup>  | 35.50%                 | 8.10%      |   |                        |            |
| <i>vps24</i> <sup>WT</sup> (c3)+ <i>snf7</i> <sup>D131K</sup> | 19.17%                 | 7.26%      |   |                        |            |
| <i>vps24</i> <sup>K137R</sup> + <i>snf7</i> <sup>D131K</sup>  | 19.80%                 | 4.82%      |   |                        |            |
| <i>vps24</i> <sup>D160G</sup> + <i>snf7</i> <sup>D131K</sup>  | 33.12%                 | 17.58%     |   |                        |            |
| <i>vps24</i> <sup>D107N</sup> + <i>snf7</i> <sup>D131K</sup>  | 32.47%                 | 9.70%      |   |                        |            |

|  |        |        |
|--|--------|--------|
| <i>vps24</i> <sup>K205E</sup> + <i>snf7</i> <sup>D131K</sup>           | 6.74%  | 10.39% |
| <i>vps24</i> <sup>I141V</sup> + <i>snf7</i> <sup>D131K</sup>           | 40.94% | 11.05% |
| <i>vps24</i> <sup>Y69F</sup> + <i>snf7</i> <sup>D131K</sup>            | 16.62% | 11.48% |
| <i>vps24</i> <sup>R25E K26E</sup> + <i>SNF7</i>                        | 30.76% | 22.65% |
| <i>vps24</i> <sup>R25E K26E</sup> + <i>snf7</i> <sup>D131K</sup>       | 16.40% | 6.52%  |
| <i>vps24</i> <sup>R25E K26E</sup> + <i>snf7</i> <sup>D127K D131K</sup> | 14.94% | 4.54%  |

Notes:

- 1) “\*\*” representing data provided by Nicholas J. Buchkovich
- 2) Mutants for the *vps24* Random Mutagenesis are listed in Figure A1.5.

**Table A4.4 Summary of Mup1-pHluorin MVB Sorting in *vps2Δ* Yeast**

| Mutants expressed in <i>vps2Δ</i>  | MVB Sorting | STD    | Mutants expressed in <i>vps20Δ vps2Δ</i>  | MVB Sorting | STD    |
|------------------------------------|-------------|--------|---|-------------|--------|
| Vector                             | 0.00%       | 3.07%  | Vector+Vector                             | 0.00%       | 4.38%  |
| VPS2                               | 100.00%     | 0.82%  | VPS2+VPS20                                | 100.00%     | 1.56%  |
|                                    |             |        | VPS2+Vector                               | 11.92%      | 10.18% |
| <b>α0</b>                          |             |        | Vector+VPS20                              | 11.69%      | 6.42%  |
| ΔN *                               | 73.7%       | 8.3%   | Vector+SNF7                               | 10.61%      | 5.49%  |
| N(Snf7) *                          | 99.0%       | 4.5%   | Vector+myrsnf7 <sup>R52E Q90L</sup>       | 16.99%      | 3.82%  |
| N(Vps24) *                         | -32.9%      | 5.8%   | Vector+myrsnf7 <sup>R52E Q90L N100I</sup> | 12.32%      | 7.59%  |
| F4E *                              | 69.2%       | 5.4%   |   |             |        |
|                                    |             |        |   |             |        |
| <b>α1</b>                          |             |        |   |             |        |
| R27E *                             | 85.2%       | 8.3%   |   |             |        |
| K51E *                             | 89.2%       | 11.0%  |   |             |        |
| K51E K52E *                        | 74.2%       | 9.8%   |   |             |        |
| R27E K30E *                        | 3.45%       | 3.8%   |   |             |        |
| R37E K30E K51E *                   | 4.9%        | 5.6%   |   |             |        |
| R37E K30E K51E K52E *              | 7.7%        | 10.1%  |   |             |        |
|                                    |             |        |   |             |        |
| <b>α3</b>                          |             |        |   |             |        |
| N117R                              | 96.28%      | 5.72%  |   |             |        |
|                                    |             |        |   |             |        |
| <b>α4</b>                          |             |        |   |             |        |
| Q126D                              | 91.57%      | 9.26%  |   |             |        |
| M130D                              | 96.53%      | 7.30%  |   |             |        |
| E133R                              | 97.42%      | 4.86%  |   |             |        |
| Q141D                              | 96.24%      | 6.67%  |   |             |        |
| E148R                              | 105.20%     | 0.53%  |   |             |        |
|                                    |             |        |   |             |        |
| <b>Snf7 Mutant</b>                 |             |        |   |             |        |
| VPS20                              | 2.58%       | 8.51%  |   |             |        |
| SNF7                               | 5.47%       | 14.92% |   |             |        |
| myrsnf7 <sup>R52E Q90L</sup>       | 13.16%      | 13.58% |   |             |        |
| myrsnf7 <sup>R52E Q90L N100I</sup> | 5.27%       | 10.90% |   |             |        |
|                                    |             |        |   |             |        |
| <b>Vps2-Snf7 chimera</b>           |             |        |   |             |        |
| vps2 <sup>148-151</sup> snf7 *     | 7.9%        | 4.8%   |   |             |        |

Notes: “\*” representing data provided by Nicholas J. Buchkovich

**Table A4.5 Summary of Mup1-pHluorin MVB Sorting in *vps4Δ* Yeast**

| Mutants expressed in<br><i>vps4Δ</i>     | MVB<br>Sorting | STD   | Mutants expressed in<br><i>vps4Δ vps20Δ</i>      | MVB<br>Sorting | STD    |
|--|----------------|-------|--|----------------|--------|
| Vector                                   | 0.00%          | 7.21% | Vector+Vector                                    | 0.00%          | 3.56%  |
| VPS4                                     | 100.00%        | 0.59% | VPS4+VPS20                                       | 100.00%        | 2.34%  |
| VPS20                                    | 1.19%          | 7.56% | VPS4+Vector                                      | 4.52%          | 10.82% |
| SNF7                                     | 5.44%          | 7.15% | Vector+VPS20                                     | 6.21%          | 12.54% |
| <i>myrsnf7<sup>R52E Q90L</sup></i>       | 10.02%         | 7.66% | Vector+SNF7                                      | 1.97%          | 11.55% |
| <i>myrsnf7<sup>R52E Q90L N100I</sup></i> | 12.54%         | 1.56% | Vector+ <i>myrsnf7<sup>R52E Q90L</sup></i>       | 7.81%          | 7.94%  |
|  |                |       | Vector+ <i>myrsnf7<sup>R52E Q90L N100I</sup></i> | 8.57%          | 5.07%  |

**Table A4.6 Summary of Mup1-pHluorin MVB Sorting in *escrt-iΔ* Yeast**

| Mutants expressed in <i>vps36Δ</i>                    | MVB Sorting | STD    | Mutants co-expressed in <i>vps36Δ vps20Δ</i>                                      | MVB Sorting | STD    |
|---|-------------|--------|---|-------------|--------|
| Vector  | 0.00%       | 1.26%  | Vector+Vector   | 0.00%       | 2.91%  |
| VPS36-MYC   | 100.00%     | 1.28%  | VPS20+VPS36-MYC   | 100.00%     | 2.17%  |
| D548R-MYC   | 34.35%      | 9.59%  | Vector+VPS36-MYC  | 17.23%      | 0.27%  |
| VPS20   | 2.74%       | 4.81%  | VPS20+Vector  | 11.49%      | 3.33%  |
| SNF7  | 20.52%      | 1.38%  | Vector+SNF7   | 5.61%       | 6.43%  |
| <i>myrsnf7</i> <sup>R52E Q90L</sup>                   | 57.27%      | 5.09%  | Vector+ <i>myrsnf7</i> <sup>R52E Q90L</sup>                                       | 57.40%      | 13.64% |
| <i>myrsnf7</i> <sup>R52E Q90L N100I</sup>             | 69.42%      | 3.67%  | Vector+ <i>myrsnf7</i> <sup>R52E Q90L N100I</sup>                                 | 69.51%      | 5.60%  |
|   |             |        | <i>myrsnf7</i> <sup>R52E Q90L</sup> +<br><i>vps36</i> <sup>D548R</sup> -MYC       | 48.50%      | 11.43% |
|   |             |        | <i>myrsnf7</i> <sup>R52E Q90L N100I</sup> +<br><i>vps36</i> <sup>D548R</sup> -MYC | 60.65%      | 14.44% |
|   |             |        | VPS20+ <i>vps36</i> <sup>D548R</sup> -MYC   | 72.79%      | 7.09%  |
| Mutants expressed in <i>vps22Δ</i>                    | MVB Sorting | STD    | Mutants co-expressed in <i>vps22Δ vps20Δ</i>                                      | MVB Sorting | STD    |
| Vector  | 0.00%       | 5.38%  | Vector+Vector   | 0.00%       | 3.14%  |
| VPS22-HA  | 100.00%     | 0.61%  | Vps20+Vps22-HA  | 100.00%     | 2.50%  |
| D214A-HA  | 18.99%      | 3.04%  | Vector+Vps22-HA   | 14.08%      | 7.65%  |
| VPS20   | 22.85%      | 2.72%  | Vps20+Vector  | 9.28%       | 9.81%  |
| SNF7  | 8.67%       | 6.42%  | Vector+Snf7   | 1.74%       | 3.96%  |
| <i>myrsnf7</i> <sup>R52E Q90L</sup>                   | 56.66%      | 11.38% | Vector+MyrSnf7R52EQ90L  | 53.32%      | 15.58% |
| <i>myrsnf7</i> <sup>R52E Q90L N100I</sup>             | 80.65%      | 2.20%  | Vector+MyrSnf7R52EQ90LN100I   | 63.23%      | 22.61% |
|   |             |        | <i>myrSnf7R52E</i><br><i>Q90L</i> + <i>Vps22D214A-HA</i>                          | 49.20%      | 11.65% |
|   |             |        | <i>myrSnf7R52E</i><br><i>Q90L N100I</i> + <i>Vps22D214A-HA</i>                    | 78.76%      | 6.40%  |
|   |             |        | Vps20+Vps22D214A-HA   | 14.02%      | 13.37% |
| Mutants expressed in <i>vps25Δ</i>                    | MVB Sorting | STD    | Mutants co-expressed in <i>vps25Δ vps20Δ</i>                                      | MVB Sorting | STD    |
| Vector  | 0.00%       | 5.20%  | Vector+Vector   | 0.00%       | 9.90%  |
| VPS25   | 100.00%     | 1.63%  | VPS20+VPS25-FLAG  | 100.00%     | 2.02%  |
| VPS25-FLAG  | 100.00%     | 2.13%  | Vector+VPS25-FLAG   | 17.27%      | 9.02%  |
| R83D-FLAG   | 7.16%       | 3.17%  | VPS20+Vector  | 13.74%      | 3.69%  |
| V148E   | 19.50%      | 8.49%  | Vector+SNF7   | 9.22%       | 7.68%  |
| T150K   | 20.70%      | 6.49%  | Vector+ <i>myrsnf7</i> <sup>R52E Q90L</sup>                                       | 53.10%      | 10.34% |
| VPS25-SNF7  | 66.99%      | 10.93% | Vector+ <i>myrsnf7</i> <sup>R52E Q90L N100I</sup>                                 | 63.05%      | 12.10% |
| <i>vps25</i> <sup>V148E</sup> -SNF7                   | 4.15%       | 3.71%  | Vector+VPS25-SNF7   | 25.07%      | 8.96%  |
| <i>vps25</i> <sup>T150K</sup> -SNF7                   | 8.38%       | 6.80%  | VPS25+VPS25-SNF7  | 29.05%      | 2.96%  |
| <i>vps25</i> <sup>R83D</sup> -SNF7                    | 15.98%      | 5.18%  | VPS20+VPS25-SNF7  | 62.41%      | 14.45% |
| <i>vps25</i> -snf7 <sup>Q90L</sup>                    | 59.82%      | 23.19% |   |             |        |
| VPS20   | 16.88%      | 9.60%  |   |             |        |
| SNF7  | 17.48%      | 10.06% |   |             |        |
| <i>myrsnf7</i> <sup>R52E Q90L</sup>                   | 61.64%      | 4.47%  |   |             |        |
| <i>myrsnf7</i> <sup>R52E Q90L N100I</sup>             | 71.64%      | 20.71% |   |             |        |
| <i>myrsnf7</i> <sup>R52E Q90L N100I L231K L234K</sup> | 2.93%       | 3.35%  |   |             |        |

|  |                    |            |   |                    |            |
|--|--------------------|------------|---|--------------------|------------|
| <i>snf7</i> <sup>L231KL234K</sup>                              | -2.74%             | 8.00%      | <i>Vector+vps25</i> <sup>V148E</sup> -SNF7  | 14.82%             | 5.49%      |
|  |                    |            | <i>VPS20+vps25</i> <sup>V148E</sup> -SNF7   | 23.31%             | 12.73%     |
| <b>Mutants co-expressed in <i>vps25Δ</i></b>                   | <b>MVB Sorting</b> | <b>STD</b> | <i>VPS25+vps25</i> <sup>V148E</sup> -SNF7   | 15.74%             | 11.59%     |
| <i>Vector+Vector</i>   | 0.00%              | 5.76%      | <i>Vector+vps25</i> <sup>T150K</sup> -SNF7  | 27.52%             | 6.47%      |
| <i>VPS25+Vector</i>  | 100.00%            | 2.22%      | <i>VPS20+vps25</i> <sup>T150K</sup> -SNF7   | 30.55%             | 7.15%      |
| <i>VPS25+HSE1-DUB</i>  | 4.05%              | 5.59%      | <i>VPS25+vps25</i> <sup>T150K</sup> -SNF7   | 18.73%             | 6.29%      |
| <i>myrsnf7</i> <sup>R52E Q90L</sup> +<br><i>HSE1-DUB</i>       | 1.63%              | 6.20%      | <i>Vector+vps25</i> <sup>R83D</sup> -SNF7   | 9.54%              | 8.55%      |
| <i>myrsnf7</i> <sup>R52E Q90L N100I</sup> +<br><i>HSE1-DUB</i> | 10.01%             | 1.38%      | <i>VPS25+vps25</i> <sup>R83D</sup> -SNF7  | 2.75%              | 10.64%     |
|  |                    |            | <i>VPS20+vps25</i> <sup>R83D</sup> -SNF7  | 15.40%             | 14.14%     |
| <b>Mutants co-expressed in <i>vps25Δ vps36Δ</i></b>            | <b>MVB Sorting</b> | <b>STD</b> | <i>myrsnf7</i> <sup>R52E Q90L</sup> +<br><i>vps25</i> <sup>R83D</sup> -FLAG       | 50.21%             | 15.42%     |
| <i>Vector+Vector</i>   | 0.00%              | 8.97%      | <i>myrsnf7</i> <sup>R52E Q90L N100I</sup> +<br><i>vps25</i> <sup>R83D</sup> -FLAG | 56.85%             | 3.13%      |
| <i>VPS25+VPS36-MYC</i>   | 100.00%            | 0.60%      | <i>VPS20+vps25</i> <sup>R83D</sup> -FLAG  | 16.68%             | 6.25%      |
| <i>VPS25+Vector</i>  | 3.21%              | 5.62%      |   |                    |            |
| <i>Vector+VPS36-MYC</i>  | 3.73%              | 3.93%      | <b>Mutants co-expressed in <i>vps25Δ chm7Δ</i></b>                                | <b>MVB Sorting</b> | <b>STD</b> |
| <i>Vector+VPS20</i>  | 2.95%              | 2.38%      | <i>Vector+Vector</i>  | 0.00%              | 10.46%     |
| <i>Vector+SNF7</i>   | 1.91%              | 4.83%      | <i>VPS25+CHM7</i>   | 100.00%            | 0.13%      |
| <i>Vector+myrsnf7</i> <sup>R52E Q90L</sup>                     | 52.19%             | 13.04%     | <i>VPS25+Vector</i>   | 101.60%            | 1.12%      |
| <i>Vector+myrsnf7</i> <sup>R52E Q90L N100I</sup>               | 68.31%             | 1.46%      | <i>Vector+CHM7</i>  | 0.15%              | 8.65%      |
|  |                    |            | <i>VPS25+myrsnf7</i> <sup>R52E Q90L N100I</sup>                                   | 103.07%            | 0.49%      |
|  |                    |            | <i>myrsnf7</i> <sup>R52E Q90L N100I</sup> +CHM7                                   | 66.54%             | 1.64%      |
|  |                    |            | <i>Vector+myrsnf7</i> <sup>R52E Q90L N100I</sup>                                  | 64.86%             | 13.79%     |
|  |                    |            | <i>SNF7+Vector</i>  | 14.21%             | 6.91%      |
|  |                    |            | <i>VPS20+Vector</i>   | 10.93%             | 11.73%     |

**Table A4.7 Summary of Mup1-pHluorin MVB Sorting in *escrt-iΔ* Yeast**

| Mutants expressed in <i>vps23Δ</i>                             | MVB Sorting        | STD        | Mutants co-expressed in <i>vps23Δ vps20Δ</i>        | MVB Sorting        | STD        |
|--|--------------------|------------|---|--------------------|------------|
| Vector   | 0.00%              | 4.29%      | Vector+Vector                                       | 0.00%              | 5.45%      |
| VPS23  | 100.00%            | 1.53%      | VPS23+VPS20   | 100.00%            | 2.95%      |
| VPS20  | 14.72%             | 3.06%      | VPS23+Vector  | 6.63%              | 9.69%      |
| SNF7   | 2.23%              | 15.31%     | Vector+VPS20  | 3.66%              | 6.68%      |
| <i>myrsnf7<sup>R52E Q90L</sup></i>                             | 82.98%             | 6.00%      | Vector+SNF7   | 20.50%             | 10.14%     |
| <i>myrsnf7<sup>R52E Q90L N100I</sup></i>                       | 96.05%             | 2.88%      | Vector+ <i>myrsnf7<sup>R52E Q90L</sup></i>          | 96.49%             | 3.58%      |
| <i>myrsnf7<sup>R52E Q90L N100I L231K</sup></i><br><i>L234K</i> | 12.86%             | 5.78%      | Vector+ <i>myrsnf7<sup>R52E Q90L N100I</sup></i>    | 89.93%             | 29.33%     |
| <i>snf7<sup>L231K L234K</sup></i>                              | 5.61%              | 5.71%      |   |                    |            |
| <i>ESCRT-II (2μ) *</i>   | 32.1%              | 6.8%       | <b>Mutants expressed in <i>vps28Δ vps20Δ</i></b>    | <b>MVB Sorting</b> | <b>STD</b> |
|  |                    |            | Vector+Vector                                       | 0.00%              | 6.21%      |
| <b>Mutants co-expressed in <i>vps23Δ</i></b>                   | <b>MVB Sorting</b> | <b>STD</b> | VPS20+VPS28   | 100.00%            | 3.22%      |
| Vector+Vector  | 0.00%              | 5.49%      | Vector+VPS28  | 3.68%              | 12.50%     |
| VPS23+Vector   | 100.00%            | 2.41%      | VPS20+Vector  | 9.93%              | 15.12%     |
| VPS23+HSE1-DUB   | 1.08%              | 4.46%      | Vector+SNF7   | 12.39%             | 22.47%     |
| <i>myrsnf7<sup>R52E Q90L</sup></i> +<br>HSE1-DUB               | 4.94%              | 7.10%      | Vector+ <i>myrsnf7<sup>R52E Q90L</sup></i>          | 78.20%             | 2.17%      |
| <i>myrsnf7<sup>R52E Q90L N100I</sup></i> +<br>HSE1-DUB         | 1.00%              | 7.42%      | Vector+ <i>myrsnf7<sup>R52E Q90L N100I</sup></i>    | 80.57%             | 5.82%      |
|  |                    |            |   |                    |            |
| <b>Mutants expressed in <i>vps28Δ</i></b>                      | <b>MVB Sorting</b> | <b>STD</b> | <b>Mutants expressed in <i>vps37Δ vps20Δ</i></b>    | <b>MVB Sorting</b> | <b>STD</b> |
| Vector   | 0.00%              | 6.37%      | Vector+Vector                                       | 0.00%              | 3.04%      |
| VPS28  | 100.00%            | 1.06%      | VPS37+VPS20   | 100.00%            | 3.10%      |
| VPS20  | 16.04%             | 8.60%      | VPS37+Vector  | 10.63%             | 9.42%      |
| SNF7   | 20.68%             | 7.54%      | Vector+VPS20  | 6.50%              | 4.99%      |
| <i>myrsnf7<sup>R52E Q90L</sup></i>                             | 88.34%             | 7.36%      | Vector+SNF7   | 16.39%             | 16.75%     |
| <i>myrsnf7<sup>R52E Q90L N100I</sup></i>                       | 93.10%             | 2.09%      | Vector+ <i>myrsnf7<sup>R52E Q90L</sup></i>          | 102.01%            | 1.37%      |
|  |                    |            | Vector+ <i>myrsnf7<sup>R52E Q90L N100I</sup></i>    | 91.58%             | 3.51%      |
| <b>Mutants expressed in <i>vps37Δ</i></b>                      | <b>MVB Sorting</b> | <b>STD</b> |   |                    |            |
| Vector   | 0.00%              | 0.85%      | <b>Mutants co-expressed in <i>vps23Δ vps25Δ</i></b> | <b>MVB Sorting</b> | <b>STD</b> |
| VPS37  | 100.00%            | 3.10%      | Vector+VPS20  | 0.86%              | 7.39%      |
| VPS20  | 10.28%             | 3.00%      | Vector+SNF7   | 24.58%             | 2.79%      |
| SNF7   | 23.60%             | 3.05%      | Vector+ <i>myrsnf7<sup>R52E Q90L</sup></i>          | 103.91%            | 1.01%      |
| <i>myrsnf7<sup>R52E Q90L</sup></i>                             | 89.65%             | 0.33%      | Vector+ <i>myrsnf7<sup>R52E Q90L N100I</sup></i>    | 96.39%             | 4.07%      |
| <i>myrsnf7<sup>R52E Q90L N100I</sup></i>                       | 94.33%             | 5.12%      |   |                    |            |
| <b>Mutants expressed in <i>vps23Δ chm7Δ</i></b>                | <b>MVB Sorting</b> | <b>STD</b> |   |                    |            |

|   |         |        |
|---|---------|--------|
| <i>Vector+Vector</i>                            | 0.00%   | 4.67%  |
| <i>VPS23+CHM7</i>                               | 100.00% | 1.38%  |
| <i>VPS23+Vector</i>                             | 99.52%  | 4.28%  |
| <i>Vector+CHM7</i>                              | 5.04%   | 20.59% |
| <i>VPS23+<sup>R52E Q90L N100I</sup>myrsnf7</i>  | 106.35% | 3.68%  |
| <i>myrsnf7<sup>R52E Q90L N100I</sup>+CHM7</i>   | 96.89%  | 1.42%  |
| <i>myrsnf7<sup>R52E Q90L N100I</sup>+Vector</i> | 97.75%  | 2.05%  |
| <i>SNF7+Vector</i>                              | 5.27%   | 13.04% |
| <i>VPS20+Vector</i>                             | 3.18%   | 3.17%  |

Notes: "\*" representing data provided by Nicholas J. Buchkovich

**Table A4.8 Summary of Mup1-pHluorin MVB Sorting in *escrt-0Δ* Yeast**

| Mutants expressed in <i>vps27Δ</i>  | MVB Sorting | STD    | Mutants co-expressed in <i>vps27Δ vps20Δ</i>                                | MVB Sorting | STD    |
|---|-------------|--------|---|-------------|--------|
| Vector  | 0.00%       | 2.87%  | Vector+Vector   | 0.00%       | 4.99%  |
| VPS27   | 100.00%     | 0.76%  | VPS27+VPS20   | 100.00%     | 1.66%  |
| VPS20   | 0.98%       | 3.85%  | VPS27+Vector  | 6.54%       | 16.19% |
| SNF7  | 1.70%       | 6.21%  | Vector+VPS20  | 7.98%       | 9.12%  |
| <i>myrsnf7</i> <sup>R52E Q90L</sup>   | 12.47%      | 6.83%  | Vector+SNF7   | 8.35%       | 20.74% |
| <i>myrsnf7</i> <sup>R52E Q90L N100I</sup>                                   | 27.80%      | 8.83%  | Vector+ <i>myrsnf7</i> <sup>R52E Q90L</sup>                                 | 13.16%      | 7.70%  |
| <i>SNF7-BRO1</i> <sup>PRD</sup>   | 16.33%      | 14.97% | Vector+ <i>myrsnf7</i> <sup>R52E Q90L N100I</sup>                           | 18.71%      | 12.92% |
| <i>myrsnf7</i> <sup>R52E Q90L N100I</sup> -<br><i>BRO1</i> <sup>PRD</sup>   | 12.88%      | 5.60%  | VPS20+vps27 <sup>S270D S313D</sup>  | 18.03%      | 8.13%  |
| <i>snf7</i> <sup>L231K L234K</sup>  | 15.12%      | 12.05% | <i>myrsnf7</i> <sup>R52E Q90L N100I</sup> +<br>VPS27                        | 53.75%      | 12.16% |
| <i>myrsnf7</i> <sup>R52E Q90L N100I L231K L234K</sup>                       | 5.96%       | 18.08% | <i>myrsnf7</i> <sup>R52E Q90L N100I</sup> +<br>vps27 <sup>S270D S313D</sup> | 4.43%       | 10.94% |
| <i>snf7</i> <sup>L234K</sup>  | 9.83%       | 20.11% | <i>myrsnf7</i> <sup>R52E Q90L N100I</sup> +<br>vps27 <sup>1-580</sup>       | 8.94%       | 4.50%  |
| <i>myrsnf7</i> <sup>R52E Q90L N100I L234K</sup>                             | 13.67%      | 7.26%  | VPS20+vps27 <sup>1-580</sup>  | 11.88%      | 5.86%  |
| <i>snf7</i> <sup>1-225</sup>  | 9.89%       | 2.30%  |   |             |        |
| <i>myrsnf7</i> <sup>R52E Q90L 1-225</sup>                                   | -4.04%      | 6.74%  | Mutants co-expressed in <i>hse1Δ vps20Δ</i>                                 | MVB Sorting | STD    |
| <i>myrsnf7</i> <sup>R52E Q90L N100I 1-225</sup>                             | 11.90%      | 0.75%  | Vector+Vector   | 0.00%       | 7.98%  |
| S270D S313D   | 99.08%      | 1.10%  | VPS20+HSE1  | 100.00%     | 0.73%  |
| 1-580   | 14.96%      | 16.35% | VPS20+Vector  | 79.06%      | 1.93%  |
| Mutants co-expressed in <i>vps27Δ</i>                                       | MVB Sorting | STD    | Vector+HSE1   | 3.50%       | 4.19%  |
| Vector+Vector   | 0.00%       | 2.01%  | Vector+SNF7   | 4.96%       | 10.23% |
| VPS27+Vector  | 100.00%     | 0.24%  | <i>myrsnf7</i> <sup>R52E Q90L</sup> +VPS20                                  | 55.48%      | 4.46%  |
| VPS27+HSE1-DUB  | 24.31%      | 3.87%  | <i>myrsnf7</i> <sup>R52E Q90L N100I</sup> +<br>VPS20                        | 64.47%      | 9.05%  |
| <i>myrsnf7</i> <sup>R52E Q90L</sup> +<br>HSE1-DUB                           | -1.66%      | 13.42% | <i>myrsnf7</i> <sup>R52E Q90L</sup> +HSE1                                   | 45.57%      | 11.89% |
| <i>myrsnf7</i> <sup>R52E Q90L N100I</sup> +<br>HSE1-DUB                     | 8.00%       | 9.65%  | <i>myrsnf7</i> <sup>R52E Q90L N100I</sup> +HSE1                             | 56.37%      | 11.87% |
| Mutants co-expressed in <i>vps27Δ hse1Δ</i>                                 | MVB Sorting | STD    | Vector+ <i>myrsnf7</i> <sup>R52E Q90L</sup>                                 | 8.25%       | 2.04%  |
| Vector+Vector   | 0.00%       | 4.84%  | Vector+ <i>myrsnf7</i> <sup>R52E Q90L N100I</sup>                           | 10.03%      | 1.39%  |
| VPS27+HSE1  | 100.00%     | 0.63%  | Mutants co-expressed in <i>vps27Δ vps23Δ</i>                                | MVB Sorting | STD    |
| VPS27+Vector  | 98.89%      | 0.62%  | Vector+Vector   | 0.00%       | 4.09%  |
| Vector+HSE1   | 5.47%       | 7.78%  | VPS23+VPS27   | 100.00%     | 2.37%  |
| <i>myrsnf7</i> <sup>R52E Q90L N100I</sup> +VPS27                            | 88.60%      | 4.53%  | VPS23+Vector  | 15.77%      | 5.01%  |
| <i>myrsnf7</i> <sup>R52E Q90L N100I</sup> +<br>vps27 <sup>S270D S313D</sup> | 18.85%      | 6.15%  | Vector+VPS27  | 9.08%       | 0.86%  |
| <i>myrsnf7</i> <sup>R52E Q90L N100I</sup> +<br>vps27 <sup>580</sup>         | 47.70%      | 5.55%  | Vector+VPS20  | 8.67%       | 1.12%  |
|   |             |        | Vector+SNF7   | 1.30%       | 8.54%  |

|   |                    |            |  |                    |            |
|---|--------------------|------------|--|--------------------|------------|
| <i>myrsnf7</i> <sup>R52E Q90L N100I</sup> +HSE1       | 22.28%             | 4.32%      | <i>Vector+myrsnf7</i> <sup>R52E Q90L</sup>   | 4.78%              | 1.26%      |
|   |                    |            | <i>Vector+myrsnf7</i> <sup>R52E Q90L N100I</sup>                                   | 32.76%             | 3.92%      |
| <b>Mutants co-expressed in <i>vps23Δ hse1Δ</i></b>    | <b>MVB Sorting</b> | <b>STD</b> | <i>VPS23+</i><br><i>vps27</i> <sup>S270D S313D</sup>                               | 5.87%              | 8.64%      |
| <i>Vector+Vector</i>                                  | 0.00%              | 9.34%      | <i>myrsnf7</i> <sup>R52EQ90LN100I</sup> + <i>VPS27</i>                             | 98.47%             | 6.15%      |
| <i>VPS23+HSE1</i>                                     | 100.00%            | 1.37%      | <i>myrsnf7</i> <sup>R52E Q90L N100I</sup> +<br><i>vps27</i> <sup>S270D S313D</sup> | 6.55%              | 18.03%     |
| <i>VPS23+Vector</i>                                   | 77.24%             | 5.54%      |  |                    |            |
| <i>Vector+HSE1</i>                                    | 13.08%             | 10.94%     | <b>Mutants co-expressed in <i>vps27Δ vps25Δ</i></b>                                | <b>MVB Sorting</b> | <b>STD</b> |
| <i>VPS23+myrsnf7</i> <sup>R52E Q90L N100I</sup>       | 47.86%             | 3.32%      | <i>Vector+Vector</i>   | 0.00%              | 10.45%     |
| <i>myrsnf7</i> <sup>R52E Q90L N100I</sup> +HSE1       | 92.69%             | 2.11%      | <i>VPS27+VPS25</i>   | 100.00%            | 5.36%      |
| <i>myrsnf7</i> <sup>R52E Q90L N100I</sup> +Vector     | 17.67%             | 6.66%      | <i>VPS27+Vector</i>  | 9.05%              | 8.82%      |
| <i>SNF7+Vector</i>                                    | 20.39%             | 2.77%      | <i>Vector+VPS25</i>  | 1.94%              | 10.11%     |
| <i>VPS20+Vector</i>                                   | 7.97%              | 18.09%     | <i>Vector+VPS20</i>  | -0.13%             | 9.84%      |
|   |                    |            | <i>Vector+SNF7</i>   | 6.83%              | 8.78%      |
| <b>Mutants co-expressed in <i>vps25Δ hse1Δ</i></b>    | <b>MVB Sorting</b> | <b>STD</b> | <i>Vector+myrsnf7</i> <sup>R52E Q90L</sup>   | 11.06%             | 14.14%     |
| <i>Vector+Vector</i>                                  | 0.00%              | 9.18%      | <i>Vector+myrsnf7</i> <sup>R52E Q90L N100I</sup>                                   | 24.18%             | 16.91%     |
| <i>VPS25+HSE1</i>                                     | 100.00%            | 1.41%      | <i>VPS25+vps27</i> <sup>S270D S313D</sup>  | 1.27%              | 7.15%      |
| <i>VPS25+Vector</i>                                   | 80.84%             | 3.32%      | <i>myrsnf7</i> <sup>R52E Q90L N100I</sup> +<br><i>VPS27</i>                        | 60.97%             | 13.48%     |
| <i>Vector+HSE1</i>                                    | 8.58%              | 9.35%      | <i>myrsnf7</i> <sup>R52E Q90L N100I</sup> +<br><i>vps27</i> <sup>S270D S313D</sup> | 19.23%             | 4.59%      |
| <i>VPS25+myrsnf7</i> <sup>R52E Q90L N100I</sup>       | 61.00%             | 10.04%     |  |                    |            |
| <i>myrsnf7</i> <sup>R52E Q90L N100I</sup> +HSE1       | 64.09%             | 10.11%     |  |                    |            |
| <i>myrsnf7</i> <sup>R52E Q90L N100I</sup> +<br>Vector | 9.91%              | 15.98%     |  |                    |            |
| <i>SNF7+Vector</i>                                    | 11.46%             | 6.96%      |  |                    |            |
| <i>VPS20+Vector</i>                                   | 9.93%              | 7.32%      |  |                    |            |

**Table A4.9 Summary of Mup1-pHluorin MVB Sorting in *bro1Δ* yeast**

| Mutants expressed in <i>bro1Δ</i>                       | MVB Sorting        | STD        | Mutants expressed in <i>bro1Δ vps25Δ</i>  | MVB Sorting        | STD        |
|---|--------------------|------------|---|--------------------|------------|
| Vector  | 0.00%              | 3.41%      | Vector+Vector   | 0.00%              | 3.45%      |
| WT  | 100.00%            | 0.28%      | VPS25+BRO1  | 100.00%            | 1.10%      |
| <i>I144D L336D</i>                                      | 82.19%             | 4.93%      | VPS25+Vector  | 8.77%              | 9.28%      |
| <i>I377R L386R</i>                                      | 100.51%            | 1.29%      | Vector+BRO1   | 4.23%              | 2.86%      |
| 1-710 ( $\Delta$ PRD)                                   | 43.03%             | 2.42%      | Vector+VPS20  | 17.38%             | 2.86%      |
| VPS20   | 4.77%              | 2.77%      | Vector+SNF7   | 4.71%              | 12.39%     |
| SNF7  | 18.93%             | 4.68%      | Vector+myrsnf7 <sup>R52E Q90L</sup>   | 4.29%              | 11.40%     |
| myrsnf7 <sup>R52E Q90L</sup>                            | 27.76%             | 7.95%      | Vector+myrsnf7 <sup>R52E Q90L N100I</sup>   | 3.06%              | 8.75%      |
| myrsnf7 <sup>R52E Q90L N100I</sup>                      | 11.29%             | 9.57%      | myrsnf7 <sup>R52E Q90L</sup> +BRO1  | 66.30%             | 4.07%      |
| SNF7-BRO1 <sup>PRD</sup>                                | 17.62%             | 11.95%     | myrsnf7 <sup>R52E Q90L</sup> + <i>bro1</i> <sup>I144D L336D</sup>                             | 2.41%              | 2.73%      |
| myrsnf7 <sup>R52E Q90L N100I</sup> -BRO1 <sup>PRD</sup> | 21.73%             | 18.34%     | myrsnf7 <sup>R52E Q90L N100I</sup> +BRO1  | 64.36%             | 9.96%      |
| <i>snf7</i> <sup>L231K L234K</sup>                      | 22.78%             | 0.07%      | myrsnf7 <sup>R52E Q90L N100I</sup> +<br><i>bro1</i> <sup>I144D L336D</sup>                    | 13.87%             | 1.05%      |
| myrsnf7 <sup>R52E Q90L N100I L231K L234K</sup>          | 19.15%             | 2.04%      | myrsnf7 <sup>R52E Q90L N100I L231K</sup><br><i>L234K</i> +BRO1                                | 9.82%              | 14.18%     |
| <i>snf7</i> <sup>L234K</sup>                            | 13.42%             | 20.72%     | myrsnf7 <sup>R52E Q90L N100I L231K</sup><br><i>L234K</i> + <i>bro1</i> <sup>I144D L336D</sup> | 18.99%             | 1.97%      |
| myrsnf7 <sup>R52E Q90L N100I L234K</sup>                | 13.76%             | 12.17%     | VPS25+ <i>bro1</i> <sup>I377R L386R</sup>   | 102.19%            | 2.79%      |
| <i>snf7</i> <sup>1-225</sup>                            | 14.95%             | 13.01%     | myrsnf7 <sup>R52E Q90L N100I</sup> +<br><i>bro1</i> <sup>I377R L386R</sup>                    | 13.02%             | 7.64%      |
| myrsnf7 <sup>R52E Q90L 1-225</sup>                      | 11.51%             | 10.00%     |   |                    |            |
| myrsnf7 <sup>R52E Q90L N100I 1-225</sup>                | 3.09%              | 3.93%      | <b>Mutants expressed in <i>bro1Δ vps23Δ</i></b>   | <b>MVB Sorting</b> | <b>STD</b> |
| <b>Mutants co-expressed in <i>bro1Δ</i></b>             | <b>MVB Sorting</b> | <b>STD</b> | Vector+Vector   | 0.00%              | 4.01%      |
| Vector+Vector   | 0.00%              | 2.35%      | VPS23+BRO1  | 100.00%            | 0.40%      |
| BRO1+Vector   | 100.00%            | 0.19%      | VPS23+Vector  | 0.22%              | 4.25%      |
| BRO1+HSE1-DUB   | 24.06%             | 2.98%      | Vector+BRO1   | 8.26%              | 12.52%     |
| myrsnf7 <sup>R52E Q90L</sup> +<br>HSE1-DUB              | 16.30%             | 10.23%     | Vector+VPS20  | 6.85%              | 7.76%      |
| myrsnf7 <sup>R52E Q90L N100I</sup> +<br>HSE1-DUB        | 14.41%             | 9.46%      | Vector+SNF7   | 10.81%             | 5.72%      |
| <b>Mutants expressed in <i>bro1Δ vps20Δ</i></b>         | <b>MVB Sorting</b> | <b>STD</b> | Vector+myrsnf7 <sup>R52E Q90L</sup>   | 3.48%              | 5.08%      |
| Vector+Vector   | 0.00%              | 1.64%      | Vector+myrsnf7 <sup>R52E Q90L N100I</sup>   | 11.49%             | 7.92%      |
| VPS20+BRO1  | 100.00%            | 2.47%      | myrsnf7 <sup>R52E Q90L</sup> +BRO1  | 93.31%             | 1.80%      |
| Vector+BRO1   | 8.85%              | 4.21%      | myrsnf7 <sup>R52E Q90L</sup> +<br><i>bro1</i> <sup>I144D L336D</sup>                          | 15.28%             | 0.89%      |
| VPS20+Vector  | 3.54%              | 6.16%      | myrsnf7 <sup>R52E Q90L N100I</sup> +BRO1  | 80.99%             | 1.18%      |
| Vector+SNF7   | 11.30%             | 1.39%      | myrsnf7 <sup>R52E Q90L N100I</sup> +<br><i>bro1</i> <sup>I144D L336D</sup>                    | 6.22%              | 7.70%      |
| Vector+myrsnf7 <sup>R52E Q90L</sup>                     | 7.23%              | 3.47%      | myrsnf7 <sup>R52E Q90L N100I L231K</sup><br><i>L234K</i> +BRO1                                | 14.90%             | 11.23%     |
|   |                    |            | myrsnf7 <sup>R52E Q90L N100I L231K</sup><br><i>L234K</i> + <i>bro1</i> <sup>I144D L336D</sup> | 19.07%             | 2.22%      |
|   |                    |            | VPS23+ <i>bro1</i> <sup>I377R L386R</sup>   | 99.32%             | 2.54%      |

|  |         |        |  |                        |            |
|--|---------|--------|--|------------------------|------------|
| <i>Vector+myrsnf7</i> <sup>R52E Q90L N100I</sup>   | 11.06%  | 3.78%  | <i>myrsnf7</i> <sup>R52E Q90L N100I</sup> +<br><i>bro1</i> <sup>I377R L386R</sup>              | 5.88%                  | 1.19%      |
| <i>myrsnf7</i> <sup>R52E Q90L</sup> + <i>BRO1</i>  | 48.92%  | 2.79%  |  |                        |            |
| <i>myrsnf7</i> <sup>R52E Q90L</sup> +<br><i>bro1</i> <sup>I144D L336D</sup>                  | 16.82%  | 4.47%  | <b>Mutants expressed in<br/><i>bro1</i><math>\Delta</math> <i>vps27</i><math>\Delta</math></b> | <b>MVB<br/>Sorting</b> | <b>STD</b> |
| <i>myrsnf7</i> <sup>R52E Q90L N100I</sup> + <i>BRO1</i>                                      | 51.94%  | 1.77%  | <i>Vector+Vector</i>   | 0.00%                  | 9.66%      |
| <i>myrsnf7</i> <sup>R52E Q90L N100I</sup> +<br><i>bro1</i> <sup>I144D L336D</sup>            | 10.99%  | 10.20% | <i>VPS27+BRO1</i>  | 100.00%                | 3.12%      |
| <i>myrsnf7</i> <sup>R52E Q90L N100I L231K</sup> + <i>BRO1</i>                                | 11.41%  | 7.94%  | <i>VPS27+Vector</i>  | 9.37%                  | 9.37%      |
| <i>myrsnf7</i> <sup>R52E Q90L N100I L231K</sup> +<br><i>bro1</i> <sup>I144D L336D</sup>      | 6.59%   | 3.45%  | <i>Vector+BRO1</i>   | 9.35%                  | 17.91%     |
| <i>VPS20+bro1</i> <sup>I377R L386R</sup>   | 102.12% | 1.61%  | <i>Vector+VPS20</i>  | 4.70%                  | 9.87%      |
| <i>myrsnf7</i> <sup>R52E Q90L N100I</sup> +<br><i>bro1</i> <sup>I377R L386R</sup>            | 9.57%   | 13.35% | <i>Vector+SNF7</i>   | 2.71%                  | 0.91%      |
| <i>myrsnf7</i> <sup>R52E Q90L N100I</sup> +<br><i>bro1</i> <sup><math>\Delta</math>PRD</sup> | 4.72%   | 6.81%  | <i>Vector+myrsnf7</i> <sup>R52E Q90L</sup>   | 9.83%                  | 5.52%      |
|  |         |        | <i>Vector+myrsnf7</i> <sup>R52E Q90L N100I</sup>   | 15.13%                 | 8.01%      |